# FABRICATION OF NANOSTRUCTURED ELECTRODES AND INTERFACES USING COMBUSTION CVD

A Dissertation
Presented to
The Academic Faculty
By

Ying Liu

In Partial Fulfillment
Of the Requirements for the Degree of
Doctor of Philosophy in Materials Science and Engineering

Georgia Institute of Technology
December 2005

# FABRICATION OF NANOSTRUCTURED ELECTRODES AND INTERFACES USING COMBUSTION CVD

Approved by:


Dr. Meilin Liu, Advisor
School of Materials Science and Engineering
*Georgia Institute of Technology*

Dr. Robert L. Snyder
School of Materials Science and Engineering
*Georgia Institute of Technology*

Dr. W. Brent Carter
School of Materials Science and Engineering
*Georgia Institute of Technology*

Dr. C. P. Wong
School of Materials Science and Engineering
*Georgia Institute of Technology*

Dr. Dennis W. Hess
School of Chemical and Biomolecular Engineering
*Georgia Institute of Technology*



Date Approved: August 19, 2005

## ACKNOWLEDGMENTS

The author would like to sincerely thank Dr. Meilin Liu for his academic guidance in the research and study.

The author is grateful to each of my committee members, Dr. W. Brent Carter, Dr. Dennis W. Hess, Dr. Robert L. Snyder, and Dr. C. P. Wong for their precious time and expertise in helping me gain a better understanding of my research.

Thanks are also extended to the researchers in the Solid State Ionics group at Georgia Institute of Technology for their assistance.

The author would like to pay tribute to his parents, Kexin Liu and Fuyuan Chen, who supported the author continuously and unconditionally throughout.

The authors wish to gratefully acknowledge Dr. Radenka Maric and Dr. Miodrag Oljaca at nGmat Co. for technical discussions and assistance on combustion CVD.

This work was supported by the Office of Science, Department of Energy under Grant No. DE-FG02-01ER15220, Department of Energy National Energy Technology Laboratory under Grant No. DE-FG26-01NT41274, and by the Georgia Institute of Technology Molecular Design Institute under prime contract N00014-95-1-1116 from the Office of Naval Research.

## TABLE OF CONTENTS

**ACKNOWLEDGMENTS** ..... **iii**

**LIST OF TABLES** ..... **vii**

**LIST OF FIGURES** ..... **viii**

**LIST OF ABBREVIATIONS** ..... **xvi**

**SUMMARY** ..... **xviii**

**CHAPTER I INTRODUCTION** ..... **1**

**CHAPTER 2 BACKGROUND** ..... **4**
2.1 Solid Oxide Fuel Cell (SOFC) Technology ..... 4
2.1.1 Advantages of Solid Oxide Fuel Cells ..... 5
2.1.2 Cell Configuration ..... 6
2.1.3 Materials for SOFC Components ..... 13
2.1.4 Cell Fabrication Techniques ..... 21
2.1.5 Applications of SOFCs ..... 23
2.2 Combustion Chemical Vapor Deposition (CVD) ..... 25
2.2.1 Thin Film Deposition Methods ..... 25
2.2.2 Combustion CVD Process ..... 28
2.2.3 Advantages of Combustion CVD ..... 29
2.2.4 Applications of Combustion CVD ..... 31
2.2.5 Modeling of Combustion CVD ..... 32
2.3 Research Motivation and Objectives ..... 38

**CHAPTER 3 TECHNICAL APPROACHE** ..... **44**
3.1 Combustion CVD System ..... 44
3.2 Sample Preparation ..... 46
3.3 Film Characterization ..... 47
3.3.1 Microstructure characterization ..... 47
3.3.2 Phase identification ..... 48
3.3.3 Electrochemical analysis ..... 48
3.4 Experimental Design ..... 50
3.4.1 Parametric Studies ..... 50
3.4.2 SOFC Electrodes with Superior Performance ..... 51
3.4.3 SOFC Electrodes with “Designed” Microstructures ..... 51

3.4.4 Modified Combustion CVD Process ..... 51
3.4.5 Porous Films and Novel Structures for Other Applications ..... 52

**CHAPTER 4 NOVEL ELECTRODES FOR SOLID OXIDE FUEL CELLS..... 53**
4.1 Optimization of Deposition Parameters in Term of Interfacial Resistance..... 53
4.1.1 Experimental..... 53
4.1.2 Results and Discussion..... 55
4.1.3 Summary..... 66
4.2 Nanostructured Electrodes with Dramatically Low Interfacial Resistances ..... 68
4.2.1 Experimental..... 71
4.2.2 Results and Discussion ..... 72
4.2.3 Summary..... 79
4.3 Functionally Graded Electrodes ..... 80
4.3.1 Experimental..... 82
4.3.2 Results and Discussion ..... 84
4.3.3 Summary..... 89
4.5 Electrodes Produced by A Dual-Phase (Particle-Solution) Spraying Process..... 90
4.5.1 Experimental..... 92
4.5.2 Results and Discussion ..... 93
4.5.3 Summary..... 100
4.4 Electrodes Fabricated by A Modified Combustion Spray Process..... 102
4.4.1 Description of the Process ..... 103
4.4.2 Experimental Procedures..... 106
4.4.3 Results and Discussion ..... 107
4.4.4 Summary..... 109
4.5 Porous Ceramic Monoliths Created by the Removal of a Sacrificial Metal Oxide Phase during Sintering..... 112
4.5.1 Experimental..... 113
4.5.2 Results and Discussion ..... 114
4.5.3 Summary..... 121
4.6 SOFC Anodes with Metal Oxide Induced Porosity Variation..... 123
4.6.1 Experimental..... 124
4.6.2 Results and Discussion ..... 126
4.6.3 Summary..... 129

**CHAPTER 5 NANOSTRUCTURED $SNO_2$ THIN FILMS FOR GAS SENSORS ..... 132**
5.1 Experimental..... 133
5.2 Results and Discussion ..... 136
5.3 Summary..... 145

**CHAPTER 6 NANOMATERIALS OF SEMICONDUCTING OXIDES ..... 147**
6.1 Aligned $SnO_2$ Nanotubes..... 147
6.1.1 Experimental..... 148
6.1.2. Results and Discussion ..... 149
6.1.3 Summary..... 166

6.2 Ordered ZnO Rods ..... 167
6.2.1 Experimental ..... 168
6.2.2 Results and Discussion ..... 169
6.2.3 Summary ..... 174
6.3. Two Dimensional ZnO Flakes ..... 177
6.3.1 Experimental ..... 178
6.3.2 Results and Discussion ..... 179
6.5.3 Summary ..... 187

**REFERENCES ..... 188**

## LIST OF TABLES

Table 2-1 Nernst potentials of several reactions 9

Table 2-2 Characteristics of single cell configurations 10

Table 2-3 Requirements for solid oxide fuel cell components 13

Table 2-4 Selected fabrication approaches for SOFC electrolytes 22

Table 2-5 Commonly used methods for SOFC electrodes fabrication 23

Table 2-6 Major vapor phase thin film deposition methods 26

Table 2-7 Film deposition processes similar to combustion CVD 27

Table 4-1 Major deposition variables 54

Table 5-1 Characteristics of $SnO_2$ sensors fabricated by different approaches 141

## LIST OF FIGURES

Figure 2-1 A schematic of a solid oxide fuel cell 6

Figure 2-2 Tubular solid oxide fuel cell design 13

Figure 2-3 Planar solid oxide fuel cell design 13

Figure 2-4 The cubic fluorite structure of $CaF_2$ or $CeO_2$ 17

Figure 2-5 Comparison between combustion CVD and traditional CVD system 28

Figure 2-6 Surface energies of heterogeneously nucleated particles 33

Figure 2-7 (a) Ostwald ripening, (b) Sintering, and (c) cluster migration. 36

Figure 2-8 Deposition matrix showing which microstructural zone is present at each deposition condition. 38

Figure 2-9 Various structures created by combustion CVD 41

Figure 3-1 A schematic of combustion CVD process. 45

Figure 3-2 Schematic of the new version of atomizer 45

Figure 3-3 (a) Schematic and (b) actual appearance of fuel cell testing assembly. (c) Fuel cell testing apparatus consisting of a tube furnace, cell assembly, and fuel supply. (d) Solartron 1287 interface and 1250 FRA. 49

Figure 4-1 Typical SEM micrographs of 70wt.% SSC+30wt.%SDC cathodes fabricated by combustion CVD at different temperatures for 20 minutes on a 250 μm thick GDC electrolyte substrate. 56

Figure 4-2 Interfacial polarization resistances of symmetrical cells as determined from impedance spectroscopy. The temperature adjacent to each curve represents the temperature at which the electrodes were fabricated by combustion CVD. 57

Figure 4-3 X-ray diffraction patterns of SSC-SDC cathodes fabricated at different deposition temperatures (800°C, 1000°C, 1200°C, and 1400°C) by combustion CVD (deposition time: 20 minutes; precursor concentration: 0.05 M; substrate: GDC). 58

Figure 4-4 Cross-sectional views (SEM micrographs) of cathodes fabricated by combustion CVD with different deposition time. (deposition temperature: 1200°C; precursor concentration: 0.05 M; substrate: GDC). 60

Figure 4-5 A plot of electrode thickness as a function of deposition time (deposition temperature: 1200°C; precursor concentration: 0.05 M; substrate: GDC). The thicknesses were determined from SEM cross-section micrographs. 61

Figure 4-6 Interfacial polarization resistances of symmetrical cells with electrodes fabricated by CCVD with different deposition times (2, 5, 10, 20 minutes). 62

Figure 4-7 Cross-sectional views (SEM micrographs) of cathodes fabricated by combustion CVD with different precursor concentration: (a) 0.005 M for 50 minutes; (b) 0.05 M for 5 minutes, and (c) 0.25 M for 1 minute. (Deposition temperature: 1250°C; substrate: GDC) 63

Figure 4-8 Interfacial polarization resistances of symmetrical cells with electrodes fabricated by CCVD with different precursor concentration. The interfacial polarization resistances were determined from impedance spectroscopy under open circuit conditions. 64

Figure 4-9 Cross-sectional views of cathodes fabricated by combustion CVD on two different substrates: (a) GDC and (b) YSZ. 66

Figure 4-10 Cross-sectional views of an SOFC with both anode and cathode fabricated using combustion CVD: (a) the entire cell with Ni-SDC anode, GDC electrolyte, and SSC-SDC cathode, (b) anode-electrolyte interface, (c) cathode-electrolyte interface, (d) higher magnification of Ni-SDC composite anode, and (e) higher magnification of SSC-SDC composite cathode. 73

Figure 4-11 X-ray diffraction patterns of the anode (70wt.% Ni and 30wt.% SDC) and the cathode (70wt.% SSC and 30wt.% SDC) fabricated using combustion CVD. 74

Figure 4-12 (a) Impedance spectra of a single fuel cell as measured using a two-electrode configuration, and (b) The bulk electrolyte and interfacial polarization resistances obtained from impedance spectra acquired at different temperatures. 75

Figure 4-13 Comparison of interfacial polarization resistances as determined from impedance spectra for electrodes fabricated using different techniques: slurry-painting,[19] spin-coating,[8] and screen-printing.[27] 77

Figure 4-14 Cell voltages and power densities as a function of current density for fuel cells with: (a) both cathode (SSC-SDC) and anode (Ni-SDC) fabricated using combustion CVD on a GDC electrolyte membrane with thickness of 250 μm, and (b) a 20 μm thick GDC electrolyte. 78

Figure 4-15 A schematic diagram of the functionally graded SOFC configuration 83

Figure 4-16 (a) Cross-sectional view of the functionally graded cathode fabricated on an YSZ pellet using a combustion CVD process, (b) higher magnification image of the cathode showing the nanostructure, (c) EDS dot mapping showing Mn distribution on the cross-section surface, and (d) EDS dot mapping of Co distribution. 85

Figure 4-17 (a) Impedance spectra of a single fuel cell as measured using a two-electrode configuration, and (b) bulk electrolyte resistance ($R_b$) and interfacial polarization resistances ($R_a$ + $R_c$) determined from impedance spectra acquired at different temperatures. 86

Figure 4-18 Comparison of interfacial polarization resistances for YSZ electrolyte/LSM based electrodes fabricated using different techniques: spin-coating (symmetrical cell, tested in air),[8] slurry-spraying (symmetrical cell, tested in air),[126] ion impregnation (asymmetrical cell with Pt counter electrode on the other side of electrolyte, tested in air),[119] and combustion CVD (full cell, tested in air). 88

Figure 4-19 Electrical performance of a fuel cell with functionally graded cathode and anode fabricated using combustion CVD on a YSZ electrolyte membrane of 240 μm thick (Testing conditions: hydrogen with 3 v% of water vapor as the fuel and stationary air as the oxidant, both at ambient pressure). 89

Figure 4-20 A TEM micrograph of the GDC nano-particles synthesized by a glycine-nitrate method. 93

Figure 4-21 (a) Cross-sectional view of solid oxide fuel cell with SSC-GDC cathode fabricated by a particle-solution spraying process. (b) and (c) higher magnification SEM micrographs of the SSC-GDC cathode showing larger particles surrounded by nano-structured smaller particles. 94

Figure 4-22 An X-ray diffraction pattern of the SSC-GDC cathode (70wt.% SSC and 30wt.% GDC) fabricated by the particle-solution spraying process. 95

Figure 4-23 (a) Impedance spectra of a single fuel cell as measured using a two-electrode configuration.(b) Comparison of interfacial polarization resistances as determined from impedance spectra for electrodes fabricated using different techniques: screen-printing,[27] Combustion CVD,[99] and particle-solution spraying. 98

Figure 4-24 Cell voltages and power densities as a function of current density for fuel cells with SSC-GDC cathode SSC-GDC fabricated by the particle-solution spraying process. 99

Figure 4-25 Schematic illustrations of the formation processes of the porous SSC-GDC composite cathodes: (a) three nucleation sites of SSC nano-particles, (b), (c), and (d) different growth stages of composite grains. 101

Figure 4-26 A schematic apparatus for combustion spray. 104

Figure 4-27 (a) A cross-sectional view of a solid oxide fuel cell with SSC-GDC cathode fabricated by a combustion spray process and (b) a higher magnification SEM micrographs of the cathode. 107

Figure 4-28 (a) Impedance spectra of a single fuel cell as measured using a two-electrode configuration, and (b) comparison of interfacial polarization resistances as determined from impedance spectra for electrodes fabricated using different techniques: screen-printing,[17] and combustion spray. 110

Figure 4-29 Cell voltages and power densities as a function of current density for fuel cells with SSC-GDC cathode fabricated by a combustion spray process. 111

Figure 4-30 X-ray diffraction (XRD) patterns of the as-prepared $SnO_2$, $CeO_2$, and $SnO_2$-$CeO_2$ nanocomposite powders. 115

Figure 4-31 TEM bright field images and the corresponding selected area electron diffraction (SAED) patterns of the as-prepared nanopowders. (a) $SnO_2$, (b) $CeO_2$, (c) 40vol.%$SnO_2$-60vol.% $CeO_2$ composite. 117

Figure 4-32 SEM images of pellet prepared with 40vol% $SnO_2$ – 60vol% $CeO_2$ nano-powders. $SnO_2$ and $CeO_2$ nano-powders were prepared by combustion CVD separately and then mixed together. (a) Surface view of pellet sintered at 1450ºC × 5 hrs. (b) Cross-sectional view of pellet sintered at 1450ºC × 5 hrs. (c) Surface view of pellet after reduction at 750ºC × 3 hrs. (d) Cross-sectional view of pellet after reduction at 750ºC × 3 hrs. 118

Figure 4-33 SEM images of pellet prepared with 40vol% $SnO_2$ – 60vol% $CeO_2$ nano-powders made by combustion CVD from single precursor solution. (a) Surface view of pellet sintered at 1450ºC × 5 hrs. (b) Cross-sectional view of pellet sintered at 1450ºC × 5 hrs. (c) Surface view of pellet after reduction at 750ºC × 3 hrs. (d) Cross-sectional view of pellet after reduction at 750ºC × 3 hrs. 120

Figure 4-34 A schematic of anode supported SOFC. Bilayer anode and GDC electrolyte were co-pressed and sintered at 1400ºC for 5 hours. SSC-GDC cathode was screen-printed onto the surface of GDC electrolyte and fired at 950ºC for 5 hours. 125

Figure 4-35 X-ray diffraction pattern of the as-prepared $SnO_2$-NiO-$Gd_{0.1}Ce_{0.9}O_2$ composite nanopowder. 126

Figure 4-36 Cross-sectional SEM images of SOFC anode and electrolyte. (a) GDC electrolyte and NiO-GDC interface after sintering. (b) NiO-GDC and $SnO_2$-NiO-GDC boundary after sintering. (c) GDC electrolyte and NiO-GDC interface after cell testing. (d) NiO-GDC and $SnO_2$-NiO-GDC boundary after cell testing. 128

Figure 4-37 Electrochemical performance of the SOFC with porosity differed bilayer anode measured at temperature range of 500-650°C. (a) impedance measurements of the cell (bulk resistances have been deducted). (b) comparison of interfacial resistances of anode supported cells with similar composition: screen-printed cathode and single layer anode,[27] combustion CVD deposited cathode and single layer anode,[99] and screen-printed cathode and porosity differed double layer anode (this work). (c) close circuit voltage and output power density as a function of current density drawn from the cell. 131

Figure 5-1Schematic of interdigitated Pt electrodes design 133

Figure 5-2 (a) Schematic of gas sensor testing apparatus. (b) Actual gas sensor testing setup in the laboratory. 135

Figure 5-3 (a) SEM image of platinum interdigitated electrodes with a strip width of 10 μm and line space of 10 μm. (b) Top view of nanostructured $SnO_2$ gas sensor fabricated at 850°C by a combustion CVD process. (c) Higher magnification SEM micrograph of $SnO_2$ thin film, showing each individual particle is less than 30 nm. (d) Cross-sectional view of $SnO_2$ sensor. The left portion shows $SnO_2$ thin film directly deposited on quartz substrate, while the right part shows $SnO_2$ film grown on Pt electrode. 137

Figure 5-4 X-ray diffraction pattern of $SnO_2$ film fabricated at 850°C for 20 minutes. $SnO_2$ thin film is determined to has a tetragonal structure. 138

Figure 5-5 (a) Typical electrical response of a $SnO_2$ gas sensor to 500ppm ethanol vapor measured at 450°C. (b) Response and recovery time of the sensor to 500 ppm ethanol vapor as a function of testing temperature from 200 °C to 500°C. 140

Figure 5-6 (a) Sensitivity of a $SnO_2$ sensor fabricated at 850°C and tested for 500ppm ethanol at different temperatures. (b) Relative conductance change with ethanol vapor concentrations for a $SnO_2$ sensor tested at 300°C. 144

Figure 6-1 Microscopic features of $SnO_2$ tubes synthesized at 1150°C: (a) cross-sectional view. (b) a single $SnO_2$ tube with partially opened top end. (c) a $SnO_2$ tube with fully open top end. and (d) $SnO_2$ tubes with open tips. 150

Figure 6-2 (a) A TEM image of a single $SnO_2$ box beam synthesized at 950°C for 30 minutes. (b) A HRTEM image and the corresponding SAED pattern near the internal surface of a $SnO_2$ box beam. 151

Figure 6-3 SEM micrographs of vertically oriented $SnO_2$ tubes synthesized at different temperatures: (a) 850°C. (b) 950°C.[130] (c) 1050°C. and (d) 1150°C. 153

Figure 6-4 An Arrhenius plot showing the dependence of cross-sectional width of as-synthesized $SnO_2$ tube arrays on synthesis temperature. 154

Figure 6-5 (a) an EDX spectrum. (b) an XRD pattern. and (c) a Raman spectrum of $SnO_2$ nanotubes synthesized at 950°C. 155

Figure 6-6 Various growth patterns of $SnO_2$ tubules: (a) two $SnO_2$ tubules grown coaxially. (b) a smaller tubule grown within a larger one with two shared walls. (c) two $SnO_2$ tubes grown in parallel with a common outer wall. (d) and (e) $SnO_2$ tubes with minute structures. (f) secondary $SnO_2$ tubes grown perpendicular to the peripheral surfaces of larger tubes. 158

Figure 6-7 SEM photographs of $SnO_2$ tube captured at different stages of growth: (a) fine $SnO_2$ polycrystalline with random orientations. (b) a favorably oriented grain grown into a top cap by Ostwald ripening. (c) and (d) growth of the existing tubules. 160

Figure 6-8 Schematics showing the proposed growth mechanism for $SnO_2$ tube arrays: (a) accumulation of a polycrystalline $SnO_2$ layer. (b) nucleation of end caps on the surface of larger grains grown by Ostwald ripening. (c) and (d) growth of $SnO_2$ tube arrays by lifting tubes up from the bottom. 161

Figure 6-9 A gas sensor based on a single $SnO_2$ nanotube: (a) SEM micrograph of a $SnO_2$ nanotube sensor. (b) response of the $SnO_2$ nanotube sensor to 7.8 v% ethanol vapor in argon at 400°C. 165

Figure 6-10 SEM images of ZnO rods synthesized using combustion CVD. (a) a top-view. (b) a higher magnification image showing the hexagonal tips. (c) a cross-sectional view of ZnO rods deposited on Si substrate at 1050°C for 30 min. (d) ZnO rods deposited at 1200°C for 30min. 170

Figure 6-11 X-ray diffraction pattern of ZnO rods synthesized at 1050°C using combustion CVD, indicating the as-synthesized ZnO rods had a hexagonal structure. 171

Figure 6-12 (a) TEM bright field image of a single ZnO rod. (b) The corresponging SAED pattern of the ZnO rod reveals [0001] growth direction. 172

Figure 6-13 A solid-state gas sensor based on a single ZnO rod placed on interdigitated Pt electrodes on a quartz substrate. 175

Figure 6-14 (a) Electrical response of a single ZnO rod sensor to ethanol vapor measured at 400°C. (b) sensitivity change with ethanol vapor concentrations for the ZnO rod sensor at 400°C. 176

Figure 6-15 SEM images of ZnO flakes synthesized at 1100°C using a combustion CVD process. 180

Figure 6-16 (a) EDX analysis of the ZnO flakes, and (b) XRD spectra. 181

Figure 6-17 (a) TEM image and the corresponding SAED pattern of a ZnO single crystal flake, and (b) A schematic showing the preferential growth orientation. 182

Figure 6-18 SEM images of ZnO flakes taken at different stages of growth. Synthesis temperature was 1100°C. 184

Figure 6-19 A solid-state gas sensor based a single crystal ZnO flake. (a) SEM micrograph of the sensor consisting of a ZnO flake and Pt interdigitated electrodes, and (b) Current variation with time under a constant voltage of 100 mV as sample gas was switched from air to different concentrations of ethanol vapor at 400°C. Data were collected at one-second intervals. 185

## LIST OF ABBREVIATIONS

| | |
|---|---|
| CCVD | Combustion chemical vapor deposition |
| EDS | Energy dispersive spectroscopy |
| EVD | Electrochemical vapor deposition |
| FAVD | Flame assisted vapor deposition |
| FRA | Frequency response analyzer |
| GDC | Gadolinia doped ceria |
| HPLC | High performance liquid chromatography |
| IPA | Isopropyl alcohol |
| LSC | Strontium doped lanthanum cobaltite |
| LSM | Strontium doped lanthanum manganite |
| MIEC | Mixed ionic and electronic conductor |
| MOCVD | Metal organic chemical vapor deposition |
| OCV | Open circuit voltage |
| SAED | Selected area electron diffraction |
| SCCM | Standard cubic centimeter |
| SDC | Samaria doped ceria |
| SEM | Scanning electron microscopy |
| SOFC | Solid oxide fuel cell |
| SSC | Strontium doped samarium cobaltite |
| TEM | Transmission electron microscopy |
| TPB | Triple phase boundary |

| | |
|---|---|
| XRD | X-ray diffractometer |
| YSZ | Yttria stabilized zirconia |

## SUMMARY

Reducing fabrication and operation costs while maintaining high performance is a major consideration for the design of a new generation of solid-state ionic devices, such as fuel cells, batteries and sensors. One of the key issues is to enhance mass and charge transport throughy porous electrodes, improve electrode/electrolyte interfacial conditions, thus facilitate reaction kinetics and improve electrochemical/catalytic properties of the system. In addition to searching for new materials, developing new fabrication approaches and creating novel microstructures are effective methodologies to achieve this goal.

The objective of this research is to fabricate nanostructured materials for energy storage and conversion applications, particularly porous electrodes with nanostructured features for solid oxide fuel cells (SOFCs) and high surface area films with desired crystallographic structures for gas sensing using combustion CVD process. The extremely large surface area combined with optimum pathway for mass and charge transport will greatly facilitate electrochemical kinetics. High fabrication temperature ensures the formation of desired crystallographic structures and improves interfacial bonding, while relatively short period of time required for combustion CVD process alleviates tendency of deleterious electrode/electrolyte boundary phases, which are normally present in systems fabricated by conventional firing approach.

Four most important deposition parameters are evaluated in this study: deposition temperature, deposition time, precursor concentration, and substrate. Deposition temperature has a significant influence on electrode microstructure (grain size, porosity, and pore size). Deposition time and precursor concentration, on the other hand, have little effect on

microstructure but determine the electrode thickness. The nature of the substrate has no observable effect on microstructure but dramatically influences the interfacial polarization resistance. The optimum combination of deposition parameters for $Sm_{0.5}Sr_{0.5}CoO_3$ (SSC)-$Sm_{0.1}CeO_2$ (SDC) cathodes on $Gd_{0.1}Ce_{0.9}O_2$ (GDC) substrates is found to be a deposition of 5 to 10 minutes using a 0.05 M solution and a deposition temperature of 1200 –1300°C.

With the optimum deposition parameters, highly porous and nano-structured electrodes for low-temperature SOFCs have been fabricated using a combustion CVD process. The electrodes fabricated consist of nano-grains of about 50 nm, exhibiting extremely high surface area and remarkably low polarization resistances. XRD patterns confirmed the formation of desired crystalline phases for as-prepared NiO-SDC anodes and SSC-SDC cathodes. It is evident that combustion CVD is a highly effective approach to fabrication of high-performance electrodes for low-temperature SOFCs, producing the lowest interfacial polarization resistances (1.09 Ω $cm^2$ at 500°C, and 0.17 Ω $cm^2$ at 600°C) ever reported for the cathode materials. Anode supported cell with a 20 μm thick electrolyte demonstrated a power density of 375 $mW/cm^2$ at 600°C. Little deterioration in either microstructure or performance was observed after 172 hours of operation.

Further, nanostructured and functionally graded $La_{0.8}Sr_{0.2}MnO_2$ (LSM)-$La_{0.8}SrCoO_3$ (LSC)-GDC composite cathodes are fabricated on 240 μm thick YSZ electrolyte supports using a combustion CVD method. The fabricated cathodes were graded in both composition and structure with higher strontium-doped lanthanum manganite (LSM) content and finer primary grain size at electrolyte side while higher strontium doped lanthanum cobaltite (LSC) content and coarser primary grain size at air/oxygen side. Extremely low interfacial polarization resistances (i.e. 0.43 Ω$cm^2$ at 700°C) and impressively high power densities (i.e.

481 mW/cm$^2$ at 800°C) were generated over the operating temperature range of 600°C–850°C.

The original combustion CVD process is modified for fabrication of porous electrodes for solid oxide fuel cells. GDC particles suspended in an SSC–ethanol solution were burned in a combustion flame, depositing a porous cathode on an anode supported GDC electrolyte. Extremely small interfacial polarization resistances were obtained, especially at low temperatures such as 450°C (1.06 Ωcm$^2$) and 500°C (0.45 Ωcm$^2$). A peak power density of 385 mW/cm$^2$ was achieved at 600°C. Finally, all parts of the composite electrodes are introduced in the form of solid ceramic particles, which are suspended in a flammable liquid carrier, and fed to the atomizer. The high velocity flame provides the energy needed for collision and sintering of the contained solid particles to produce porous electrodes. The demonstrated fast deposition rates (i.e. 40 μm in 10 min) and the elimination of post-deposition firing make this process practically valuable. The performance of the porous SOFC electrodes fabricated by the modified process is equal or better than those prepared by the conventional techniques, especially at low operating temperatures.

We have demonstrated a new, simple route for preparing highly porous ceramic monoliths through the removal of metal oxide ($SnO_2$) during high temperature sintering. Unlike the existing strategies, the new method requires neither time consuming chemical leaching nor following-up gas reduction procedures. The most critical step for our new approach is the preparation of intimately distributed 40vol.%$SnO_2$-60vol.%$CeO_2$ composite nanopowder using combustion CVD. This method provides a simple way to introduce additional porosity into ceramic materials, and can be directly incorporated into ceramic production routes without introducing extra procedures.

Composite nanopowder (20wt%$SnO_2$-50wt%NiO-30wt%GDC) was prepared using combustion CVD from a single precursor source. Bilayer SOFC anodes differing in porosity were fabricated by co-pressing of NiO-GDC powders and $SnO_2$-NiO-GDC composite nanopowder. An anode supported SOFC with bilayer anode was constructed and tested for electrochemical performance. Porosity variation in the anodes was achieved by the removal of $SnO_2$ phase during sintering and cell testing. Interfacial resistances of the bilayer anode cell were 1.20, 0.49, 0.22, and 0.1 $\Omega cm^2$ at 500, 550, 600, and 650°C respectively. Peak output power densities measured at the corresponding temperatures were 171, 301, 441, and 544 $mW/cm^2$, respectively.

Highly porous and nanostructured $SnO_2$ thin film gas sensors with Pt interdigitated electrodes have been fabricated via a combustion CVD process. The $SnO_2$ films were less than 1 μm thick and consisted of nanocrystallines smaller than 30 nm. The as-prepared $SnO_2$ gas sensors have been tested for ethanol vapor sensing behavior in the temperature range of 200–500°C. At 300°C the sensitivity to 500 ppm ethanol vapor was 1075 while the corresponding response time and recovery time were 31 and 8 seconds, respectively. The corresponding low detection limit was found to be below 1 ppm.

Several novel nanostrucutres, such as $SnO_2$ nanotubes with square-shaped or rectangular cross sections, well-aligned ZnO nanorods, and two-dimensional ZnO flakes, are synthesized using combustion CVD process. Solid state gas sensors based on single piece of these nanostructures have demonstrated superior gas sensing performances. The new nanostructure has significant scientific and technological implications. The curiosity that these nanostructures grew into particular morphologies (e.g. square or rectangular shape rather than circular shape (as carbon nanotubes do)) may stimulate interesting investigation

into the crystallization behavior of these materials during vapor phase deposition. These size-tunable nanostructures could be the building blocks of or a template for fabrication of functional devices.

In summary, this research aims to produce significant impact on concept and fabrication technology of solid-state ionic devices, as well as on fundamental understanding of the correlation between processing conditions, microstructure, and properties of the synthesized structures.

# CHAPTER I INTRODUCTION

The expanding economy of the world relies on the continued availability of reliable and affordable energy sources. Fossil fuels, coal, oil and natural gas, currently provide more than 85% of all the energy consumed in the United States, nearly two-thirds of our electricity, and virtually all of our transportation fuels. However, the fossil fuel supply will be exhausted in the next few decades as a result of the increasing demand from our economy. Alternative and renewable energy source must be secured to ensure the continuous development of our society. Aggressive exploration and deployment of new energy storage and conversion technologies is being conducted all over the world. Some of the examples are nuclear energy, wind power, solar cells, and fuel cells.

Solid oxide fuel cell (SOFC) is regarded as a promising power generation technology due to its highest energy conversion efficiency and lowest emission. It uses hydrogen (also hydrocarbon fuels) as fuel and oxygen as oxidant. The overall efficiency could be as high as 80% whilst the emission is almost zero since the only material by-product is water. The ceramic nature of all the components gives SOFC substantial advantage over other types of fuel cells and batteries in terms of fabrication, transport, and operation. In recent years, many new materials and fabrication techniques have been developed to improve the performance and lower the costs of SOFCs.

Conventional SOFCs operate over the temperature range of 800-1000°C. Though the high operating temperature promotes reaction and transport kinetics, it also puts dramatic challenges on material selection. Reduction of the operating temperature of SOFCs is desirable to lower the costs and alleviate the technical issues associated with elevated

temperatures. For example, inexpensive stainless steels could be used as interconnect materials to replace the high Cr-content ceramics if the operating temperature of the SOFCs is reduced to below 700°C. Also, sealing, a notorious problem for high temperature SOFCs, will not be an important issue. However, as the operating temperature is reduced, other issues such as lagged kinetics arise.

It has been demonstrated that the performances of the SOFCs at reduced operating temperatures are primarily limited by the properties of the electrode-electrolyte interfaces. The effective approach to radically improving interface characteristics and properties is to develop and employ mesoporous electrodes and nanostructured interfaces. The advantages offered by these structures for fuel cells include (i) dramatically-increased active surface areas (or surface-to-volume ratio) for fast electrode kinetics; (ii) significantly-increased population of defects at surfaces/interfaces and shorter diffusion lengths in the solid state for rapid transport of charge and mass; and (iii) increased flexibility in surface modification for chemically-selective catalysis. It is thus anticipated that functionally graded mixed ionic and electronic conducting (MIEC) electrodes and nanostructured interfaces will have extraordinary electrochemical behavior and will dramatically enhance the performance of batteries and fuel cells.

Combustion CVD is a relative new approach for film deposition. It uses a flammable solvent (e.g. ethanol and toluene) to carrier metal precursors. The solution is atomized by a specially designed nozzle and combusted with the help of fuel/oxidant gases. The high temperature in the combustion flame provides the thermal environment for precursor decomposition, chemical reaction, film nucleation and growth. No reaction chamber or

auxiliary heating source is required for combustion CVD. This simple approach has been used to produce many kinds of high quality thin dense films and nanopowders.

Combustion CVD has the potential to produce porous ceramic films which have the morphology in between dense films and individual particles. The desire of this research is to adopt combustion CVD to fabrication of highly porous ceramic films for solid oxide fuel cells. Porous films fabricated by combustion CVD can also be used for other related solid state electrochemical applications such as batteries and gas sensors.

The first step of this research is to study the correlation between processing conditions, microstructure, and the performance of the films. Once the optimum combination of deposition parameters is determined for the material, the porous film is fabricated as electrodes and subjected to fuel cell performance tests. Eventually, it may become reality that different microstructures (e.g. particle size, porosity, and composition) are "designed" using combustion CVD. Success in fabrication of these novel microstructures would exert great impact on technical and fundamental issues of many areas.

# CHAPTER 2 BACKGROUND

## 2.1 Solid Oxide Fuel Cell (SOFC) Technology

A solid oxide fuel cell (SOFC) is an energy conversion device, producing electricity from fuel gases (hydrogen or hydrocarbon gases) and oxygen through electrochemical reactions. Working in the same principal as a regular battery, a single SOFC has a three-layer structure: a dense electrolyte is sandwiched between two porous electrodes, an anode and a cathode. During the operation, oxygen is reduced at the cathode and hydrogen undergoes an oxidization reaction at the anode. The resulting ions (usually oxygen) diffuse through the dense electrolyte and then combine with hydrogen, producing water. Meanwhile electrons pass through the external circuit, providing electricity. In a SOFC stack, multiple cells are connected in series to generate higher voltage and power output via interconnects. Traditional high-temperature SOFCs, which usually employ a yttria-stabilized zirconia (YSZ) electrolyte, a LSM cathode and a nickel-YSZ cermet anode, operate at the temperature range of 800°C−1000°C. The biggest difference between SOFCs and batteries is that all the components of SOFCs are solid ceramic phases, which gives them great advantages in fabrication, operation, and storage. Despite being first demonstrated over 100 years ago, it is only in the last two decades that SOFC technology has received tremendous attention and now is regarded as next generation of power supply technology for military, residential, and automotive applications.

### 2.1.1 Advantages of Solid Oxide Fuel Cells

SOFCs are a radically different way of making electrical power from a variety of fuels. In addition to high conversion efficiency, SOFCs have the characteristics of environmental compatibility, modularity, siting flexibility, and multifuel capability.

(a) High conversion efficiency: The primary advantage of an SOFC is its high fuel-to-electricity conversion efficiency (45 to 60%). An SOFC converts the chemical energy of fuel directly into electrical energy. Thus the usual losses involved in the conversion of fuel to heat, to mechanical energy, and then to electrical energy are avoided. The efficiency of an SOFC is further improved up to 80% when the byproduct heat is fully utilized.

(b) Environmental compatibility: SOFCs are capable of using practical fuels as an energy source with insignificant environmental impact. Emissions of key pollutants from fuel cells are several orders of magnitude lower than those produced by conventional power generators. Production of undesirable materials such as $NO_x$, $SO_x$, and particulates is either negligible or undetectable for fuel cell systems.

(c) Modularity: Cell size can be easily increased or decreased. Since the efficiency of a fuel cell is relatively independent of size, SOFCs can be designed to follow loads with fast response times without significant efficiency loss at part-load operation.

(d) Siting flexibility: Since SOFCs can be made in a variety of sizes, they can be placed at various locations with minimum siting restrictions. SOFCs operation is quiet because a fuel cell has no moving parts. The only noises are those from auxiliary equipment.

(e) Multifuel capability: SOFCs, particularly high-temperature fuel cells, can process (reform) hydrocarbon fuels internally and do not need expensive subsystems to process conventional fuels into simple forms.

### 2.1.2 Cell Configuration

A schematic of an SOFC is shown in Figure 2-1. A single cell consists of three major components: a porous cathode, a porous anode, and a dense electrolyte.

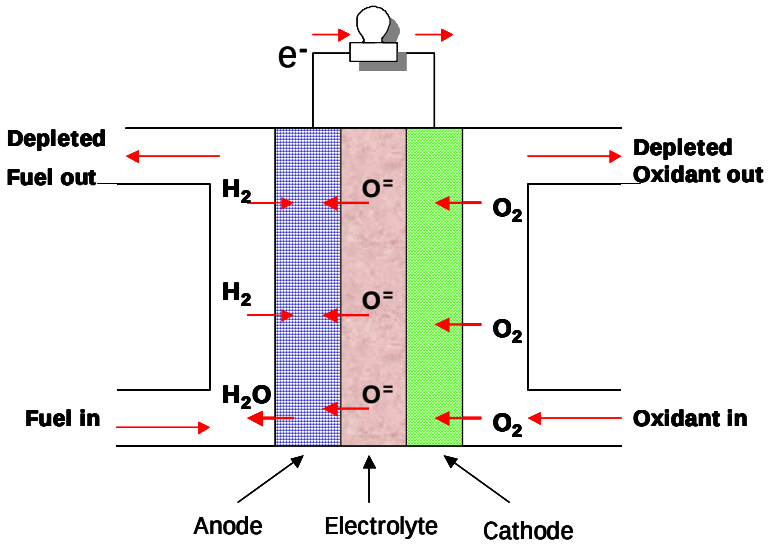


Figure 2-1 A schematic of a solid oxide fuel cell

At the anode, a fuel such as hydrogen, natural gas, or hydrocarbons, is oxidized into protons and electrons, while at the cathode, oxygen is reduced to oxygen ions. Water is

formed on either anode or cathode side depending upon the electrolyte, either a proton or oxygen ion conductor. In most cases for SOFC, the electrolyte is an oxygen ion conducting material (as illustrated in Figure 2-1) and an electronic insulator. Oxygen ions migrate through the dense ceramic electrolyte membrane, while electrons generated at anode travel along an external circuit delivering electric power.

Anode reaction: $H_2 + O_O^{\times} \leftrightarrow H_2O + V_O^{\bullet\bullet} + 2e^{'}$ Equation 2-1

Cathode reaction: $O_2 + 2V_O^{\bullet\bullet} + 4e^{'} \leftrightarrow 2O_O^{\times}$ Equation 2-2

Overall reaction: $H_2 + ½\ O_2 = H_2O + \Delta E$ Equation 2-3

The electromotive force (emf) or reversible voltage, $E_r$ is governed by Nernst equation

$$E_r = \frac{RT}{4F} \ln \frac{P_{O_{2(c)}}}{P_{O_{2(a)}}}$$ Equation 2-4

where R is the gas constant, T the temperature, F the Faraday constant, and $P_{O_2}$ the partial pressure of oxygen at the electrode ((c) cathode and (a) anode).

For a certain oxygen partial pressure at the cathode, the magnitude of $E_r$ depends on the anode oxygen partial pressure, thus on the type and composition of the fuel fed to the anode. For example, when CO is fed to the anode, the following reaction takes place at the anode:

$$CO_{(a)} + \tfrac{1}{2}\, O_{2(a)} = CO_{2(a)} \qquad \text{Equation 2-5}$$

The oxygen partial pressure at the anode is given by

$$P_{O_{a(a)}} = \left[ \frac{P_{CO_{2(a)}}}{P_{CO_{(a)}} K} \right]^2 \qquad \text{Equation 2-6}$$

where K is the equilibrium constant . Combining the above three equations yields

$$E_r = E^0 + \frac{RT}{4F} \ln P_{O_{2(c)}} + \frac{RT}{2F} \ln \frac{P_{CO_{(a)}}}{P_{CO_{2(a)}}} \qquad \text{Equation 2-7}$$

where $E^0$ is the reversible voltage at the standard state and is given as

$$E^0 = \frac{RT}{2F} \ln K \qquad \text{Equation 2-8}$$

Similar equations can be obtained when other gases are used as the fuel. For example, for hydrogen fuel, the reversible cell voltage is given as

$$E_r = E^0 + \frac{RT}{4F} \ln P_{O_{2(c)}} + \frac{RT}{2F} \ln \frac{P_{h_{2(a)}}}{P_{h_2 o_{(a)}}} \qquad \text{Equation 2-9}$$

The Nernst voltages for several cell reactions are summarized in Table 2-1

Unlike other types of fuel cell such as alkaline fuel cells (AFC), phosphoric acid fuel cells (PAFC) and polymer electrolyte membrane (PEM) fuel cells, which use liquid or polymer membranes electrolytes, SOFCs employ solid ceramic films as electrolyte materials and require operation at elevated temperatures, typically 750-1000ºC.

Table 2-1 Nernst potentials of several reactions

| Reaction | T, K | $E^0$, V |
|---|---|---|
| $H_2 + ½ O_2 = H_2O$ | 1000 | 0.997 |
| | 1250 | 0.924 |
| $CO + ½ O_2 = CO_2$ | 1000 | 1.013 |
| | 1250 | 0.898 |
| $CH_4 + 2 O_2 = CO_2 + 2 H_2O$ | 1000 | 1.039 |
| | 1250 | 1.039 |
| $C + O_2 = CO_2$ | 1000 | 1.027 |
| | 1250 | 1.027 |

From geometric point of view, SOFC single cell can be classified into two broad categories: tubular cell and planar cell. Tubular cells have the advantage of easy sealing while planar cells are easy to fabricate and handle. From fabrication consideration, SOFC can be designed as different configurations: electrolyte-supported, cathode-supported, anode-

supported, interconnect-supported, and porous substrate-supported. The major characteristics of different cell configurations are summarized in Table 2-2.[1]

Table 2-2 Characteristics of single cell configurations

| Cell configuration | Advantage | Disadvantage |
|---|---|---|
| Self-supporting | | |
| Electrolyte-supported | Relatively strong structural support dense electrolyte; Less susceptible to failure due to anode reoxidation and cathode reduction | Higher resistance due to low electrolyte conductivity; Higher operating temperatures required to minimize electrolyte ohmic losses |
| Anode-supported | Highly conductive anode; Lower operating temperature via use of thin electrolytes | Potential anode reoxidation; Mass transport limitation due to thick anodes |
| Cathode-supported | No oxidation issues but potential cathode reduction; Lower operating temperature via use of thin electrolyte | Lower conductivity; Mass transport limitation due to thick cathodes |
| External-supported | | |
| Interconnect-supported | Thin cell components for lower operating temperature; Strong structures from | Interconnect oxidation; Flowfield design limitation due to cell support requirement |

Table 2-2 Characteristics of single cell configurations (continued)

| | | |
|---|---|---|
| | metallic interconnects | |
| Porous substrate | Thin cell components for lower operating temperature; Potential for use of non-cell material for support to improve properties | Increased complexity due to addition of new materials; Potential electrical shorts with porous metallic substrate due to uneven surface |

*Stack design*

On the stack level, generally four designs have been proposed for SOFCs: the segmented-cell-in-series design, the tubular design, the monolithic design, and the planar design.

(a) Segmented-cell-in-series design: the design consists of segmented cells connected in electrical and gas flow series. The cells are either arranged as a thin banded structure on a porous support or fitted one into the other to form a tubular self-supporting structure (electrolyte supported).

(b) Tubular design: in this design, the cell is configured as a tube, and a stack consists of a bundle of single cell tubes. In the most common tubular design, the tube is made of cathode material (cathode supported) and closed at one end. Electrolyte and anode layers are formed on the outside of the tube.

(c) Monolithic design: the design consists of cell components formed into a corrugated structure of either gas coflow or crossflow configurations. The cell is commonly based on electrolyte support.

(d) Planar design: the single cell is configured as flat plates which are connected in electrical series. Common plate shapes are rectangular or circular.

At present, tubular and planar designs are the most common designs. Siemens Westinghouse has pioneered in tubular cell fabrication. As shown in Figure 2-2, the cell components are deposited in the form of thin layers on an extruded and sintered tube made of cathode material (e.g. doped lanthanum manganite).[2] YSZ electrolyte is deposited by electrochemical vapor deposition.[3] The Ni/YSZ anode is deposited by slurry coating and followed by sintering. Finally, the doped lanthanum chromite interconnection strip along the length of the cell is deposited by plasma spraying.[4] Such tubular cells have a power density at 1000°C of abut 0.25-0.3 W/cm$^2$. These low power densities make tubular SOFCs suitable only for stationary power generation and not very attractive for transportation applications.[5]

Planar SOFCs, in contrast, are capable of achieving very high power densities of up to about 2 W/cm$^2$. In the planar design as illustrated in Figure 2-3, the cell components are configured as thin, flat plates. The interconnection, which is ribbed on both sides, forms gas flow channels and serves as a bipolar gas separator contacting the anode and the cathode of adjoining cells. The cells can be fabricated by low-cost conventional ceramic processing techniques such as tape casting, slurry sintering, screen-printing, or by plasma spraying. Planar cells are more versatile in cell design since electrolyte-supported, cathode-supported, and anode-supported cell configurations can all be considered. Major problems associating with planar design include sealing the stacks to prevent fuel and oxidant gases mixing and

the thermal mismatch between ceramic components, which has led to cracking during thermal cycling.

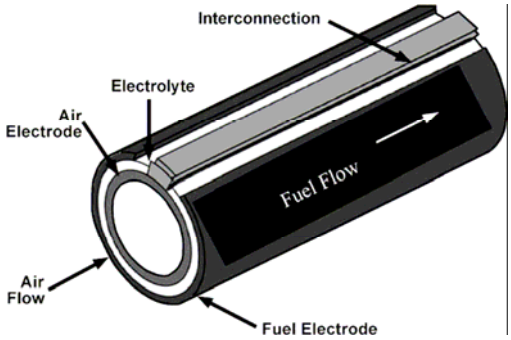


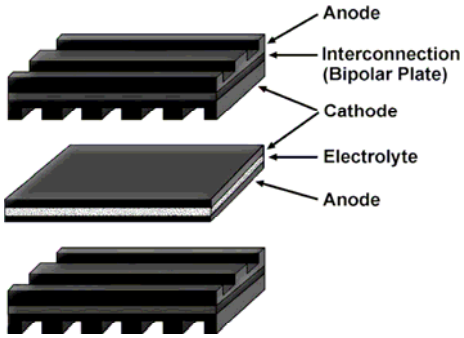


Figure 2-2 Tubular solid oxide fuel cell design  Figure 2-3 Planar solid oxide fuel cell design

2.1.3 Materials for SOFC Components

At present, the most common materials for SOFCs are oxygen ion conducting yttria-stabilized zirconia (YSZ) for electrolyte, strontium-doped lanthanum manganite (LSM) for the cathode, nickel/YSZ for the anode, and doped lanthanum chromite or high-temperature metals for the interconnect.

The requirements for the various cell components are summarized in

Table 2-3. Other general desirable properties for the cell components include high strength and toughness, fabricability, and low cost.

Table 2-3 Requirements for solid oxide fuel cell components

| Component | Electrolyte | Cathode | Anode | Interconnect |
|---|---|---|---|---|
| Conductivity | High ionic conductivity, Negligible electronic conductivity | High electronic conductivity | High electronic conductivity | High electronic conductivity, Negligible ionic conductivity |
| Stability | Chemical, phase, morphological, and dimensional stability in fuel and oxidant environments | Chemical, phase, morphological, and dimensional stability in oxidant environment | Chemical, phase, morphological, and dimensional stability in fuel environment | Chemical, phase, morphological, and dimensional stability in fuel and oxidant environments |
| Compatibility | No damaging chemical interactions or interdiffusion with adjoining cell components | No damaging chemical interactions or interdiffusion with adjoining cell components | No damaging chemical interactions or interdiffusion with adjoining cell components | No damaging chemical interactions or interdiffusion with adjoining cell components |
| Porosity | Fully dense | Porous | Porous | Fully dense |
| Thermal Expansion | Match with adjoining components | Match with adjoining components | Match with adjoining components | Match with adjoining components |

*Cathode materials*

The development of cathode materials in SOFCs has mainly focused on the doped lanthanum manganite system because this material remains stable in oxidizing atmospheres, has sufficient electrical conductivity at 1000°C, and has a close thermal expansion match to the YSZ electrolyte. The most common dopant used is strontium due to its good size match to lanthanum. The strontium dopant does not increase the oxygen vacancy concentration, a common phenomenon in most of the other perovskite cathode materials, but rather oxidizes the manganese ion.

$$SrO_2 \xleftarrow{LaMnO_3} Sr'_{La} + Mn^{\bullet}_{Mn} + 2O^{x}_{O} \qquad \text{Equation 2-10}$$

This reaction effectively increases the electron-hole concentration and improves the electrical conductivity. However, the absence of oxygen vacancies in LSM restricts the reduction of oxygen to the three-phase boundary regions. This restriction is the primary reason why LSM does not have acceptable performance at lower temperatures. Two approaches have been taken to improve the performance of LSM cathodes so that they may be used at lower temperatures. The first is to add a second ionically conducting phase to LSM to extend the surface area over which the oxygen reduction reaction can occur. Several groups are showing very good performances using LSM-YSZ[6, 7] or LSM-GDC[8] composite cathodes. The second approach is to dope LSM with an ion that promotes the formation of oxygen vacancies when strontium is doped on the A-site.

While these approaches appear to improve the performance of LSM, it is unlikely that these cathode materials will operate below 800°C. Other cathode materials are also

investigated such as $La_{0.8}Sr_{0.2}CoO_3$, $La_xSr_{1-x}TiO_3$,[9] $La_{1-x}SrCuO_{2.5-\delta}$,[10] $La_xSr_{2-x}FeO_{4+\delta}$,[11] $La_{0.8}Sr_{0.2}Co_{0.8}Fe_{0.2}O_3$,[12, 13] $La_{1-x}Sr_xAl_yFe_{1-y}O_3$,[14] $Ln_{1-x}Sr_xCo_{1-y}Fe_yO_{3-\delta}$ (Ln=Pr, Nd, Gd; x=0.2, 0.3),[15] $Sr_{0.8}Ce_{0.1}Fe_{0.7}Co_{0.3}O_{3-\delta}$,[16] $Sm_{0.5}Sr_{0.5}CoO_3$,[17] and $La_{0.8}Sr_{0.2}Ga_{0.8}Mg_{0.15}Co_{0.05}O_{3-\delta}$.[18]

*Anode materials*

In the SOFC, the fuel arriving at the anode is generally reducing in nature. Thus the criteria for anode materials are:

(a) Chemically stable in reducing atmosphere

(b) Catalytically active to hydrogen and hydrocarbon gases

(c) Both electronically and ionically conductive

(d) Compatible with electrolyte materials in thermal expansion coefficients

Metals such as Ni, Co, and noble metals are good choices since they have excellent electrical conductivities in reducing atmosphere. Among them, Ni and Cu are the most popular ones because of their relatively low costs.

Usually metals/metal oxides are mixed with electrolyte materials (e.g. YSZ, GDC) for anode application. It has been generally recognized that composites function better than pure metal/metal oxides.[8, 19, 20] Within the composites, the metals offer electronic conductivities while electrolyte materials give ionic conductivities. Thus the composites function as mixed-conductors. In this way, the triple-phase-boundary (TPB) is extended into bulk of the anode materials. In addition, the thermal expansion coefficients of metals are appreciably different to those of electrolyte materials. By including electrolyte materials into anodes, the TEC mismatch is minimized. Another consideration is that metals tend to agglomerate during

sintering and cell operation. The addition of electrolyte materials is effective to prohibit the agglomeration.

Some ceramic materials have been evaluated for SOFC anodes, such as yttrium-doped $SrTiO_3$,[21] $ZrO_2$-$Y_2O_3$-$TiO_2$ system.[22]

*Electrolytes*

With the advancements in fabrication technology, the overall performance of SOFCs is eventually limited by the conductivity of the electrolyte materials. Ideally, an electrolyte is an ionic conductor and an electronic insulator. SOFC electrolytes conduct only oxygen ions and remain electronic insulators under operating conditions. SOFC electrolytes work in the most stringent environment: hydrogen or hydrocarbons on the anode side, oxygen on the cathode side, and also high temperatures. The general criteria for the quality of a solid electrolyte material to be used in an SOFC are:

(a) Ease of fabrication into a mechanically strong dense membrane of small thickness and large area to minimize bulk resistance.

(b) An oxide-ion conductivity $\sigma_0 > 10^{-2}$ S/cm at the cell operating temperature.

(c) Excellent chemical and mechanical compatibility with electrodes to avoid formation of blocking interface phases and minimize interfacial resistances.

(d) A negligible electronic conductivity at cell operating temperature to retain a transport number close to 1.

(e) Compatibility of thermal-expansion coefficients between electrolyte, electrodes, interconnects, and seals from ambient temperature and cell operating temperature.

(f) Relatively low costs of material and fabrication.

Though many new SOFC fabrication techniques have been developed in the last decade, electrolyte materials still remain unchanged. There are only a few ionic conductors available for SOFC electrolyte application.

*Stabilized zirconia*

High temperature zirconia ($ZrO_2$) has a cubic fluorite structure of Figure 2-4. On cooling from its melting point (2680ºC), it transforms to a tetragonal form at 2370ºC and then to a monoclinic form at 1170ºC. The high-temperature structure can be stabilized to room temperature by substitution of larger cations of lower valence (e.g., $Zr_{1-x}Ca_xO_{2-x}$ or $Zr_{1-x}Y_xO_{2-0.5x}$) for $Zr^{4+}$, which also introduces oxygen vacancies on the normal sites and therefore oxygen ion conductivity. The amount of dopant required to fully stabilize the cubic structure is about 12-13mol% for CaO, 8-9 mol% for $Y_2O_3$ and $Sc_2O_3$, and 8-12 mol% for other rare-earth oxides.[23]

$$Y_2O_3 \xleftrightarrow{ZrO_2} 2Y'_{Zr} + V_O^{\bullet\bullet} + 3O_O^{\times} \qquad \text{Equation 2-11}$$

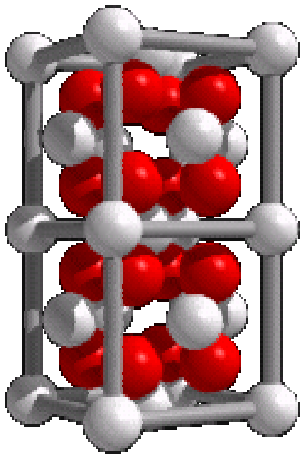

Figure 2-4 The cubic fluorite structure of $CaF_2$ or $CeO_2$

*Doped ceria*

$CeO_2$ has a higher ionic conductivity than $ZrO_2$. However, in the reducing atmosphere, $CeO_2$ is not stable and is reduced to $CeO_{2-x}$, which gives electronic conductivity. In order to introduce oxygen vacancies into ceria without reducing the cerium to $Ce^{3+}$, a rare earth $R^{3+}$ ion (e.g. $Gd^{3+}$ and $Sm^{3+}$) is substituted for Ce in $Ce_{1-x}R_xO_{2-0.5x}$.[24]

$$Gd_2O_3 \xleftrightarrow{CeO_2} 2Gd'_{Ce} + V_O^{\bullet\bullet} + 3O_O^X \qquad \text{Equation 2-12}$$

Although the strategy gives a transport number $t_0 \equiv \sigma_o/\sigma \approx 1$ in air or an inert atmosphere such as argon, $Ce^{3+}$ ions are created in a reducing atmosphere to give a measurable electronic component $\sigma_e$ in the total conductivity $\sigma$. For $Sm_{0.2}Ce_{0.8}O_2$ (SDC), which gives the highest oxide-ion conductivity of the rare-earth doped cerias,[25] the open circuit voltage of a hydrogen-air fuel cell was reduced to about 0.89 V at 650ºC.[26] GDC based SOFCs are viable in the temperature range of 450 to 600°C.[27]

*Stabilized $\delta$-$Bi_2O_3$*

High temperature $\delta$-$Bi_2O_3$ has the highest known oxide-ion conductivity, $\sigma_o \approx 2.3$ S/cm at 800ºC. However, it is only stable in the narrow temperature interval between 730ºC and its melting point at 804ºC. This phase has a fluorite-related structure with oxygen ions randomly occupying three quarters of the tetrahedral interstices of a face-centered-cubic $Bi^{3+}$-ion sublattice. Although the $\delta$ phase can be stabilized to lower temperatures by cation substitution for Bi,[28, 29] $Bi_2O_3$ based electrolytes are easily reduced in reducing atmosphere

at the anode of a SOFC. A thin layer of Sm-based ceria on the anode side of the electrolyte can be expected to alleviate this problem, but it does not prohibit it.[30]

The need to replace ceramic interconnects with alloys, as well as the cost of manufacture and maintenance of a fuel-cell stack, makes it mandatory to operate below 800ºC, but these temperatures are at technical limit that can be achieved with yttria-stabilized zirconia as the electrolyte. They require fabrication of dense ceramic membranes of large area that are only 1- to 20 μm thick. This fact continues to motivate the search for improved materials.

*Interconnects*

At current stage, a major materials challenge in SOFC development is the interconnect material, which provides the conductive path for electrical current to pass between the electrodes and to the external circuit.[31, 32] Development of high performance interconnect materials is one of the remaining critical issues for state-of –the-art SOFC technique. Since a single SOFC only produces approximately 1 volt, practically a stack of fuel cells rather than a single cell are utilized to generate power. This requires putting multiple SOFC units together in electrical series. Interconnectors are materials, which mechanically and electrically joint cathode of one cell to anode of another cell. The conventional high temperature ceramic interconnect materials are not applicable due to low electrical conductivities at reduced temperatures.[33] New interconnect materials must be developed for the still severe dual atmosphere service environment (oxidizing on cathode side and reducing on anode side). The unique operating conditions of SOFCs impose particular requirements on materials to be used for the interconnectors, the most important being: high chemical

stability, high electrical conductivity, comparable thermal expansion coefficient with electrode materials, mechanical stability, negligible ionic conductivity, gas tightness and excellent machinability.

To date, most interconnect materials investigated fall into two categories: ceramics and metals. Doped-$LaCrO_3$ has long been used as interconnect material for conventional high temperature SOFCs. These materials have high electrical conductivity, zero-ionic conductivity and high corrosion resistance in oxidizing atmosphere (air) as well as in a reducing atmosphere ($H_2$-$H_2O$ gas mixture) at high operating temperatures. Disadvantages of these materials include poor tolerance of sudden temperature changes, extreme sensitivity to oxygen partial pressure, Cr poisoning to electrodes, and difficulties in producing interconnectors with complex geometries. Since their conductivities originate from hopping effect, which is a thermally activated process, $LaCrO_3$ based interconnect materials suffer from poor electrical conductivities in reducing atmosphere and at temperatures below 800°C.

Heat-resistant alloys based on nickel, cobalt and iron with an addition of chromium may offer an interesting alternative for the ceramic interconnectors.[34, 35] For example, some investigators turn to metallic interconnect materials such as Crofer APU 22 alloys, Haynes alloy series, stainless steels and Fe-16Cr alloy.[36-38] These materials give excellent and pure electrical conductivities in reducing conditions. Other advantageous properties of these alloys include gas tightness and high oxidation resistance owing to the formation of $Cr_2O_3$ on their surface as a result of selective oxidation of chromium. However, due to high electrical resistance of this oxide layer, proportional to its thickness, application of the above-mentioned alloys is not optimistic without further modification. In addition, high chromium content in these alloys intends to “poison” electrodes especially cathodes during prolonged

service period at elevated temperature ranges. To avoid this problem, other alternative protecting coating layers such as $Mo_{1.5}Co_{1.5}O_4$ have been applied on the surface of the metallic materials. Nevertheless, the extra complexity in fabrication and high costs prohibit coating technique from practical applications.

### 2.1.4 Cell Fabrication Techniques

Wide varieties of ceramic manufacturing processes have been considered for manufacturing SOFC components. Table 2.2 lists some of the common used approaches for fabrication of electrolytes. In general, these approaches can be classified into two categories: the particulate approach and the deposition approach. The particulate approach involves consolidate of ceramic powder into cell components and sintering at elevated temperatures. The deposition approach involves formation of cell components on a substrate by a chemical or physical process.

The type of fabrication approach makes no difference for electrolyte layer if the thickness after sintering is the same. However, the performances of electrodes are dramatically influenced by the processing conditions. The most commonly used approaches for electrode fabrication are summarized in Table 2-5.

Table 2-4 Selected fabrication approaches for SOFC electrolytes

| Method | Example | Ref. |
|---|---|---|
| Spin coating | 0.2-2 μm YSZ film on porous or dense substrates | [39] |
| Vacuum evaporation | 25 μm YSZ films on Ni foils | [40] |
| Sputtering | 1-3μm YSZ films on dense or porous substrates | [41] |
| Colloidal deposition | 10 μm YSZ on porous NiO/YSZ substrates | [42] |
| Plasma spraying | 10μm cathode, 220 μm electrolyte, 10 μm anode on porous metallic support | [43] |
| Spray pyrolysis | 5-10 μm YSZ films on anode substrates | [44] |
| Sol-gel | YSZ films on porous LSM cathode substrates | [45] |
| Electrophoretic deposition | YSZ less than 10 μm on porous NiO/Ca stabilized ZrO2 substrates | [46] |
| Laser deposition | 0.5-0.7 μm YSZ films | [47] |
| Electrostatic assisted vapor deposition | 5-20 μm YSZ on NiO/YSZ substrates | [48] |
| Metal organic chemical vapor deposition (MOCVD) | YSZ thin films on fused silica substrates | [49, 50] |
| Electrochemical vapor deposition (EVD) | Dense 40 μm YSZ layers on porous substrates | [51] |

Table 2-5 Commonly used methods for SOFC electrodes fabrication

| Approach | Example | Reference |
|---|---|---|
| Spray painting | Multi-layer LSM/LSC cathodes | [52] |
| E-beam evaporation | Multi-layered NiO/YSZ anodes | [53] |
| Plasma spraying | LSM cathodes | [54] |
| Electrostatic spray | LSCF cathodes | [55] |
| Screen printing | SSC-GDC composite cathodes | [27] |
| Spin coating | LSM-GDC composite cathodes | [8] |
| Slurry painting | LSCF-GDC composite cathodes | [19] |
| Slurry coating | LSM cathodes | [56] |
| Tape casting | Pore former and YSZ | [57] |

### 2.1.5 Applications of SOFCs

The potential applications of SOFCs in our society are ever increasing, driven by the different benefits which SOFCs offer, such as environmental considerations (no $NO_x$, $SO_x$ or hydrocarbon emissions and no or much reduced $CO_2$ emissions), especially in urban areas where localized pollution is a major issue, and efficiency considerations (better utilization of fossil fuels and renewable fuels). Their potentially high reliability and low maintenance coupled to their quiet operation and modular nature makes SOFCs particularly suited to

localized power generation. Applications range all the way from very small-scale ones requiring only a few Watts to large-scale distributed power generation of hundreds of MW.

SOFCs offer significantly higher power densities than batteries, as well as being smaller and lighter and having much longer lifetimes. Thus there is an increasing number of applications emerging where only a few Watts are required, such as computer systems in vehicles and portable electronic devices for military applications.

The combination of their high efficiency and significantly reduced emissions of pollutants mean that fuel cell powered vehicles are a very attractive proposition, especially in heavily populated urban areas. The concept of a fuel cell powered vehicle running on hydrogen, the so-called “zero emission” vehicle, is a very attractive one and is currently an area of intense activity for almost all the major motor manufacturers.

SOFCs are particularly suited to combined heat and power applications, ranging from less than 1 kW to several MW, which covers individual households, larger residential units and business and industrial premises, providing all the power and hot water from a single system.

SOFCs offer potential for large scale distributed power generation (hundreds of MW), where the heat from the SOFC is used to drive a gas turbine to produce more electricity and increase the system efficiency to levels as high as 89%, significantly higher than any conventional electricity generation.

A rapidly developing market for fuel cells is in those applications where there is a real need for high quality, uninterrupted power supply. Such applications include information technology companies, airports and hospitals where there is a willingness to pay much higher prices for the guarantee of high quality, uninterrupted power to protect very valuable IT

equipment or life-supporting equipment. SOFCs are also well suited to high current, low voltage applications such as power tools wheelchairs, electric bicycles, scooters, and boats. Other applications include auxiliary power unites in vehicles and aircrafts.

## 2.2 Combustion Chemical Vapor Deposition (CVD)

Combustion CVD is a relatively new thin film fabrication process, which was invented by A. T. Hunt in 1993 at Georgia Institute of Technology.[58] Combustion CVD is an open-air flame assisted deposition process, which uses a combustible solvent to carry precursors. The high temperature combustion provides all the energy needed for reaction and film growth. Combustion CVD is different from other thin film deposition methods.

### 2.2.1 Thin Film Deposition Methods

Combustion CVD are different from the existing film deposition approaches. The most common vapor phase deposition approaches for thin film fabrication are summarized in Table 2-6.

Several coating processes are similar to combustion CVD. The characteristics are summarized in

Table 2-7.

Table 2-6 Major vapor phase thin film deposition methods

| Deposition method | Description |
|---|---|
| Physical vapor deposition | |
| Evaporation | The source materials are evaporated at low pressure by either resistance heating (Thermal Evaporation) or electron beam (E-beam Evaporation). The evaporated materials then condense on the surface of the substrate to form a thin film. |
| Sputtering | The source material (target) is placed in a high vacuum and bombarded with gas ions (usually Ar), which have been accelerated by a high voltage, producing a glow discharge or plasma. Atoms from the source are physically ejected by momentum transfer and move across the vacuum chamber to be deposited on the substrate. |
| Chemical vapor deposition | |
| Thermal CVD | The high temperature (generally from 800 to 2000°C) required for deposition can be generated by resistance heating, high frequency induction, radiant heating or hot plate heating. |
| Plasma enhanced CVD (PECVD) | The reaction is activated by a plasma and the deposition temperature is substantially lower. |
| Metal-organic CVD (MOCVD) | Metal-organics are used as precursor materials. This technique is popular in for fabrication of high quality thin films. |

Table 2-7 Film deposition processes similar to combustion CVD

| Process | Description | Ref. |
|---|---|---|
| Spray pyrolysis | Spray pyrolysis uses a gas-atomized spray of solution, which contains all the ingredients for the final product directed at a heated substrate. Upon reaching the substrate, the solvent in the solution evaporates and a chemical reaction occurs at the sample surface. | [59] |
| Flame pyrolysis | A water based solution containing acetate precursors of Y, Ba, and Cu is nebulized by a 1.7 MHz vibrator. The mist is carried to a $H_2/O_2$ flame by $N_2$ gas. The flame is directed to a heated substrate where c- axis oriented films of YBCO are deposited. | [60] |
| Flaming solvent spray | Precursors (metal nitrates or acetates) are dissolved in liquid ammonia, ethanol, and ethylene glycol. The solution is then nibulized by a pneumatic atomizer and ignited. YBCO films are deposited on polycrystalline MgO substrates. | [61] |
| Thermal spraying | Powders are introduced into a gas combustion torch (flame spraying) or a plasma torch (plasma spraying) in order to melt the powder so it can be sprayed onto a substrate to form a film. The coating is formed by the impact, spread, and rapid solidification of the individual droplets to form a porous and often lamellar microstructure. | [62] |
| Oxyacetylene combustion deposition | A simple brazing or welding torch using oxygen ($O_2$) and acetylene ($C_2H_2$) gas is used to deposit diamond films at atmospheric pressures. | [63-66] |

2.2.2 Combustion CVD Process

Figure 2-5 compares combustion CVD system with traditional CVD system for film deposition. In combustion CVD process, the deposition is carried out in open air, ambient pressure environment. Precursors containing desired metal elements are dissolved in a combustible solvent (e.g. ethanol, isopropyl alcohol (IPA), and toluene). The clear solution is then injected by an HPLC pump into the atomizer, where it is mixed with oxygen, atomized into aerosol and combusted with the help of pilot flames. A film is produced if a substrate is presented within or close to the combustion flame. The high temperature flame provides all the energy and thermal environment for precursor decomposition, chemical reaction and film nucleation and growth.

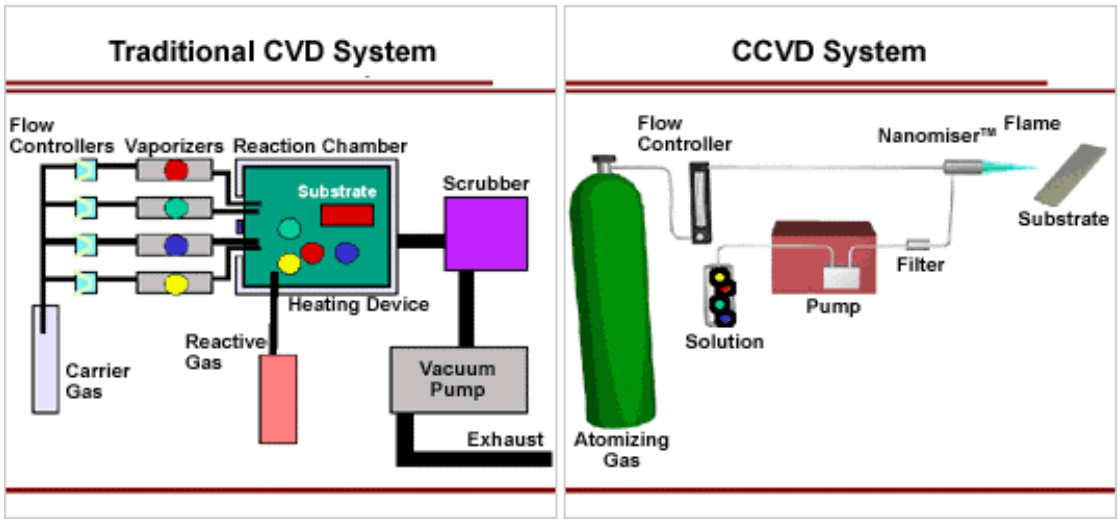


Figure 2-5 Comparison between combustion CVD and traditional CVD system

### 2.2.3 Advantages of Combustion CVD

In comparison with other thin film deposition methods, combustion CVD has many advantages:

- Open-atmosphere process, easy to adjust and operate

  The atomizer is small in size which usually sits inside a fume hood. During deposition, all parts of the system are accessible to the operator. Every parameter is controllable and adjustable.

- No furnace, auxiliary heating / reaction chamber required

  For conventional CVD system, furnace/reaction chamber is essential and very expensive. A heating unit (e.g. thermal heater or plasma) is needed to provide the thermal environment. The chamber also functions as a "black box". No information about the deposition is accessible until the deposition is completed and the chamber is cooled down to room temperature. In combustion CVD, the energy is solely provided by the combustion flame. Deposition progress can be observed and adjustment can be made at any moment.

- Flexible deposition rate

  It has been demonstrated that the deposition rate can be easily adjusted in a wide range. For example, when making high quality dense thin films for optical and electrical applications, the deposition rate is usually in the scale of nanometer per hour. However, when nanopowder is the final product, the rate can be as high as kilogram per hour. For porous films, the appropriate deposition rate is in the order of micrometer per minute.

- Multi-layer capability

  Apparently, composition of the film can be adjusted by switching precursor solutions. Multiple channel HPLC pump is available for making changes on film composition. This is very attractive for making functionally graded films.

- Environmental merits

  The combustion CVD deposition occurs inside the fume hood. Operators are not subject to direct exposure to any detrimental gas vapor. More important, unlike conventional CVD, which uses sulfur or chloride containing metal-organic precursors, combustion CVD uses metal nitrates or sulfur/chloride free metal-organic precursor materials. After combustion, the by-products are only $CO_2$ and $H_2O$. Thus combustion CVD is a clean process.

- Low capital and operating costs

  Due to the elimination of expensive furnace/chamber and precursor materials, the expenses on initial investment, maintaining, and operating are substantially lower than those for conventional CVD processes.

However, some shortcomings come along with all these merits. Film uniformity is a major concern for combustion CVD process due to the big temperature variation along the flame radius direction. Deposition in large area remains a challenge for this process. The system is very simple. On the other hand, there are so many variables that establishing a repeatable and controllable procedure for a successful deposition is difficult. These variables include:

- Flame temperature
- Fuel gas/oxidant ratio and flow rate

- Substrate temperature
- Substrate composition
- Precursor composition and concentration
- Solvent composition
- Solution flow rate
- Aerosol size and size distribution
- Deposition temperature

### 2.2.4 Applications of Combustion CVD

Since its invention, combustion CVD has been employed to fabricate different thin films and nonopowders for a variety of applications:

- Electronic applications

  $Ba_xSr_{1-x}TiO_3$ (BST), [67, 68]

- Buffer layer

  $CeO_2$,[69] $LaPO_4$,[70] $SrTiO_3$, $LaAlO_3$, $Y_2O_3$, $Yb_2O_3$,[71]

- Optical applications

  $MoO_3$ and $WO_3$,[72] ZnO,[73, 74]

- Superconductor

  $YBa_2Cu_3O_x$,[75]

- High temperature protecting coating

  $Al_2O_3$,[76] $Cr_2O_3$, $SiO_2$,[77] $CeO_2$, $MgAl_2O_4$, $NiAl_2O_4$,[78] YSZ,[79]

- Nanopowders

  $Al_2O_3$, $SiO_2$, YSZ, Pt, [80]

2.2.5 Modeling of Combustion CVD

The film nucleation and growth in combustion CVD process can be described using classical CVD theories.[81]

It is believed that several simplified models of nucleation and growth explain film deposition via combustion CVD. The prediction of the critical size and free energy necessary to form nuclei from the gas phase on a surface, heterogeneous nucleation has been developed from Capillarity Theory.[81] For nuclei to form on a substrate surface, the increase in surface free energy, including the changes for both the nuclei and the substrate, must be more than balanced by the decrease in bulk free energy. The total free energy change due to the formation of a single nucleus is given by:

$$\Delta G = a_3 r^3 \Delta G_v + a_1 r^2 \gamma_{vf} + a_2 r^2 \gamma_{fs} + a_2 r^2 \gamma_{sv} \qquad \text{Equation 2-13}$$

where $a_1$, $a_2$, $a_3$ are geometric constants,

r is the radius of the spherical cap shaped nucleus,

$\Delta G_v$ is the bulk free energy change per volume of nuclei,

$\gamma_{vf}$ is the surface free energy per area of the vapor-nuclei interface,

$\gamma_{fs}$ is the surface free energy per area of the nuclei-substrate interface, and

$\gamma_{sv}$ is the surface free energy per area of the substrate-vapor interface.

The heterogeneous nucleation model of film from vapor phase is illustrated in Figure 2-6.

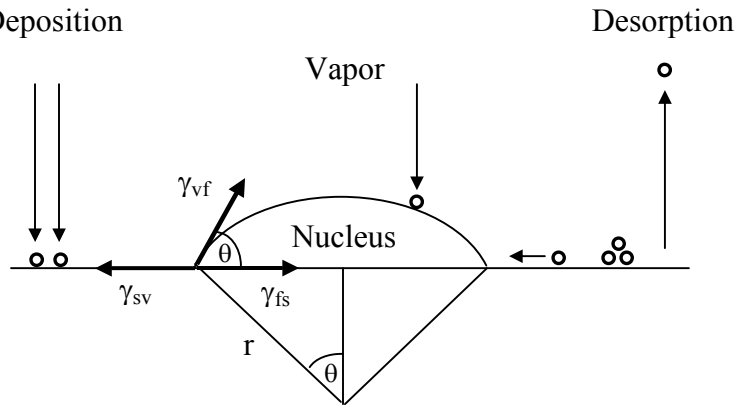


Figure 2-6 Surface energies of heterogeneously nucleated particles

By maximizing the total free energy change of ΔG by taking its derivative with respect to r and setting it equal to zero, one obtains the critical radius, r*. The critical radius is calculated with the following equation:

$$r^* = \frac{2(a_1\gamma_{vf} + a_2\gamma_{fs} + a_2\gamma_{sv})}{3a_3\Delta G_v}$$ Equation 2-14

For r ≥ r*, the nucleus lowers its free energy by increasing in size and thus growth proceeds. Nuclei with r < r* are unstable as ΔG increases when these particles grow (until r = r*).

The vapor particle impingement rate can be used as a starting point for determining the nucleating rate.

$$\phi = \frac{p}{\sqrt{2\pi MkT_0}}$$ Equation 2-15

where p is the vapor pressure,

M is the molecular weight of the particles, and

$T_0$ is the source temperature.

The adatoms impinging on the surface will either desorb from the surface or diffuse on the surface. The desorption rate can be estimated by the following Arrhenius equation.[82]

$$\nu \propto e^{\frac{-E_{des}}{kT}}$$ Equation 2-16

With $E_{des}$ being the activation energy for desorption and making substitutions, the nucleation rate, $\dot{N}$, can be approximated by:

$$\dot{N} = 2\pi r^* a_0 \sin\theta \frac{PN_A}{\sqrt{2\pi MRT}} n_s e^{\frac{E_{des} - E_s - \Delta G^*}{kT}}$$ Equation 2-17

where $a_0$ is a constant with units of length and is of atomic dimension,

P is pressure,

M is the molecular weight,

$N_A$ is the Avogadro's number,

K is Boltzman's constant,

R is the universal gas constant,

T is the temperature,

$E_S$ is the activation energy for surface diffusion, and

$\Delta G^*$ is the energy change for a nucleus of r*.

The nuclei growth can be described phenomenologically by one of theree methods: island growth (Vollmer-Weber), layer growth (Frank-van der Merwe), and layer-plus-island (Strasky-Kranstanov). Island growth occurs when the interaction between neighboring film atoms exceeds that of between the film and substrate. Layer growth is when the interaction between the film atoms is less than that of between the film and substrate. Layer-plus-island growth combines the two. This relationship can be described using the following equations.

Layer growth $\gamma_{sv} \geq \gamma_{fs} + \gamma_{vf}$ Equation 2-18

Island growth $\gamma_{sv} \leq \gamma_{fs} + \gamma_{vf}$ Equation 2-19

Nuclei continue to form and grow on the surface of the substrate until a critical density is reached. At this point the number of individual nuclei begins to decrease due to the coalescence of existing nuclei. Three methods of coalescence have been determined to exist. The first mechanism is Ostwald ripening in which mass is transported from the smaller nuclei to the larger nuclei. The second mechanism is sintering. Sintering involves surface diffusion between nuclei in contact with one another. The last mechanism is cluster migration, which results from the random motion and collision of nuclei on the surface. These three coalescence mechanisms combine to coarsen the grain structure of the film on the surface of the substrate. The following diagram represents these three mechanisms.

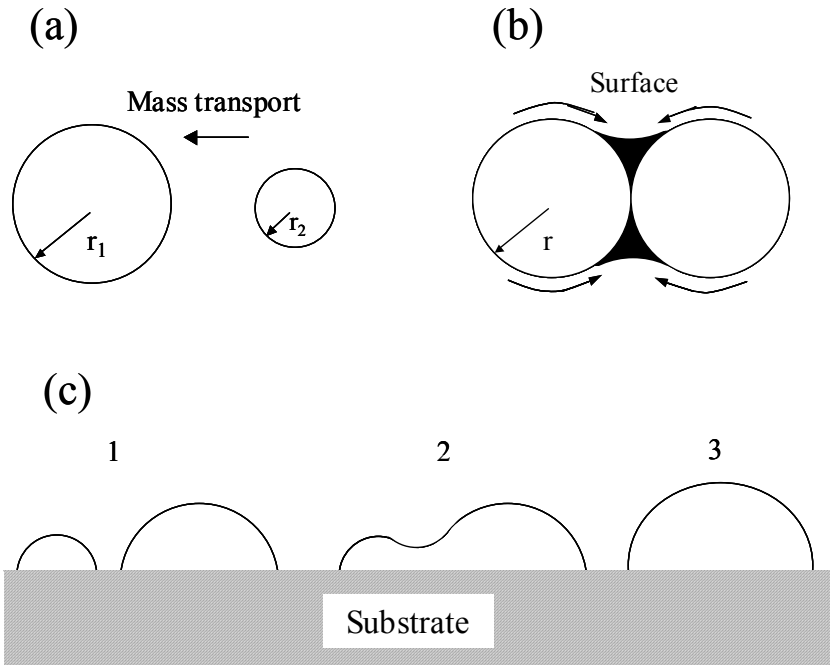


Figure 2-7 (a) Ostwald ripening, (b) Sintering, and (c) cluster migration.

Once the surface of the substrate is covered, film thickening may begin. Initially the depositing atoms will fill the gaps between the coarsened nuclei to smooth the film surface. Once completed, the depositing atoms will begin to thicken the deposited film. These initial coarsened nuclei for the foundation for the microstructure, which will form as the film thickens. However, film thickening may begin before the substrate is completely covered resulting in films containing pinholes.

The first step in modeling combustion CVD process was taken by Brook, who developed a model for homogeneous nucleation of oxide particles within the combustion flame with respect of aerosol droplet size, solute concentration, and precursor composition.[83] It was concluded that the critical amount of precursor in a droplet, $(d_{aero}^3 c)^*$, (where $d_{aero}$ is the droplet diameter and c is the precursor concentration) is the determining factor for the formation of clusters within the flame. Aerosols that contained no droplets with values of $(d_{aero}^3 c)$ exceeding $(d_{aero}^3 c)^*$ produced dense vapor deposited material with no clusters. Aerosols containing droplets with values of $(d_{aero}^3 c)$ exceeding $(d_{aero}^3 c)^*$ produced coatings containing clusters and dense, vapor deposited material.

By adopting existing zone models for microstructure evolution during vapor deposition,[84, 85] Polley developed a model to correlate the microstructure and deposition conditions for ZnO films deposited by combustion CVD.[73]

In his model, the microstructure of ZnO deposited by combustion CVD can be divided into three general zones: Zone A, Zone T, and Zone II. Zone A is characterized by cauliflower-like growths of amorphous material. Zone A is formed at low substrate

temperatures. Zone II is characterized by will-defined columnar grains with (002) plane sitting parallel to the substrate surface. Zone II microstructures are produced at high substrate temperatures. Zone T is an intermediate zone between Zone A and Zone II that is crystalline and smoother than Zone A, but does not have the will-defined columnar grain characteristic of Zone II structures.

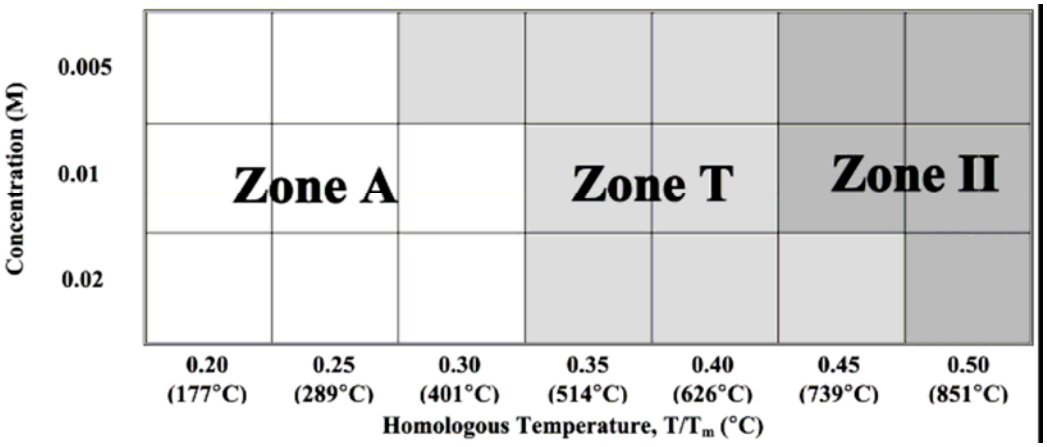


Figure 2-8 Deposition matrix showing which microstructural zone is present at each deposition condition.

## 2.3 Research Motivation and Objectives

Low cost and long-term durability of solid oxide fuel cells can be achieved with the emergence of low-temperature SOFCs since relatively inexpensive materials can be employed, sealing problems can be alleviated, and much more flexible stack designs can be

adopted if the operating temperature is reduced to less than 700°C. [2, 86, 87] Increased resistance of the electrolyte caused by the lowered operating temperatures can be addressed either by decreasing the electrolyte thickness or by introducing alternative materials with higher ionic conductivity at lower temperatures. Nevertheless, the polarization resistances of electrode/electrolyte interfaces increase dramatically and become dominant as the operating temperature is reduced, especially the resistance at the cathode side. Therefore, minimizing interfacial resistances remains one of the major challenges facing the development of low-temperature SOFCs.

A variety of fabrication techniques, such as dry pressing, sol-gel, slurry coating, screen-printing, and tape casting, have been extensively used in both laboratory and industrial practices due to their simplicity, low-cost, and high productivity. To get better control on film quality, other techniques, mostly vapor processing approaches, such as chemical vapor deposition (CVD),[88, 89] physical vapor deposition (PVD),[90, 91] thermal spray,[92] sputtering,[93] electrochemical vapor deposition (EVD),[3, 94] metal-organic chemical vapor deposition (MOCVD),[95] and flame assisted vapor deposition (FAVD) are currently available for fabrication of SOFC components.[96, 97] Most of these techniques are best suited for the preparation of dense films at relatively low deposition rates. Generally, these methods require special raw materials/targets, sophisticated equipment and well-controlled atmosphere, thus increasing capital investment and fabrication costs. Moreover, films prepared by some of these approaches require post deposition heat-treatment, which is costly and time consuming and usually undesired. A deposition technique that is simple to perform, capable of creating a variety of microstructures, and cost effective is needed for fabrication of SOFC components.

Combustion CVD is an open air, flame-assisted chemical deposition process, capable of producing films from amorphous to crystalline, dense to porous, and nano-scale to micro-scale dimensions.[58] In addition to the very low apparatus and maintenance costs, the desired stoichiometry can be easily controlled by simply dissolving inexpensive precursors (usually nitrates or metal organics) into an organic solvent. This is critical for SOFC fabrication since SOFC electrodes are usually very complicated in composition. Moreover, the combustion CVD process, just like other CVD processes, is insensitive to and has no specific requirement for the flatness of the substrate. Initially, combustion CVD was only employed to prepare thin, dense oxide films for high temperature and semiconductor applications. However, other film morphologies produced by combustion CVD have not drawn sufficient attention by researchers. As to fuel cell applications, combustion CVD can be used to deposit not only thin, dense electrolytes but also thick, porous electrodes. It has been demonstrated that the combustion CVD process can be employed to prepare either nano-sized powders or a variety of nano-structured films with controllable thickness and porosity as shown in Figure 2-9.[98, 99] Another advantage of the combustion CVD process is that multi-layer films can be prepared in a single run simply by switching precursor solutions, thus avoiding film cracking during thermal cycling in conventional multiple-firing processing. Hence combustion CVD is a very attractive technique for the fabrication of compositionally and structurally graded SOFC electrodes.

The overall goal of this research is to understand the correlations between properties, microstructure, and processing parameters, including solution chemistry, flame conditions, and substrate temperature, hence gaining a profound understanding of the relationship between the processing conditions and the electrochemical/catalytic behavior of the fabricated structures.

Control and design of microstructure are feasible once the underlying fundamental principles are revealed. More specifically, this research will achieve the following objectives:

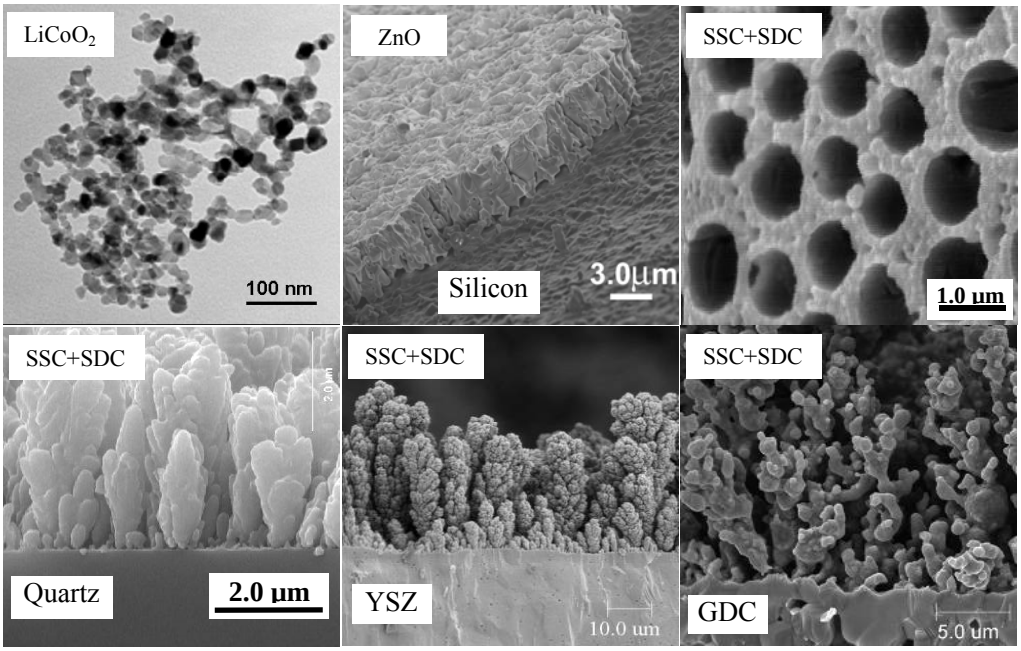


Figure 2-9 Various structures created by combustion CVD

- To investigate the effects of major deposition parameters on microstructure and electrochemical performances of porous films deposited by combustion CVD process.
- To prepare nano-structured and/or functionally graded porous electrodes showing reduced interfacial polarization and enhanced electrode kinetics;
- To further modify the original combustion CVD process to accommodate low-cost solid phase ceramic electrode materials and thus gaining better control of phase distribution in composite electrode materials;
- To prepare low dimensional structures of functional materials with desired morphologies, crystallographic structure, and excellent electrochemical performances for energy storage and conversion.

This research could exert great impact on the existing concept and technology of energy storage and conversion. Firstly, it is demonstrated that electrodes for SOFCs with dramatically improved interfacial conditions can be fabricated by combustion CVD in a simple, open environment. Nanostructured electrodes could enhance electrochemical/catalytic kinetic in orders of magnitude, yielding much higher current density and total capacity for SOFCs at reduced operating temperatures; Functionally graded electrodes further optimize fuel cell microstructure and stack design, facilitating mass, ionic and electronic transport; successful synthesis multi-composition, appropriately doped nanopowders is crucial for new generation of lithium ion batteries; Well-aligned low-dimensional nanostructures could be used as building blocks, a template, or even directly employed for many functional devices, especially those relevant to energy storage and conversion such as nano-batteries, nano-fuel cells, and nano-sensors.

More generally, the proposed research will result in a fundamental understanding of combustion CVD process for fabrication of nanostructured electrodes and interfaces. This is essential not only to rational design or creation of a new generation of batteries and fuel cells but also to advance our ability to design novel materials or structures for other related applications such as gas separation, methane conversion, and pollutant removal.

# CHAPTER 3 TECHNICAL APPROACHE

## 3.1 Combustion CVD System

Schematically shown in Figure 3-1 is a state-of-the-art system for Combustion CVD in our laboratory. A single combustion CVD system consists of a gas distribution unit, a precursor supply unit, a combustion unit, a sample support unit, and a temperature control unit. In the combustion CVD process, a solution is prepared by dissolving the desired precursors into an organic solvent. An HPLC pump supplies the solution into the combustion unit after passing through a filter and a damper. The inline filter is used to remove any possible tiny particles present in the solution. The damper helps to reduce the flow and pressure pulse between strokes of the piston pump. The gas distribution unit supplies fuel gas/oxidant to the combustion unit. Gas pressure and flow rate are controlled by the gauges on gas tanks and flow meters. The essential part of the whole system is the combustion unit (nozzle), which is able to atomize the precursor solution into micro-sized aerosols and then produce a combustion flame. After extensive evolution, the new generation atomizer can generate aerosol droplets with smaller size and narrower size distribution. A diagram of the atomizer is illustrated in Figure 3-2. The flammable organic based solution is atomized by a high velocity stream of oxygen, which also helps combustion and reaction. The resulting flammable aerosol is then ignited by twelve small $CH_4/O_2$ premixed pilot flames. All the energy for the reaction and deposition is supplied by the combustion of organic solvent. The carbon and hydrogen in the organic solvent and fuel gas are burned off and metallic elements in the precursors are oxidized to metal oxides after reaction.

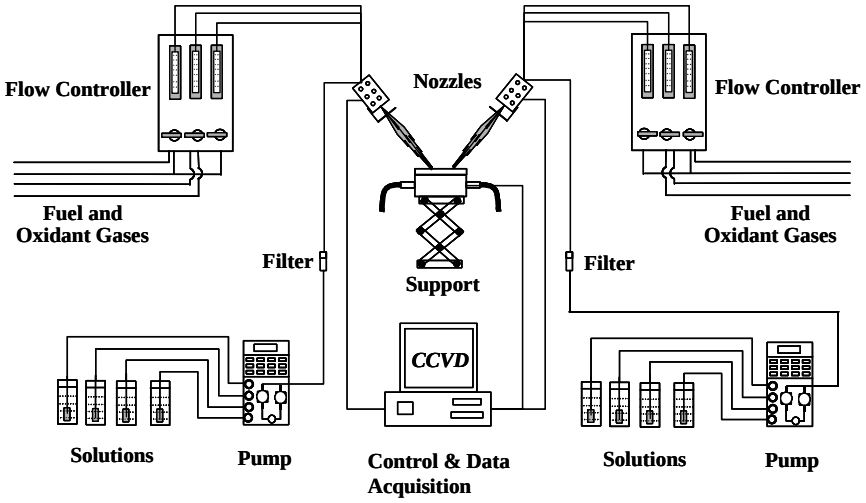


Figure 3-1 A schematic of combustion CVD process.

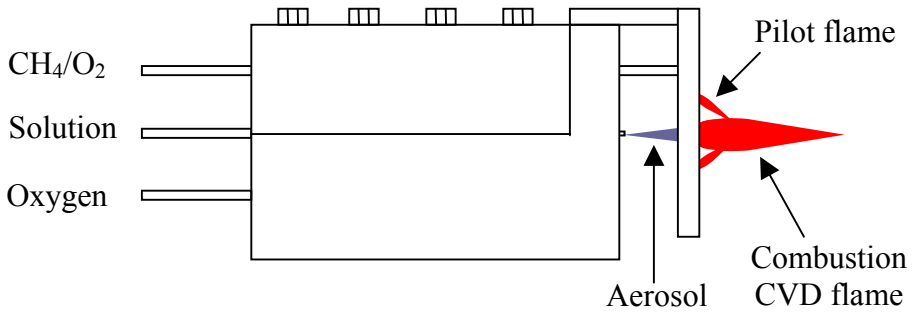


Figure 3-2 Schematic of the new version of atomizer

The substrates can be mounted on different sample holders depending on the desired deposition temperature and deposition procedure. For low substrate temperatures, the substrates sit on a 6″×6″ water cooled aluminum plate. The deposition temperature is controlled by adjusting water flow rate and the location of the substrate in the flame. For high substrate temperature, the substrates are heated. The sample holder is made of refractory material and covered by a stainless steel plate. Resistance heating element is embedded in the refractory material. The substrates can be pre-heated to 650°C prior to deposition.

The control unit is composed of a computer and a temperature controller, which is used to monitor and control the temperatures of atomizer and the substrate holder (if substrate pre-heating is needed). In addition, there are channels available in the control unit for monitoring precursor solution pressures at different locations between HPLC pump and atomizer.

### 3.2 Sample Preparation

For deposition, either metal-nitrates or metal-organics are used as precursor materials. Precursor solutions are prepared by dissolving precursor species in stoichiometric ratios into organic solvents (i.e. ethanol, IPA, and toluene) and mixed ultrasonically until clear solutions are obtained. Methane is used as the fuel gas and dry oxygen served as the oxidizer for the flame. The flammable solution was delivered through a HPLC pump to the atomizer at flow rate from 2 to 5 ml/min, where the solution is aerosolized and then ignited to create a flame. Thin film is produced if a substrate is present within the flame, while nanoparticles are collected if the homogeneously nucleated and free-traveling particles are captured by suitable mechanism.

Various substrates are used for deposition depending on the application of the film. For the purpose of parameter study, polished, fused quartz substrates are purchased from Quartz Scientific as 76.2 mm × 25.4mm × 1.0 mm slides. The slides are cut into approximately 10 mm × 10 mm pieces with a diamond scribe. Each one of these pieces serves as an individual substrate. Each substrate is cleaned ultrasonically in acetone then rinsed with ethanol prior to use. When depositing SOFC electrodes, YSZ or GDC electrolyte substrates are prepared by dry-pressing of commercial powders and sintered at 1400°C for 5 hours. For porous films for gas sensors, the interdigitated Pt electrodes are put on Si wafer substrates by soft lithography. The details about substrate preparation are discussed in the corresponding chapters.

The flame temperature is managed by adjusting flow rate of mixing oxygen, the type of solvent, and type and flow rate of fuel gas as well. The deposition temperature is determined by the flame temperature, the location of the substrate in the combustion flame, and the temperature of the substrate. The deposition temperature is monitored by a type K thermocouple placed in the vicinity of substrate. Temperature variation on the substrate surface was measured to be ±30°C.

## 3.3 Film Characterization

### 3.3.1 Microstructure characterization

The deposited samples are initially examined by naked eyes. The mechanical property of the as-prepared films and bonding strength between the films and the substrates are evaluated by scratching the films with nails and peeling off the films with Scotch® tape. The microscopic features of the prepared films are characterized in plan-view and in cross-section using a scanning electron microscope (SEM, Hitachi S-800). The films are coated with gold

in an Anatech Limited Hummer VI-A sputter coater for 120 seconds. Cross-sections were prepared by breaking the specimen into smaller pieces. Powder and 1D nanostructure samples are characterized using a transmission electron microscope (HRTEM, JEOL 4000EX) equipped with an energy dispersive spectroscopy (EDS) attachment. In addition to the bright field images, dark field images and selected area electron diffraction (SAED) patterns are taken to reveal the structural information of the samples. Powder samples are ultrasonically dispersed in acetone and transported to Cu grids by a dropper.

### 3.3.2 Phase identification

X-ray diffraction was performed on a Phillips PW-1800 diffractormeter with a scanning step of 0.005 degree. The diffractometer uses Cu $K_\alpha$ radiation as incident source. To study the size confinement effect of nanostructures produced by combustion CVD, laser Raman spectroscopy was obtained using a Renishaw 2000 Raman spectromicroscope scanning from 200 $cm^{-1}$ to 1000 $cm^{-1}$ at room temperature in open-air. An Ar-ion laser beam with a wavelength of 488 nm was used to excite the nano-crystals.

### 3.3.3 Electrochemical analysis

Electrochemical performances of fuel cells are measured in a laboratory scale station. As shown in Figure 3-3(a) and (b), the button fuel cells are sealed at one end of a 3/8″ high purity alumina tube. A 1/8″ stainless steel tube is inserted in the larger ceramic tube for fuel gas delivery. The whole fuel cell testing assembly is placed in a vertical tube furnace (Figure 3-3(c)). Impedances were measured in the frequency range from 0.01 Hz to 100K Hz with a Solartron 1287 interface and a 1250 frequency response analyzer (FRA) (Figure 3-3(d)). The performance tests are carried out in the temperature range of 500°C to 750°C at 50°C

increase with humidified (3 vol.% water) hydrogen as fuel and stationary air as oxidant at ambient pressure.

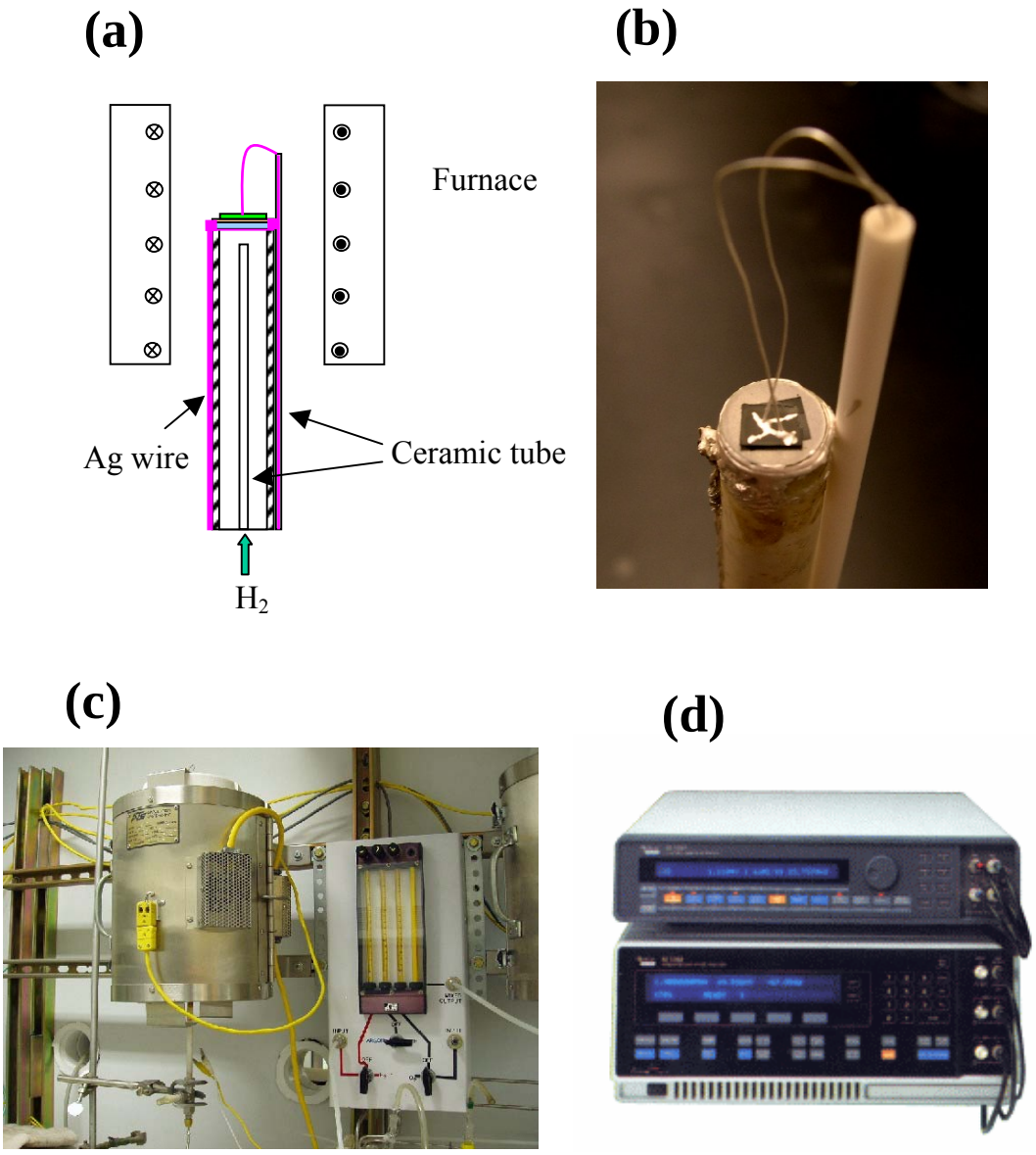


Figure 3-3 (a) Schematic and (b) actual appearance of fuel cell testing assembly. (c) Fuel cell testing apparatus consisting of a tube furnace, cell assembly, and fuel supply. (d) Solartron 1287 interface and 1250 FRA.

## 3.4 Experimental Design

The purpose of this research is to explore the viability of fabrication of porous ceramic films for electrodes for solid oxide fuel cells and novel structures for other energy storage and conversion applications. The strategy is first to establish the correlation between processing conditions, microstructure, and the electrochemical performance of the resulting films. After each major deposition parameter is evaluated, porous films with desired microstructures and properties can be fabricated. Films with other novel microstructures for other electrochemical applications can be further produced.

### 3.4.1 Parametric Studies

As discussed in previous chapter, there are so many processing parameters, which impact on film morphology and properties. It is impractical to carry out experiments for each of these deposition parameters. The most important deposition parameters should be screened out and given detailed study. The effects of these parameters on microstructure and electrochemical properties of the deposited films are evaluated and compared. For this study, only one electrode material, $Sm_{0.5}Sr_{0.5}CoO_3$ (SSC)+$Gd_{0.1}Ce_{0.9}O_2$ (GDC) is used. Most depositions are deposited on quartz substrates. Symmetrical cells (both electrodes are made of the same material and have the identical microstructure) are fabricated using GDC or YSZ substrates. These samples are evaluated at 500-700°C for impedance measurements.

### 3.4.2 SOFC Electrodes with Superior Performance

Once the relative importance of each major deposition parameter is determined, the parameter combination, which gives optimum microstructure and lowest impedance, is adopted to fabricate electrodes and tested for electrochemical performances in full cells. Either electrolyte supported or anode supported cells with combustion CVD fabricated cathodes are used for evaluation. In addition, electrode materials other than SSC-GDC will be deposited on electrolyte substrates for performance evaluation.

### 3.4.3 SOFC Electrodes with "Designed" Microstructures

Novel electrodes for SOFCs were designed and fabricated using combustion CVD. For example, electrodes with both composition and microstructure gradients were deposited on electrolyte substrates and tested for cell performances. The ideal electrodes should have compositions more compatible with electrolyte materials close to electrode-electrolyte interfaces, while materials more electronically conductive on the air/fuel gas side. Structurally, small grain size (high surface area) is preferred at the electrode-electrolyte interface since this area is most active for electrochemical reactions. On the contrary, the outer layers should have larger grain size, which facilitates gas transport.

### 3.4.4 Modified Combustion CVD Process

The original combustion CVD process still has relatively high requirement for precursor materials and solvent. All the precursor materials must completely dissolve into the solvent prior to deposition. Otherwise atomizer needles are prone to get clogged. In addition, for composite electrode materials such as SSC-GDC, the distribution of each phase is

difficult to control for combustion CVD. Additional modification of the process may further improve film performance and lower the cost as well.

In the modified deposition process, larger needles, which allow the use of micro-size solid particles, are fabricated to replace the fine aerosol generating needles. One component of the composite electrode, $Sm_{0.5}Sr_{0.5}CoO_3$ (SSC), was introduced in the form of nitrates dissolved in a flammable solvent, while the other component of the electrode, GDC, was introduced in the form of solid particles dispersed in the SSC solution. Eventually, both of the composite electrode components, SSC and GDC are introduced in the form of low-cost solid ceramics.

### 3.4.5 Porous Films and Novel Structures for Other Applications

Porous films were fabricated for other electrochemical applications such as gas sensors and batteries. High surface area, porous films are required for gas sensing. To enhance the gas sensing performance, interdigitated Pt electrodes were fabricated on silicon wafer by soft lithography. Nanostructured $SnO_2$ thin films were then deposited on the substrates. The sensors were tested for gas responses at different temperatures. The effect of doping was investigated in this study.

Other novel structures, which may be interesting for advanced electrochemical applications, were also explored. More specifically, 0D nanoparticles, 1D, and 2D functional materials will be focused for research.

# CHAPTER 4 NOVEL ELECTRODES FOR SOLID OXIDE FUEL CELLS

## 4.1 Optimization of Deposition Parameters in Term of Interfacial Resistance

The objective of this study is to reveal the correlation between processing conditions, microstructures, and electrochemical properties of porous electrodes prepared using the combustion CVD method by systematically changing deposition parameters, including deposition temperature, deposition time, solution concentration, and type of substrate. These relationships are vital for intelligent design of electrode structures and the corresponding properties.

### 4.1.1 Experimental

The apparatus and operational details of the combustion CVD approach have been described elsewhere.[98, 99] Composite consisting of 70wt.% $Sm_{0.5}Sr_{0.5}CoO_{3-\delta}$ (SSC) and 30wt.% $Sm_{0.1}Ce_{0.9}O_{3-\delta}$ (SDC) was chosen as the cathode material. Precursor solutions were prepared by dissolving nitrates of Sr, Sm, Co, and Ce (from Aldrich) in stoichiometric ratios into absolute ethanol and mixing ultrasonically for at least a half hour until clear solutions were obtained. Methane was used as the fuel gas and dry oxygen served as the oxidizer for the flame. The flammable solution was delivered to the nebulizer through a HPLC pump at a flow rate of 3.0 ml/min. Deposition temperatures were measured by placing a K-type thermocouple in the vicinity of substrate's surface.

Four major processing parameters were studied in a sequential order: deposition temperature, deposition time, precursor concentration, and substrate material. Experimental design of the latter parameters was based on the results of the studies already performed. For

example, the deposition temperature used for the deposition time study was the optimal temperature determined from the first set of experimental runs to keep the total number of experiments manageable. All deposition variables are summarized in Table 4-1.

A symmetrical cell with configuration of electrode/GDC/electrode was used for electrochemical testing. Dense $Gd_{0.1}Ce_{0.9}O_{1.95}$ (GDC) pellets of 10 mm diameter and 250 μm thickness were prepared by dry pressing and sintering in air at 1350°C for 5 hours to achieve a relative density higher than 95%. During deposition, the substrates were held at the tip position of the flame for a predetermined period of time. Then substrates were turned over to continue deposition on the other side.

The microscopic features of the prepared electrodes were characterized using a scanning electron microscope (SEM, Hitachi S-800) equipped with an energy dispersive spectroscopy (EDS) attachment. X-ray diffraction was performed on a Phillips PW-1800 diffractometer with a scanning step of 0.005 degree. Electrochemical performances of the symmetrical cells were measured in ambient air from 500°C to 700°C. Impedances were typically acquired in the frequency range from 0.01 Hz to 100 kHz with an EG&G Potentiostat/Galvanostat (Model 273A) and a Lock-in Amplifier (5210).

Table 4-1 Major deposition variables

| Serial | Deposition temp (°C) | Deposition time (min) | Precursor conc. (M) | Substrate |
|---|---|---|---|---|
| 1 | 800/1000/1200/1400 | 20 | 0.05 | GDC |
| 2 | 1200 | 2/5/10/20 | 0.05 | GDC |
| 3 | 1250 | 50/5/1 | 0.005/0.05/0.25 | GDC |
| 4 | 1250 | 7 | 0.05 | GDC/YSZ |

### 4.1.2 Results and Discussion

*Effect of deposition temperature*

Shown in Figure 4-1 are the microstructures of electrodes (70 wt.% SSC and 30 wt.% SDC) deposited at different temperatures. To assure continuous electrodes, deposition time was 20 min, which was later found to result an electrode thickness of 150 to 200 μm. It is evident from Figure 4-1 that temperature has dramatic impact on the morphology and microstructure of the electrodes. Shown in Figure 4-1(a) is the micrograph of an electrode deposited at 800°C, consisting of 200 nm loosely compacted particles. The film is highly porous, but the particle-to-particle contact and particle-to-substrate adhesion are very poor. The electrode films can easily be scratched off after deposition, as is evidenced by the many loose particles seen in Figure 4-1(a) that were produced during SEM sample preparation. Deposition at 1000°C results in a better microstructure as shown in Figure 4-1(b). Particles are well attached to each other and also adhesion between the film and substrate is improved. Even better electrode morphology for SOFCs appeared at a 1200°C deposition, at which branched grain structure is developed as shown in Figure 4-1(c). Meanwhile, pore size of this sample is much larger, providing pathway for easier gas transport. Grain size is about 400 nm for the sample deposited at 1200°C. As deposition temperature further increased up to 1400°C, over-densification occurred, resulting in very large grain size and a highly dense electrode, which could obstruct gas flow and thus is not preferred for SOFC applications.

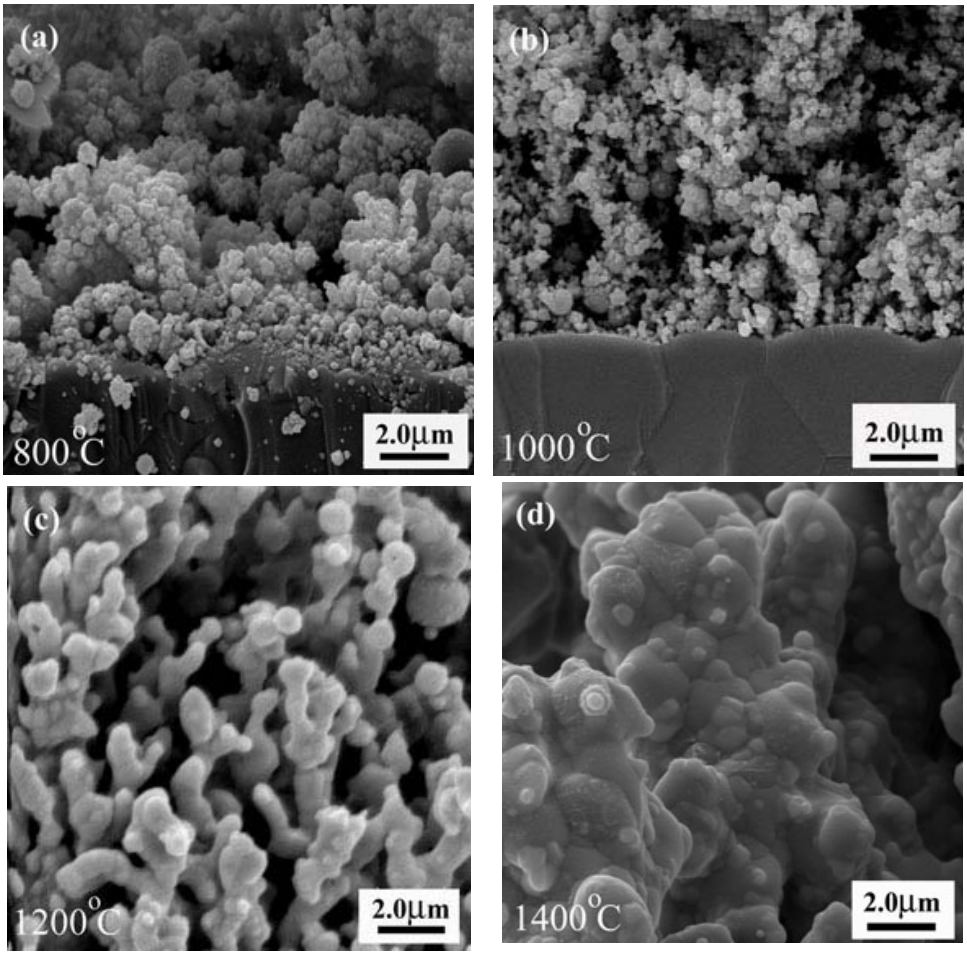


Figure 4-1 Typical SEM micrographs of 70wt.% SSC+30wt.%SDC cathodes fabricated by combustion CVD at different temperatures for 20 minutes on a 250 μm thick GDC electrolyte substrate.

Shown in Figure 4-2 are the interfacial polarization resistances as determined from impedance spectroscopy of symmetrical cells, further confirming the significant influence of deposition temperature. For example, the polarization resistance of the cathode-electrolyte interface at 600°C decreased from 24.8 to 2.4, to 0.71, and to 0.26 $\Omega$ cm$^2$ as the temperature for electrode deposition increased from 800 to 1000, to 1200, and to 1400°C. It appears, however, that some over-densification has occurred at 1400°C as shown in Figure 4-1(d), which is undesirable for gas transport.

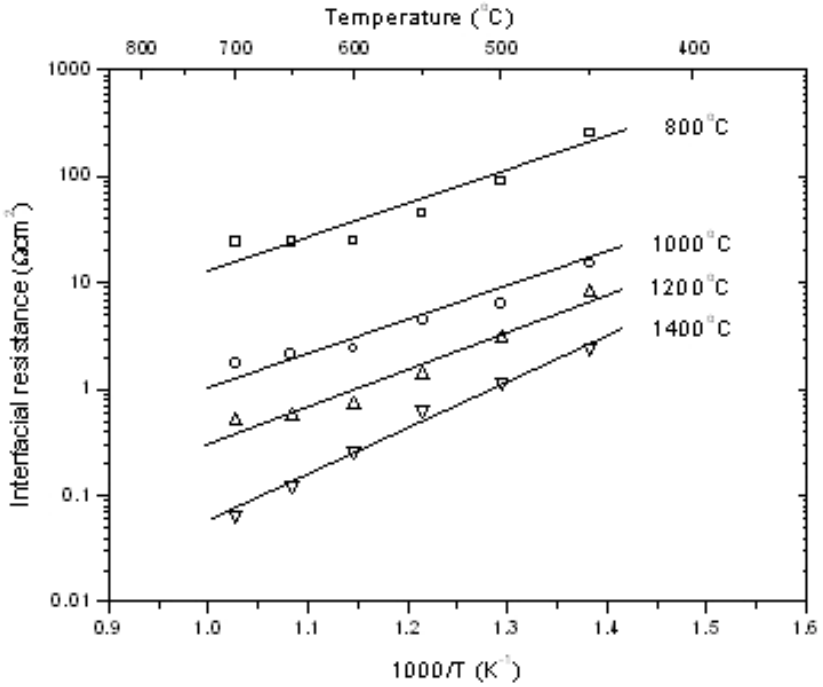


Figure 4-2 Interfacial polarization resistances of symmetrical cells as determined from impedance spectroscopy. The temperature adjacent to each curve represents the temperature at which the electrodes were fabricated by combustion CVD.

Obtaining the perovskite structure is essential for SOFC electrode fabrication. Shown in Figure 4-3 are the XRD patterns of electrodes deposited at different temperature. Since deposition time is very short, depositions at 800°C and 1000°C produced partially crystallized films with small peaks on their XRD patterns. However, samples deposited at 1200°C and 1400°C show fully crystalline structures.

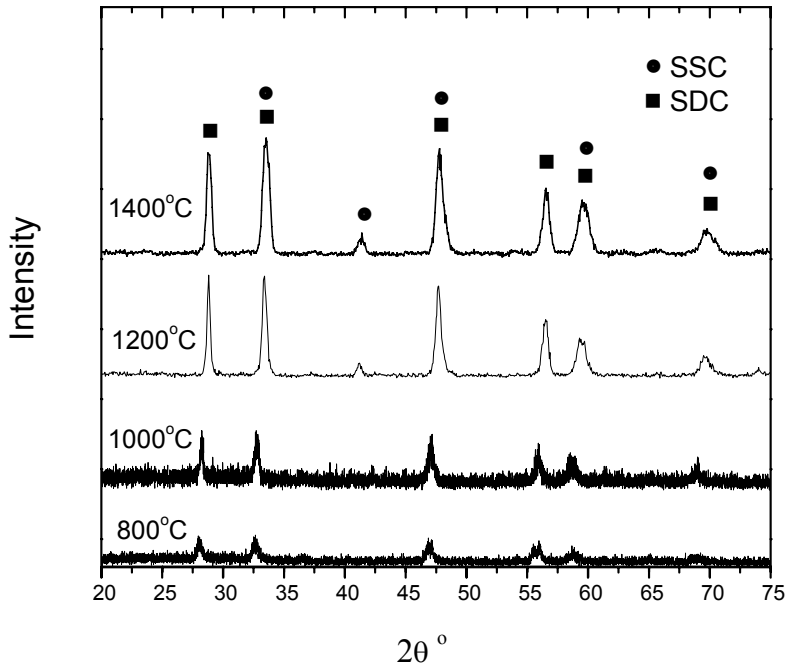


Figure 4-3 X-ray diffraction patterns of SSC-SDC cathodes fabricated at different deposition temperatures (800°C, 1000°C, 1200°C, and 1400°C) by combustion CVD (deposition time: 20 minutes; precursor concentration: 0.05 M; substrate: GDC).

*Effect of deposition time*

Shown in Figure 4-4 are some typical morphologies of the electrodes deposited at 1200°C for 2 to 20 minutes. The morphological features of these electrodes are almost the same except for an increase of film thickness and a slight increase in grain size with deposition time. SEM observation reveals that there is a roughly 3 – 5 μm variation in film thickness due to fluctuations in temperature as well solute along flame radius direction during deposition. This difference in film thickness may have a large impact on polarization behavior of the film especially when the deposition time is short (for example, 2 minutes). Once a critical deposition time is reached, this effect is not as significant as before. Movement of the sample within the combustion flame during deposition might help to eliminate the variations of the film.

Electrode thickness was determined from SEM micrographs. Two-minute depositions resulted in an electrode with an average thickness of 13±1.5 μm. While 5, 10, and 20 minute-depositions produced cathodes of 22±2.0, 40±3.2, and 89±7.5 μm thickness, respectively. Film growth kinetics can be learned from the plot of electrode thickness vs. deposition time as shown in Figure 4-5. The growth rate of electrodes deposited at 1200°C obeys the linear growth law:

$$L = Kt + C_0 \qquad \text{Equation 4-1}$$

where L is the electrode thickness and K is the rate constant. In this situation, K equals to 4.3 μm/min. This value is orders higher than deposition rates of most CVD processes, indicating combustion CVD is an ideal process for industrial mass production. The intercept $C_0$ (1.3 μm) originates during sample insertion and withdrawing from the flame, which takes half to one minute.

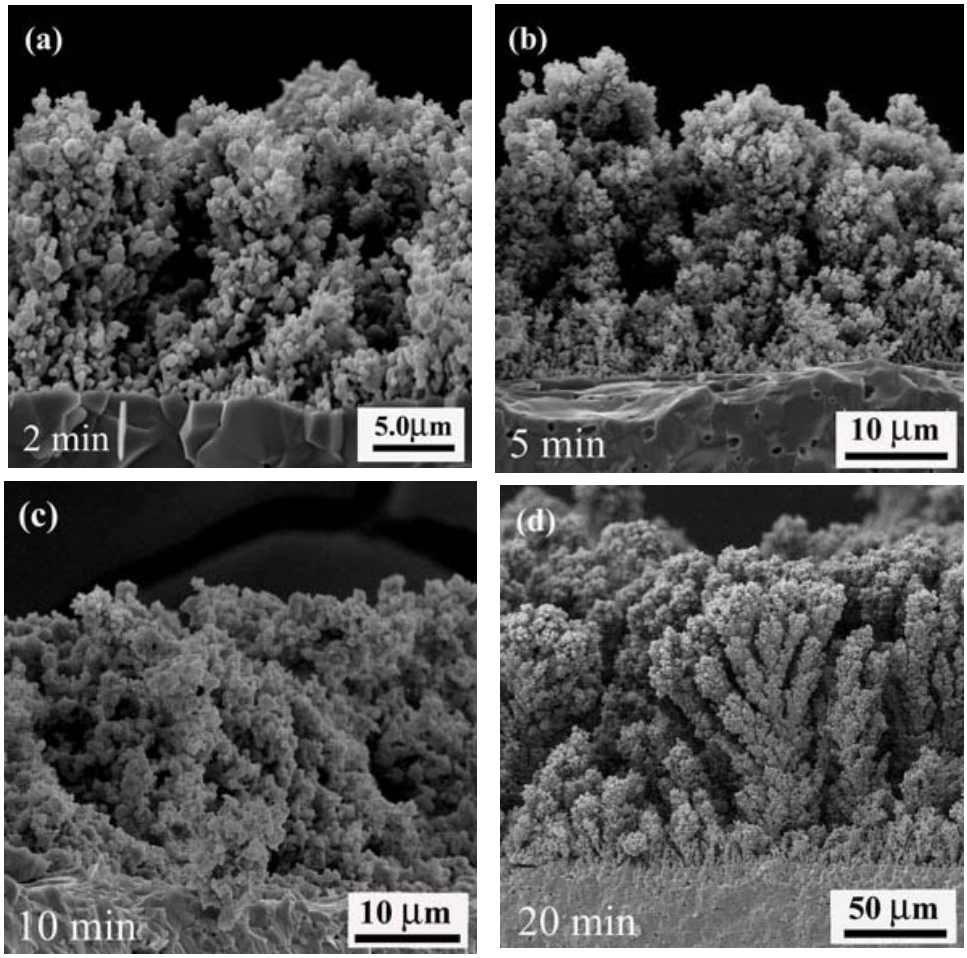


Figure 4-4 Cross-sectional views (SEM micrographs) of cathodes fabricated by combustion CVD with different deposition time. (deposition temperature: 1200°C; precursor concentration: 0.05 M; substrate: GDC).

Similar to a conventional CVD process, there are several sequential steps occurring during combustion CVD. The rate-limiting step could be either the mass transport through the boundary layer adjacent to the substrate or the surface reaction kinetics. [100] A mass transport controlling mechanism tends to show a linear relation while the later mechanism usually leads to parabolic film growth behavior. In the case of combustion CVD, both the gas pressure resulting from the high velocity of fuel gas and the chosen deposition temperature (1200°C) are much higher than conventional CVD, resulting in a much thicker diffusion boundary layer and faster surface reaction rate. This suggests that the controlling factor is the diffusion rate of the reactant through the boundary layer to the substrate surface.

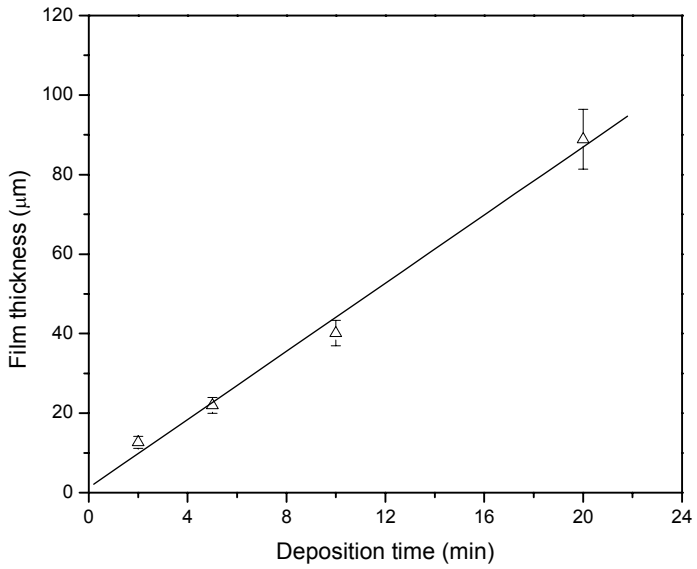


Figure 4-5 A plot of electrode thickness as a function of deposition time (deposition temperature: 1200°C; precursor concentration: 0.05 M; substrate: GDC). The thicknesses were determined from SEM cross-section micrographs.

Figure 4-6 shows the interfacial polarization resistances for cathodes fabricated with different deposition time. Cathodes prepared with a 2-minute deposition time have much higher interfacial resistances than those fabricated using longer deposition time. Electrodes fabricated for 5 minutes or more showed similar interfacial resistances at measurement temperatures higher than 600°C. As an example, a 10-minute deposition produced electrodes with interfacial resistances of 3.39, 1.4, and 0.64 Ω $cm^2$ at testing temperature of 550, 600, and 650°C, respectively. Ideally, the electrode thickness should be sufficient to have low sheet-resistance but not so thick as to generate resistance to mass transport through the porous electrodes. In general, the influence of deposition time on microstructure as well as interfacial polarization resistance is not as significant as that of deposition temperature.

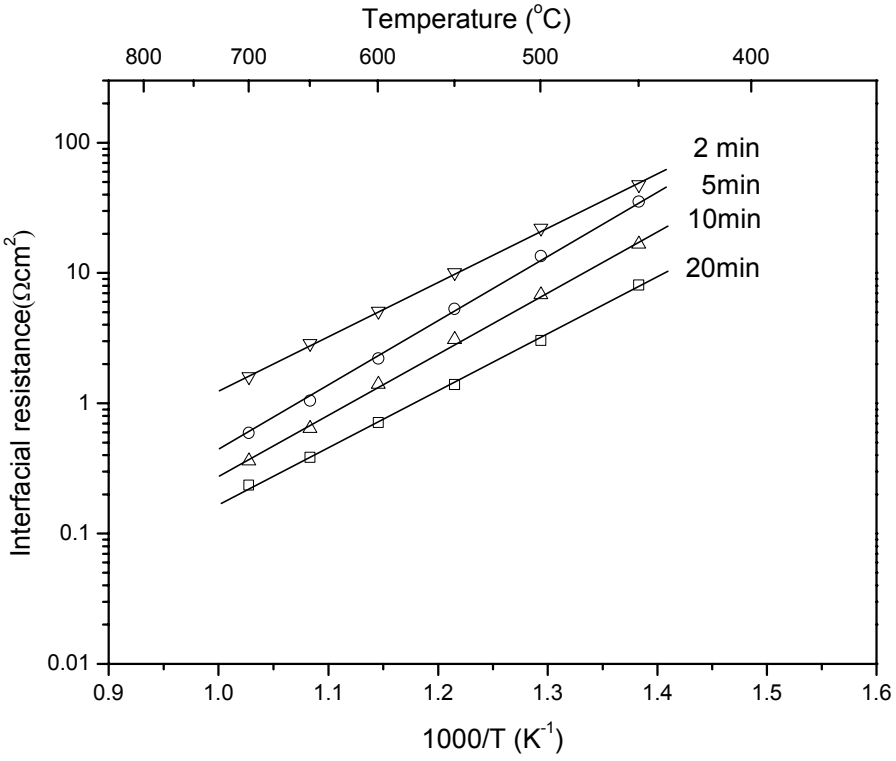


Figure 4-6 Interfacial polarization resistances of symmetrical cells with electrodes fabricated by CCVD with different deposition times (2, 5, 10, 20 minutes).

*Effect of precursor concentration*

Since electrode thickness might have impact on interfacial polarization resistance, for instance, it might affect diffusion of gas species to the active bottom layers, the deposition time was adjusted accordingly as the concentration of precursor solution was changed to do a fair study of precursor concentration effect. To keep approximately the same amount of solute on substrates, deposition time for 0.005, 0.05, and 0.25 M solutions were chosen as 50, 5, and 1 minute, respectively. Depositions were performed on GDC substrates at 1250°C. The microstructures of the resulting electrodes are shown in Figure 4-7. These electrodes are about 20 μm thick and highly porous, all having excellent adhesion with the substrates.

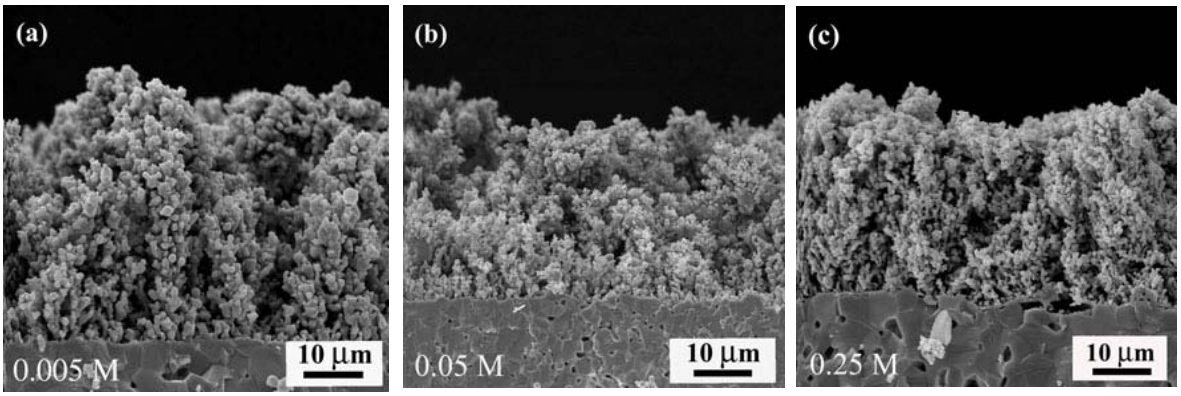


Figure 4-7 Cross-sectional views (SEM micrographs) of cathodes fabricated by combustion CVD with different precursor concentration: (a) 0.005 M for 50 minutes; (b) 0.05 M for 5 minutes, and (c) 0.25 M for 1 minute. (Deposition temperature: 1250°C; substrate: GDC)

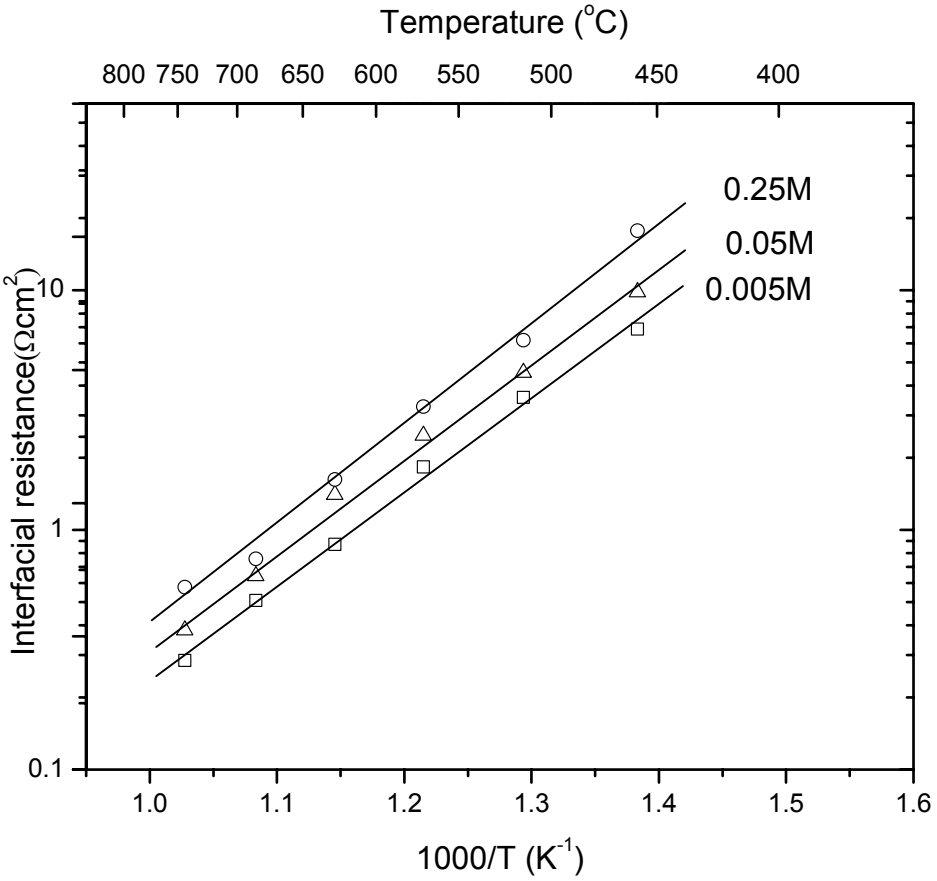


Figure 4-8 Interfacial polarization resistances of symmetrical cells with electrodes fabricated by CCVD with different precursor concentration. The interfacial polarization resistances were determined from impedance spectroscopy under open circuit conditions.

The interfacial polarization resistances as determined from impedance measurements are shown in Figure 4-8. These electrodes have very similar interfacial resistances at most of the testing temperatures except very low temperatures (such as 450°C). Electrodes prepared from 0.005 M solution generally exhibited a little better performance. This can be explained by the much longer dwell time (50 min) under high deposition temperature, which may lead to better particle-to-particle contact and particle-to-substrate adhesion.

*Effect of substrate*

Shown in Figure 4-9 are the microstructures of two electrodes deposited on two different electrolytes: YSZ and GDC. There is no noticeable difference between electrode microstructures prepared with two different substrates. Both electrodes have a thickness of about 25 μm and an average grain size of 300 nm. However, interfacial polarization resistances are dramatically different, as shown in Figure 10. The interfacial polarization resistances between the electrode and YSZ were two orders of magnitude higher than those between the electrode and GDC, indicating that the TPB might significantly influence the overall electrode performance.[101] High interfacial polarization resistances between a cobalt-containing cathode and YSZ electrolyte have also been noted by others.[102, 103] Possible causes include a large mismatch in thermal expansion coefficient and chemical reaction between Co and YSZ to form resistive zirconate compounds. This problem could be alleviate by partially replacing Co with other transition metals (such as Fe), applying a thin layer of GDC between the cathodes and YSZ electrolyte, or fabricating compositional graded cathodes with lower Co content near YSZ electrolyte.[104]

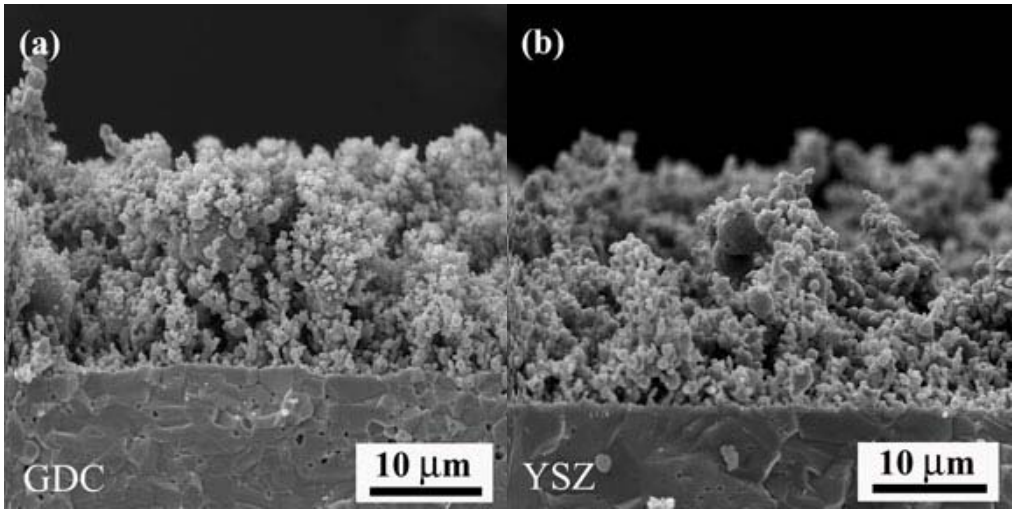


Figure 4-9 Cross-sectional views of cathodes fabricated by combustion CVD on two different substrates: (a) GDC and (b) YSZ.

### 4.1.3 Summary

Combustion CVD has been successfully applied to the fabrication of highly porous and nano-structured SSC-SDC cathodes for solid oxide fuel cells. Four most important processing parameters are evaluated in this study: deposition temperature, deposition time, precursor concentration, and substrate. Deposition temperature has a significant influence on electrode microstructure (grain size, porosity, and pore size). Deposition time and precursor concentration, on the other hand, have little effect on microstructure but determine the electrode thickness. The nature of the substrate has no observable effect on microstructure but dramatically influence the interfacial polarization resistance. The optimum combination of deposition parameters for SSC-SDC cathodes on GDC substrates is believed to be a deposition of 5 to 10 minutes using a 0.05 M solution and a deposition temperature of 1200 –1300°C.

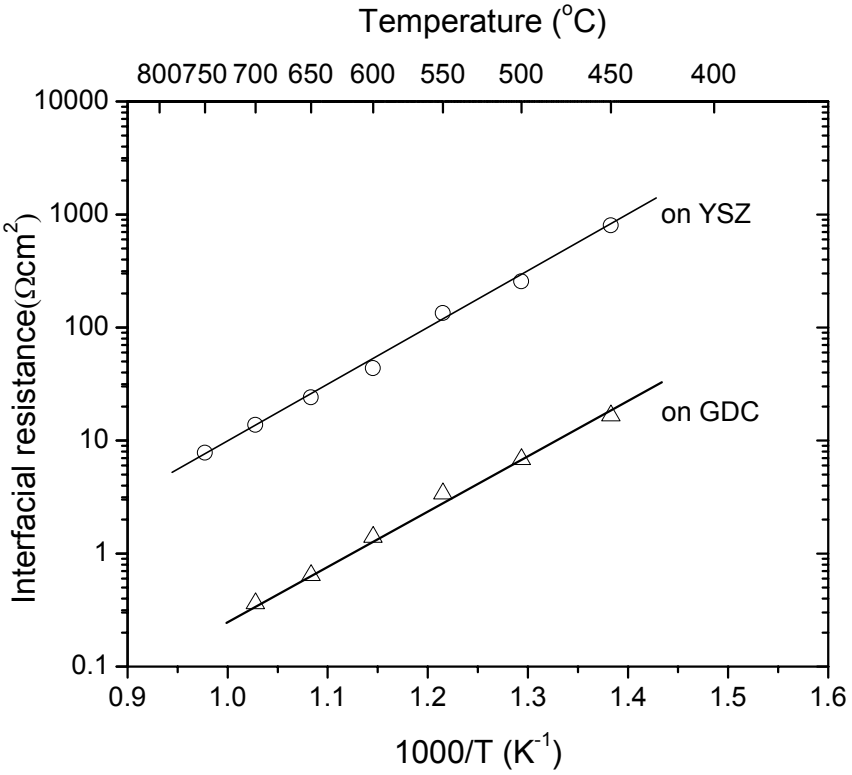


Figure 10 Interfacial polarization resistances of symmetrical cells with electrodes fabricated by combustion CVD on two different substrates. (Deposition temperature: 1200°C; deposition time: 7 minutes; precursor concentration: 0.05 M).

## 4.2 Nanostructured Electrodes with Dramatically Low Interfacial Resistances

Low-temperature solid oxide fuel cells (SOFCs) have attracted much attention in recent years because of their potential to dramatically reduce the cost of the materials and cell fabrication in addition to improved reliability, portability, and operational life.[5, 42, 105-108] To lower the resistance of dense electrolyte membranes at lower operating temperatures, either the thickness of traditional YSZ (8 %mol$Y_2O_3$-$ZrO_2$) electrolyte must be reduced or alternate electrolyte materials with much high conductivities at low temperatures (such as doped ceria and lanthanum gallate) must be used. Meanwhile, the performance of electrodes (both anode and cathode) must be significantly improved to reduce the operating temperature, either through development of new materials or creation of novel structures. It has been demonstrated that the viability to operate an SOFC at low temperatures is determined primarily by the cathode/electrolyte interface, since its polarization resistance increases rapidly as the temperature is decreased.[86] The work reported in this communication aims at developing novel nanostructured electrodes of extremely low interfacial polarization resistances by a versatile and cost-effective method, combustion CVD, in an effort to significantly reduce the operating temperature. This is a critical step toward making SOFCs affordable for a wide variety of applications.

An SOFC is an all-solid-state device that converts chemical energy of fuels (such as hydrogen, natural gas, and other hydrocarbon fuels) directly to electricity with the highest energy efficiency and minimal pollutant emission. It is desirable to have a porous structure of mixed-conducting electrodes for fast transport of ionic and electronic defects through the solid phase, rapid flow of gases through the pores, and for efficient electrochemical reactions at the interfaces. [109-111] For example, in a Ni–$Ce_{0.9}Gd_{0.1}O_{1.95}$ (GDC) composite anode, Ni acts as both

the catalyst and the electronic conducting phase, while GDC acts mainly as a matrix to support the catalyst and prohibit the metal from agglomeration under operating conditions. Ceria is reported to improve the anode catalytic activity as well, especially in SOFCs using hydrocarbon fuels.[112, 113] It has been demonstrated that the length of the triple-phase boundary (TPB) correlates well with the interfacial resistances to electrochemical oxidation of hydrogen at the anode and reduction of oxygen at the cathode; thus, the extension of the TPB or the number of active reaction sites becomes a determining factor in improving electrode performance. This can be achieved by developing electrode materials of higher ambipolar conductivity and/or optimizing the architecture/microstructure of the electrodes. Consequently, extensive efforts have been devoted to searching for alternative cathode materials such as the composites consisting of $La_{0.6}Sr_{0.4}Co_{0.2}Fe_{0.8}O_{3-\delta}$ (LSCF), $Sm_{0.5}Sr_{0.5}CoO_{3-\delta}$ (SSC), and $Ce_{0.9}Gd_{0.1}O_{1.95}$ (GDC) or YSZ.[19, 114] While considerable progress has been made on developing new electrode materials, little has been reported in cell performance enhancement by optimizing microstructure of the electrodes through new electroding processes. Although there is little argument that the creation of nanostructured electrodes with finer grain size could considerably improve the performance of fuel cells, especially at lower operating temperatures, the major technical challenge is how to fabricate designed microstructure cost-effectively.

Combustion CVD is an open-air, flame-assisted chemical deposition process, capable of producing a wide range of coating morphologies from very dense to highly porous structures. [15, 16] In liquid fuel combustion CVD, chemical precursors of the electrode materials are dissolved in a flammable organic solvent. The resulting solution is nebulized and the resulting aerosol is then combusted in open air, depositing a layer of porous electrodes onto an electrolyte substrate placed within tip region of the flame. Electrode compositions can be easily controlled by simply

adjusting the ratios of the various chemical precursors in the solution. This technique is cost-effective because it uses inexpensive precursors (e.g., nitrates and metal-organics) and does not need a furnace nor a vacuum chamber, which are costly and essential for conventional CVD process. Moreover, the combustion CVD process, just like other CVD processes, is insensitive to and has no specific requirement for the flatness of the substrate. It has been demonstrated that the combustion CVD process can be employed to prepare either nano-sized powders or a variety of nano-structured films with controllable thickness and porosity.[98] Technique similar to combustion CVD has been used on $La_{1-x}Sr_xMnO_{3-\delta}$ (LSM)/YSZ system earlier.[96, 97, 115] Interfacial resistances of the resulted electrodes were reported comparable to those fabricated by conventional techniques. Unfortunately, only symmetrical cells, not functional full cells, were fabricated and tested using that technique. In addition, there was no attempt to fabricate ceria-based SOFC systems, the performance of which is more sensitive to interfacial resistances because of the intended operating temperature is low. For example, for a SOFC based on a 26 μm-thick GDC electrolyte, Ni-GDC/GDC/SSC-GDC, the electrolyte resistances were reported to be 0.96 $\Omega cm^2$ and 0.67 $\Omega cm^2$ at 450°C and 500°C, respectively, while the interfacial polarization resistances were 5.2 $\Omega cm^2$ and 1.8 $\Omega cm^2$, much higher than the bulk electrolyte resistances.[27] Thus, reducing interfacial polarization resistances is the most effective way of enhancing the performances of low-temperature SOFCs.

In this chapter, we present our recent advance in fabrication of functional SOFCs by depositing both cathode (70wt% $Sm_{0.5}Sr_{0.5}CoO_{3-\delta}$ and 30wt% $Sm_{0.1}Ce_{0.9}O_{3-\delta}$ (SDC)) and anode (70wt% Ni and 30wt% $Sm_{0.1}Ce_{0.9}O_{3-\delta}$) on a 250μm thick GDC electrolyte pellets using a combustion CVD process.

4.2.1 Experimental

Detailed description of combustion CVD apparatus used for this study is available elsewhere. [98] Metal nitrates of Sr, Sm, Co, Ce, and Ni were obtained from Aldrich. Solution was prepared by dissolving stoichiometric amounts of precursors into an organic solvent and agitated by a magnetic stirring bar until completely dissolved. Methane was used as the fuel gas and oxygen served as the oxidizer for the combustion flame.

Dense GDC ($Gd_{0.1}Ce_{0.9}O_{1.95}$) pellets of 10 mm diameter and 250 μm thickness were prepared by a dry-pressing process and sintered at 1350°C for 5 hours to achieve relative density of greater than 96%. Before deposition, the GDC substrates were held at the tip position of flame for 7 minutes. After deposition of each electrode, the precursor solution was switched, and substrates were turned over for deposition of the other electrode material. Anode supported half cells were fabricated by a co-firing process. The dry-pressed Ni-GDC/ GDC bilayer pellets were co-sintered at 1350°C for 5 hours, resulting in an GDC film of about 20 μm on a Ni-GDC substrate.

The microscopic features of the prepared electrodes were characterized using a scanning electron microscope (SEM, Hitachi S-800) with an energy dispersive spectroscopy (EDS) attachment. Electrochemical performances of the cells were measured at 500°C to 700°C with humidified (3 vol.% water) hydrogen as fuel and stationary air as oxidant at ambient pressure. Impedances were measured in the frequency range from 0.01 Hz to 100K Hz with an EG&G Potentiostat/Galvanostat (Model 273A) and Lock-in Amplifier (5210).

### 4.2.2 Results and Discussion

Figure 4-10 (a) shows a cross-sectional view of a fuel cell supported by a 250 μm-thick GDC electrolyte membrane with combustion CVD-fabricated NiO–SDC anode (top layer) and SSC–SDC cathode (bottom layer). Both electrodes are relatively uniform with thickness of about 40 μm. The micrographs shown in Figure 4-10(b) and (c) reveal that both anodes and cathodes are highly porous and appear to adhere well to the electrolyte. The agglomerate size appears to be smaller for the anode than for the cathode. However, higher magnification SEM micrographs, shown in Figure 4-10(d) and (e), reveal that each agglomerate actually consists of much smaller grains of about 50 nm in diameter. The primary grain sizes are also smaller for the anode than for the cathode. These nanostructured electrodes have extremely high surface area and are expected to significantly improve the electrochemical functionality.

Shown in Figure 4-11 are the XRD patterns of as-prepared cathodes and anodes, indicating that the composite anode consists of NiO and SDC phases whereas the cathode is composed of SSC and SDC phases.

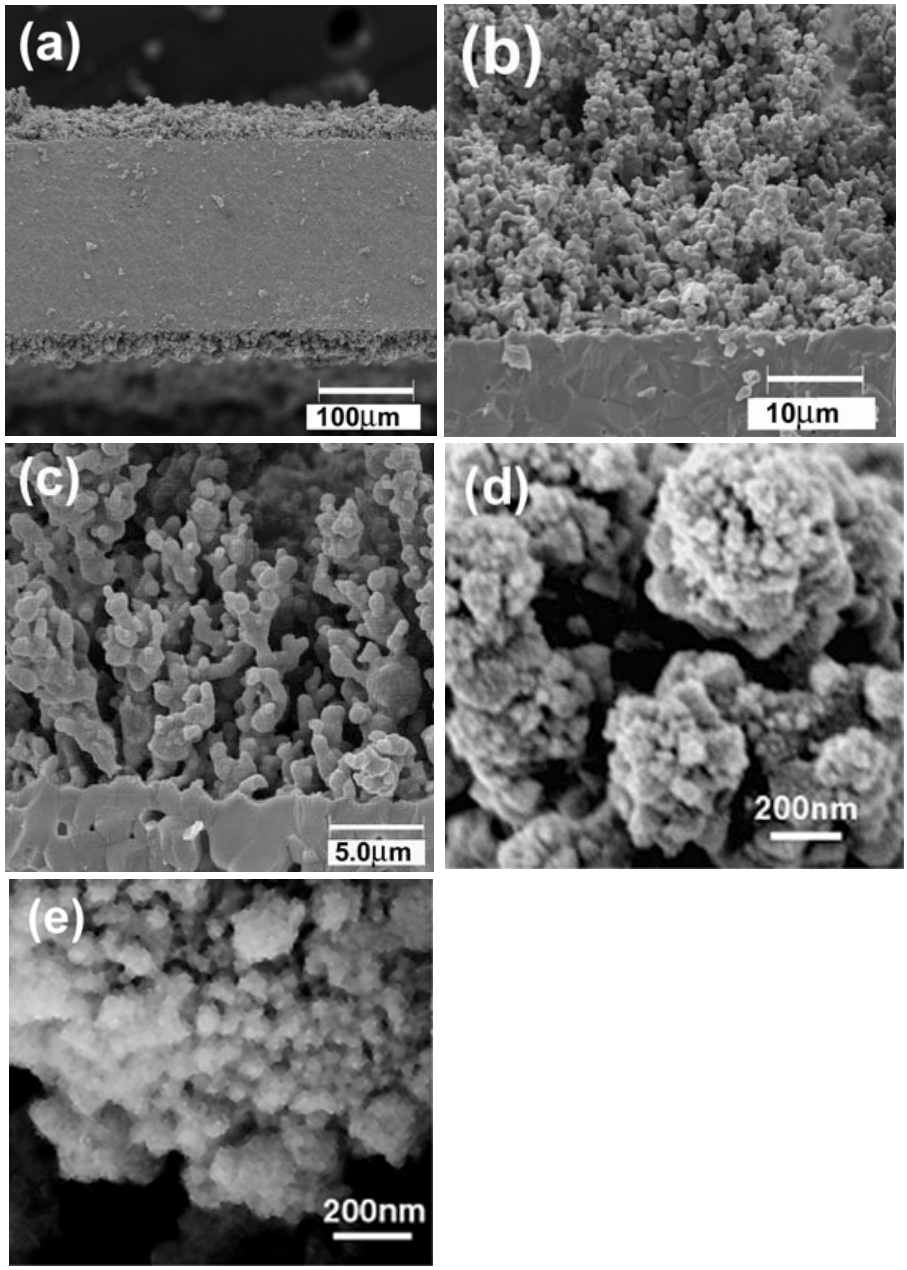


Figure 4-10 Cross-sectional views of an SOFC with both anode and cathode fabricated using combustion CVD: (a) the entire cell with Ni-SDC anode, GDC electrolyte, and SSC-SDC cathode, (b) anode-electrolyte interface, (c) cathode-electrolyte interface, (d) higher magnification of Ni-SDC composite anode, and (e) higher magnification of SSC-SDC composite cathode.

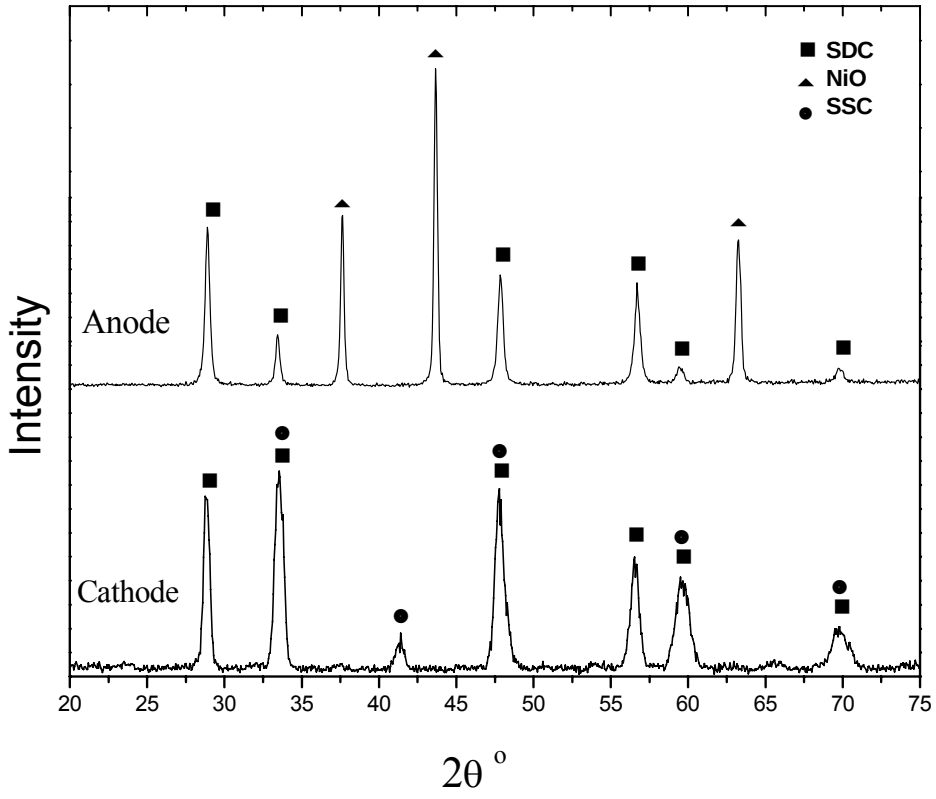


Figure 4-11 X-ray diffraction patterns of the anode (70wt.% Ni and 30wt.% SDC) and the cathode (70wt.% SSC and 30wt.% SDC) fabricated using combustion CVD.

Shown in Figure 4-12(a) are the impedance spectra of the fuel cell measured at 500°C and 600°C under open circuit conditions using a two-electrode configuration. Since the electronic conduction in GDC is not negligible under the fuel cell conditions, [22] The bulk resistance of the electrolyte ($R_b$) and the polarization resistances of the electrode-electrolyte interfaces ($R_a$+$R_c$) can no longer be determined just from the impedance data. The combination of impedance measurement and open circuit voltage (OCV) measurement becomes necessary to correct the partial shorting effect due to electronic conduction of GDC. Shown in Figure 4-12(b) are the electrolyte resistances ($R_b$) and the total interfacial resistances ($R_a$+$R_c$) as calculated from the impedance data and OCV measurements. [23] The electrode-electrolyte interfacial polarization resistance is estimated to be 1.09 Ω cm$^2$ at 500°C, 0.43 Ω cm$^2$ at 550°C, and 0.17 Ω cm$^2$ at 600°C, respectively.

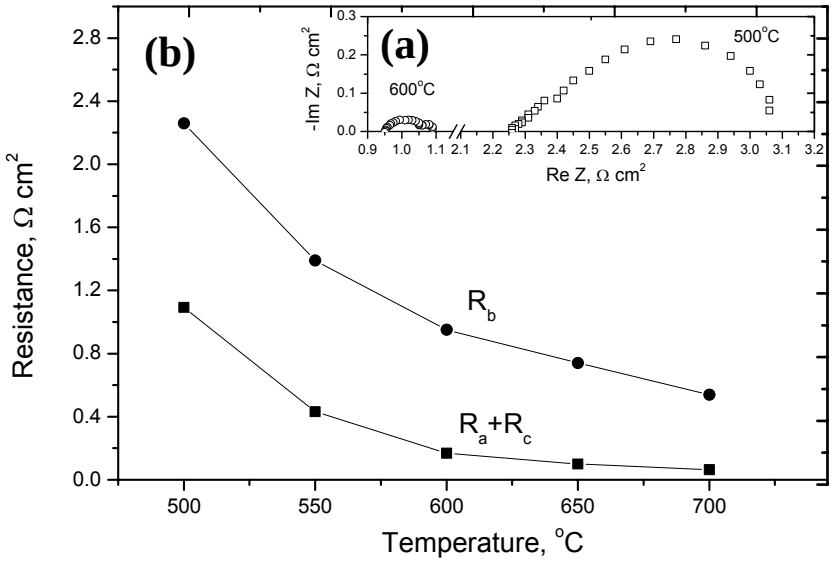


Figure 4-12 (a) Impedance spectra of a single fuel cell as measured using a two-electrode configuration, and (b) The bulk electrolyte and interfacial polarization resistances obtained from impedance spectra acquired at different temperatures.

Shown in Figure 4-13 are the polarization resistances of the cell with electrodes fabricated by combustion CVD, together with data reported in literature for doped ceria-based SOFCs. While some of the data [19, 114] were obtained using symmetrical cells, they should be comparable to those obtained from fuel cells if correctly analyzed,[116] i.e., taking into consideration of partial shorting due to electronic conduction of the electrolyte GDC under functional cell conditions. Clearly, the fuel cell with electrodes fabricated by combustion CVD displayed much lower interfacial polarization resistances than those prepared by conventional methods: slurry-painting,[19] spin-coating,[114] and screen-printing.[27] The observed interfacial polarization resistances of the electrodes fabricated by combustion CVD represent the lowest ever reported for these cathode/electrolyte systems.

Shown in Figure 4-14(a) are the cell voltages and power densities as a function of current density for a single cell with both anode and cathode fabricated by combustion CVD. The maximum power densities are 60, 108, 159, 202, and 243 mW/cm$^2$ at 500, 550, 600, 650, and 700°C, respectively. These are impressive performance data for a fuel cell based on an electrolyte of 250 μm thick. As revealed from impedance spectra shown in Figure 4-12(a), electrolyte resistances were much higher than the electrode-electrolyte interfacial polarization resistance and, thus, the cell performance was mainly limited by the electrolyte resistance. To further demonstrate the benefit brought about by low interfacial polarization resistances, anode-supported half cells with 20 μm thick GDC electrolytes were fabricated by a dry-pressing and co-firing process as described elsewhere. [27] Subsequently, SSC-SDC cathodes were fabricated onto the GDC electrolyte films (supported by anode) using combustion CVD. As expected, much higher powder densities were achieved for an anode-supported cell with a 20 μm thick

GDC electrolyte. The peak power densities are 204, 286, 375, and 481mW/cm$^2$ at 500, 550, 600, and 650 °C, respectively, as shown in Figure 4-14(b).

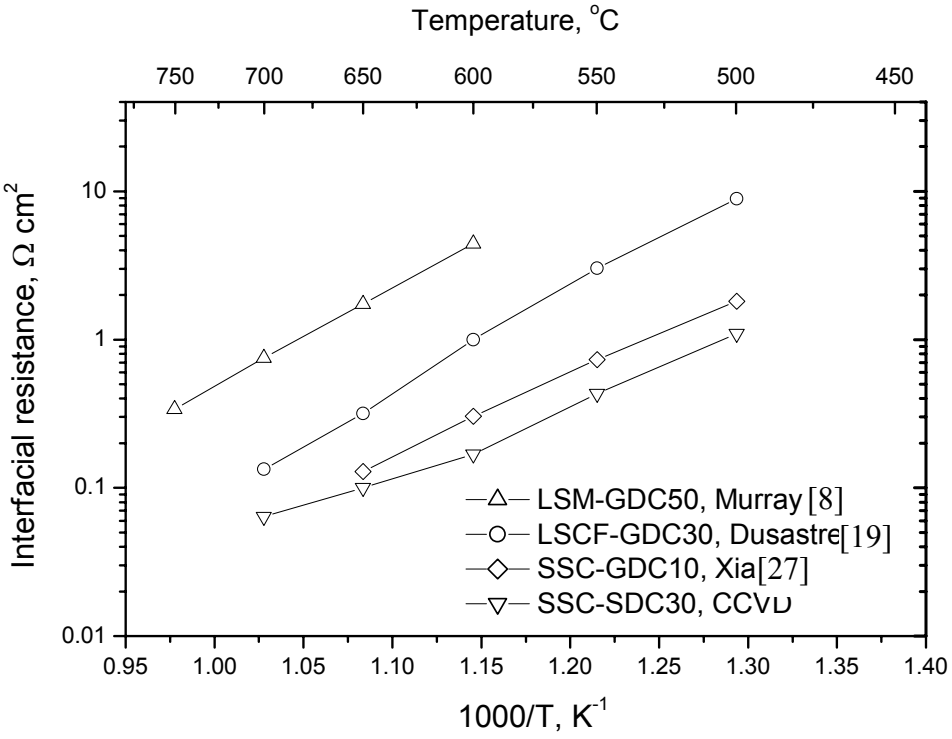


Figure 4-13 Comparison of interfacial polarization resistances as determined from impedance spectra for electrodes fabricated using different techniques: slurry-painting,[19] spin-coating,[8] and screen-printing.[27]

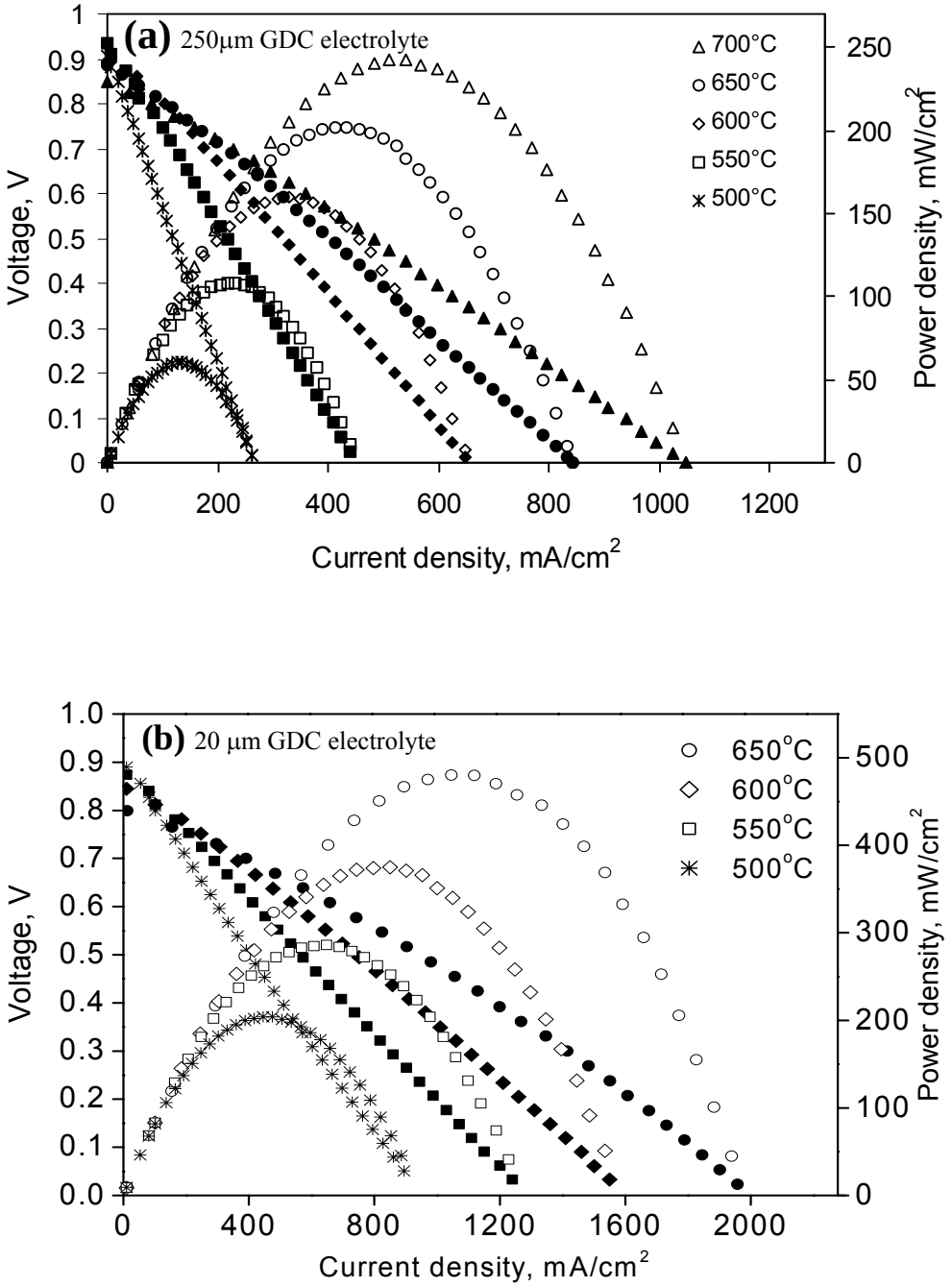


Figure 4-14 Cell voltages and power densities as a function of current density for fuel cells with: (a) both cathode (SSC-SDC) and anode (Ni-SDC) fabricated using combustion CVD on a GDC electrolyte membrane with thickness of 250 μm, and (b) a 20 μm thick GDC electrolyte.

### 4.2.3 Summary

Highly porous and nano-structured electrodes for low-temperature SOFCs have been successfully fabricated using a combustion CVD process. The electrodes fabricated by combustion CVD consist of nano-grains of about 50 nm, exhibiting extremely high surface area and remarkably low polarization resistances. XRD patterns confirmed the formation of desired crystalline phases for as-prepared NiO-SDC anodes and SSC-SDC cathodes. It is evident that combustion CVD is a highly effective approach to fabrication of high-performance electrodes for low-temperature SOFCs, producing the lowest interfacial polarization resistances (1.09 $\Omega$ cm$^2$ at 500°C, and 0.17 $\Omega$ cm$^2$ at 600°C) ever reported for the cathode materials. Anode supported cell with a 20 μm thick electrolyte demonstrated a power density of 375 mW/cm$^2$ at 600°C. Little deterioration in either microstructure or performance was observed after 172 hours of operation. While the long-term stability of these electrodes is yet to be determined, the results indicate a new direction to significantly improve the performance of low temperature SOFCs. The high deposition rate, short deposition time, and high temperature deposition conditions result in nano-sized grains, superior bonding to electrolyte, and desired crystalline phases, which are important attributes to achieving low interfacial polarization resistances, high power densities, and potentially lower operating temperatures.

## 4.3 Functionally Graded Electrodes

Solid oxide fuel cells (SOFCs) will inevitably exert a great impact on the development of next generation energy technology and hydrogen economy as fossil fuels are running out of supply. For conventional SOFCs, high operating temperature (for example, 800°C–1000°C) is required to insure sufficiently high ionic conductivity and fast electrode kinetics. Reduction of operating temperature of SOFCs is desirable to lower materials cost and elapse technical issues associated with elevated temperatures.[5, 42, 105, 107, 108, 112] However, conductivities of cell component materials decrease exponentially as temperature drops, and interfacial polarization resistances increase significantly, dramatically diminishing output power densities of fuel cells. Previous researchers have reported fabrication of compositionally graded composite cathodes using various techniques to tailor the mismatch between the physical properties of new electrode materials and the electrolyte. Traditional high-temperature SOFCs, which usually employ a yttria-stabilized zirconia (YSZ) electrolyte, a LSM cathode and a nickel-YSZ cermet anode, operate at the temperature range of 800°C–1000°C. LSM perovskite is widely used as a cathode material due to its high electrochemical activity, good stability, and thermal expansion compatibility with YSZ at cell operating temperature. Reducing the operating temperature down to 600°C–800°C brings both dramatic technical and economical benefits. The cost of SOFC technology may be dramatically reduced since much less expensive materials can be used in cell construction and novel fabrication techniques can be applied to the stack and system integration. Further, as the operating temperature is reduced, system reliability and operational life increase and so does the possibility of using SOFCs for a wide variety of applications, including residential and automotive applications. However, as the operating temperature is reduced, some

issues arise and become critical, such as the exponential reduction in conductivity for LSM, and the dramatic increase of interfacial polarization resistances between the LSM cathode and YSZ electrolyte. It has been recognized that LSC offers much higher electrical conductivity than LSM at all temperatures. Unfortunately, higher thermal expansion coefficient and reactivity restrict its direct use with YSZ electrolyte.

Several strategies have been adopted to improve interfacial conditions and electrochemical performance of LSM/YSZ system, including introduction of ionically conducting secondary phases to form composite electrodes, development of compositionally graded structures, and employment of other fabrication approaches. It was found that the interfacial polarization resistance could be reduced to one fourth of its original value by adding 50 wt.% YSZ into LSM cathode.[117, 118] It was later reported that addition 50 wt.% gadolinia-doped ceria (GDC) instead YSZ reduces the value to 1.06 $\Omega cm^2$ at 700°C and 0.49 $\Omega cm^2$ at 750°C, which is two to three times lower than those for LSM-YSZ composite cathodes on YSZ electrolyte.[8] Jiang demonstrated that by using ion impregnation methods, the interfacial polarization resistances of LSM–GDC/YSZ system can be further reduced down to 0.72 $\Omega cm^2$ at 700°C.[119]

Functionally graded materials (FGM) have been employed to join dissimilar materials or to achieve unique properties. Compositional gradient is required in a large number of engineering applications, such as joining metallic materials with ceramics.[120] On the other hand, materials exhibiting graded porosity are attractive for other applications, including graded ceramic performs,[121] special heat insulation and/or thermal shock resistant structures,[122] and medical implants,[123, 124] The concept of FGM was introduced to fabricate SOFC components recently. Either single-phase cathode materials (such as LSM/LSC) or composite cathodes (such as LSM/LSC-YSZ/GDC) were prepared on YSZ electrolyte by different methods, such as screen

printing,[125] slurry spraying,[126] spray painting,[52] and slurry coating.[104] Reduced interfacial polarization resistances and improved electrochemical performances have been reported (i.e. 0.47 Ω $cm^2$ [104] and 0.2 Ω $cm^2$ [52] at 750°C). However, all the work reported in the literature only focused on cathodes with compositional gradient. Ideally, the best structure for a functional SOFC should be the one with both compositional gradient and porosity gradient, consisting of fine grains (and high surface area) close to the electrode/electrolyte surface, and large grains (and thus large pore size) at air/oxygen side.

It has been demonstrated that nanostructured electrodes with significantly high surface area offer superior electrochemical properties as long as sufficiently large pore size and enough porosity are provided.[110, 111] Our recent work showed that nanostructured electrodes dramatically reduce electrode/electrolyte interfacial polarization resistances and improve cell performance.[99] In this section, research work on fabrication of nanostructured and functionally graded composite cathodes, which are graded in microstructure as well as in composition, using a combustion CVD process is described. A schematic diagram of the fabricated SOFC system is depicted in Figure 4-15. The resulting SOFCs exhibited extremely low interfacial polarization resistances and high powder density at the operating temperature range of 600ºC-800ºC.

### 4.3.1 Experimental

Detailed description of combustion CVD apparatus used for this study is available elsewhere.[98] Metal nitrates of Sr, Sm, Co, Ce, and Ni were obtained from Aldrich. Solution was prepared by dissolving stoichiometric amounts of precursors into an organic solvent and agitated by a magnetic stirring bar until completely dissolved. Methane was used as the fuel gas and oxygen served as the oxidizer for the combustion flame.

Dense YSZ pellets of 14 mm diameter, 240 μm thickness were prepared by tape casting and sintered at 1400°C for 5 hours. Figure 4-15 shows a schematic diagram of the SOFC design. Starting with a tape cast YSZ pellet of 14 mm diameter and 240 μm thickness, a 30 μm layer of porous 60 wt.% NiO-40 wt.% GDC was deposited onto one side of the pellet using combustion CVD at a temperature of 1250ºC. After deposition of one electrode, precursor solution was switched, and substrates were turned over for deposition of cathode materials. Firstly, 10 μm thick fine grained 60 wt.% LSM–40 wt.% GDC was deposited on YSZ electrolyte. Following this, the composition of the precursor solution was changed to 30 wt.% LSM–30 wt.% LSC–40 wt.% GDC. Sequentially, a coarse layer of 60 wt.% LSC–40 wt.% GDC was deposited on top of the cathode.

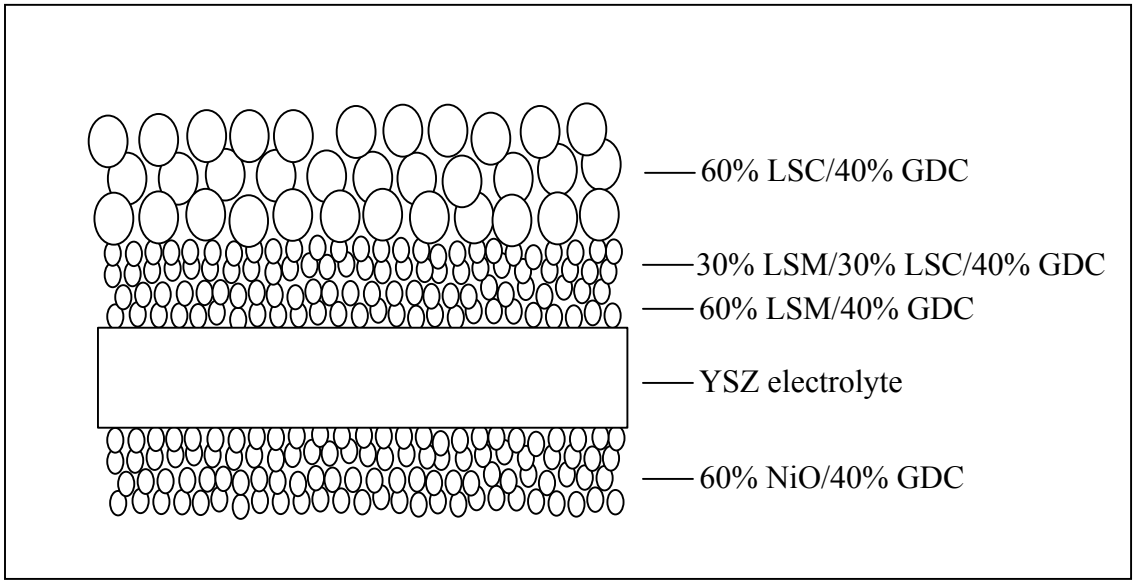


Figure 4-15 A schematic diagram of the functionally graded SOFC configuration

The microscopic features of the prepared electrodes were characterized using a scanning electron microscope (SEM, Hitachi S-800) with an energy dispersive spectroscopy (EDS) attachment. Electrochemical performances of the cells were measured at 600°C to 850°C at 50°C increase with humidified (3 vol.% water) hydrogen as fuel and stationary air as oxidant at ambient pressure. Impedances were measured in the frequency range from 0.01 Hz to 100K Hz with an EG&G Potentiostat/Galvanostat (Model 273A) and Lock-in Amplifier (5210).

### 4.3.2 Results and Discussion

Shown in Figure 4-16(a) is a cross sectional view (as fractured) of a half-cell with composite cathode supported by a 240 μm thick dense YSZ electrolyte.The cathode fabricated by combustion CVD consists of three porous layer structures and is graded in both microstructure and composition, with about 5 μm thick 60 wt.% LSM–40 wt.% GDC fine agglomerates (0.5 μm diameter) at the bottom (close to YSZ electrolyte), followed by 5 μm thick 30 wt.% LSM–30 wt.% LSC–40 wt.% GDC fine agglomerates (0.5 μm diameter), and 15 μm thick 60 wt.% LSC–40 wt.% GDC coarse agglomerates (2~3 μm diameter) on the top (air side). The two bottom layers are actually nanostructured as shown in Figure 4-16(b), offering extremely high surface area for oxygen reduction. In addition, these Mn rich layers provide fast electrochemical reaction rate, high stability and satisfying match in thermal expansion coefficient with YSZ electrolyte. Meanwhile, the large interconnected pore channels within the coarse top layer facilitate oxygen mass transport. The Co rich top layer has higher conductivity as well.

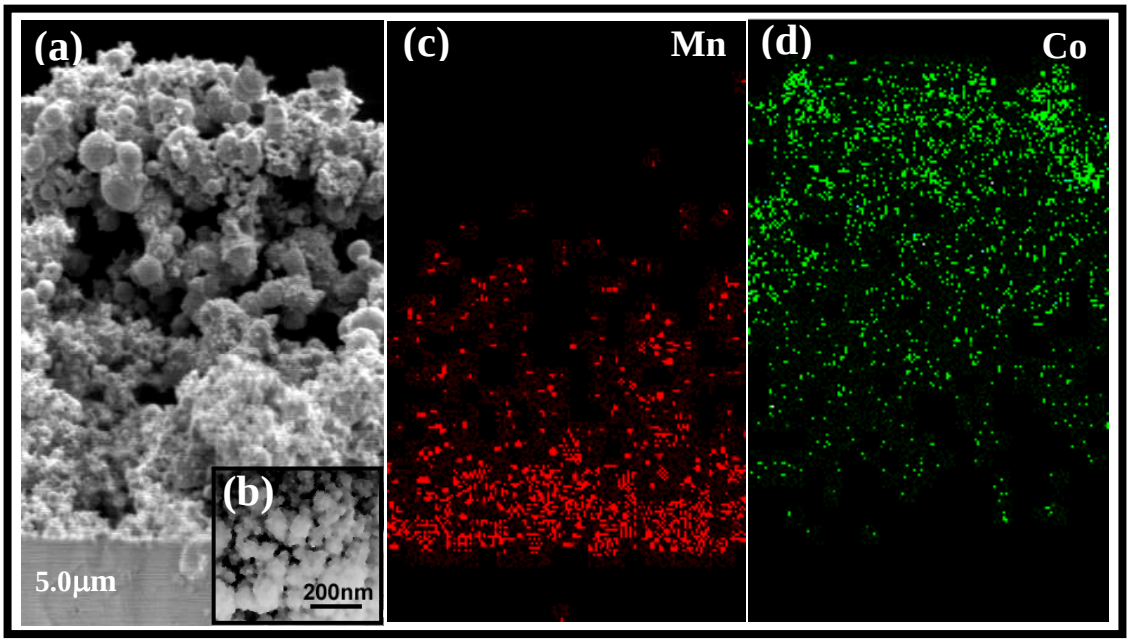


Figure 4-16 (a) Cross-sectional view of the functionally graded cathode fabricated on an YSZ pellet using a combustion CVD process, (b) higher magnification image of the cathode showing the nanostructure, (c) EDS dot mapping showing Mn distribution on the cross-section surface, and (d) EDS dot mapping of Co distribution.

It is difficult to distinguish the bottom layers, 60 wt.% LSM–40 wt.% GDC and 30 wt.% LSM–30 wt.% LSC–40 wt.% GDC from SEM micrographs, indicating that the porosity and microstructure feature were similar. However, EDS dot mapping technique revealed the compositional changes on the cross sectional micrograph. As shown in Figure 4-16(c), Mn content gradually declined from YSZ/LSM–GDC interface to LSC–GDC airside, while Co

signal exhibited the opposite trend as shown in Figure 2(d). Unlike compositional layered structures fabricated by stacking or spray-painting, where compositional abruptness was usually easily observed between adjacent layers, composition of the structures fabricated by combustion CVD change gradually across interfaces.

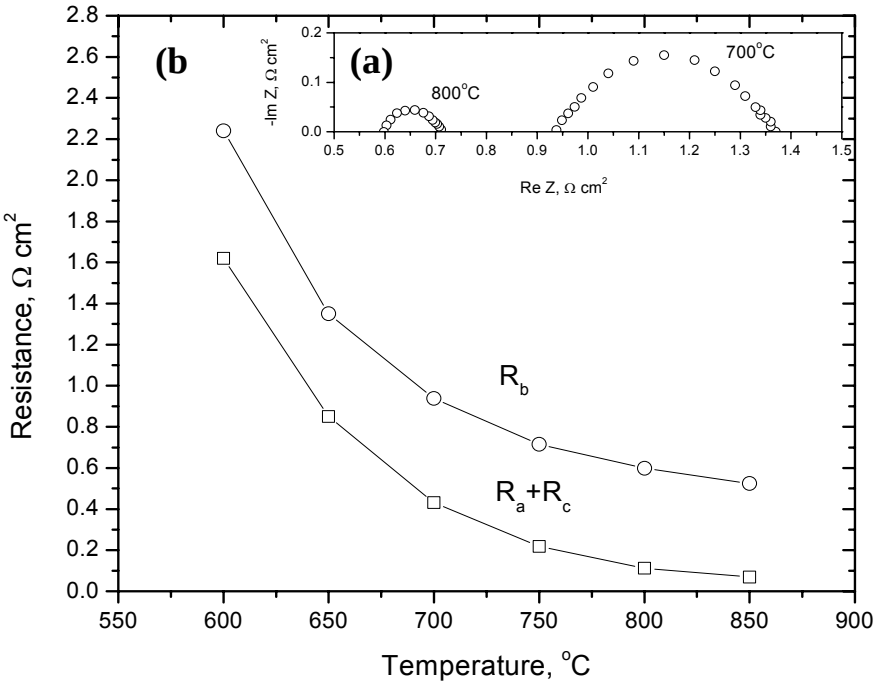


Figure 4-17 (a) Impedance spectra of a single fuel cell as measured using a two-electrode configuration, and (b) bulk electrolyte resistance ($R_b$) and interfacial polarization resistances ($R_a + R_c$) determined from impedance spectra acquired at different temperatures.

Shown in Figure 4-17(a) are the impedance spectra of the fuel cell measured at 700°C and 800°C under open circuit conditions using a two-electrode configuration. The open circuit voltages (OCV) were 1.06 V, 1.03 V and 1.0 at testing temperatures of V 600°C, 700°C and 800°C, respectively, indicating no gas crossover and negligible electronic conductivity of the YSZ electrolyte. The bulk resistance of the electrolyte ($R_b$) and the polarization resistances of the electrode-electrolyte interfaces ($R_a$+$R_c$) can thus be determined directly from the impedance data. Shown in Figure 4-17(b) are the electrolyte resistances ($R_b$) and the total interfacial resistances ($R_a$+$R_c$) The electrode-electrolyte interfacial polarization resistance is estimated to be 1.62 Ω $cm^2$ at 600°C, 0.43 Ω $cm^2$ at 700°C, and 0.11 Ω $cm^2$ at 800°C, respectively. At the same testing temperatures, the bulk resistances are 2.24, 0.94, and 0.60 $cm^2$, respectively.

Figure 4-18 shows the polarization resistances of the cell with electrodes fabricated by combustion CVD, together with data reported in the literature for SOFCs with LSM based cathodes and YSZ electrolyte. While most polarization resistances reported in the literature were measured using a symmetrical cell configuration, they should be comparable to those obtained from fuel cells if the cathode-electrolyte interfacial polarization resistances are properly separated from the rest of the cell since partial shorting due to electronic conduction of YSZ is negligible under fuel cell conditions. Clearly, the fuel cell with electrodes fabricated by combustion CVD displayed lower interfacial polarization resistances than those prepared by other methods: spin-coating,[8] slurry-spraying,[126] and ion impregnation.[119] All electrodes were tested in stationary air using a symmetrical cell configuration except the electrodes prepared by ion impregnation, which were tested in an asymmetric cell with porous Pt as the counter electrode. In fact, the observed interfacial polarization resistances of the electrodes fabricated by combustion CVD represent the lowest ever reported for these cathode/electrolyte systems.

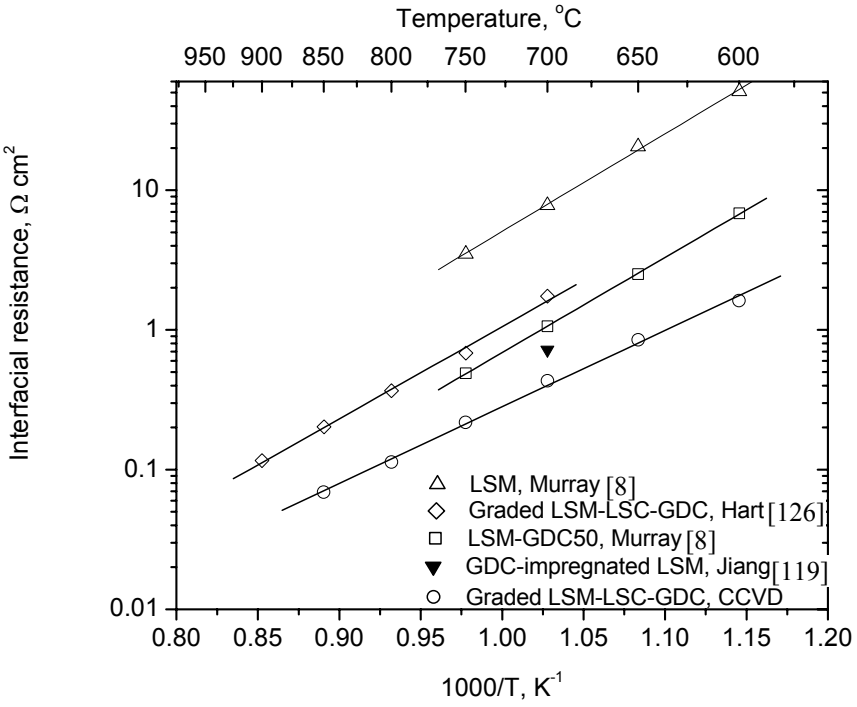


Figure 4-18 Comparison of interfacial polarization resistances for YSZ electrolyte/LSM based electrodes fabricated using different techniques: spin-coating (symmetrical cell, tested in air),[8] slurry-spraying (symmetrical cell, tested in air),[126] ion impregnation (asymmetrical cell with Pt counter electrode on the other side of electrolyte, tested in air),[119] and combustion CVD (full cell, tested in air).

Shown in Figure 4-19 are the cell voltages and power densities as a function of current density for a single cell with both anode and functionally graded cathode fabricated by combustion CVD. The maximum power densities are 138, 319, and 481 mW/cm$^2$ at 600, 700, and 800°C, respectively. At 850°C, the highest power density of 551W/cm$^2$ was recorded. These are impressive performance data for a fuel cell based on an electrolyte of 240 μm thick. As revealed from impedance spectra shown in Figure 4-17(a), electrolyte resistances were much

higher than the electrode-electrolyte interfacial polarization resistance and, thus, the cell performance was mainly limited by the electrolyte resistance.

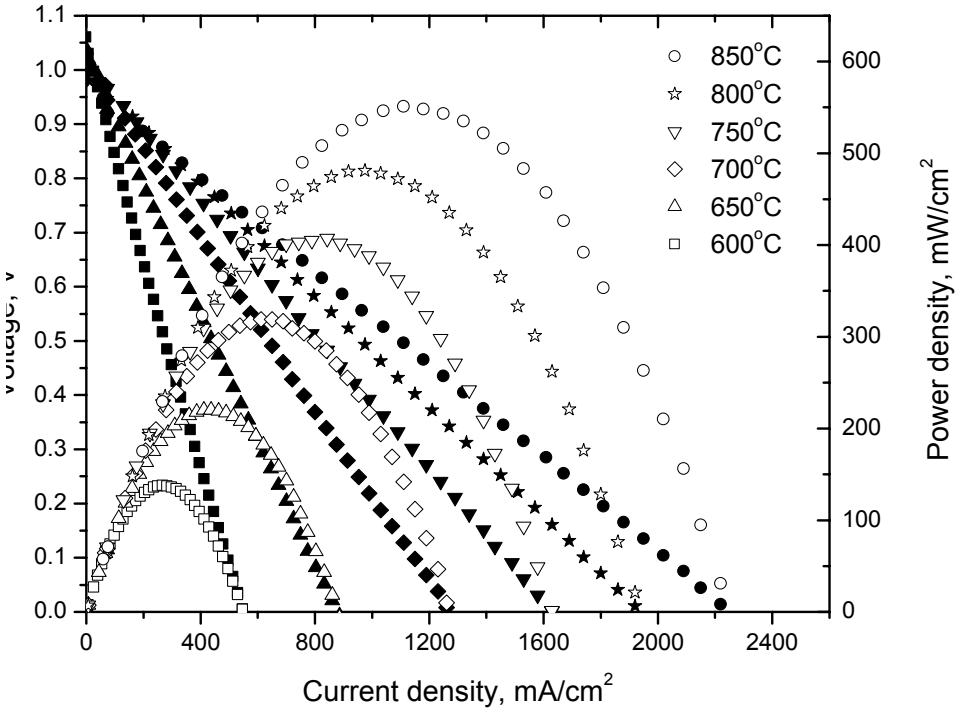


Figure 4-19 Electrical performance of a fuel cell with functionally graded cathode and anode fabricated using combustion CVD on a YSZ electrolyte membrane of 240 μm thick (Testing conditions: hydrogen with 3 v% of water vapor as the fuel and stationary air as the oxidant, both at ambient pressure).

4.3.3 Summary

Nanostructured and functionally graded LSM-LSC-GDC composite cathodes have been successfully fabricated on 240 μm thick YSZ electrolyte supports using a combustin CVD

method. The fabricated cathodes were graded in both composition and structure with higher strontium-doped lanthanum manganite (LSM) content and finer primary grain size at electrolyte side while higher strontium doped lanthanum cobaltite (LSC) content and coarser primary grain size at air/oxygen side. Extremely low interfacial polarization resistances (i.e. 0.43 $\Omega cm^2$ at 700°C) and impressively high power densities (i.e. 481 $mW/cm^2$ at 800°C) were generated at operating temperature range of 600°C–850°C. It is the first time to verify the existing ideal SOFC model experimentally. The promising results suggest that high power density, intermediate operating temperature, and low cost SOFCs can be fabricated using combustion CVD method.

### 4.5 Electrodes Produced by A Dual-Phase (Particle-Solution) Spraying Process

Solid oxide fuel cells (SOFCs) have a great potential to be the power of the future because of their high energy-conversion efficiency, low pollutant emission, and excellent flexibility with practical fuels (e.g., hydrocarbon fuels with contaminants). Efforts are being made to lower the operating temperature from 800–1000°C to 600–800°C in order to reduce cost and improve reliability and operational life.[5, 42, 107, 108, 110-112, 127] One of the critical challenges for operation of SOFCs at low temperatures is how to reduce interfacial polarization resistances ($R_p$).[27] New materials must be identified or developed to improve the intrinsic catalytic properties of the electrode materials. Further, novel fabrication techniques have to be developed in order to create unique microstructures in a cost-effective manner.

It has been generally recognized that composite electrodes offer better performance than single-phase electrodes for SOFCs due to the extension of triple-phase-boundary (TPB) into the

porous electrode body away from the traditional electrode-electrolyte interface. As a result, the overpotential at the electrodes can be dramatically reduced. This approach has been very successful for the cathode, which is usually the major factor limiting cell performance. The composite cathodes typically consist of a mixed-conducting material and an ionic conductor such as YSZ[7, 117] or GDC.[19, 20, 128]

Various fabrication techniques have been studied to optimize the microstructure and distribution of each component. It was demonstrated that cell performance could be improved by sol-gel coating of $La_{0.85}Sr_{0.15}MnO_3$ (LSM) with YSZ or $Sm_{0.2}Ce_{0.8}O_2$ (SDC).[56] Similarly, Jiang et al. modified LSM cathode with $Gd_{0.2}Ce_{0.8}O_2$ (GDC) by an ion impregnation method.[119] The interfacial polarization resistance of the LSM–GDC/YSZ system at 700°C was reduced to 0.72 $\Omega cm^2$ by multiple coatings to obtain the required thickness and by subsequent firing following each coating to ensure desired crystallographic phases.

Recently, a combustion CVD process has been successfully introduced to fabricate components for solid oxide fuel cells. Highly porous, nano-structured electrodes with superior electrochemical performances have been prepared using this method.[99, 129] In combustion CVD, precursors such as nitrates or organic salts are dissolved in a flammable solvent. The resulting solution is then pumped into a nanomizer, where a combustion flame is created. A film or coating is deposited when a substrate is within or near the tip of the flame. Electrodes of uniform composition, but with vastly different microstructures, have been created under different conditions. In this chapter, a new process for fabrication of SOFC electrodes, a particle-solution spraying process is described. One component of the composite electrode, $Sm_{0.5}Sr_{0.5}CoO_3$ (SSC), was introduced in the form of nitrates dissolved in a flammable solvent, while the other component of the electrode, GDC, was introduced in the form of solid particles dispersed in the

SSC solution. The desired crystalline phase of SSC forms within the flame during deposition. The resulting cathodes have very unique microstructures: each large grain consists of smaller particles, which in turn contains even smaller particles. The smallest feature is within nanoscale. SOFCs with these electrodes have shown very low interfacial polarization resistances and high cell performance at low operating temperatures.

### 4.5.1 Experimental

Anode (65wt.% NiO and 35wt.% GDC) supported GDC substrates were prepared by co-pressing followed by sintering as described elsewhere.[27] Cathodes consisting of SSC and GDC were deposited onto the GDC/NiO-GDC substrates using a particle-solution spraying process. The apparatus for the spraying process is similar to that for combustion CVD as described elsewhere. [98, 130] Nitrates of Sm, Sr, and Co in a molar ratio of 1:1:2 (to form $Sm_{0.5}Sr_{0.5}CoO_3$ after combustion) were dissolved into absolute ethanol. GDC particles were prepared by the glycine-nitrate method[131] and were directly dispersed in the SSC ethanol solution. The weight ratio of SSC and GDC was kept at 7:3 corresponding to a volume ratio of 71:29. Before deposition, the solid-solution mixture was ultrasonically dispersed to break apart the large agglomerates. During deposition, a magnetic stirrer was used to prevent particles from settling down. Deposition of cathodes was carried out at 1250°C for 10 minutes. Deposition temperature was measured by placing type K thermocouples in the vicinity of substrate surfaces.

The microscopic features of the prepared electrodes were characterized using a scanning electron microscope (SEM, Hitachi S-800) equipped with an energy dispersive spectroscopy (EDS) attachment. X-ray diffraction analysis was performed on a Phillips PW-1800 diffractometer with a scanning step of 0.005 degree. Electrochemical performances of the

symmetrical cells were measured in ambient air from 450°C to 650°C. Impedances were typically acquired in the frequency range from 0.01 Hz to 100 kHz with an EG&G Potentiostat/Galvanostat (Model 273A) and a Lock-in Amplifier (5210).

### 4.5.2 Results and Discussion

Shown in Figure 4-20 is a typical TEM micrograph of the GDC nano-particles synthesized by a glycine-nitrate process. The particle size varies from 10 to 30 nm with some agglomeration.

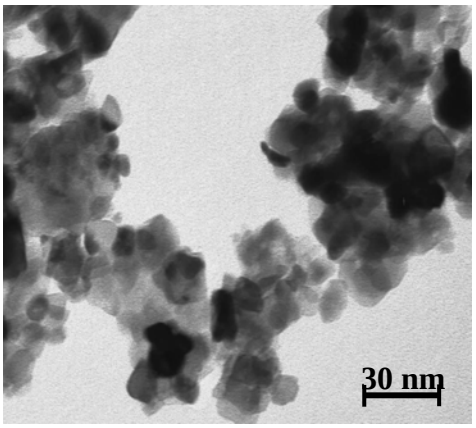


Figure 4-20 A TEM micrograph of the GDC nano-particles synthesized by a glycine-nitrate method.

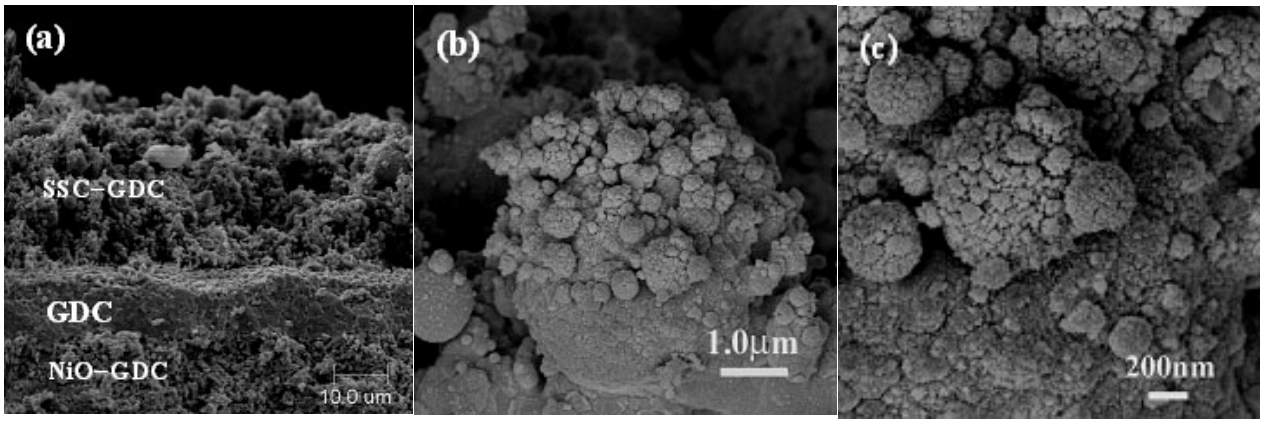


Figure 4-21 (a) Cross-sectional view of solid oxide fuel cell with SSC-GDC cathode fabricated by a particle-solution spraying process. (b) and (c) higher magnification SEM micrographs of the SSC-GDC cathode showing larger particles surrounded by nano-structured smaller particles.

Shown in Figure 4-21(a) is a cross-sectional view of an SOFC with the cathode fabricated by a particle-solution spraying process. The dense GDC electrolyte had a thickness of about 20 μm. The cathode is highly porous and is about 30 μm thick. Higher magnification SEM micrographs shown in Figure 4-21(b) and (c) indicate that the large particles (1–2 μm) consist of particles smaller than 50 nm in diameter.

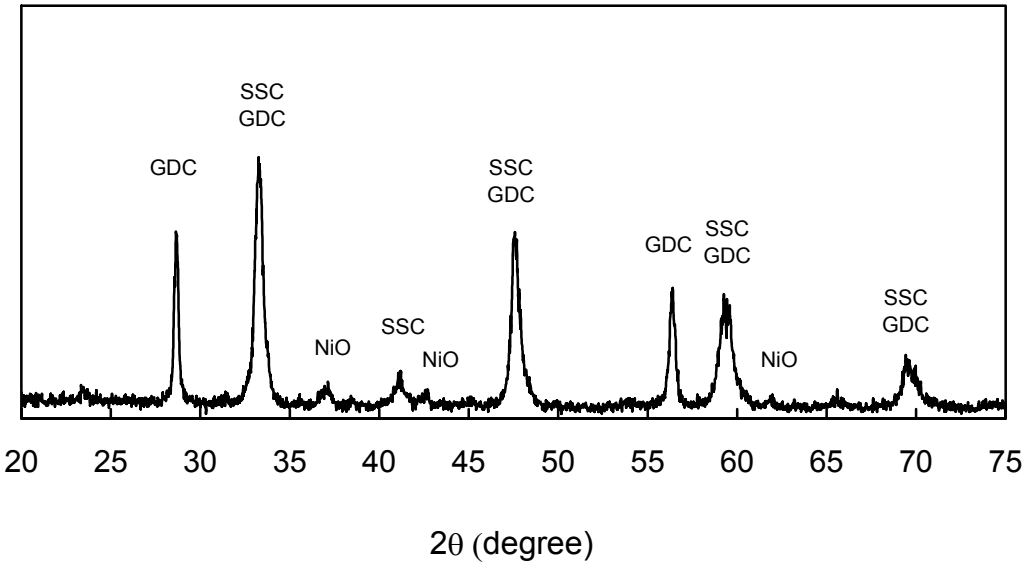


Figure 4-22 An X-ray diffraction pattern of the SSC-GDC cathode (70wt.% SSC and 30wt.% GDC) fabricated by the particle-solution spraying process.

The X-ray diffraction pattern of the cathode shown in Figure 4-22 indicates that the cathode consists of two highly crystallized phases: SSC and GDC. The GDC peaks came from particles dispersed in solution, while the SSC phase was formed during deposition through chemical vapor reaction. A previous study suggested that highly crystallized SSC phase can be formed at deposition temperatures higher than 1200°C.[98] In addition, trace of NiO was also observable on the XRD pattern. The NiO signal must be collected from the peripheral surface of the substrate, a NiO-GDC composite anode. It is noted that the baseline of the XRD pattern is not very smooth. Small amount of other phases may be present as implied by the unidentified small peaks.

Impedance spectra of a single cell with configuration of SSC–GDC/GDC/NiO–GDC were measured using a two-electrode configuration in the temperature range of 450°C to 650°C. Shown in Figure 4-23(a) are two typical impedance spectra measured at 500°C and 600°C, respectively. It is noted that each spectrum consists of at least two overlapped semicircles. While it is apparent that multiple processes contributed to the impedance spectra, no attempts were made to separate theses processes. Instead, the impedance data was used only to separate the interfacial polarization resistances ($R_p$) from other contributions. Clearly, the interfacial polarization resistances ($R_p$) were much smaller than the bulk resistances ($R_b$) even though the electrolyte was only 20 μm thick. For example, interfacial resistances were 0.45 $\Omega cm^2$ and 0.15 $\Omega cm^2$ at 500°C and 600°C, respectively, while the bulk resistances were 0.58 $\Omega cm^2$ and 0.38 $\Omega cm^2$ at the two temperatures, respectively. These interfacial polarization resistances ($R_p$) are compared in Figure 4-23(b) with those of the cells having identical materials and configuration but were fabricated using different processes. Bulk resistances ($R_b$) and interfacial polarization resistances ($R_p$) were extracted from the measured impedance spectra and corrected by taking into consideration of electronic conduction at corresponding temperature using the following equation:[116]

$$R_p = \frac{R_T - R_b}{\frac{V_{OC}}{E_N}\left[1 - \frac{R_b}{R_T}\left(1 - \frac{V_{OC}}{E_N}\right)\right]} \qquad \text{Equation 4-2}$$

Where $R_T$ is the total resistance of the SOFC as determined from the intercept of impedance spectrum with the real-axis at low frequencies, $R_b$ is the bulk resistance as read from the

intercept at high frequencies, $V_{OC}$ represents the open cell voltage, and $E_N$ is the Nernst potential across the cell at testing temperatures.

It is evident that fuel cells with cathodes fabricated by the particle-solution spraying process had very low interfacial polarization resistances, especially at low operating temperatures. Typical performances of the SOFC are shown in Figure 4-24. It is noted that the open circuit voltage (OCV) dropped from 0.9 V to 0.8 V as the testing temperature arose from 450°C to 650°C, implying that the mixed-conducting is getting more significant at higher temperatures and the correction using equation (1) is necessary. The observed peak power densities were about 223, 316, 385, and 411 mW/cm$^2$ at 500, 550, 600, and 650°C, respectively.

The activation energies calculated from the slope of the curves shown in Figure 4-23(b) are 1.08 eV (104.4 kJ/mol) for cathodes made by screen-printing,[27] 0.90 eV (90.1 kJ/mol) for combustion CVD derived cathodes,[99] and 0.65 eV (62.5 kJ/mol) for electrodes fabricated using the particle-solution spraying. From the microstructural point of view, the particle-solution spraying process offers the advantages of both conventional ceramic techniques and combustion CVD. Each GDC particle was surrounded by numerous tiny, nano-sized SSC particles. Electrochemical kinetics was thus dramatically enhanced.

The particle-solution spraying process combines the merits of combustion and flame spraying. SSC precursors serve as bonding agent for GDC solid particles as well as active composite component. The unique structure created by this process contributes to the superior cell performance. Based on the fundamental principle of the process and the observation of microstructures, the proposed growth mechanism of the nano-composite cathode is schematically illustrated in Figure 4-25.

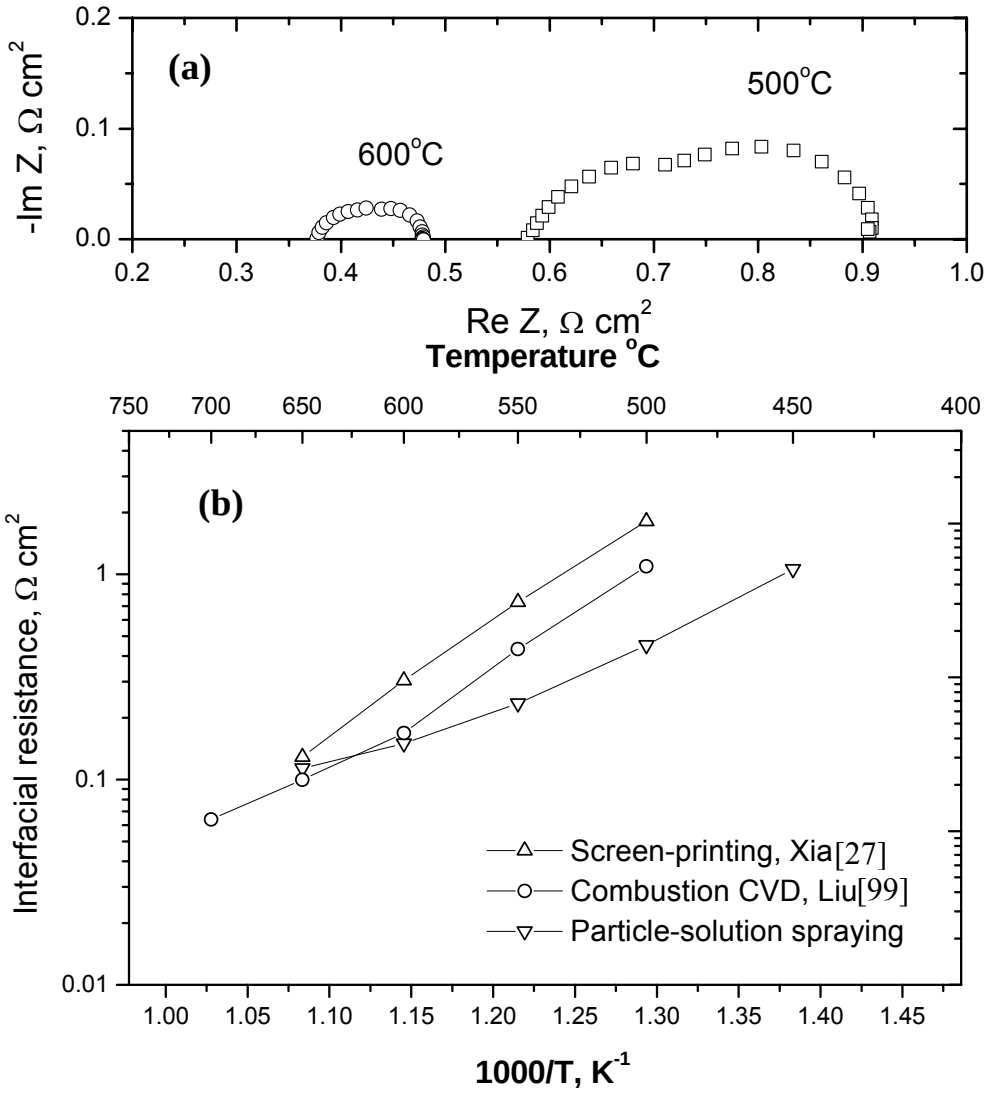


Figure 4-23 (a) Impedance spectra of a single fuel cell as measured using a two-electrode configuration.(b) Comparison of interfacial polarization resistances as determined from impedance spectra for electrodes fabricated using different techniques: screen-printing,[27] Combustion CVD,[99] and particle-solution spraying.

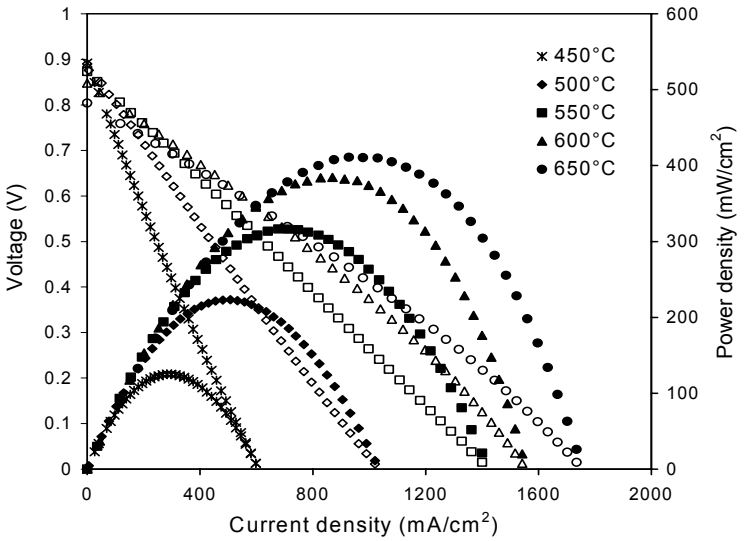


Figure 4-24 Cell voltages and power densities as a function of current density for fuel cells with SSC-GDC cathode SSC-GDC fabricated by the particle-solution spraying process.

The chemical reaction can be retrieved to the combustion flame. As shown in Figure 4-25(a), microscale liquid droplets containing Sm, Sr, and Co nitrates is sprayed out of orifice of the atomizer together with solid GDC particles. Because these precursor species exist in gaseous phase throughout the entire combustion flame, nucleation and growth of SSC particles could occur at three locations: on the surface of the GDC substrate, within the combustion flame due to the high precursor concentration, or on the surface of the readily available GDC particles inside the flame. Particle growth, collision, and agglomeration are also expected within the flame during deposition.

At the second stage of growth as shown in Figure 4-25(b), the agglomerates consisting of GDC particles and SSC nano-phase are deposited on the surface of GDC electrolyte substrate.

The newly nucleated SSC phase on the substrate and the traveling SSC nano-particles within the flame facilitate formation of good bonding between the large agglomerates and the substrate.

Both sintering and the arrival of new material contribute to the coarsening of the porous film grains as illustrated in Figure 4-25(c) and (d). This process continues until the deposition is terminated. The final microstructure has fractal features: each large grain consists of smaller particles, which in turn contains even smaller particles. The resulting porous structures have large pores for rapid gas transport and extremely large surface area for fast electrochemical reactions; the porous structures are ideally suited for electrodes in solid state electrochemical systems.

### 4.5.3 Summary

A particle-solution spraying process has been developed for fabrication of nano-structured, highly porous electrodes for solid oxide fuel cells. GDC particles suspended in an SSC–ethanol solution were burned in a combustion flame, depositing a porous cathode on an anode supported GDC electrolyte. Extremely small interfacial polarization resistances were obtained, especially at low temperatures such as 450°C (1.06 $\Omega cm^2$) and 500°C (0.45 $\Omega cm^2$). A peak power density of 385 $mW/cm^2$ was achieved at 600°C. The superior performance was attributed to the unique microstructure: pre-introduced GDC powders were bonded by nanosized SSC particles synthesized within the flame.

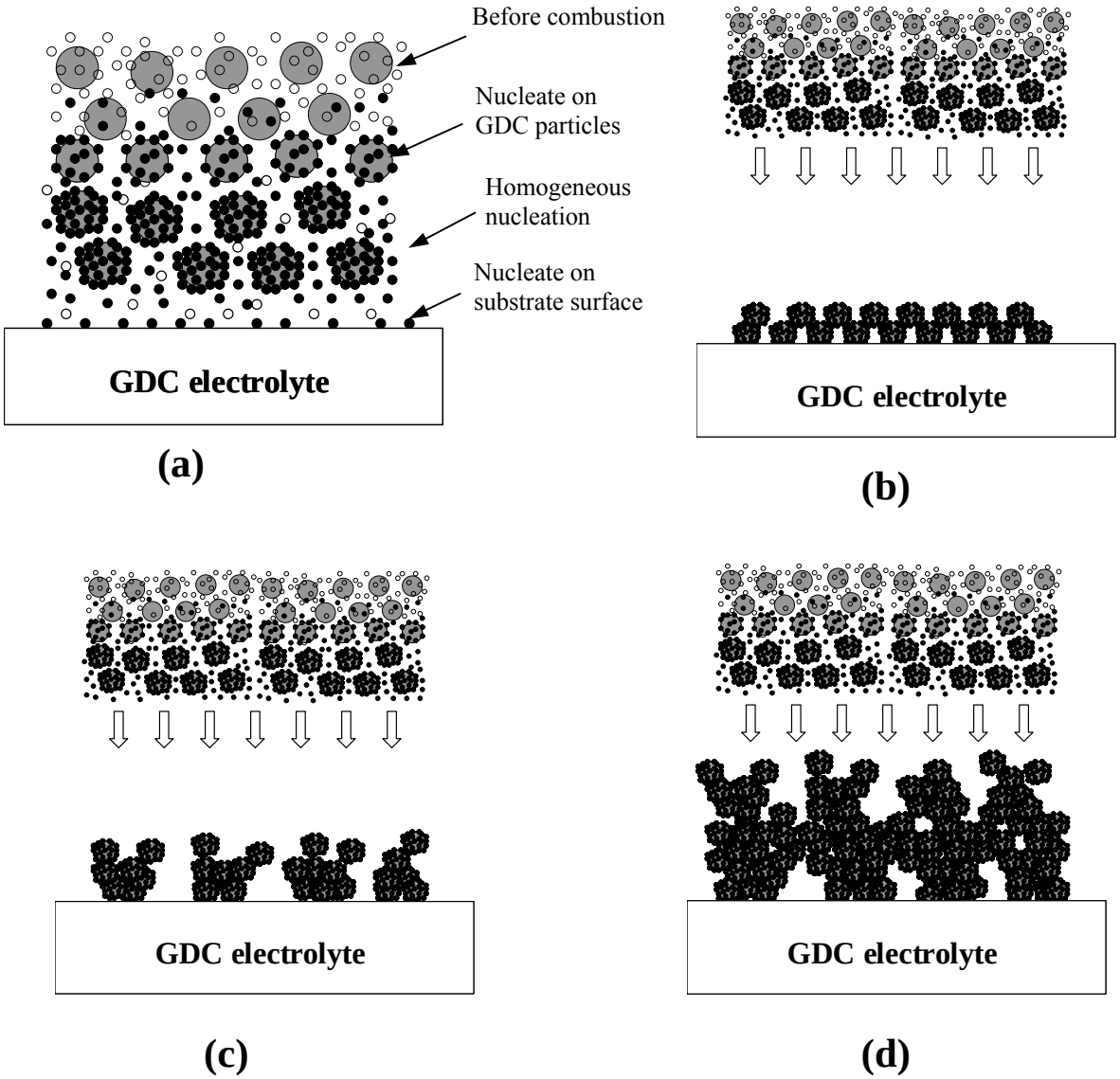


Figure 4-25 Schematic illustrations of the formation processes of the porous SSC-GDC composite cathodes: (a) three nucleation sites of SSC nano-particles, (b), (c), and (d) different growth stages of composite grains.

## 4.4 Electrodes Fabricated by A Modified Combustion Spray Process

Highly porous films and/or coatings with extremely large surface areas are important to many applications such as catalysis, chemical sensing, and energy storage and conversion. In particular, fabrication of highly efficient porous electrodes for solid oxide fuel cells (SOFCs) represents a great challenge facing the successful realization of low-temperature SOFCs. To date, various fabrication processes have been studied, including physical and chemical deposition processes based on slurry, solution, or vapor phase.[8, 27, 55, 96, 97, 131-136]

The conventional approaches such as tape-casting,[132] dry-pressing,[131] screen-printing,[27] and spin-coating[8] have the merits of simplicity, high productivity, and good repeatability. However, the requisite post-process sintering at high temperatures for a prolonged period of time often leads to limited surface area and poor electrochemical performance. Accordingly, advanced techniques for producing high-quality porous electrodes have been explored, including chemical vapor deposition,[133] rf magnetron sputtering,[134] microwave plasma coating,[135] laser-assisted deposition,[136] electrostatic spray deposition (ESD),[55] and flame assisted vapor deposition (FAVD).[96, 97]

Recently, a relatively new technique, combustion CVD has been adopted to fabricate SOFC components.[98, 99, 129] Porous composite electrodes with nano-structured features and excellent electrochemical performances have been successfully prepared using combustion CVD. Later, the combustion CVD process (that uses only soluble precursors) was further modified by introducing one component of the composite electrodes, $Gd_{0.2}Ce_{0.8}O_2$ (GDC), in the form of solid particles.[137] The other component of the composite electrodes, $Sm_{0.5}Sr_{0.5}CoO_3$ (SSC), was introduced as a liquid (metal nitrates dissolved in a flammable solvent), formed during deposition, and served as binding agent. The major benefits associating with the suspension

rather solution precursors are low cost and the elimination of solubility limitation. In this study, a new process, combustion spray is invented for fabrication of porous films and coatings. In this approach, all components of the electrode material are introduced as solid particles carried by a flammable liquid. SOFC cathodes fabricated by this method showed much lower interfacial polarization resistances at relatively low operating temperatures.

### 4.4.1 Description of the Process

Combustion spray is mainly a physical deposition process, which utilizes solid powders in the size range of nanometer up to millimeter suspended in flammable liquid carrier. The detailed apparatus setup is schematically illustrated in Figure 1. Solid powders are suspended in an organic liquid carrier by magnetic or ultrasonic stirring or other mechanisms. The resulting mixture is then transported into an atomizer where a fine mist of solution is generated using high-pressure oxidant gas such as air or oxygen. After ignition, a combustion flame is created and sustained by a small pilot ox-hydrogen pilot flame. Upon burning, collision and sintering of the contained solid particles occur. A coating could be formed if a substrate is present within or near tip of the flame.

A simple mechanism was employed to atomize the suspension. The atomizer consists of two concentric stainless steel tubes. The outer tube has an outer diameter of 3.2 mm and the inner tube has an outer diameter of 0.79 mm. Mixture of solid powder and flammable liquid carrier is supplied to the inner tube. Atomizing oxidant gas is introduced into the gap between the two tubes. Upon leaving the concentric tubes, the high-pressure gas mixes with the solid-liquid mixture, producing a fine mist. The oxygen/air serves as both oxidant and atomizing gas.

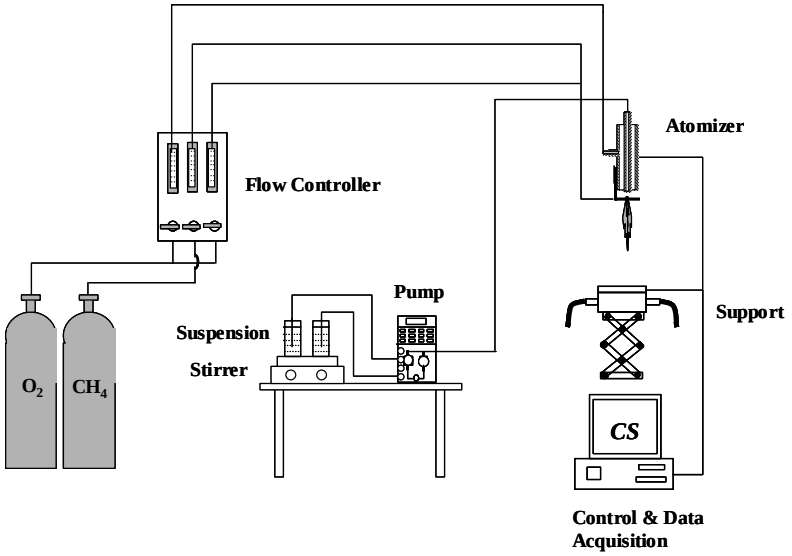


Figure 4-26 A schematic apparatus for combustion spray.

Alternatively, solutions containing desired precursors instead of pure liquid might be used together with solid powders. Two purposes can be achieved: enhancing bonding between particles and particle-substrate when porous films are produced, or producing an active coating on the surface of existing solid powders when double layer particles are desired.

The combustion spray process distinguishes itself from any chemical vapor deposition processes since it is manly a physical method. Meanwhile, combustion spray is different from all approaches using pure solutions or dry powders as feeding materials[138] because combustion spray directly utilizes solid particles carried by a flammable liquid. Further, combustion spray is different from approaches using heating sources other than a combustion flame. In particular, several deposition techniques come close to combustion spray, but they are different in nature.

Spray pyrolysis is a thin film forming technique in which a solution is sprayed onto a heated substrate to form a film. The resulting film usually receives additional heat treatment to form the desired phase(s). Another one is thermal spraying, in which dry powders are fed into a gas combustion torch (flame spraying) or plasma torch (plasma spraying), and the melted materials are splattered onto the substrate to form a film. Although a variation of flame spraying uses a solution instead of a powder as feeding materials,[139, 140] so far there is no method found employing a flammable liquid to carry the solid powder. The method most similar to combustion spray is the technique termed combustion CVD, in which the combustion flame is created by the flammable solution rather an additional torch.[58] However, it uses solutions containing precursor species, instead of solid powder.

The major advantages of combustion spray over other existing film deposition processes include dramatic reduction in capital investment and operating costs, great flexibility, easy process control, availability of raw materials, little environmental impairment, capability of producing multi-layer structures, and flexibility in composition. Combustion spray is carried out in open atmosphere. The thermal environment for bonding of particles and substrate is provided by the combustion flame. No reaction chamber, furnace, or auxiliary heating source is necessary for this process. Solid particles rather expensive organic reagents common for other deposition processes are used, significantly reducing deposition cost and eliminating solubility problem. The open-air condition makes it very easy to adjust and control deposition parameters at any stage during deposition. The use of inexpensive, readily available raw materials (usually oxides) also brings environmental advantages comparing with other deposition process where toxic precursors (e.g., chloride or sulfide) must be used. Further, films fabricated using combustion spray do not require post-deposition heat treatment. Comparing with conventional press and

firing processes, in which several hours of high temperature sintering is often required, the combustion spray approach takes only a few minutes to achieve a film thickness up to 20 μm.

Combustion spray can be used for deposition of films and coatings with a wide variety of compositions, structures, and morphologies, from thin films to thick coatings, from dense films to porous films, and also for surface coated particles. Some of the potential applications include (a) porous films for energy storage and conversion, such as electrodes for solid oxide fuel cells, batteries, and sensors; (b) catalysts for chemical reactions; (c) dense oxide coating for high-temperature applications; (d) semiconductors and buffer layers; and (e) electro-potic materials and devices.

### 4.4.2 Experimental Procedures

Anode (65wt.% NiO – 35wt.% GDC) supported GDC substrates were prepared by co-pressing follwed by sintering as described elsewhere.[17] Cathodes were deposited onto the substrates using a combustion spray process. Powders of SSC and GDC (Rhodia E & C, Cranbury, NJ) have an average particle size of 0.9 and 0.3 μm, respectively. The solid particles of SSC and GDC were put in ethanol in a weight ratio of 7:3. Before deposition, the solid-liquid mixture was ultrasonically dispersed to break down particle agglomeration. During deposition, a magnetic stir bar was used to prevent particles from settling down. Deposition was carried out at 1250°C for 10 minutes. Deposition temperature was measured by placing type K thermocouples near substrate surfaces.

The microscopic features of the prepared electrodes were characterized using a scanning electron microscope (Hitachi S-800) equipped with an energy dispersive spectroscopy (EDS) attachment. Electrochemical performances of the symmetrical cells were measured in ambient air

from 450°C to 650°C. Impedance spectra were typically acquired in the frequency range from 0.01 Hz to 100 kHz with an EG& Potentiostat/Galvanostat (Model 273A) and a Lock-in Amplifier (Model 5210).

4.4.3 Results and Discussion

Shown in Figure 4-27(a) is a cross-sectional view of an SOFC with a composite cathode consisting of SSC and GDC fabricated by combustion spray. The bottom layers are a 30 μm dense GDC electrolyte supported by a porous anode consisting of 65wt.% NiO and 35wt.% GDC and the top layer is a 40 μm thick cathode prepared using combustion spray. A higher magnification SEM micrograph of the cathode,

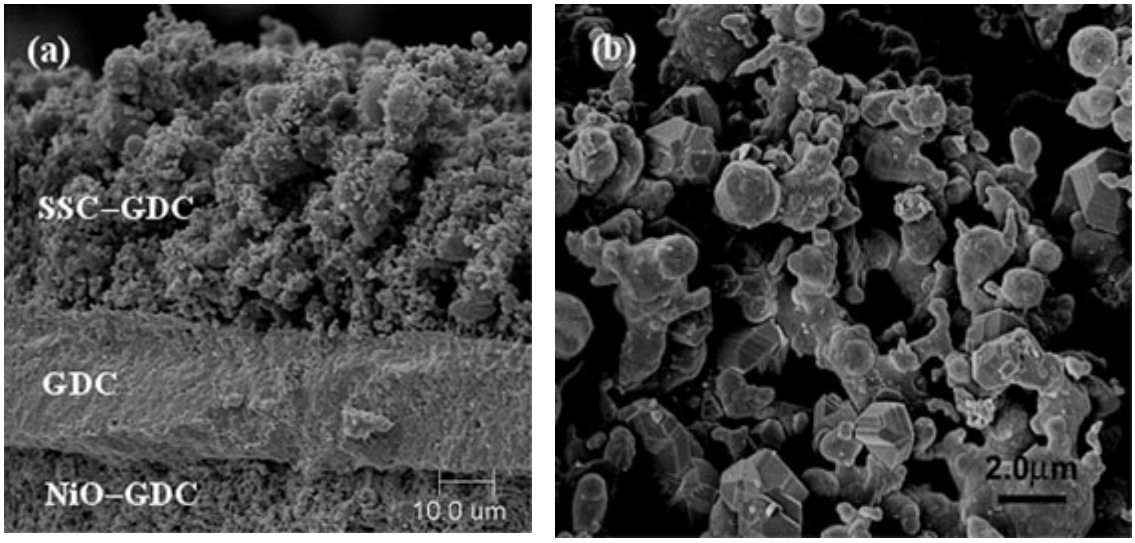


Figure 4-27 (a) A cross-sectional view of a solid oxide fuel cell with SSC-GDC cathode fabricated by a combustion spray process and (b) a higher magnification SEM micrographs of the cathode.

Figure 4-27(b), shows that the sizes of most grains are in the range of 0.5 to 2.0 μm and the grains are well attached to each other. The necking or bridging between grains is evident. Meanwhile, very large voids present between grains. This microscopic characteristic is different from samples prepared by conventional dry pressing and firing processes, in which interconnected gas channels are limited. Another obvious feature is that most grains have a spherical shape; however, some grains are faceted, suggesting limited vapor phase mass transport has occurred during deposition.

Shown in Figure 4-28 are some typical impedance spectra of the fuel cells as measured at 450°C to 650°C. It appears that each spectrum consists of at least two overlapped loops, implying that more than two processes have contributed to the impedance responses. While it is not clear how to correlate the details of the impedance features with interfacial processes, it is straightforward to determine the total interfacial polarization resistances of the cell, $R_p$. Since GDC has some electronic conduction under fuel cell conditions, the interfacial polarization resistances cannot be directly read from the impedance data. Open cell voltages and Nernst potential have been combined with the impedance data to calculate the interfacial polarization resistances.[116] After the correction due to electronic conduction of GDC, the interfacial polarization resistances of the cell at 500 and 600°C were 1.045 and 0.195 Ω $cm^2$, respectively, as shown in Figure 4-28(a). Shown in Figure 4-28(b) are the interfacial polarization resistances compared with data for cells of identical composition with electrodes fabricated using screen-printing. The interfacial polarization resistances for the cell with cathodes fabricated by combustion spray are comparable to those with screen printed electrodes at 550°C to 600°C, but a little smaller at temperature below 550°C. In addition, the activation energy for combustion sprayed cathodes appears to be lower than that of screen-printed cathodes. It is noted that the

interfacial polarization resistances ($R_p$) include both the anode-electrolyte polarization resistance ($R_{p,a}$) and the cathode-electrolyte ($R_{p,c}$) polarization resistance. However, the anode-electrolyte ($R_{p,a}$) polarization resistances remain the same for all cells and are relative small.[17]

Shown in Figure 4-29 is the performance of the fuel cell operated at different temperatures. The peak power densities at 500, 550, 600, and 650°C were 145, 248, 352, and 425 mW/cm$^2$, respectively. The electrochemical performance of the fuel cell with cathode prepared by combustion spray is equal or better than those fabricated using conventional firing processes, which usually require 3 to 5 hours of high temperature sintering.

### 4.4.4 Summary

A combustion spray process has been developed for fabrication of porous electrodes for solid oxide fuel cells. Solid ceramic particles, suspended in a flammable liquid carrier, are fed to an atomizer where a fine mist of solution is generated and combusted. The high velocity flame provides the energy needed for collision and sintering of the contained solid particles to produce porous electrodes. The demonstrated fast deposition rates (i.e. 40 μm in 10 min) and the elimination of post-deposition firing make this process practically valuable. This technique has been successfully used for fabrication of porous SSC-GDC cathodes for SOFCs. The performance of the porous SOFC electrodes fabricated by combustion spray is equal or better than those prepared by the conventional techniques, especially at low operating temperatures.

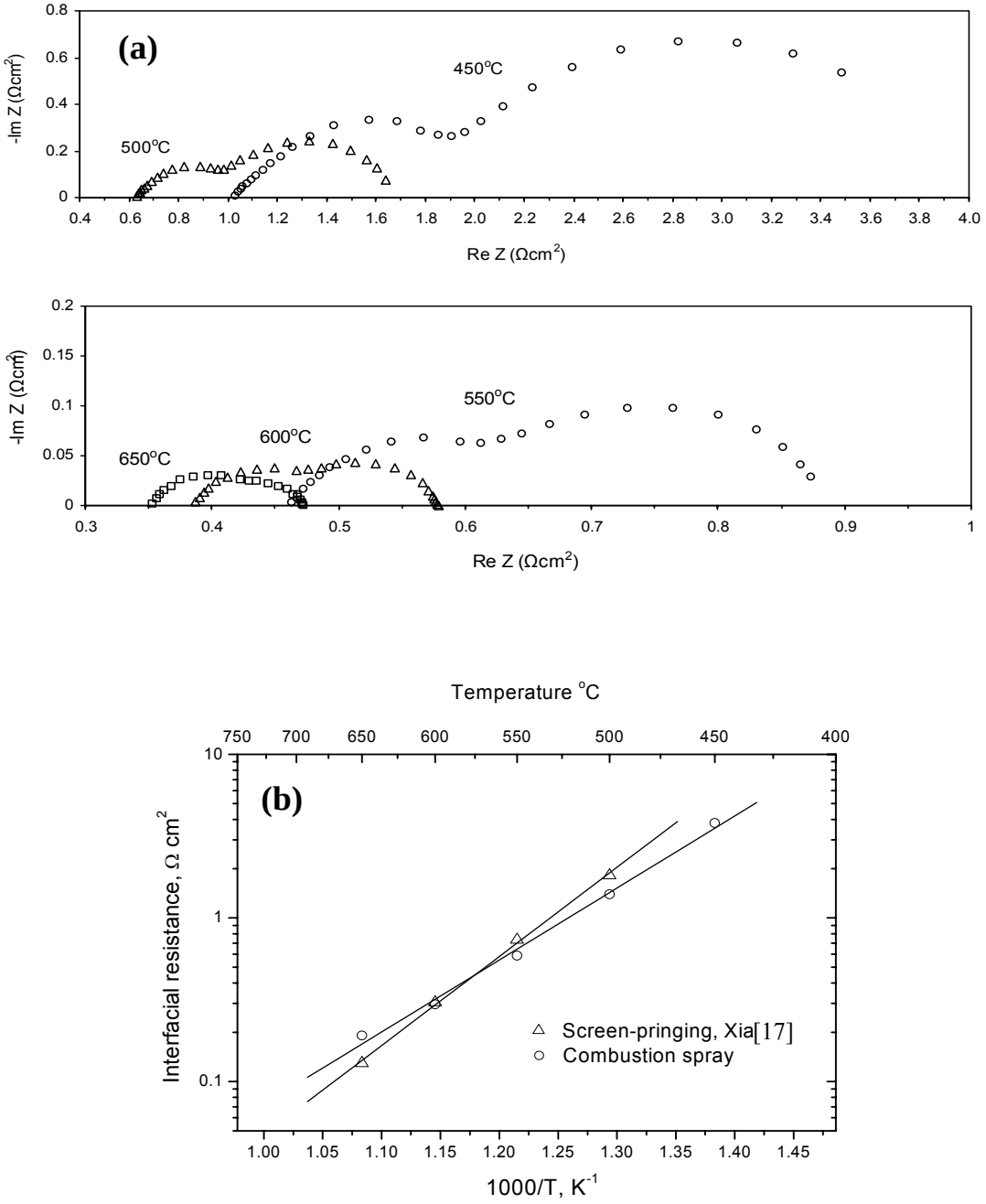


Figure 4-28 (a) Impedance spectra of a single fuel cell as measured using a two-electrode configuration, and (b) comparison of interfacial polarization resistances as determined from impedance spectra for electrodes fabricated using different techniques: screen-printing,[17] and combustion spray.

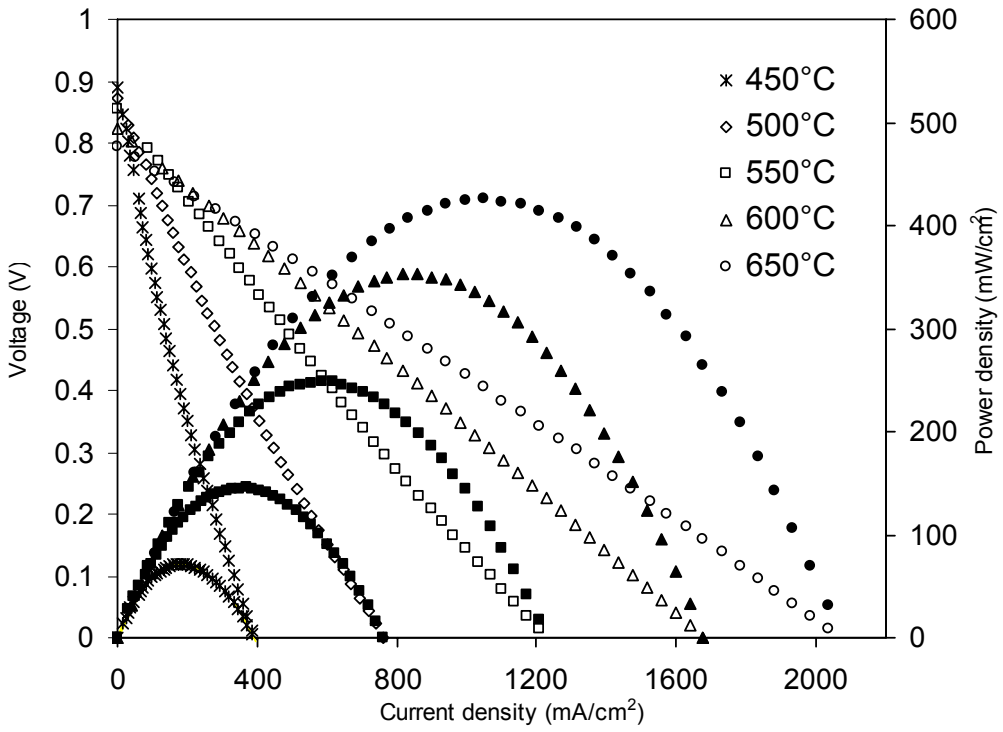


Figure 4-29 Cell voltages and power densities as a function of current density for fuel cells with SSC-GDC cathode fabricated by a combustion spray process.

## 4.5 Porous Ceramic Monoliths Created by the Removal of a Sacrificial Metal Oxide Phase during Sintering

Porous structures play crucial roles in many applications such as medical implants, [123, 124] heat insulation and/or thermal shock resistant structures,[122] chemical catalysis,[141] water purification,[142] gas separation,[143] sensors,[144] and fuel cells.[1, 33] Many different strategies have been adopted to control morphology, size and size distribution, the total volume, and connectivity of the voids in porous materials. Template method is one of the most popular approaches for creating pores with desired size and geometry. With is method, uniform porous nanostructures (e.g. nanotubes and honeycombs) have been produced by template methods.[145-147]

Porous microstructures can be created by controlled sintering of particles. The degree of sintering can be controlled by adjusting sintering temperature, sintering time, atmosphere, pressure, and the amount of sintering additives.[148]

An interesting methodology for creating desired level of porosity is found in the fabrication of solid oxide fuel cell (SOFC) anodes, where porosity is caused by the volume change occurred when NiO is reduced to Ni metal.[27] To fabricate SOFC anodes, appropriate amount of NiO and YSZ (or GDC) powders are dry pressed and sintered to achieve full density at temperatures range of 1300-1500°C. Under cell operation conditions, NiO is reduced in-situ by hydrogen fuel. Approximately 33% volume change is induced during the reduction of NiO to Ni. The total amount of porosity in the cermet is determined by the ratio of NiO to YSZ (or GDC) and cannot exceed 33%.

Variation in porosity can be achieved by adding so-called “pore formers” (e.g. graphite and cellulose).[57, 149-151] These pore formers occupy the desired amount of space during shape

forming stages, such as tape-casting and dry pressing. They are burned off in the earlier stages of sintering. Sometimes distortion or even collapse of the host material is observed during the following up sintering, especially when large amount pore formers is used. In addition, these type of pore formers are not suitable for fabrication processes requiring high temperature or high energy for initial shape formation, such as plasma pyrolysis and laser ablation.

To avoid this problem, ceramic "pore formers" such as ZnO are chosen to replace the more commonly used carbon and hydrocarbons. In this method, two immiscible oxide phases (the host material and the pore former) are intimately mixed together. One component is then selectively leached out chemically or by reduction/evaporation, leaving an equal amount of porosities in the host material.[152-156] This technique is not practically viable since either a long time is required for chemical leaching (e.g. at least 72 hours) or additional gas reduction reaction is involved.[152] Moreover, host materials might also be reduced to metal elements when gas reduction method is used.

Here we demonstrate a new simple method to prepare highly porous ceramics. $CeO_2$-$SnO_2$ nanocomposite powder was synthesized using combustion CVD process from a single precursor solution. $SnO_2$ phase was then evaporated during high temperature sintering, leaving behind open matrix of $CeO_2$. Neither chemical leaching nor gas reduction is necessary for this new approach. This simple method has great potential for preparation porous materials for many applications such as solid oxide fuel cells, gas sensors, gas separation, and chemical catalysis.

### 4.5.1 Experimental

$CeO_2$-$SnO_2$ nanocomposite powder was prepared using a combustion CVD approach. The detailed description of combustion CVD process is available elsewhere.[99, 129] In this experiment,

Sn(II) 2-ethylhexanoate, and/or Ce(III) 2-ethylhexanoate (from Strem®) were dissolved in an organic solvent. The solution was sprayed out of an aerosol generating nozzle and combusted with the assistance of methane/oxygen gas mixture. The resulting nanopowder was collected using a specially designed condenser. Three different materials of nanopowders were prepared: $SnO_2$, $CeO_2$, and 40vol.%$SnO_2$-60vol.%$CeO_2$ composite. For the preparation of 40vol.%$SnO_2$-60vol.%$CeO_2$ composite nanopowder, precursor matrials containing Sn and Ce were dissolved into the same solvent. The resulting single source solution was supplied to the aerosol-generating nozzle. For comparison, $SnO_2$ and $CeO_2$ nanopowders were then mixed together in the volume ratio of 40:60 by dry-milling. Pellet samples were prepared by dry-pressing 0.2 gram nanopowder in a 10 mm diameter steel die at 250 MPa. The green pellets were fired in a high temperature tube furnace (Lindberg®) at temperature range of 1450°C for 5 hours. Some of the samples were heat treated in reducing atmosphere (4% $H_2$ balanced with argon) at 727°C for 2 hours.

Morphologies of the as-prepared nanopowders were characterized using a transmission electron microscope (TEM, JEOL 100C). Crystallographic structures were identified on an X-ray diffractometer (XRD, Phillips PW-1800) at a scanning step of 0.01°/min. Sintered samples were observed on a scanning electron microscope (SEM, Hitachi S-800) equipped with an energy dispersive spectroscopy (EDS) attachment.

### 4.5.2 Results and Discussion

X-ray diffraction (XRD) patterns of the as-prepared $SnO_2$, $CeO_2$, and 40vol.%$SnO_2$-60vol.%$CeO_2$ composite powder were plotted in Figure 4-30. The strong intensity of the peaks indicated that the sample powder was highly crystallized. $CeO_2$ powder can be indexed to a cubic

fluorite structure with lattice constant a = 5.411Å (JCPDS card # 43-1002). $SnO_2$ powder was identified as a tetragonal rutile structure with a = 4.738Å and c = 3.187Å (JCPDS card # 41-1445). The 40vol.%$SnO_2$-60vol.%$CeO_2$ composite powder also showed a profile with distinct peaks, which is exactly the combination of individual $CeO_2$ and $SnO_2$ XRD patterns, further confirming that the two phases are immiscible. In the XRD pattern for 40vol.%$SnO_2$-60vol.%$CeO_2$ composite powder, the intensity of $SnO_2$ was much weaker than that of $CeO_2$ nanopowder. This is because the mass percentage of $SnO_2$ was about 37.5%.

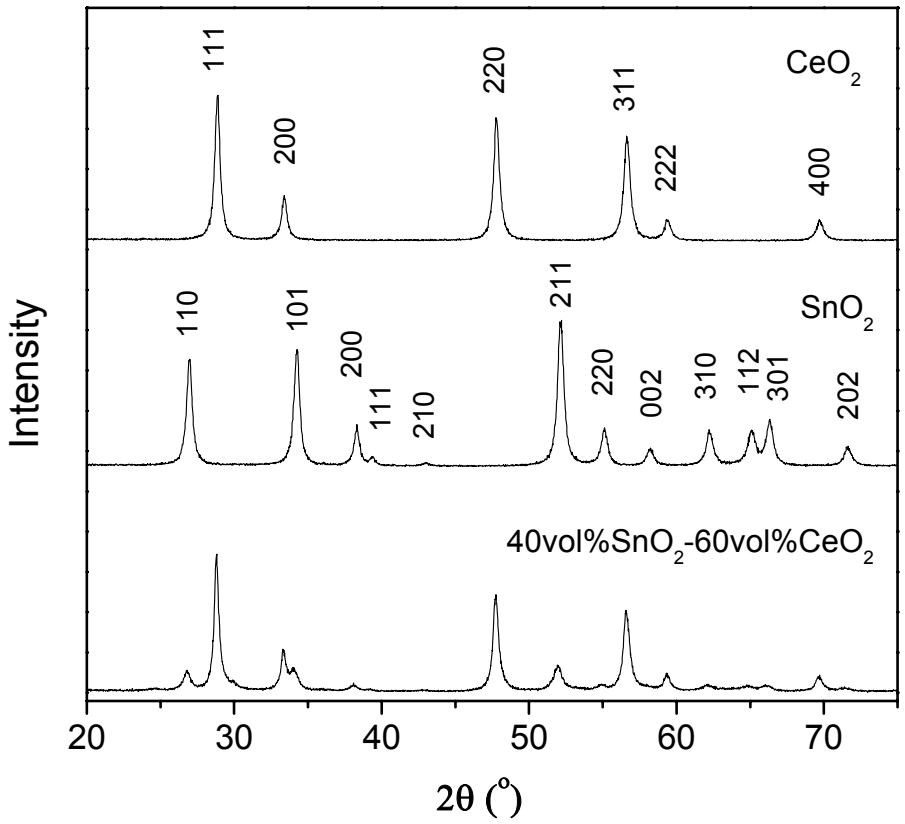


Figure 4-30 X-ray diffraction (XRD) patterns of the as-prepared $SnO_2$, $CeO_2$, and $SnO_2$-$CeO_2$ nanocomposite powders.

Morphology of as-prepared nanopowders was analyzed with TEM. Figure 4-31 shows bright field TEM images of $SnO_2$, $CeO_2$ and 40vol.%$SnO_2$-60vol.%$CeO_2$ composite powder. The insets are the corresponding selected area electron diffraction (SAED) patterns, which indicate all the samples were highly crystallized. $SnO_2$ particles (Figure 4-31a) had a polygonal morphology with a size between 20 to 50 nm. $CeO_2$ powder (Figure 4-31b) had about the same size but showed a parallelogrammic shape. In the 40vol.%$SnO_2$-60vol.%$CeO_2$ composite sample, the two kinds of nanoparticles can be distinguished by their unique morphologies (Figure 4-31c). For free grown crystalline particles, their surfaces usually are low energetic, low index compact planes. For tetragonal $SnO_2$, {101} planes are the most compact ones (noting lattice constant c is less than a and b for $SnO_2$). The interplanar angle between {101} planes is calculated to be 95.8°. This is in good agreement with our TEM observations as shown in Figure 4-31a (e.g. particle 1). $CeO_2$ has a cubic structure. The angle between its most compact planes, {111}, is 70.5° (or 109.5°) (see particle 2 in Figure 4-31b and particle 3 in Figure 4-31c).

$SnO_2$ and $CeO_2$ nanopowders prepared separately via combustion CVD were mixed together in volume ratio of 40:60 and pressed in a steel die. Figure 4-32 shows the microstructures of the pellets after sintering and further reduction. Shown in Figure 4-32a is the surface view of a pellet sintered at 1450°C for 5 hours. The average grain size has grown to around 1 μm. Many open pores can be observed on the surface, which could be the consequence of insufficient sintering or loss of material. Noting the difference of the original particle size (10 nm) and the size of the sintered grains, it is more likely that the partially open microstructure was caused by the evaporation of one component of the oxide mixture. Since the melting points of bulk $SnO_2$ and $CeO_2$ are 1630°C and 2400°C, it is easy to conclude that the evaporated material during sintering was $SnO_2$.

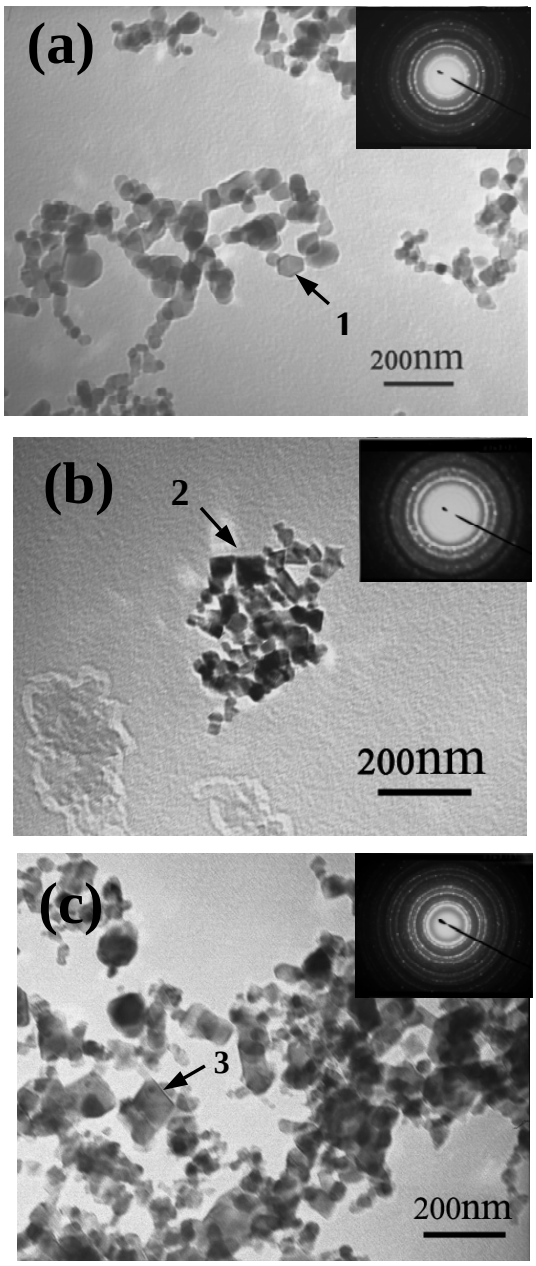


Figure 4-31 TEM bright field images and the corresponding selected area electron diffraction (SAED) patterns of the as-prepared nanopowders. (a) $SnO_2$, (b) $CeO_2$, (c) 40vol.%$SnO_2$-60vol.% $CeO_2$ composite.

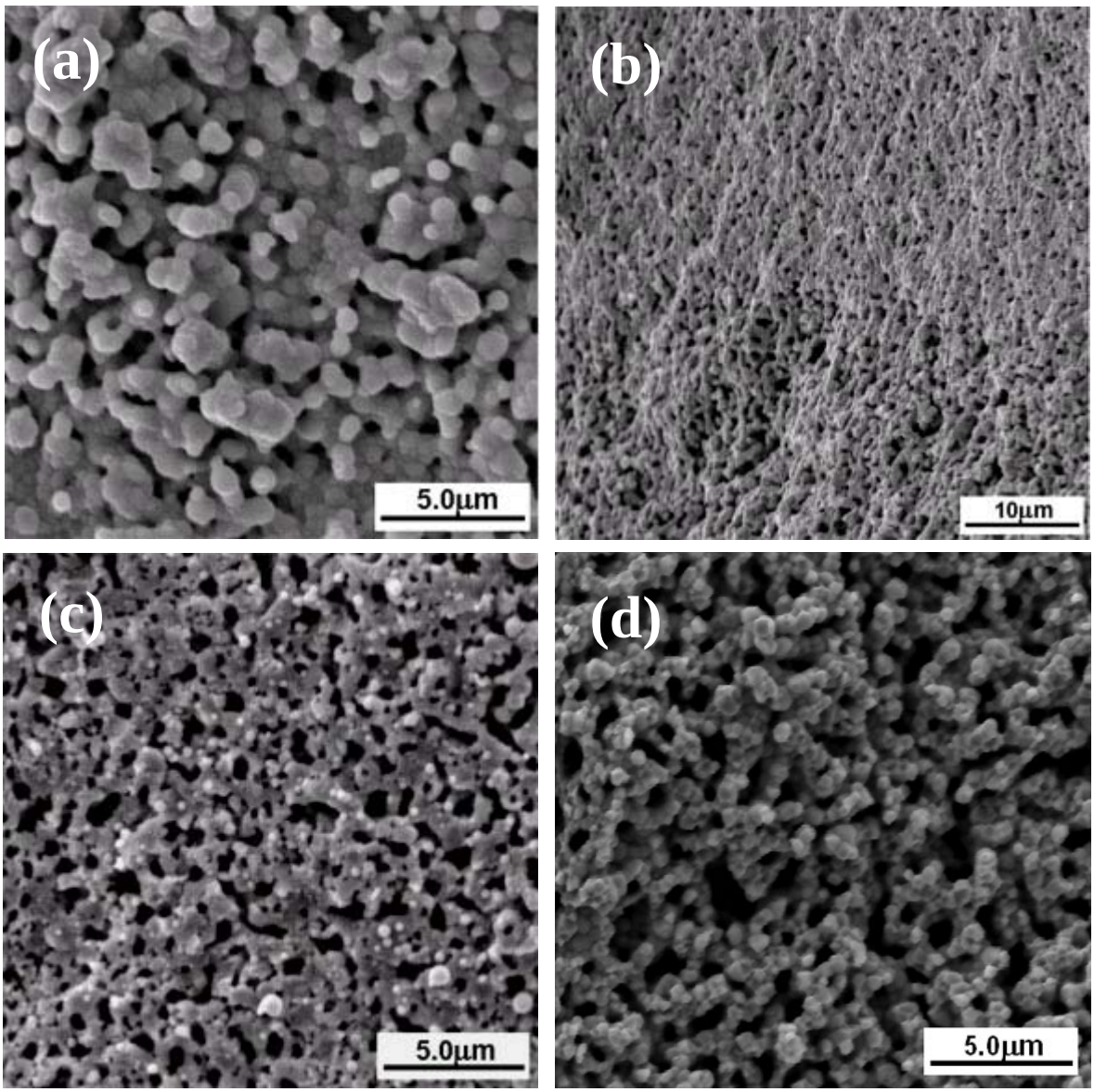


Figure 4-32 SEM images of pellet prepared with 40vol% $SnO_2$ – 60vol% $CeO_2$ nano-powders. $SnO_2$ and $CeO_2$ nano-powders were prepared by combustion CVD separately and then mixed together. (a) Surface view of pellet sintered at 1450ºC × 5 hrs. (b) Cross-sectional view of pellet sintered at 1450ºC × 5 hrs. (c) Surface view of pellet after reduction at 750ºC × 3 hrs. (d) Cross-sectional view of pellet after reduction at 750ºC × 3 hrs.

Shown in Figure 4-32b is the cross-sectional view of the sintered sample. The bottom part is close to the pellet surface. It is noticed more $SnO_2$ in the surface region than in the inner region has been removed. The more porous region only extended to 30μm underneath the surface after 5 hours' sintering.

The sintered compacts were further treated in reducing atmosphere (4%$H_2$ balanced with argon) at 727°C for 2 hours. Figure 4-32c and Figure 4-32d are the surface and internal microstructures of the sample. Apparently, $SnO_2$ phase has been completely removed after reduction in hydrogen, leaving an interconnected, highly open structure with pore size in the range of 0.5 to 1 μm.

Microstructures of 40vol.%$SnO_2$-60vol.%$CeO_2$ composite samples prepared from a single precursor source are shown in Figure 4-32. Both the surface view (Figure 4-33a) and cross-sectional micrograph (Figure 4-33b) reveal an extraordinarily open structure. Either the solid phase or the void is interconnected. The microstructure of the sample after reduction in hydrogen is shown in Figure 4-33c and Figure 4-33d. There was no significant change in microstructure could be observed, indicating most of the $SnO_2$ phase has been completely removed after sintering at 1450°C for 5 hours.

$CeO_2$ is a very stable ceramic even at high temperature and under reducing atmosphere. On the contrary, $SnO_2$ can easily be reduced to tin element and evaporated since the melting point of tin is only 231.93 °C. The Gibbs free energies for $CeO_2$, $SnO_2$ and $H_2O$ at 1000 K are -2013.469, -666.256, and 448.687 kJ/mol respectively.[157] Thus the Gibbs energies for the following reactions can be calculated:

$$CeO_2 + 2H_2 = Ce + 2H_2O \qquad \Delta G = 288.76 \text{ kJ/mol} \qquad (1)$$

$$SnO_2 + 2H_2 = Sn + 2H_2O \qquad \Delta G = -231.1 \text{ kJ/mol} \qquad (2)$$

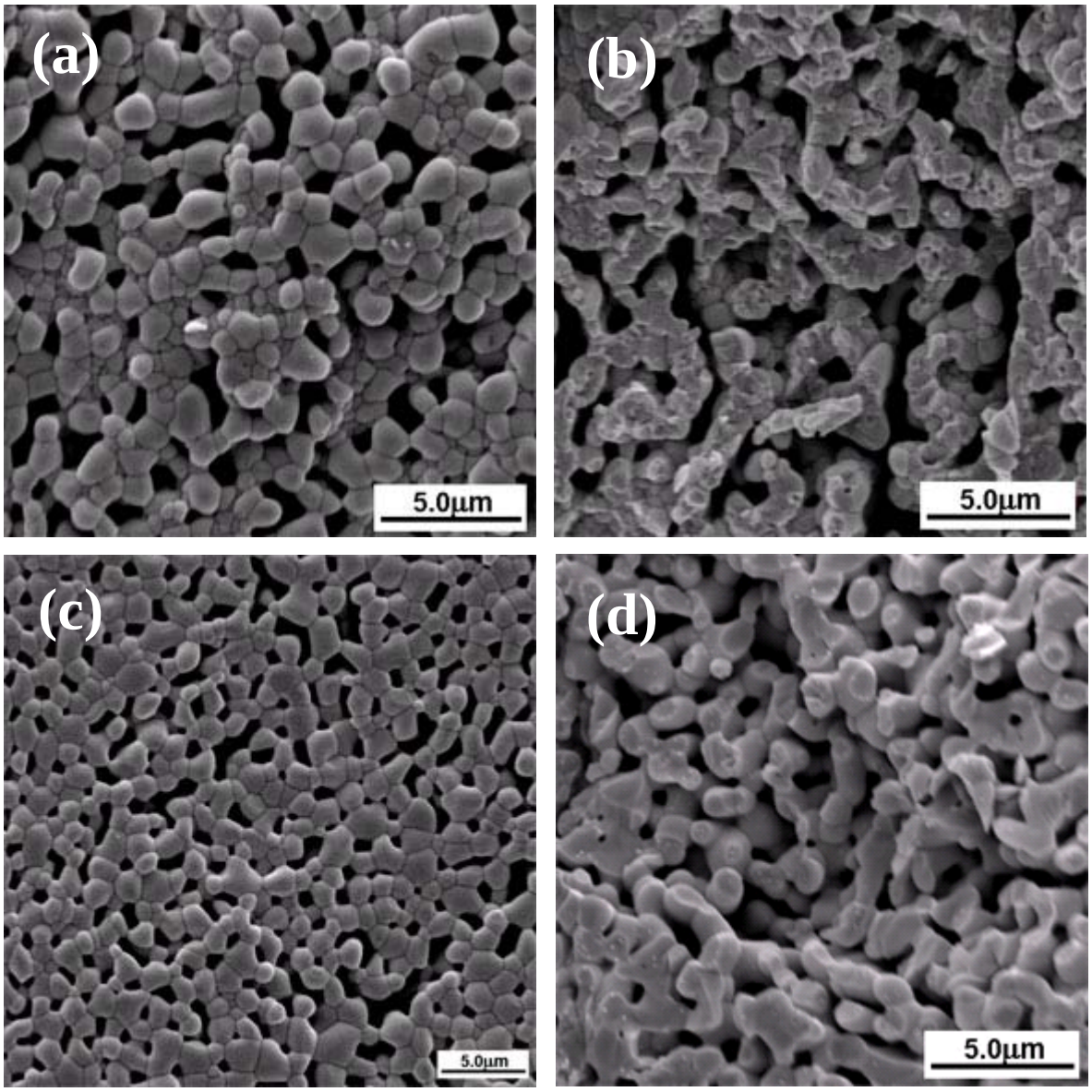


Figure 4-33 SEM images of pellet prepared with 40vol% $SnO_2$ – 60vol% $CeO_2$ nano-powders made by combustion CVD from single precursor solution. (a) Surface view of pellet sintered at 1450ºC × 5 hrs. (b) Cross-sectional view of pellet sintered at 1450ºC × 5 hrs. (c) Surface view of pellet after reduction at 750ºC × 3 hrs. (d) Cross-sectional view of pellet after reduction at 750ºC × 3 hrs.

Clearly, $CeO_2$ is stable in hydrogen while the reduction of $SnO_2$ to Sn metal is thermodynamically favored.

The difference in removal rate of $SnO_2$ in the as-prepared and dry-milled 40vol.%$SnO_2$-60vol.%$CeO_2$ samples during sintering may be attributed to the distribution of $SnO_2$ phase. Even after long time milling, agglomerates of $SnO_2$ still exist in the mixture. On the contrary, for 40vol.%$SnO_2$-60vol.%$CeO_2$ sample prepared from single precursor source, $SnO_2$ phase was uniformly distributed throughout the sample.

Our new method is very attractive for many potential applications such as solid oxide fuel cells, solid-state gas sensors, catalysis, and gas separation. It has the merits of simplicity and timesaving. In addition, this method can be incorporated into traditional ceramic production routines without introducing extra fabrication procedures. For example, solid oxide fuel cells with porous electrode and dense electrolyte layers could be produced by co-sintering of multiple layer materials. As mentioned earlier, porosity in SOFC electrodes can be created by the use of low "burning-off" temperature pore formers (e.g. graphite and cellulose). However, these materials cannot be used in some of the state-of-the-art fabrication techniques such as plasma pyrolysis, laser ablation, and combustion CVD, in which high temperature/energy is involved. Out new method is compatible with these revolutionary techniques as well as the traditional ceramic fabrication approaches. If there is some material loss during fabrication, the amount of loss can be easily taken into consideration when preparing the precursor solution.

### 4.5.3 Summary

We have demonstrated a new, simple route for preparing highly porous ceramic monoliths through the removal of metal oxide ($SnO_2$) during high temperature sintering. Unlike the existing strategies, the new method requires neither time consuming chemical leaching nor following-up

gas reduction procedures. The most critical step for our new approach is the preparation of intimately distributed 40vol.%$SnO_2$-60vol.%$CeO_2$ composite nanopowder using combustion CVD. $SnO_2$ phase was removed during high temperature sintering. This method provides a simple way to introduce additional porosity into ceramic materials, and can be directly incorporate into ceramic production routes without introducing extra procedures.

## 4.6 SOFC Anodes with Metal Oxide Induced Porosity Variation

Performances of solid oxide fuel cells (SOFCs) at reduced operating temperatures are primarily limited by electrochemical kinetics at the electrolde/electrolyte interfaces, which is indicated by the dominating overpotentials and polarization resistances at the interfaces.[27, 127, 158] To improve interfacial condition, different cell configurations and fabrication approaches have been adopted to improve interfacial conditions of SOFCs.[19, 20, 56, 159] For example, a thin intermediate $CeO_2$ layer between electrode/electrolyte was found beneficial to electrochemical performance of SOFCs.[160] SOFCs with electrodes fabricate by combustion CVD showed higher porosity and stronger bonding among electrode grains and between electrodes and electrolyte, which are reflected by much lower interfacial polarization resistances.[99]

It has been demonstrated that graded structures could facilitate gas transport and enhance solid-state kinetics. It is relatively easier to produce composition gradient in electrodes than create microstructure variations. SOFCs electrodes with multi-layers differing in compositon have been reported by several research groups.[52, 104, 126, 161] Recently, nanostructued and functionally graded cathodes were fabricated by a combustion CVD process.[162] These electrodes were graded in composition, which had more electrochemical reactive material (LSM) at electrode/electrolyte interface, and contained more electronic conductive phase (LSC) when approaching the air/fuel side. Meanwhile, pore size variation was achieved managing particle size at different regions of the cathode layer.

A practical strategy for increasing porosity in SOFC electrodes is to use pore formers (e.g. graphite and cellulose). High volume of voids has been created for later impregnation of active electrode materials.[57] However, distortion even collapse of the host material may occur during sintering because the removal temperatures of pore formers are much lower (usually lower than

400ºC) than sintering temperatures (higher than 1350°C). Here we demonstrate a new method to create additional porosity in SOFC anodes using metal oxide as a sacrificial phase. Tin dioxide nanopowders together with anode materials (NiO-GDC) were prepared using combustion CVD process from a single precursor source. $SnO_2$, serving as a pore creator, was partially removed during sintering and completed eliminated in situ during cell testing.

### 4.6.1 Experimental

The design of the anode-supported cell is illustrated in Figure 4-34. The anode has two layers, differing in the level of porosity: the bottom half layer is more porous than the top half layer, which is in contact with the GDC electrolyte. The complete cell was fabricated by co-pressing (bilayer anode and thin electrolyte) and screen-printing (cathode). NiO and $Gd_{0.1}Ce_{0.9}O_2$ (GDC) powder was prepared separately by glycine-nitrate process (GNP).[27] NiO powder was mixed with GDC powder in weight ratio of 35:65 by dry-milling. Composite nanopowder (20wt%$SnO_2$-50wt%NiO-30wt%GDC) was synthesized using combustion CVD from a single precursor source. To prepare the anode/electrolyte triple-layer structure, the $SnO_2$-NiO-GDC composite nanopowder was dry-pressed in a steel die under 100 MPa. The pre-mixed NiO-GDC powder was then added on top of the $SnO_2$-NiO-GDC composite layer and pressed at 150 MPa. Finally, appropriate amount of GDC powder was distributed on the top and pressed at 250 MPa. The triple-layer pellet was removed from the steel die and sintered in air at 1400°C for 5 hours. The amount of powder for each layer was controlled to give final thicknesses of 25, 100, and 100 μm for GDC electrolyte, NiO-GDC, and $SnO_2$-NiO-GDC layer after sintering. Slurry consisting of $Sm_{0.5}Sr_{0.5}CoO_3$ (SSC) and 30wt.%GDC was applied on top of the sintered GDC electrolyte by screen-printing. The cathode layer was fired at 950°C for 5 hours. The assembled cell subjected

to microstructure characterization (SEM, Hitachi S-800)), crystallographic phase identification (XRD, PW-1800) and electrochemical tests (Solartron SI1287 electrochemical interface coupled with SI1255 frequency response analyzer). Electrochemical performances were measured in ambient air from 500°C to 650°C using humidified hydrogen as fuel and air as oxidant.

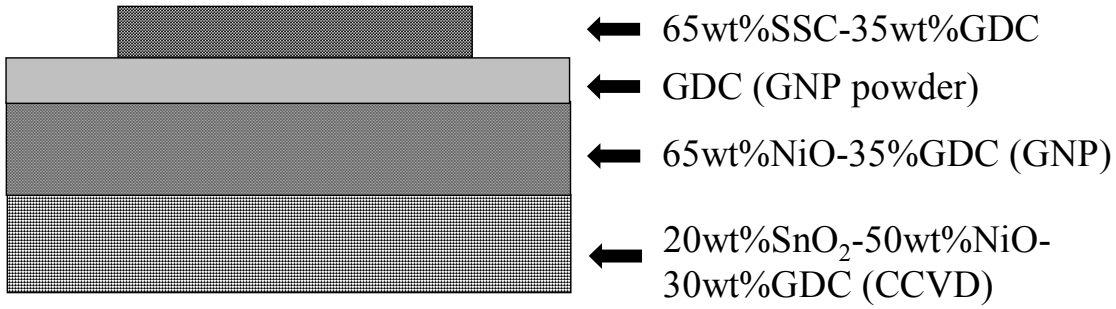


Figure 4-34 A schematic of anode supported SOFC. Bilayer anode and GDC electrolyte were co-pressed and sintered at 1400ºC for 5 hours. SSC-GDC cathode was screen-printed onto the surface of GDC electrolyte and fired at 950ºC for 5 hours.

4.6.2 Results and Discussion

The $SnO_2$-NiO-GDC composite powder was prepared by combustion CVD process. Precursor materials containing the desired metal specials were mixed together in an organic solvent. The solution was pumped into an aerosol generating nozzle and combusted with oxygen and methane. The resulting nanopowder was collected in a specially designed device. Figure 4-35 shows x-ray diffraction (XRD) pattern of the as-prepared $SnO_2$-NiO-GDC composite powder. Well-resolved peaks could be identified as individual $SnO_2$, NiO and GDC phases. There were no intermediate or undesired crystallographic phases detected from XRD spectra.

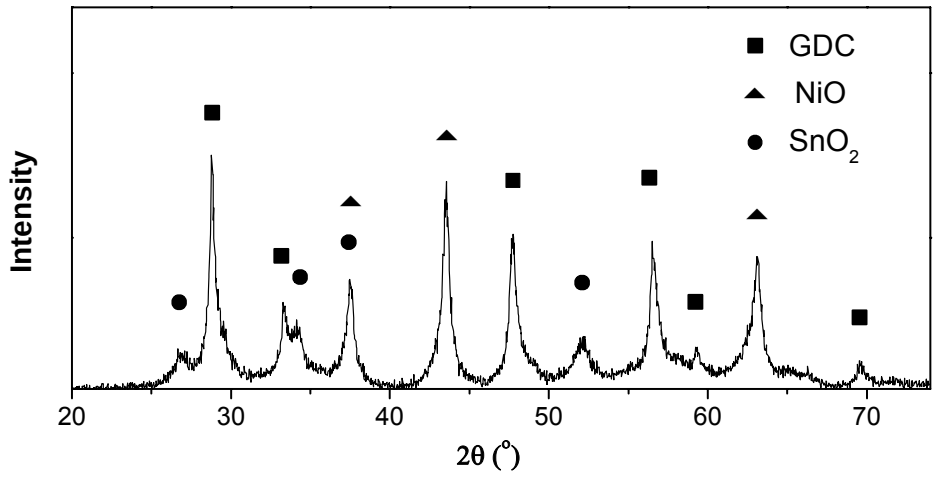


Figure 4-35 X-ray diffraction pattern of the as-prepared $SnO_2$-NiO-$Gd_{0.1}Ce_{0.9}O_2$ composite nanopowder.

Figure 4-36 shows microstructures of electrolyte and anode before and after cell testing. Shown in Figure 4-36(a) is the GDC electrolyte and NiO-GDC interface after the co-pressed triple-layer pellet was sintered at 1400°C for 5 hours. It can be observed that GDC electrolyte is fully dense except a small amount of isolated voids. In the NiO-GDC anode, two distinct phases can be easily identified: dark, large NiO grains and light GDC phase distributed around NiO grains. The NiO-GDC and $SnO_2$-NiO-GDC boundary is shown in Figure 4-36(b). It is noticed that $SnO_2$-NiO-GDC region has already had some porosity. This is due to partial removal of $SnO_2$ nanopowder during high temperature sintering since the melting temperature of $SnO_2$ is only 1630°C. For nanosized $SnO_2$ powder, its melting point is even lower. Out experimental data indicate $SnO_2$ phase within $SnO_2$-NiO-GDC composite material can be completely removed at 1450°C. After tested for electrochemical performance, the sample was examined using SEM for any microstructure change. Shown in Figure 4-36(c) is the micrograph of GDC electrolyte and NiO-GDC anode interface after cell testing. Since NiO has been fully reduced to Ni metal, the anode material become porous. The boundary between NiO-GDC and $SnO_2$-NiO-GDC within the anode is shown in Figure 4-36(d). Though the entire structure is highly porous, the two anode layers can still easily be distinguish by the level and distribution of porosity. Large voids can be observed in NiO-GDC layer due to the irregular shape of original NiO particles. On the contrary, pore size in $SnO_2$-NiO-GDC layer is much smaller and more uniform. The total amount of voids in $SnO_2$-NiO-GDC layer is apparently higher than that in NiO-GDC layer.

According to theoretical calculation, there is 33% change in density when NiO (6.7 $g/cm^3$) is reduced to Ni metal (8.9 $g/cm^3$). The total porosity in Ni-GDC layer is about 27.1% if full density is assumed. For $SnO_2$-NiO-GDC layer, 40.8% porosity is expected after NiO is reduced and $SnO_2$ is completely eliminated from the anode.

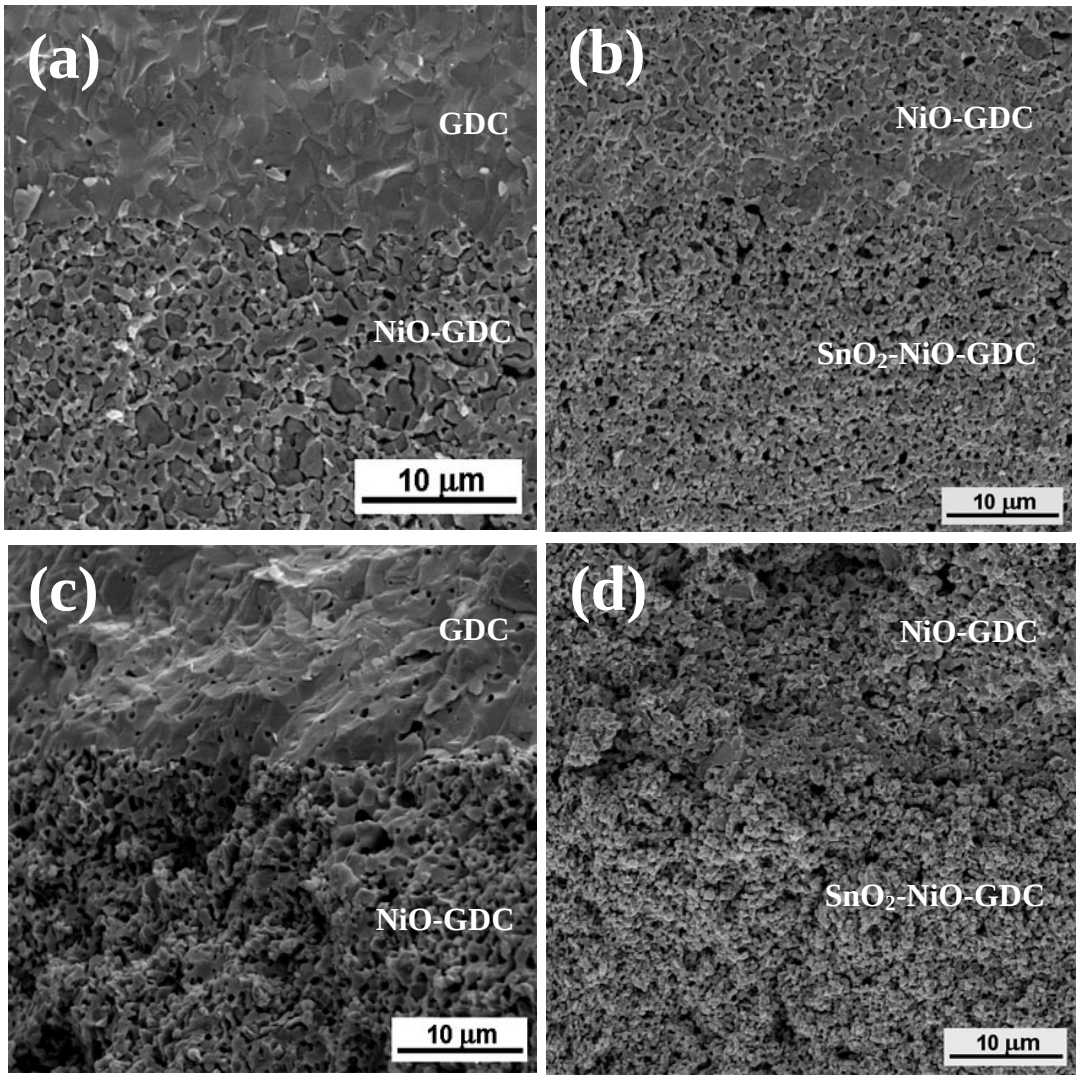


Figure 4-36 Cross-sectional SEM images of SOFC anode and electrolyte. (a) GDC electrolyte and NiO-GDC interface after sintering. (b) NiO-GDC and $SnO_2$-NiO-GDC boundary after sintering. (c) GDC electrolyte and NiO-GDC interface after cell testing. (d) NiO-GDC and $SnO_2$-NiO-GDC boundary after cell testing.

Electrochemical performance of the fuel cell is plotted in Figure 4-37. Shown in Figure 4-37(a) is the impedance semi-loops measured at 500-650°C. For convenience, bulk resistances have been deducted from the original data. Interfacial resistances read from the intercepts were 1.20, 0.49, 0.22, and 0.1 $\Omega cm^2$ at 500, 550, 600, and 650°C, respectively. In Figure 4-37(b) interfacial resistances of the cell are further compared with literature data, which were measured on SOFCs with similar composition but uniform anode structure. Interfacial resistances measured in this work are lower than those of cells with similar composition (anode supported cell, fabricated by co-pressing and screen-printing),[27] close to those of the cell with cathode fabricated by combustion CVD at the corresponding testing temperatures.[99]

The close circuit voltage and output power density are plotted in Figure 4-37(c) as a function of current density passing through the cell. Peak power densities measured at 500, 550, 600, and 650°C are 171, 301, 441, and 544 $mW/cm^2$, respectively. These values are also higher than those reported in literature. [27] For anode supported SOFCs, mass transport of fuel gas and water vapor in the anodes may hinder the entire electrochemical kinetics. High porosity is thus crucial for theses anodes. Our bilayer anodes with porosity variation seem to at least alleviate the gas mass transport problem.

### 4.6.3 Summary

A bilayer anode supported SOFC with was constructed by co-pressing and screen-printing. The bottom layer (fuel gas side) consisted of 20wt%$SnO_2$-50wt%NiO-30wt%GDC composite nanopowder prepared by combustion CVD. SnO2 was eliminated from the anode during sintering and cell testing, resulting in additional porosity in the anode layer. Good electrochemical performance was observed for the cell with bilayer anode.

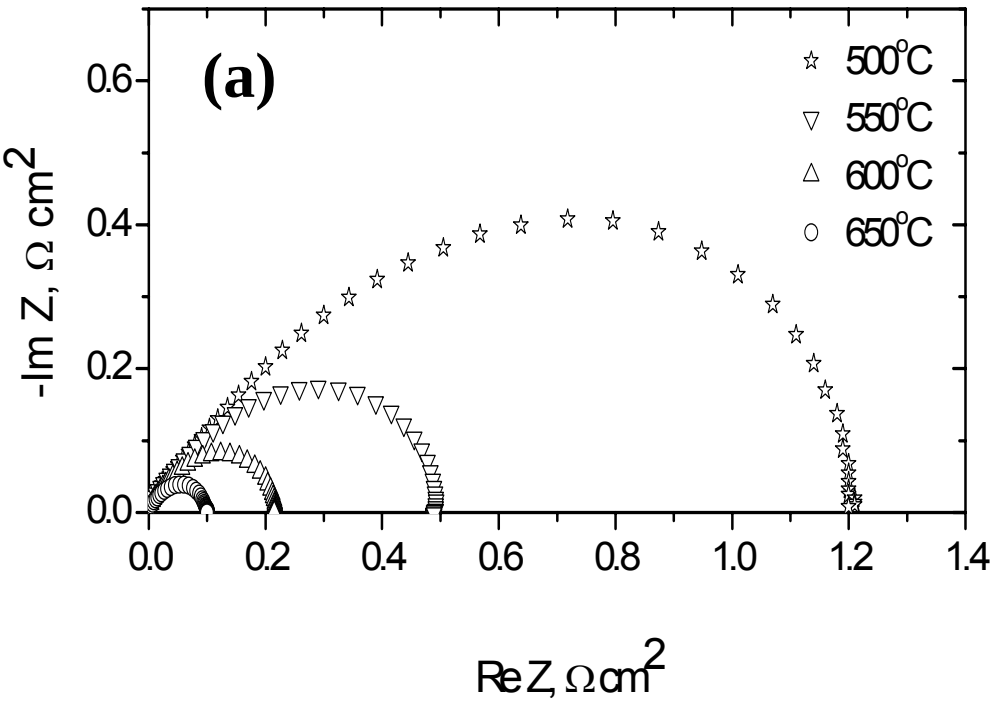
(a)
500°C
550°C
600°C
650°C
-Im Z, Ω cm2
Re Z, Ω cm2
0.0
0.2
0.4
0.6
0.8
1.0
1.2
1.4

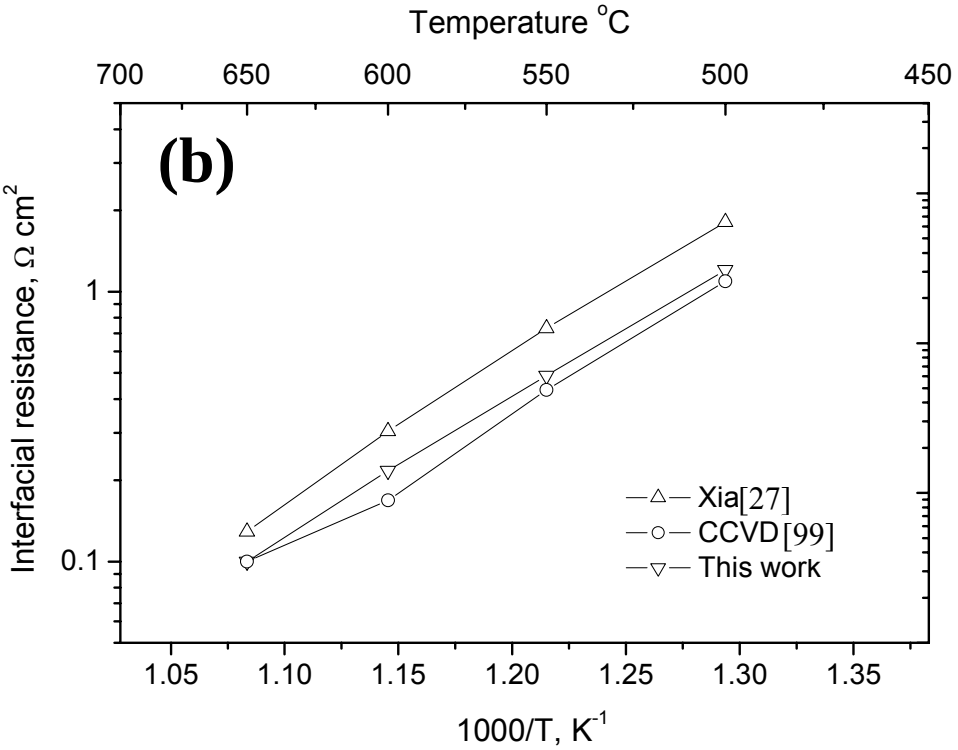
Temperature °C
700
650
600
550
500
450
(b)
Interfacial resistance, Ω cm2
1
0.1
Xia[27]
CCVD[99]
This work
1.05
1.10
1.15
1.20
1.25
1.30
1.35
1000/T, K-1

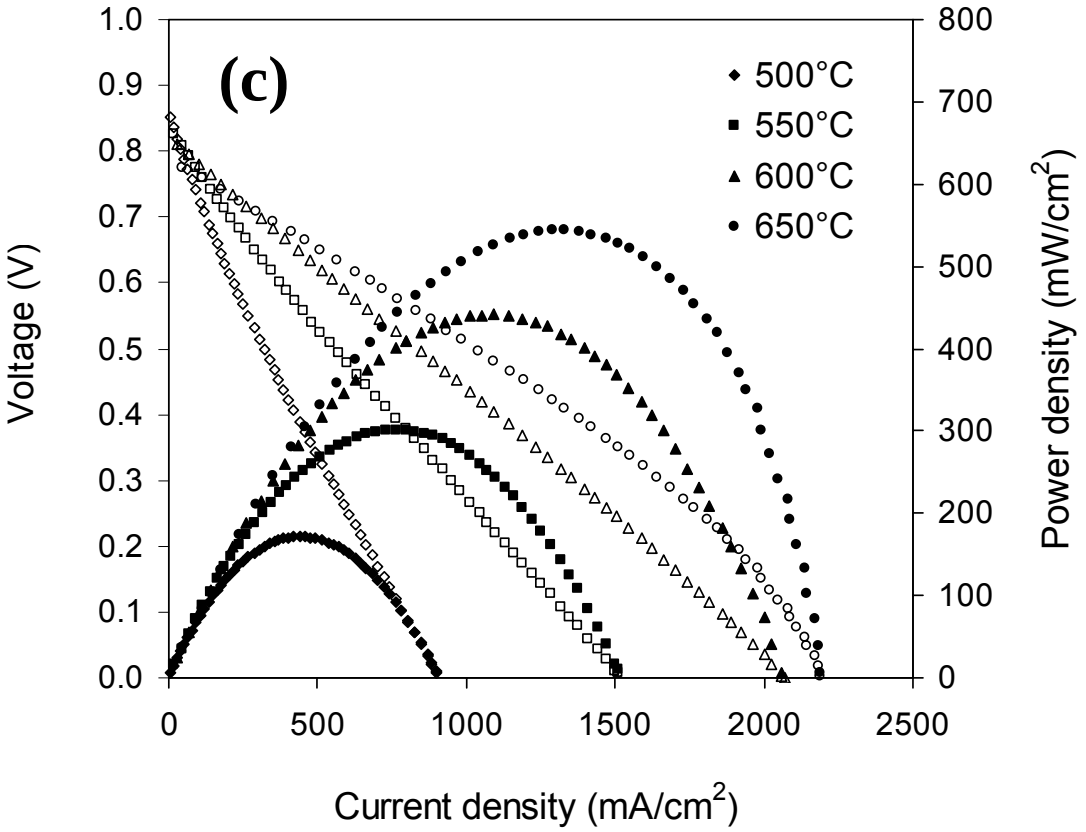


Figure 4-37 Electrochemical performance of the SOFC with porosity differed bilayer anode measured at temperature range of 500-650°C. (a) impedance measurements of the cell (bulk resistances have been deducted). (b) comparison of interfacial resistances of anode supported cells with similar composition: screen-printed cathode and single layer anode,[27] combustion CVD deposited cathode and single layer anode,[99] and screen-printed cathode and porosity differed double layer anode (this work). (c) close circuit voltage and output power density as a function of current density drawn from the cell.

# CHAPTER 5 NANOSTRUCTURED $SNO_2$ THIN FILMS FOR GAS SENSORS

Highly sensitive and reliable gas sensors are vital to many applications such as monitoring and control of air quality, detection of flammable or toxic gases, electronic noses, medical diagnosis, and optimization of combustion efficiency. Tin dioxide is an n-type semiconductor widely used for gas sensors. The gas detection mechanism is based on the reversible change in conductivity of the surface of $SnO_2$ particles/grains induced by gas-solid interaction.[163] Several strategies have been adopted to enhance the performance of $SnO_2$ gas sensors, including doping with aliovalent ions (e.g., Cu, Zn,[164] In[165]),catalytically active additives (e.g., Pt and Pd),[166, 167] and addition of carbon nanotubes.[168]

Further, it is well known that gas-sensing characteristics of $SnO_2$ can be dramatically altered by morphological and microstructural features of the sensing elements such as particle size, shape, surface/volume ratio and porosity. Ultra-thin films, porous films, and more recently, nanocrystalline films of $SnO_2$ have been fabricated by a variety of approaches, such as evaporative methods,[169, 170] sputtering,[171, 172] chemical vapor processes,[173] and chemical solution techniques.[174, 175] Many of these techniques suffer from one or more drawbacks such as low deposition rate, prolonged post-process annealing time, and expensive target/precursor and fabrication. Combustion chemical vapor deposition (CVD) is a cost-effective and versatile process capable of producing films with a wide variety of morphologies. Highly porous and nanostructured films have been synthesized for energy storage and conversion applications such as solid oxide fuel cells and batteries. [14, 15] In this study, a nanostructured, thin-film $SnO_2$ gas sensor with interdigitated Pt electrodes is fabricated using a cost-effective combustion CVD process. The extremely porous $SnO_2$ thin film demonstrated exceptionally high sensitivity and fast speed of response and recovery upon exposure to ethanol vapor.

5.1 Experimental

Platinum interdigitated electrodes were fabricated on 25.4 mm × 76.2 mm quartz slides. Titanium (20 nm in thickness) was deposited on quartz slides to improve the adhesion of metals on the substrates. The platinum was then deposited by DC sputtering over the thin titanium layer. The patterned platinum electrode stripes are 10 μm wide and the spacing between two adjacent electrode stripes is 10 μm. There were in total 40 stripes on each pattern. Approximately 20 patterned electrodes were fabricated on each quartz slide and were cut into individual pieces (4mm×10mm) after fabrication as illustrated in Figure 5-1.

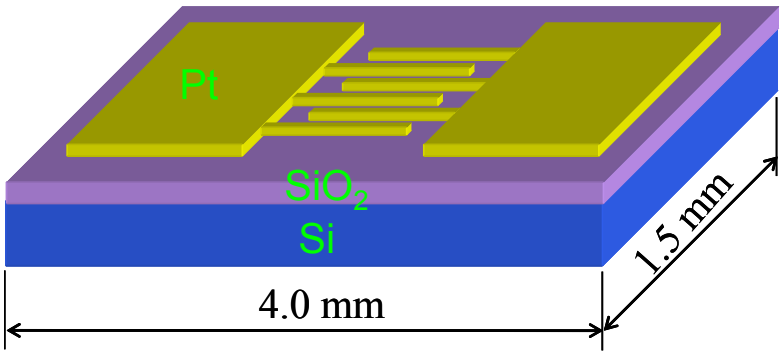


Figure 5-1Schematic of interdigitated Pt electrodes design

$SnO_2$ thin film gas sensors were deposited on patterned platinum electrodes using a flame assisted condensation process, which has been employed to fabricate many novel nanostructures

and devices recently. [14, 15] Precursor solution was prepared by dissolving Tin (II)-2-ethylhexanoate (Aldrich) in absolute ethanol. Deposition was carried out at 850°C for 20 minutes. For structural analysis, a XRD sample was prepared on a clear quartz slide without Pt electrodes under identical conditions.

The structure and morphology of the as-prepared samples were characterized using an X-ray diffractometer (XRD, Phillips PW 1800) and scanning electron microscope (SEM, LEO 1530 thermally-assisted FEG).

Ethanol sensing tests were conducted in a tube furnace from 200°C to 500°C at a 50°C interval. Dry air and air-ethanol vapor mixture was delivered to the furnace via a three-way valve at a constant rate of 100 sccm. The current flowing through the $SnO_2$ sensor was registered using a Solartron 1285 potentiostat interfaced with a PC at an applied constant voltage of 100 mV. The gas sensor testing apparatus is shown in Figure 5-2. Initially, tests were conducted from 200°C to 500°C using a constant ethanol vapor concentration of 500ppm. Once the temperature of highest sensitivity was identified, experiments were carried out at that temperature using ethanol vapor from 50 to 500ppm.

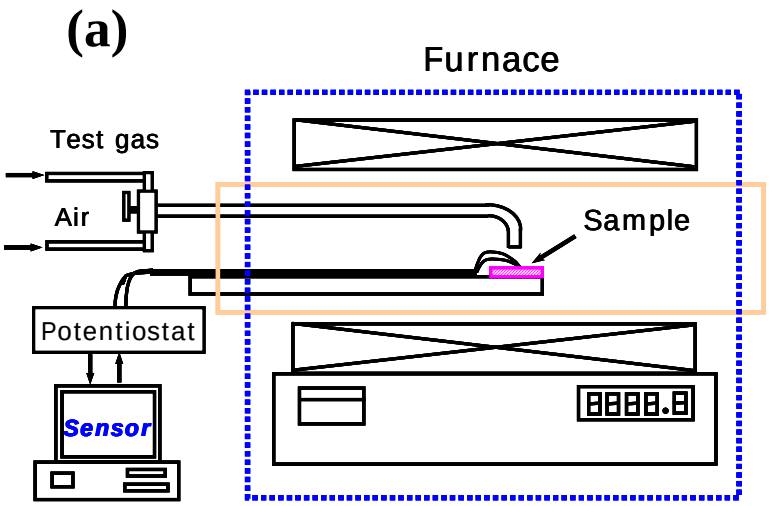



Figure 5-2 (a) Schematic of gas sensor testing apparatus. (b) Actual gas sensor testing setup in the laboratory.

5.2 Results and Discussion

Shown in Figure 5-3(a) is an SEM image of Pt interdigitated electrodes with a line width of 10 μm and line space of 10 μm. Pt strips are straight and well defined. Figure 5-3(b) is a top view of the $SnO_2$ gas sensor film deposited at 850°C. The film consists of small particles, most of which are smaller than 1 μm with the exception of some particles are as large as 3 μm in diameter. The top-view SEM micrograph also reveals a trace of Pt interdigitated electrodes, indicating the deposited $SnO_2$ film is thin and semi-transparent. As seen from a higher magnification micrograph of the $SnO_2$ film, Figure 5-3(c), each individual agglomerate that appears in Figure 5-3(b) actually consists of much finer crystals less than 30 nm in diameter. Figure 5-3(d) shows a cross-sectional SEM micrograph of the sample. The left portion shows $SnO_2$ thin film directly deposited on quartz substrate, while the right part shows $SnO_2$ film grown on Pt electrode. The $SnO_2$ film is about 1 μm thick and each grain has a columnar orientation.

Shown in Figure 5-4 is an XRD pattern for a $SnO_2$ film sample prepared on a quartz slide under the same deposition condition as for the $SnO_2$ sensor shown in Figure 5-3. The intensities and locations of all the peaks match those on JCPDS# 41-1445, confirming the as-deposited $SnO_2$ film has a tetragonal structure with a = 4.7382 Å and c = 3.1871 Å.

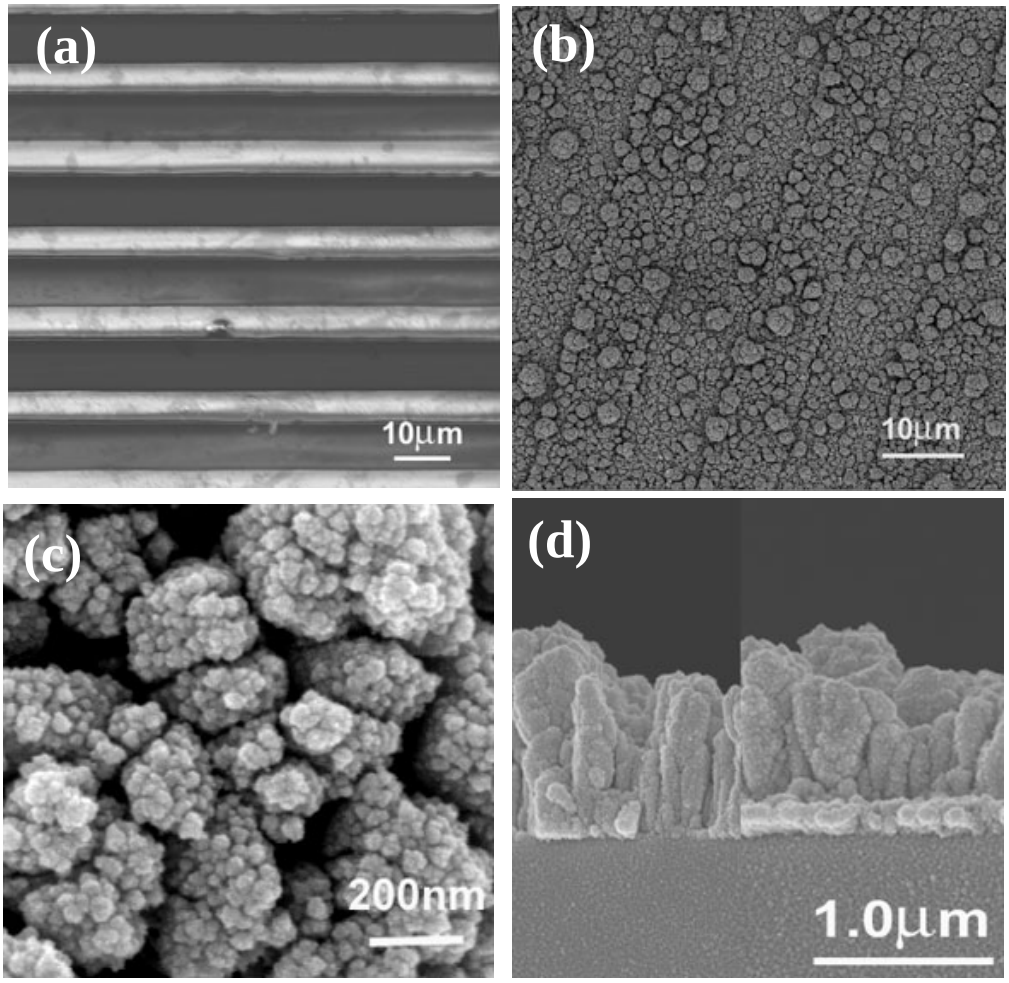


Figure 5-3 (a) SEM image of platinum interdigitated electrodes with a strip width of 10 μm and line space of 10 μm. (b) Top view of nanostructured $SnO_2$ gas sensor fabricated at 850°C by a combustion CVD process. (c) Higher magnification SEM micrograph of $SnO_2$ thin film, showing each individual particle is less than 30 nm. (d) Cross-sectional view of $SnO_2$ sensor. The left portion shows $SnO_2$ thin film directly deposited on quartz substrate, while the right part shows $SnO_2$ film grown on Pt electrode.

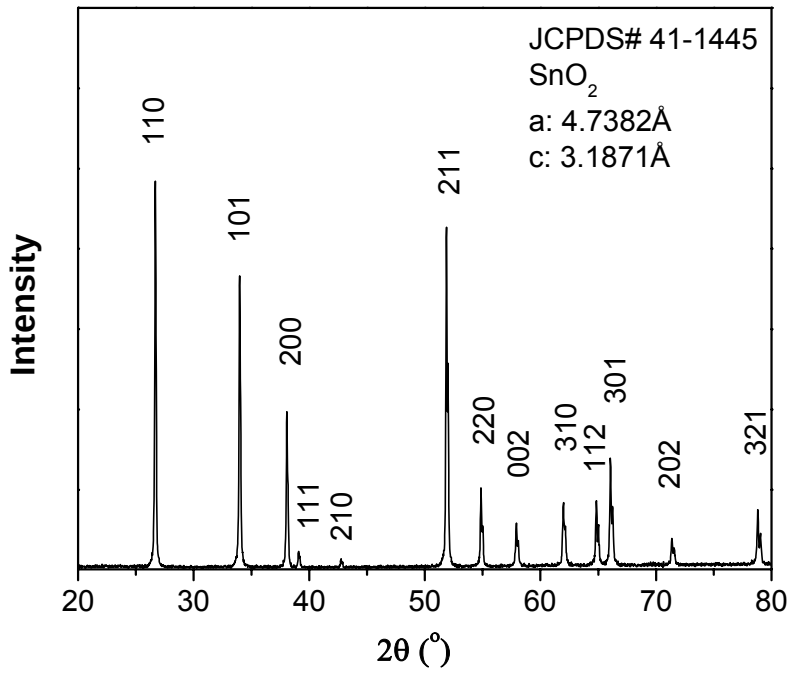


Figure 5-4 X-ray diffraction pattern of $SnO_2$ film fabricated at 850°C for 20 minutes. $SnO_2$ thin film is determined to has a tetragonal structure.

The as-prepared $SnO_2$ films were tested for ethanol sensing behavior from 200°C to 500°C at 50°C intervals. A typical electrical response of the $SnO_2$ thin film sensor to 500 ppm ethanol vapor at 450°C is shown in Figure 5-5(a). Initially, the current flowing through the sample under a constant DC voltage of 100 mV was trivial (about $2.2\times10^{-6}$ A). Upon exposure to ethanol vapor, however, the current passing through the film jumped abruptly and reached a steady plateau in a relatively short period of time. The response behavior followed an exponential correlation. The recovery process mirrored the initial process with similar characteristics, albeit at much higher speed.

Shown in Figure 5-5(b) are the Arrhenius plots for the response and recovery time, which is defined as the time needed to reach 90% of total signal change. It took 95 seconds for the $SnO_2$ sensor to respond and 26 seconds to recover at 250°C. However, the response and recovery time were reduced to 39 and 11 seconds, respectively, as the operating temperature was raised to 450°C. Generally, gas sensors made from thin films take less time to reach a saturation plateau than to fully recover. However, for $SnO_2$ sensors fabricated by combustion CVD, the speed of recovery is actually faster than that of response. Since the sensing material and testing parameters were comparable to those reported in literature, the fast speed of response/recovery should be attributed to the highly porous and nanostructured morphology of the sensor film.

As shown in Table 5-1, the response and recovery time are compared with those of $SnO_2$ sensors fabricated by other approaches. For instance, a $SnO_2$ film sensor tested at 275°C and 1000 ppm ethanol took 36-45 seconds to respond and 300-420 seconds to recover, while the corresponding characteristic constants for sensor fabricated by combustion CVD and tested at 300°C and 500 ppm were 31 and 8 seconds, respectively.

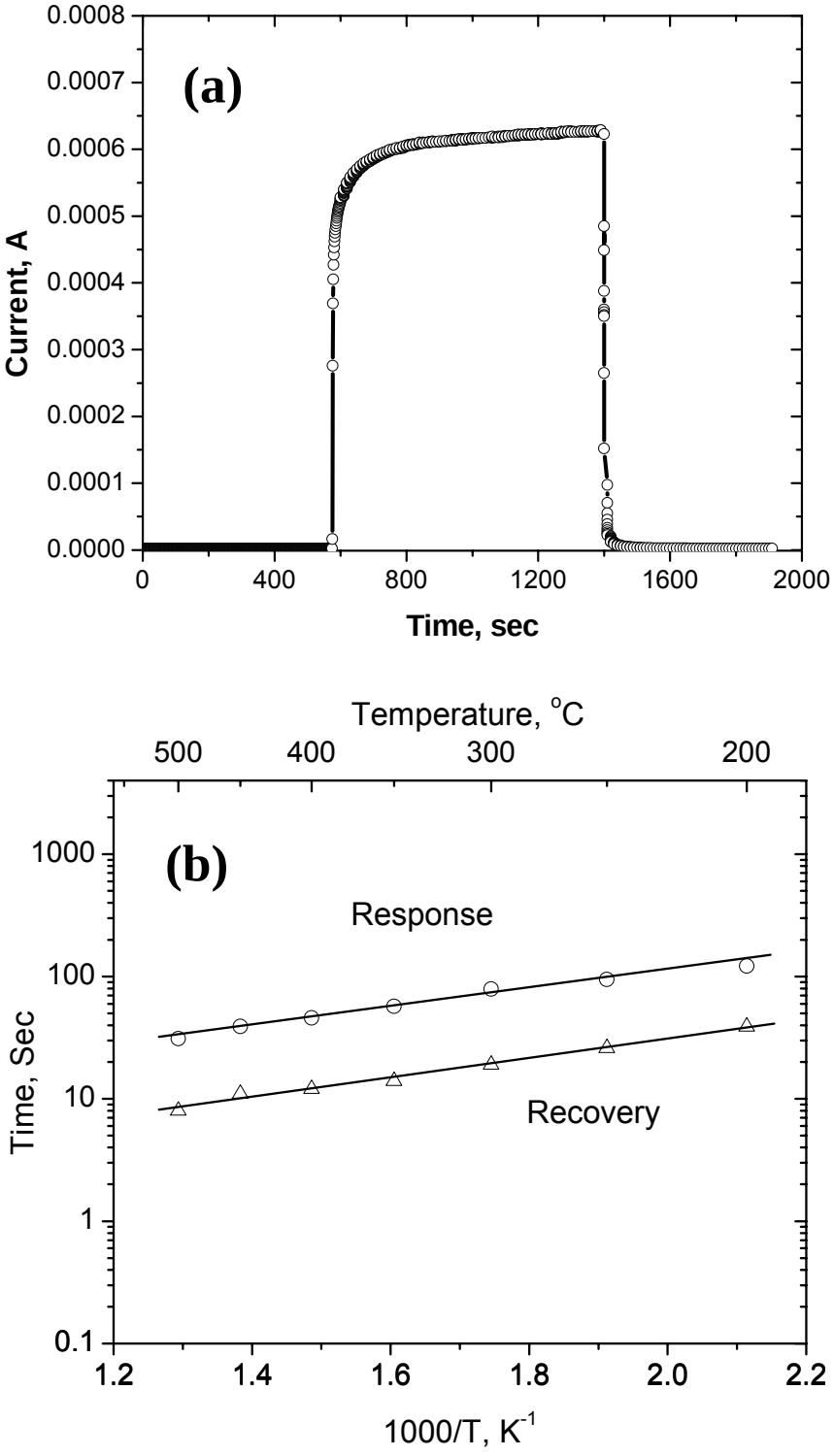


Figure 5-5 (a) Typical electrical response of a $SnO_2$ gas sensor to 500ppm ethanol vapor measured at 450°C. (b) Response and recovery time of the sensor to 500 ppm ethanol vapor as a function of testing temperature from 200 °C to 500°C.

Table 5-1 Characteristics of $SnO_2$ sensors fabricated by different approaches

| Fabrication approach | Ethanol conc. (ppm) | Temp. (˚C) | Sensitivity $S=R_{air}/R_{gas}$ | Response Time (sec) | Recovery Time (sec) |
|---|---|---|---|---|---|
| Sol-gel[176] | 150 | 250 | 3.2 | | |
| Spin coating[177] | 400 | 200 | 6.2 | 170 | |
| RT CVD[178] | 1000 | 300 | 100 | | |
| EB evaporation[179] | 300 | 300 | 160 | | |
| Not specified[180] | 1000 | 275 | 280 | 36-45 | 300-420 |
| Combustion CVD (this work) | 500 | 200 | 50.5 | 122 | 39 |
| | 100 | 300 | 280 | 55 | 17 |
| | 300 | 300 | 696 | 42 | 12 |
| | 500 | 300 | 1075 | 31 | 8 |

Usually, gas sensitivity (S) is expressed as the ratio of electrical resistance in air ($R_a$) to that in the testing gas ($R_g$): $S = R_a/R_g$. Sensitivities at different testing temperatures for $SnO_2$ sensor fabricated using combustion CVD are shown in Figure 5-6(a). At low temperatures,

sensitivity is relatively low (e.g. 50.5 at 200°C), but it increases very rapidly with temperature. At 300°C, the sensitivity peaked to its maximum value of 1070. Above 300°C, sensitivity gradually decreased as the testing temperature increased further. The trend and the most sensitive temperature are in good agreement with data reported in literature.[181] However, as shown in Table 1, sensitivities at the corresponding individual testing temperatures are dramatically higher than those reported in literature.

It is well recognized that the sensing behavior of a thin-film gas sensor is extremely sensitive to grain size and surface conditions. The gas detecting mechanism of $SnO_2$ is relevant to the electron-depletion region on the surface of $SnO_2$ particles/grains created by the pre-adsorbed surface oxygen. The resulting non- stoichiometry in surface layers leads to a higher energy barrier to electron transport through these regions. The energy barrier can be lowered when the reducing gas species in the surrounding environment interact with the pre-adsorbed surface oxygen.[163] The smaller the grain size, the higher the surface area, and the larger the change in electrical conductivity upon exposure to reducing gas species. For comparison, a porous film gas sensor consisting of large $SnO_2$ particles showed a sensitivity of 15 when exposed to 100 ppm ethanol at 300°C,[182] while our sensor with nanosize grains displayed a sensitivity of 280 under the same conditions. The relative conductance changes are also plotted on a logarithmic scale in Figure 5-6(b) as a function of ethanol concentration. The ethanol concentration dependence follows the well-known power behavior, $\Delta G/G_0=A[C_{gas}]^B$, where $C_{gas}$ is the concentration of the testing gas. If we assume a relative variation in conductance of 40%, the detection limit at 300°C is 0.05ppm; a great improvement over current sensing devices. Since an effective breath analyzer must detect at least 200 ppm ethanol corresponding approximately to 0.5 g alcohol/l in the blood,[178] the low detection limit of our sensor improves sensitivity by

several orders of magnitude. For 200 ppm ethanol, the relatively conductance change at 300°C is 46000%.

The gas sensing behavior of a semiconducting oxide can be attributed to both surface and bulk interactions, depending on grain size or film thickness. If grain size or film thickness is much larger than the Debye length $\lambda_D$ of the material, the bulk interactions will dominate the sensor response. On the other hand, if grain size or film thickness is smaller than or in the same order of magnitude as $\lambda_D$, surface interactions will dominate the sensor behavior. [183, 184] The large surface to volume ratio of the nanostructured $SnO_2$ thin film suggests that ethanol- $SnO_2$ interactions on the surface may play an important role.

The interactions between ethanol and lattice oxygen $O_O^X$ in a metal oxide such as $SnO_2$ can be described in general by the following defect reaction (in Kröger-Vink notation):

$$6O_O^X + C_2H_5OH_{(g)} = 2CO_{2(g)} + 3H_2O_{(g)} + 6V_O^{\bullet\bullet} + 12e' \qquad \text{Equation 5-1}$$

Similarly, the interactions between ethanol and the surface adsorbed oxygen species[185] such as superoxide ion $O_2^-$ and peroxide ion $O_2^{2-}$ can be described as

$$3O_2^- + C_2H_5OH_{(g)} = 3H_2O_{(g)} + 2CO_{2(g)} + 3e' \qquad \text{Equation 5-2}$$

$$3O_2^{2-} + C_2H_5OH_{(g)} = 3H_2O_{(g)} + 2CO_{2(g)} + 6e' \qquad \text{Equation 5-3}$$

These reactions produce more electrons and thus increase the conductivity of $SnO_2$ (n-type) upon exposure to ethanol. The dependence of conductivity on partial pressure of ethanol can be derived from these reactions using mass-action law and charge neutrality relations. This will be further investigated in subsequent studies.

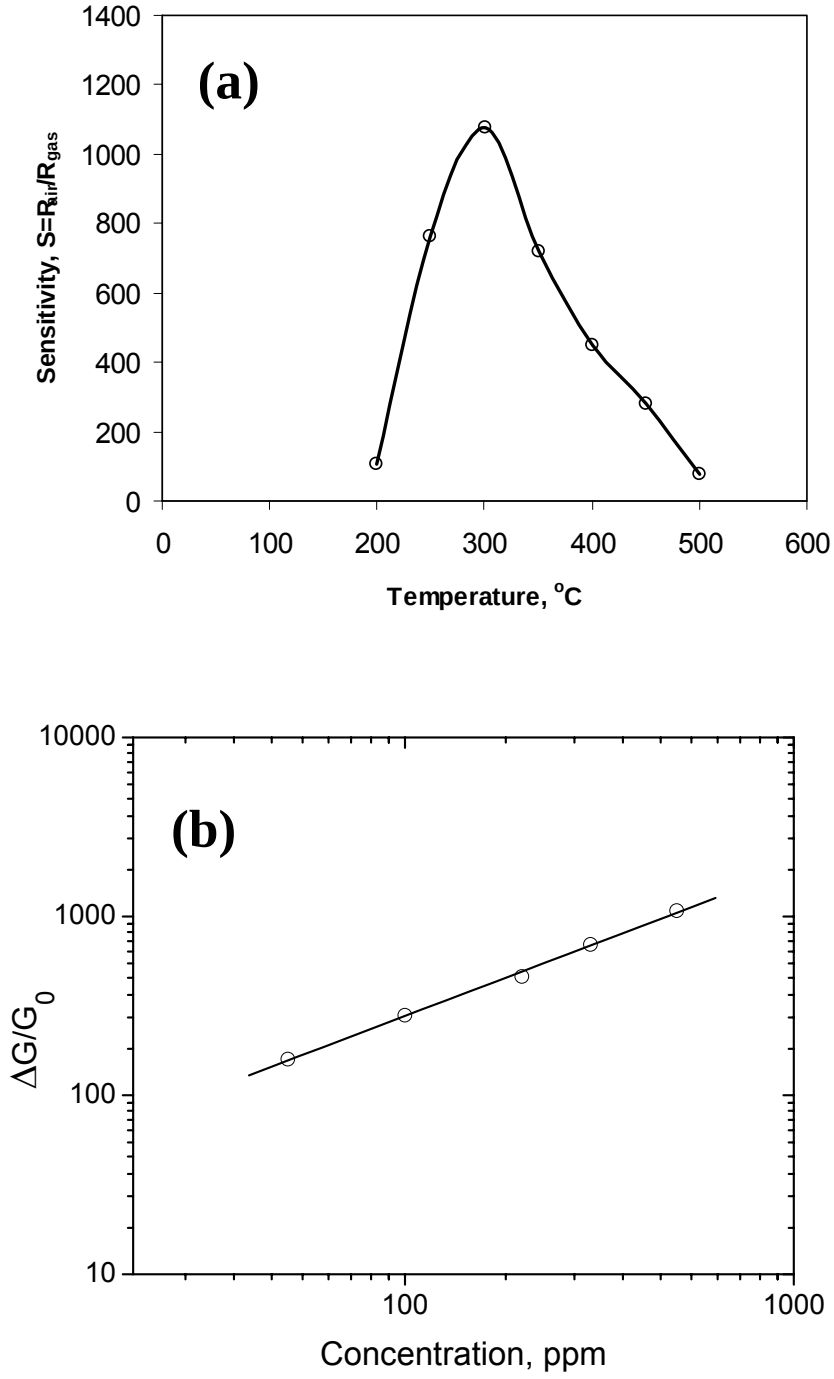


Figure 5-6 (a) Sensitivity of a $SnO_2$ sensor fabricated at 850°C and tested for 500ppm ethanol at different temperatures. (b) Relative conductance change with ethanol vapor concentrations for a $SnO_2$ sensor tested at 300°C.

The retarded recovery speed for most existing gas sensors makes them inconvenient for practical use, since either much longer waiting time or higher temperature is required for full recovery. The $SnO_2$ thin layers deposited via combustion CVD show dramatically improved surface interaction with gas molecules as indicated by the short response time, and, more particularly, the super fast recovery speed for ethanol vapor. This behavior can be tentatively justified by assuming that nanosized particles imply much higher surface areas, porosity, and stronger bonding between particles as well. While the detailed mechanism for the superior ethanol sensing performance of the thin film $SnO_2$ sensor is yet to be confirmed, the interdigitated nano-porous sensor may have significant scientific and technological implications: This makes combustion vapor phase deposited sensors quite interesting for many potential applications such as food quality control,[186] alcohol identification, electronic noses, and medical diagnosis. The ultra low detection limit (<1ppm) and high sensitivity offer unique options for cost-effective sensors with a greatly improved level of reliability. Combustion CVD presents a cost-effective technique easily scaled up for quick manufacturing of fast acting, highly sensitive, and reliable gas sensors. Further, the sensor can be miniaturized, which is essential to the development of integrated and smart systems with compact volume and less power consumption. The sensor can also be fabricated in arrays and integrated with a signal-processing unit to further enhance the sensitivity and selectivity.

## 5.3 Summary

In summary, highly porous and nanostructured $SnO_2$ thin film gas sensors with Pt interdigitated electrodes have been fabricated via a combustion CVD process. The $SnO_2$ films were less than 1 μm thick and consisted of nanocrystallines smaller than 30 nm. The as-prepared

$SnO_2$ gas sensors have been tested for ethanol vapor sensing behavior in the temperature range of 200–500°C. At 300°C the sensitivity to 500 ppm ethanol vapor was 1075 while the corresponding response time and recovery time were 31 and 8 seconds, respectively. The corresponding low detection limit was found to be below 1 ppm. Consequently, the as-fabricated sensor demonstrated significant improvements over those reported in the literature. These highly sensitive, fast responding, and low cost $SnO_2$ sensors could have many practical applications.

# CHAPTER 6 NANOMATERIALS OF SEMICONDUCTING OXIDES

## 6.1 Aligned $SnO_2$ Nanotubes

Tin dioxide has long been recognized as an important n-type semiconductor. The large band gap (3.6 eV at 300 K) and high achievable carrier concentration (up to $6\times10^{20}$ $cm^{-3}$ [187]) make it an excellent candidate for a wide range of applications such as transparent conducting electrodes,[188, 189] solid-state gas sensors,[190, 191] lithium-ion batteries,[192-194] and solar cells.[195, 196] It is well known that, for low-dimensional semiconducting materials, size confinement may dramatically alter their properties.[197-202] One-dimensional $SnO_2$ nanostructures have shown to exhibit peculiar chemical and optoelectronic properties.[203, 204]

Several 1-D $SnO_2$ nanostructures (e.g., nanowires, nanorods, and nanobelts) have been synthesized using different methods.[205-210] The synthesis processes usually fall into two categories: vapor phase deposition or solution-based crystal growth. While solution-based approaches generally offer better control of processing conditions and are easy to achieve higher productivity, vapor deposition often yields higher aspect ratio and excellent crystallinity due to the higher temperature involved. Although various nanostructures (e.g., a single $SnO_2$ nanobelt) have demonstrated exceptional properties (vs. its bulk counterpart) in a well-defined laboratory environment, fabrication of functional devices based on these nanostructures is still a challenge since it requires not only high yielding but also well alignment of these nanostructured units.

Recently, a simple combustion CVD process has been successfully used to synthesize a new 1-D nanostructure of $SnO_2$, nano-boxbeams or nanotubes with square and rectangular

cross sections.[130] One of the important features of the as-synthesized $SnO_2$ nanotubes is that they were oriented perpendicular to the quartz substrates. These rectangular-shaped, thin-walled $SnO_2$ nanotube arrays may have great potential in fundamental study of nanostructures as well as in fabrication of novel devices based on these nanostructures. Here, more detailed findings on synthesis and properties of these $SnO_2$ nanotubes are discussed. In particular, temperature dependence of lateral size, structure evolution, possible growth mechanism, and size confinement effect on Raman spectrum are discussed.

### 6.1.1 Experimental

$SnO_2$ tubes were synthesized using a combustion vapor condensation process, which has been employed for fabrication of nano-sized particles, dense coatings, and porous films with a variety of morphologies.[58, 98, 99, 129] In this process, organic solutions containing desired precursor species are burned in a combustion flame and deposit a layer of oxide material on substrates. Detailed description of this process can be found elsewhere.[58, 98] The precursor material, Tin (II)-2-ethylhexanoate (Aldrich), was dissolved into absolute ethanol. The solution was then transported to a specially designed nanomizer (from Microcoating Technologies) by a HPLC pump. Micro- and submicro-scale mists were generated and combusted in an open atmosphere. Quartz substrates with the size of 1 cm×1cm were inserted into the desired temperature zone within the flame. Depositions were performed at temperatures from 850°C to 1150°C with an interval of 100°C.

The as-grown $SnO_2$ tube arrays were characterized using an X-ray diffractometer (XRD, Phillips PW 1800), a scanning electron microscope (SEM, LEO 1530 Thermally-Assisted FEG), and a transmission electron microscope (HRTEM, JEOL 4000EX) equipped

with an energy-dispersive x-ray spectroscopy (EDS) attachment. Raman spectra were obtained using a Renishaw 2000 Raman spectromicroscope scanning from 200 $cm^{-1}$ to 1000 $cm^{-1}$ at room temperature in open-air. An Ar-ion laser beam with a wavelength of 488 nm was used to excite the $SnO_2$ nanotube crystals.

A single $SnO_2$ nanotube gas sensor was fabricated on inter-digitated Pt electrodes. As shown in Figure 6-9a, the patterned Pt electrode stripes are 5.5 μm wide and the spacing between two adjacent electrode stripes is 3.9 μm. $SnO_2$ nanotubes synthesized on a quartz substrate were scratched into ethanol. After ultrasonically dispersed, a drop of the suspension was put on the patterned Pt electrodes and dried naturally. The dropping process was repeated until a single $SnO_2$ nanotube could be observed bridging two electrodes. Gas sensing property was characterized at 400°C by bubbling argon through an ethanol bubbler at a gas flow rate of 100 ml/min. The current flowing through the $SnO_2$ nanotube was measured using a Solartron 1255 Electrochemical Interface at an applied constant voltage of 50 mV.

### 6.1.2. Results and Discussion

Shown in Figure 6-1 are SEM images of $SnO_2$ tubes synthesized at 1150°C for 30 minutes. Figure 6-1(a) is a cross-sectional view of the as-synthesized $SnO_2$ structure, showing relatively uniform lateral size of about 500 nm and length up to 7.0 μm. Each individual $SnO_2$ structure appears to be "solid" rod and have a square or rectangular cross section. These nanostructures are aligned vertically to the substrate surface. However, more careful and closer observation revealed that they actually are hollow inside. Figure 6-1(b) shows a single $SnO_2$ structure with partially broken top cap. Shown in Figure 6-1(c) is a

$SnO_2$ structure with a fully open end. The tubular nature of these $SnO_2$ structures is well illustrated in Figure 6-1(d), where most ends are open.

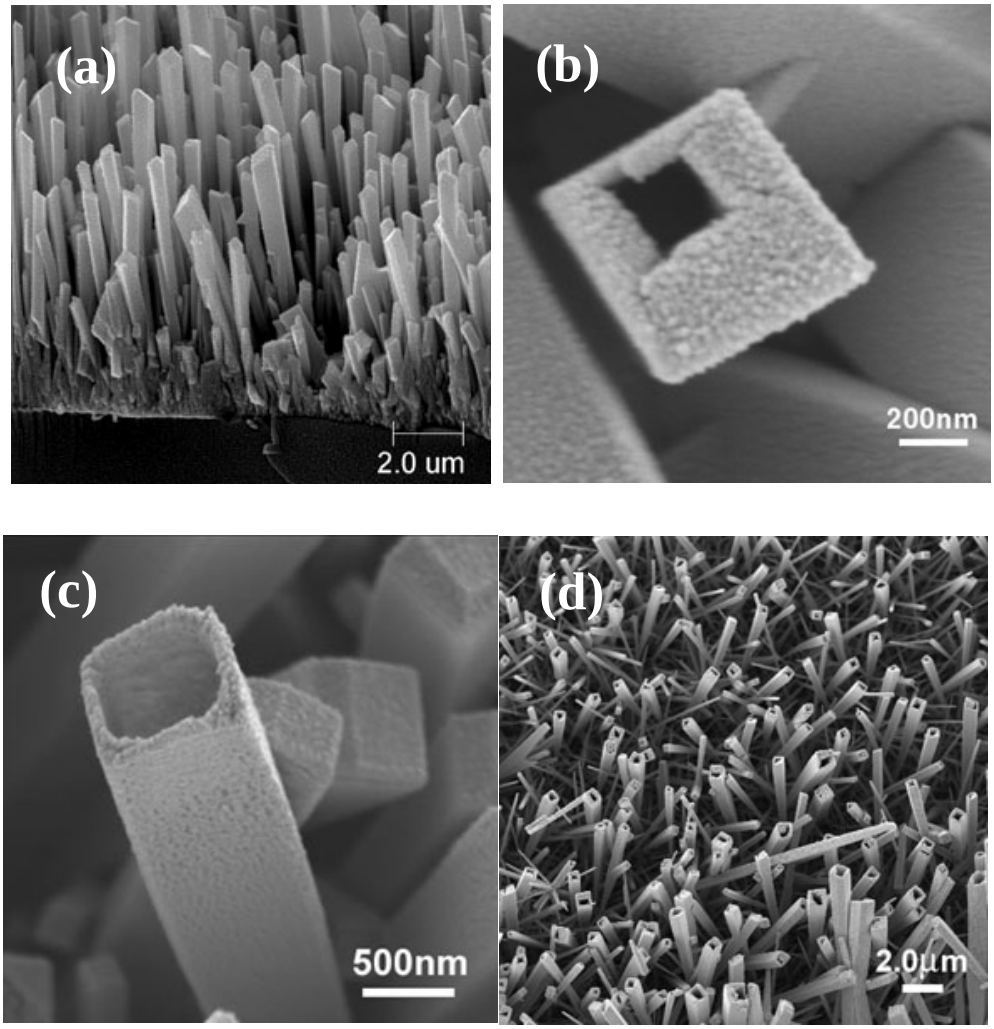


Figure 6-1 Microscopic features of $SnO_2$ tubes synthesized at 1150°C: (a) cross-sectional view. (b) a single $SnO_2$ tube with partially opened top end. (c) a $SnO_2$ tube with fully open top end. and (d) $SnO_2$ tubes with open tips.

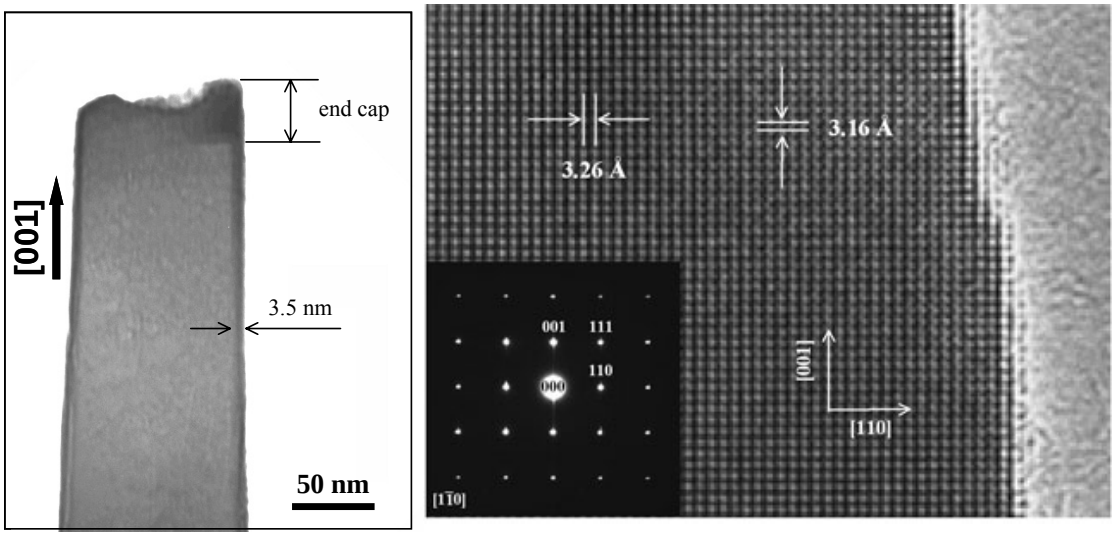


Figure 6-2 (a) A TEM image of a single $SnO_2$ box beam synthesized at 950°C for 30 minutes. (b) A HRTEM image and the corresponding SAED pattern near the internal surface of a $SnO_2$ box beam.

Shown in Figure 6-2(a) is a transmission electron microscopy (TEM) bright-field image of a single SnO2 box-beam, taken oriented with one of its side surfaces perpendicular to the electron beam. The contrast between the thin dark perimeter and the light large area in the center implies that it has a hollow structure. The cross-sectional width of these nanotubes varies from 50-150 nm and the thickness of the wall is about 3.5-5 nm. The contrast in the TEM image also shows the sealed cap of the SnO2 nunotube. Shown in Figure 6-2(b) is a HRTEM image taken near the edge of the same SnO2 nanotube, together with an insert of the corresponding selected-area electron diffraction (SAED) pattern, indicating that each SnO2 tube is a single crystal with rutile structure (a=3.26Å and c=3.16Å). The four

peripheral surfaces were determined to be {110} planes and the tubular crystals grew along the [110] direction.

A systematic study of synthesis variables showed that lateral size of the as-synthesized $SnO_2$ tubes depends critically on synthesis temperature. Shown in Figure 6-3 are micrographs of $SnO_2$ tube arrays grown at different temperatures (850 to1150°C). While the microscopic features remained similar (e.g. square shape), the cross-sectional dimensions of the $SnO_2$ tubes increased exponentially with the temperature at which they were grown, as implied by the Arrhenius plot shown in Figure 6-4. The activation energy for tube growth is estimated to be about 1.01 eV (96.9 KJ/mol). Quantitative microscopy indicated that the average cross-sectional widths were 50, 100, 200, and 450 nm for the $SnO_2$ tubes synthesized at 850, 950, 1050, and 1150°C, respectively. It is worth to mention that although the $SnO_2$ tubes synthesized at higher temperatures were sub-micron in cross-sectional dimension, the wall thickness is still in the nanometer range, varied from 3.5 to 50 nm.

Figure 6-5 shows an EDX spectrum, an XRD pattern, and a Raman spectrum of $SnO_2$ tube arrays synthesized at 1050°C. The EDX spectrum shown in Figure 6-5(a) suggests that the product consists of pure Sn element since oxygen is not detectable to the EDX attachment. The small Si peak came from the underneath quartz substrate. The XRD pattern shown in Figure 6-5(b) indicates that the as-synthesized product has a Rutile structure. Peak intensities and locations match JCPDS card 41-1445. Further, high-resolution TEM (HRTEM) imaging in adjunction with corresponding selected area electron diffraction (SAED) patterns confirm that each $SnO_2$ tube is a single crystal with lattice constants of a = 3.26 Å and c = 3.16 Å. The four peripheral surfaces were determined to be + planes and the tubular crystals grew along <001> directions. [130]

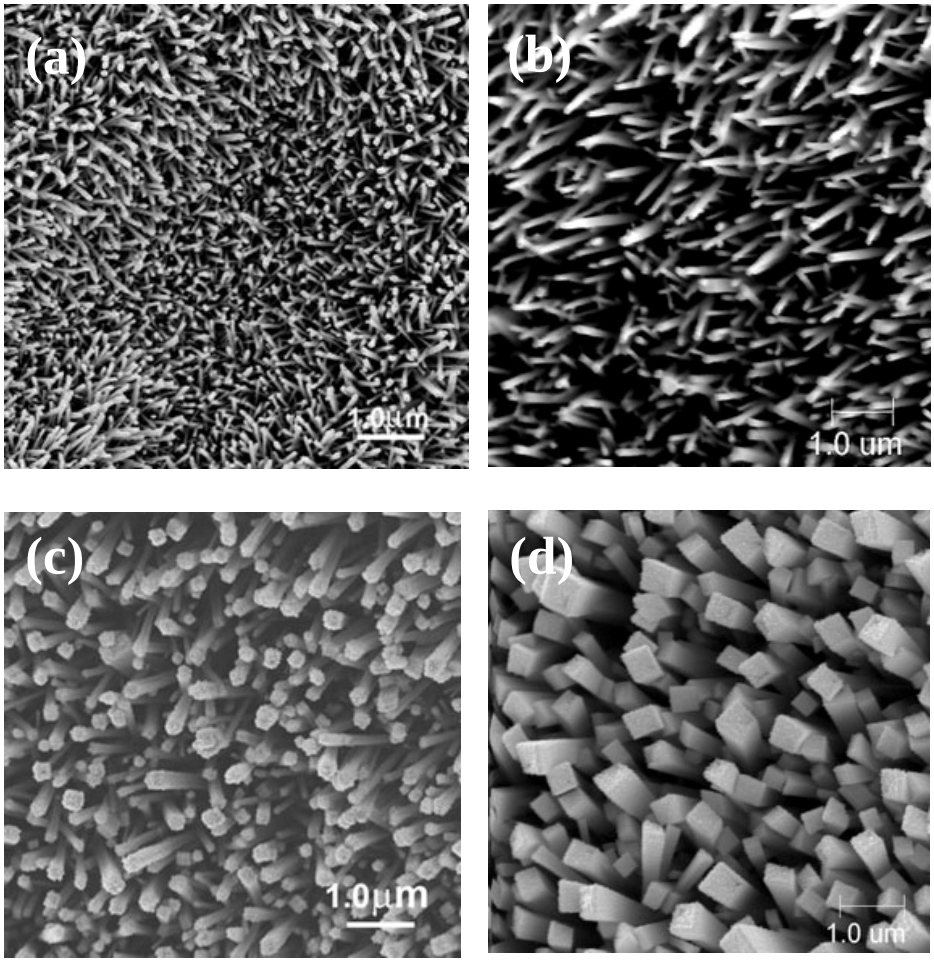


Figure 6-3 SEM micrographs of vertically oriented $SnO_2$ tubes synthesized at different temperatures: (a) 850°C. (b) 950°C.[130] (c) 1050°C. and (d) 1150°C.

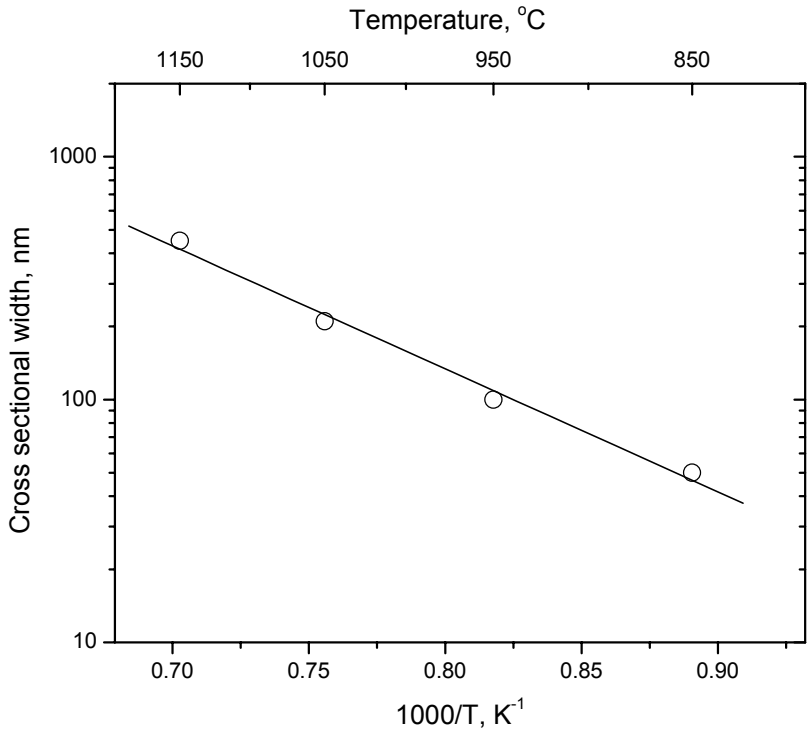


Figure 6-4 An Arrhenius plot showing the dependence of cross-sectional width of as-synthesized $SnO_2$ tube arrays on synthesis temperature.

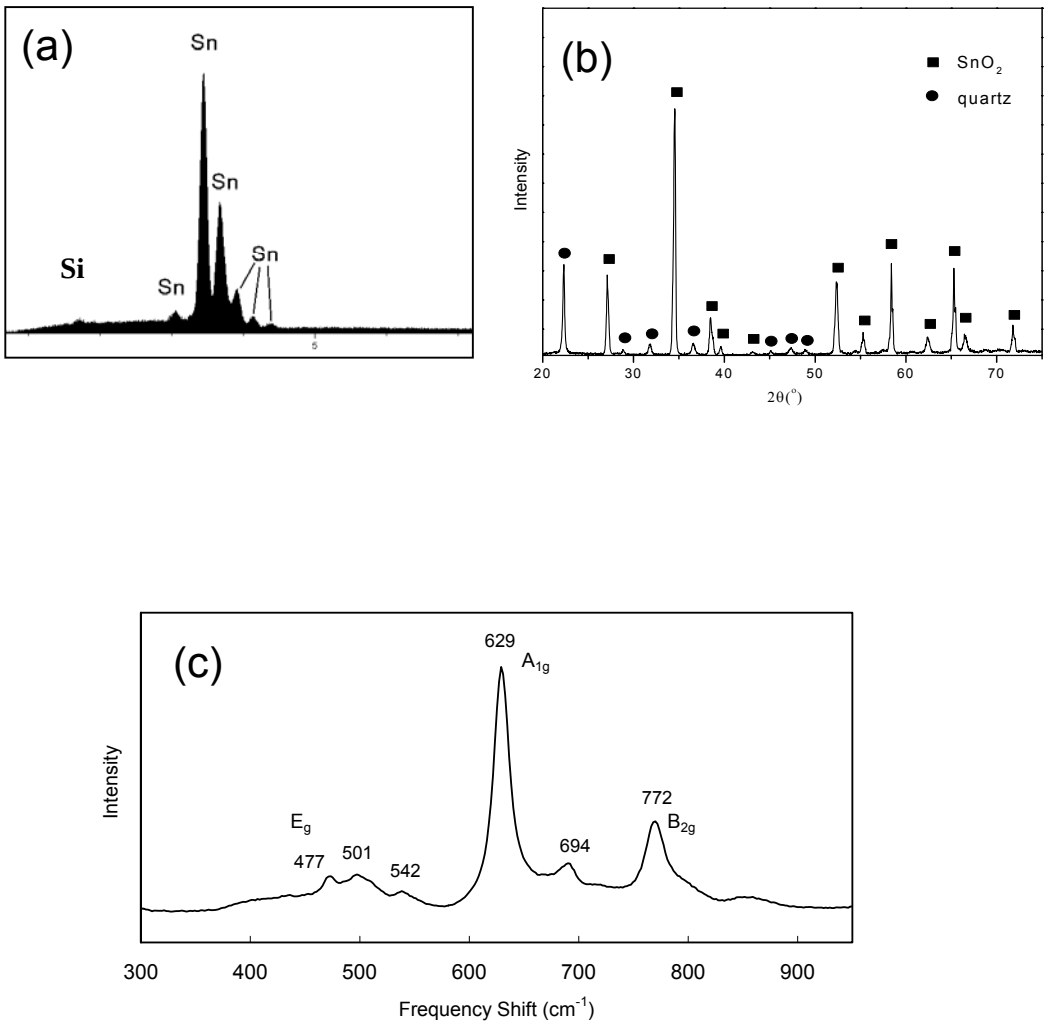


Figure 6-5 (a) an EDX spectrum. (b) an XRD pattern. and (c) a Raman spectrum of $SnO_2$ nanotubes synthesized at 950°C.

The Raman spectrum shown in Figure 6-5(c) further confirms the Rutile structure of the as-synthesized $SnO_2$. Further, three normal phonon modes, $E_g$, $A_{1g}$, and $B_{2g}$, which usually appear in large single crystals or bulk polycrystalline $SnO_2$ materials, are detected at frequency shift of 472.8, 629.5 and 771.8 $cm^{-1}$, respectively. These data are in good agreement with previous publication. [16] In addition to these classical modes, three abnormal Raman lines are observed on the spectrum at the wavenumber of 501.1, 541.9 and 693.9 $cm^{-1}$, respectively, which have been detected on Raman spectra of nanobelts[211] and nano-crystalline particles.[212, 213] Accordingly, these vibration modes can be reasonably assigned to $A_{2u}TO$ (501.1 $cm^{-1}$), $A_{2u}LO$ (693.9 $cm^{-1}$) IR active, and $B_{1u}$ (541.9 $cm^{-1}$) Raman forbidden modes. It was believed that the presence of IR modes and other forbidden Raman modes was attributed to the breaking down of the prevailing $\mathbf{q}_0 = 0$ selection rule as the degree of disorder increases (reducing crystal symmetry) or as crystal size decreases to nanoscale (limiting vibration to the size of the crystal). Another remarkable feature noticed on Raman spectrium is that the peak shifts can be found by comparing the data from bulk with those from nanostructured $SnO_2$. High-frequency modes, $B_{2g}$, $A_{2u}LO$, and $A_{1g}$, shifted to lower frequencies, whereas the low frequency modes, such as $B_{1u}$, $A_{2u}TO$, and $E_g$, shifted to higher wavenumbers. This is consistent with the findings reported by others, [212-214] which can be explained using phonon dispersion curves.

In addition to the normal independent nucleation and growth for each $SnO_2$ tubule, other growth patterns were also observed for some samples. These growth patterns were usually related to prolonged synthesis time or unstable flame. Shown in Figure 6-6(a) are two $SnO_2$ tubules grown coaxially. Figure 6-6(b) shows a smaller tubule grown within a larger one, making use of two perpendicular walls of the larger tube. On the other hand, some

$SnO_2$ tubules were found to grow in parallel with a common outer wall (Figure 6-6(c)). In some cases, the as-synthesized $SnO_2$ tubules had minute structures as shown in Figure 6-6(d) and Figure 6-6(e). Under appropriate conditions, secondary new $SnO_2$ tubules could nucleate and grow on the surface of the existing tubes with an angle of approximately 90° as seen in Figure 6-6(f).

As for other 1-D materials, growth of $SnO_2$ nanostructures was usually dominated by the vapor-liquid-solid (VLS) mechanism,[206, 215, 216] which is evidenced by the presence of a partial metallic particle at the growth tip of each nanostructure, serving as the catalyst and active sites for $SnO_2$ vapor adsorption and subsequent precipitation. However, direct vapor-solid (VS) mechanism was also adopted to explain growth of $SnO_2$ nanostructures through thermal evaporation.[210] In our case, evidence is lacking to support VLS model. First of all, no external catalytic material was introduced in the experiment. Second, the relatively high temperature and high oxygen partial pressure involved in the combustion process exclude the possibility of liquid tin formation during synthesis. Finally, there were no spherical metallic particles found at growth fronts of synthesized nanostructures: each $SnO_2$ tubule either had an open end or was enclosed by one flat plane or a cap of multiple facets. Accordingly, growth of $SnO_2$ tubule arrays was most likely dominated by the VS mechanism.

Shown in Figure 6-7 are SEM micrographs of samples capturing different stages of growth for a single $SnO_2$ tubule. Figure 6-7(a) shows $SnO_2$ polycrystalline with random orientations at early stage of deposition. Grain size appears rather small and uniform. The grains with favorable orientations then grow into top caps by Ostwald ripening mechanism (Figure 6-7(b)). Figure 6-7(c) and (d) show the growth process of the nucleated $SnO_2$ tubes. Thus, the most probable growth process is proposed as follows (Figure 6-8).

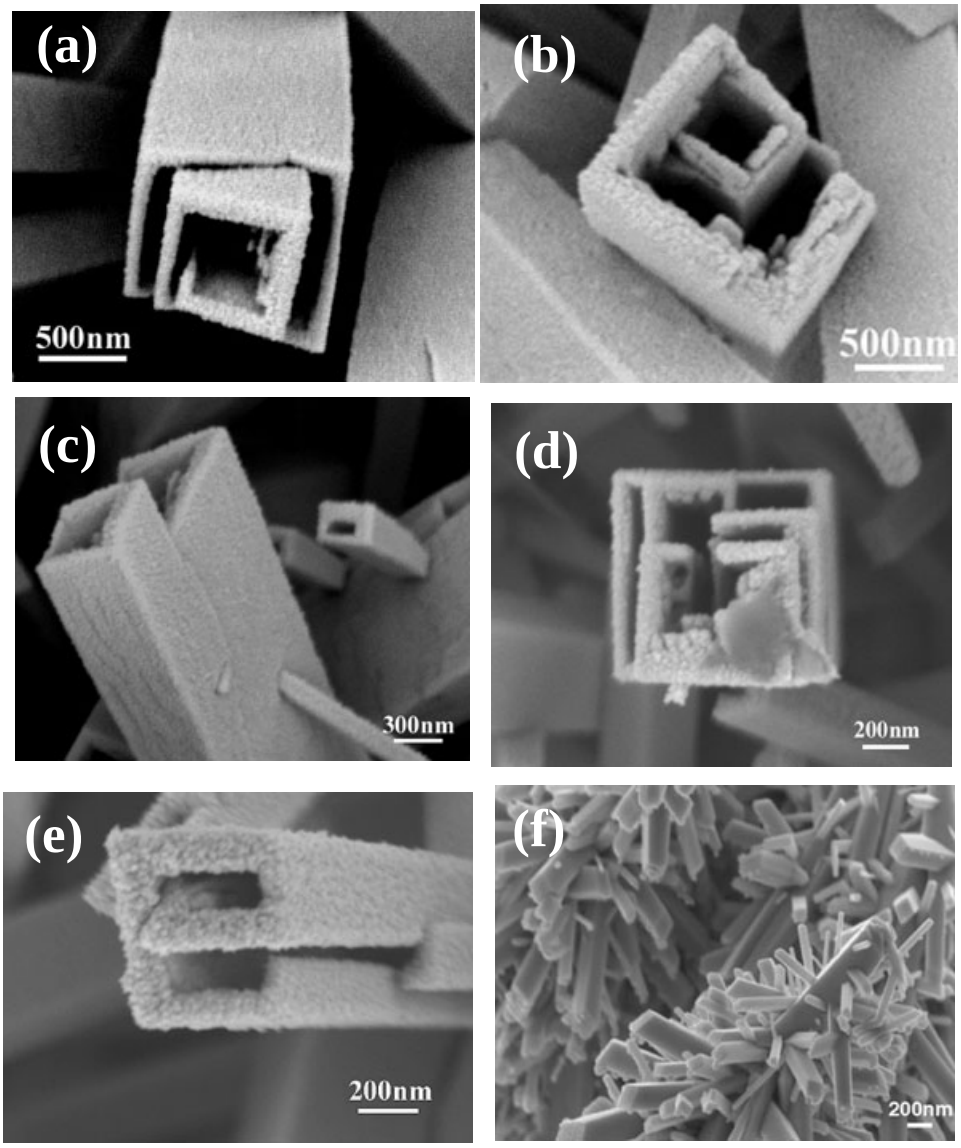


Figure 6-6 Various growth patterns of $SnO_2$ tubules: (a) two $SnO_2$ tubules grown coaxially. (b) a smaller tubule grown within a larger one with two shared walls. (c) two $SnO_2$ tubes grown in parallel with a common outer wall. (d) and (e) $SnO_2$ tubes with minute structures. (f) secondary $SnO_2$ tubes grown perpendicular to the peripheral surfaces of larger tubes.

$SnO_2$ vapor phase is originated within the high-temperature flame through direct oxidation of tin organic precursor:

$$2\ Sn[OOCCH(C_2H_5)C_4H_9]_2 + 45\ O_2 \rightarrow 2\ SnO_2 + 32\ CO_2 + 30\ H_2O \qquad \text{Equation 6-1}$$

The generated $SnO_2$ vapor is carried along the flame, followed by nucleation and growth under suitable conditions. Condensation occurs as the hot flame carrying $SnO_2$ vapor contacts the relatively cold quartz substrate. It is evident that nucleation of $SnO_2$ tube arrays does not occur until a layer of $SnO_2$ polycrystalline material with sufficient thickness has been accumulated on the quartz substrates, as seen in Figure 6-1(a) and Figure 6-7(a). This polycrystalline layer seems to be crucial for both nucleation and subsequent growth of $SnO_2$ tubes, since it provides not only energetically favorite planes for nucleation of end caps of $SnO_2$ tubes, but also pathways for surface diffusion of subsequently condensed vapor species to existing $SnO_2$ tubes. As schematically illustrated in Figure 7a, grains are small, uniform in size and randomly oriented at this stage.

Initially, grains of the condensed bulk layer are randomly oriented. As condensation continues, grains with energetically favorable crystallographic planes will preferentially grow larger and larger, while grains with energetically unfavorable surfaces gradually shrink and eventually disappear. This process is similar to Ostwald ripening, leading to grain coarsening during heat-treatment of polycrystalline materials. End caps of $SnO_2$ tubes could nucleate on these large grains with loosely packed surface planes as shown in Figure 6-8(b). The more closely packed {110} crystallographic planes are preferred to be the peripheral surfaces due to their relatively low surface energy and slow growth rate, while faster growth is encouraged in the <001> directions since {001} planes are more loosely packed.

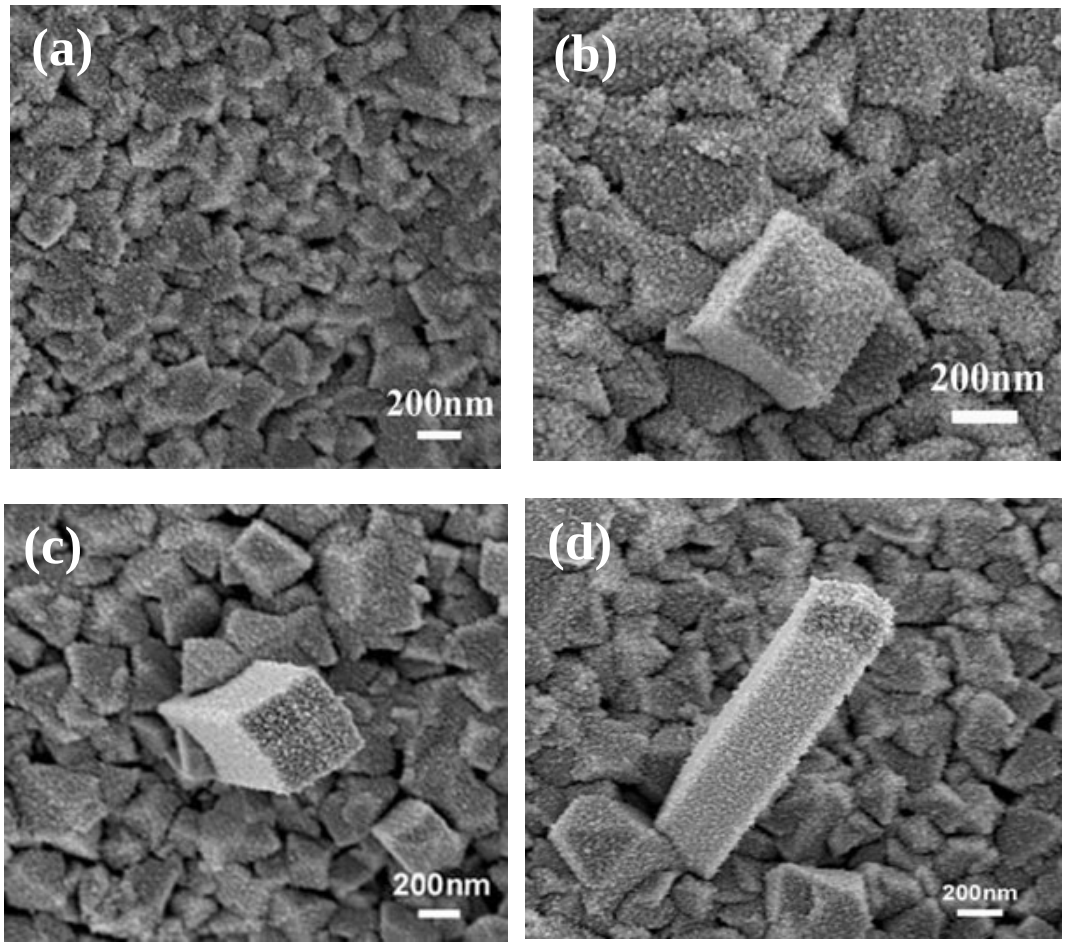


Figure 6-7 SEM photographs of $SnO_2$ tube captured at different stages of growth: (a) fine $SnO_2$ polycrystalline with random orientations. (b) a favorably oriented grain grown into a top cap by Ostwald ripening. (c) and (d) growth of the existing tubules.

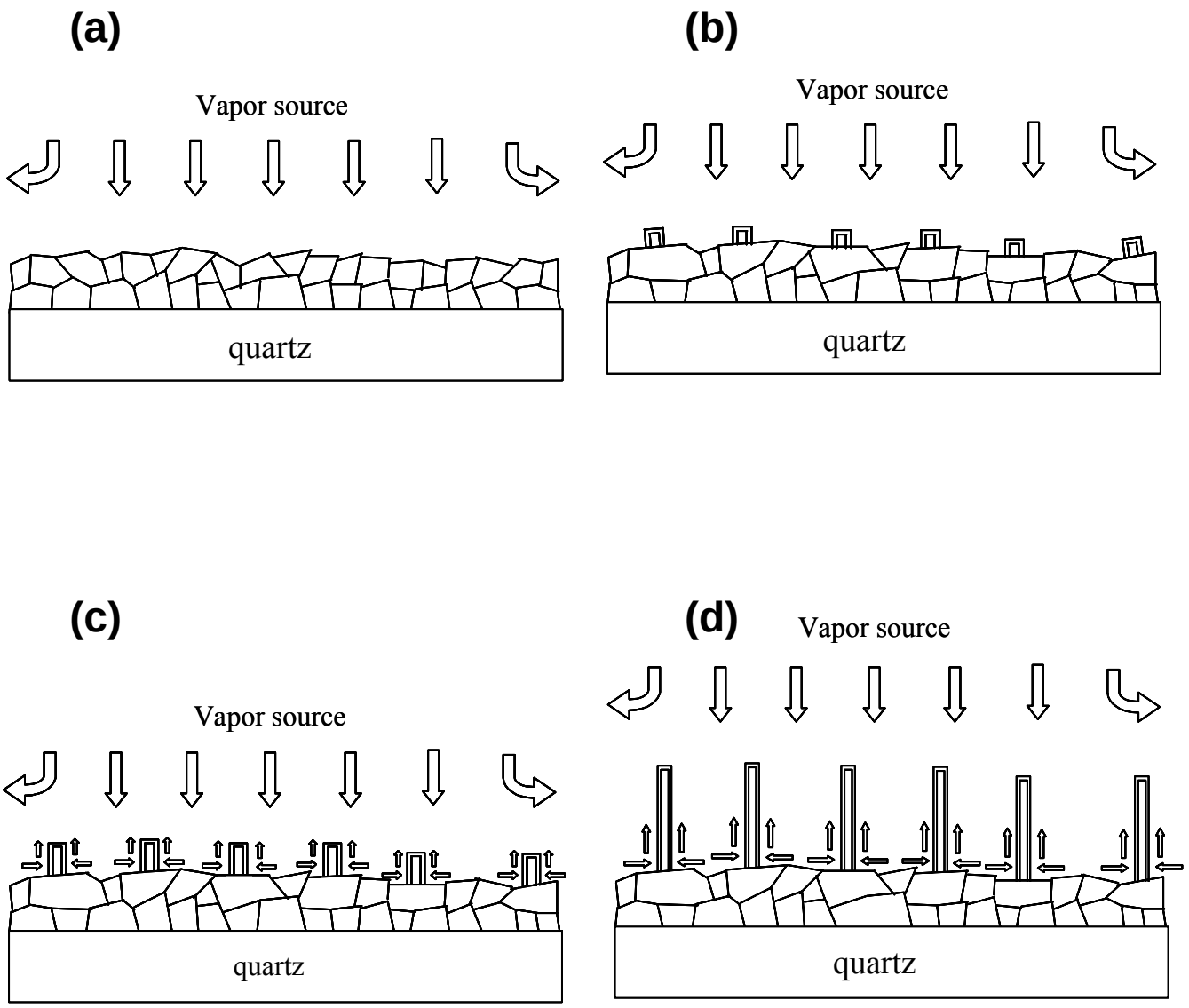


Figure 6-8 Schematics showing the proposed growth mechanism for $SnO_2$ tube arrays: (a) accumulation of a polycrystalline $SnO_2$ layer. (b) nucleation of end caps on the surface of larger grains grown by Ostwald ripening. (c) and (d) growth of $SnO_2$ tube arrays by lifting tubes up from the bottom.

Once nucleated, subsequent growth of these $SnO_2$ tubules is apparent. However, it is worth to note that surface diffusion should play a crucial role at this stage. As stated before, condensation of vapor species mostly occurs on the bottom, bulk layer, where heat can be promptly extracted across quartz substrate by conduction as well as convection of cold air on the other side of the substrate. The condensed vapor species then diffuse across the surfaces of the grains and are incorporated into the bottoms of $SnO_2$ tubules, lifting the tubes up as they grew longer. Similar growth mechanism has been identified for the growth of carbon nano-tubes. [217]

Several factors are essential during nucleation and growth of $SnO_2$ tubes, including the rate of $SnO_2$ vapor transport, degree of super-saturation, availability of nucleation sites, crystallographic orientation, and temperature gradient across substrate. For example, too low degree of saturation may result in growth of uniform film as usually occurring in conventional CVD process. On the other hand, over-saturation may lead to homogeneous nucleation of $SnO_2$ particles within the combustion flame, producing powders of $SnO_2$. Similarly, self-alignment of these $SnO_2$ tubules should be attributed to direction of vapor transport, crystallographic orientation, and temperature gradient along growth direction.

Successful growth of $SnO_2$ nano-tubes and box beams are very unique both for fundamental understanding of new nanostructures and for creation of novel functional devices. One of the attractive features of nano-tubes and these $SnO_2$ tube arrays is that their sizes (or cross-sectional widths) are tunable from nano- to micro-scale by adjusting the synthesis conditions. In addition, the $SnO_2$ box beams are aligned vertically to the substrate surface, which could be critical to fabrication of functional devices. Further, the fabrication process is simple and cost-effective; it is synthesized in open air without any chamber or

controlled atmosphere. The box beams can be packed in honeycomb-type arrays, an attractive configuration for electrochemical and catalytic applications. These $SnO_2$ tube arrays could be used as the building blocks of or a template for many functional devices, particularly those relevant to energy storage and conversion such as nano-batteries, nano-fuel cells, and nano-sensors. In fact, these $SnO_2$ nanotube arrays could be used as a sensing element for gas sensors, an electrode for lithium batteries, and an n-type semiconductor for harvesting solar energy. They can also be used as a template for construction of other nano-devices such as 3-D batteries and fuel cells. The advantages offered by this unique nanostructure include dramatically–accelerated transport of gas/liquid in and out of the box beams; significantly-increased active surface areas and increased flexibility in surface modification for chemically or biologically selective catalysis, drastically-enhanced transport of ionic and electronic defects in the solid state (perpendicular to the wall thickness) due to shorter diffusion lengths, radically-increased population of defects at surfaces/interfaces for fast electrode kinetics, and quantum interactions at the nano-scale, which are yet to be fully exploited. When used for gas sensing, for example, $SnO_2$ nanotubes could display extremely fast response because the internal channel will facilitate fast transport of gas in and out of the box beams, the large surface area will enhance the gas-$SnO_2$ interactions, and the small wall thickness (3.5 to 5 nm) tend to diminish the time needed for $SnO_2$ to reach a new equilibrium when the sample gas is changed, in addition to the quantum confinement effect yet to be discovered.

Figure 6-9(a) shows SEM micrograph of a single $SnO_2$ nanotube sensor fabricated on interdigitated Pt electrodes. The isothermal response of the current flowing through the $SnO_2$ nanotube is shown in Figure 6-9(b) as the gas in the testing chamber was switched between

argon and 7.8 v% ethanol vapor in argon. The current increased 60 times as the testing gas was switched from argon to the ethanol vapor, implying a change in resistance of the nanotube for 60 times. Since $SnO_2$ is an n-type semiconductor, the exposure to ethanol vapor will induce additional electrons, thus reducing the resistance of the nanotube. While the concept of a single $SnO_2$ nanotube gas sensor has been demonstrated, the effect of its nano-dimension on sensitivity, speed of response, and selectivity to different gas species is still under study and will be reported in subsequent communications.

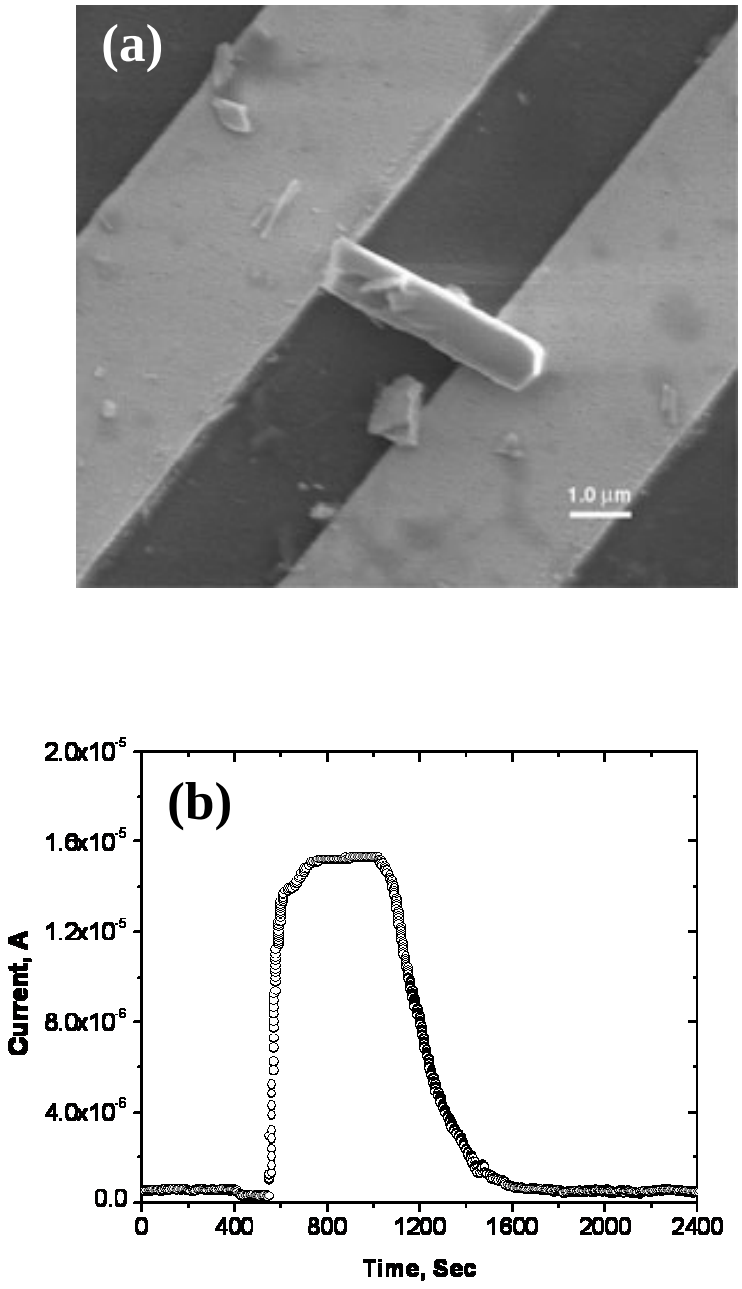


Figure 6-9 A gas sensor based on a single $SnO_2$ nanotube: (a) SEM micrograph of a $SnO_2$ nanotube sensor. (b) response of the $SnO_2$ nanotube sensor to 7.8 v% ethanol vapor in argon at 400°C.

### 6.1.3 Summary

In summary, we have successfully synthesized a new nanostrucutre, nanotubes with square-shaped or rectangular cross sections, of tin dioxide on quartz substrates using a vapor deposition process at 850°C to 1150°C in an open atmosphere. The cross-sectional width of the as-synthesized $SnO_2$ tubes was tunable from nano-size to submicro-size, depending exponentially on the synthesis temperature. Several characterization techniques revealed each tubule was a single crystal with a Rutile structure. Size confinement effect, as studied using Raman spectroscopy, was also observed on samples synthesized at lower temperatures.

The growth mechanism is revealed by interrupting growth of $SnO_2$ tubes at different stages. It is believed that the growth of $SnO_2$ tube arrays follows a self-catalyzed, vapor-solid (VS) process. Starting with an end cap, new material condensed from vapor phase was incorporated into the bottom parts of the already existing $SnO_2$ tubes, lifting up the entire tube during growth. Surface diffusion of the deposited $SnO_2$ along the base layer may play a vital role during the growth process.

The new nanostructure has significant scientific and technological implications. The curiosity that these tubules grew into square or rectangular shape rather than circular shape (as carbon nanotubes do) may stimulate interesting investigation into the crystallization behavior of $SnO_2$ during vapor phase deposition. These size-tunable $SnO_2$ tubules could be the building blocks of or a template for fabrication of functional devices. For example, the concept of a single $SnO_2$ nanotube gas sensor has been demonstrated. However, the effect of nano-dimension on sensitivity, speed of response, and selectivity of a single $SnO_2$ nanotube gas sensor is yet to be determined.

## 6.2 Ordered ZnO Rods

Zinc oxide (ZnO) is a semiconducting material with a wide direct band gap (3.37 eV) and a high excitaon binding energy (60 meV) at room temperature. It has been extensively used as high-frequency piezoelectric tranducer, transparent conductor, ultraviolet (UV) light emitter, and gas sensor.[218-221] In recent years, researchers have demonstrated that nanoscale ZnO has extraordinary optoelectronic properties.[222-224] Many preparative approaches have been used to synthesize one-dimensional ZnO such as nanowires/nanorods and nanobelts with high purity and crystallinility, including sol-gel,[225, 226] vapor phase transport,[210, 222, 227-231] pyrolysis, electrodeposition,[232] chemical[233, 234] or physical vapor deposition,[223, 235] and hydrothermal processes.[236, 237] Unidirectional growth has been achieved on a verity of substrates such as sapphire, silicon, and MgO.[238-241] The major challenge is to guide or manipulate the growth directions so that all the nanostructures could be aligned in the same direction. Normally, ZnO forms a hexagonal (wurtzite) crystal structure. Different compacting densities in different crystallographic facets result in different growth speed in the corresponding directions. Generally, the use of templates and catalysts are the two most common strategies for the growth of 1-D ZnO nanostructures. However, cost-intensive vacuum facilities, expensive target materials, complicated fabrication procedures, and hazardous by-products make it practically prohibitive to synthesize 1-D ZnO material on large scale by these approaches. It is desirable to synthesize 1-D ZnO material using readily available and less expensive precursors in an easily accessible environment. In this chapter, the synthesis of aligned ZnO rods using a simple combustion CVD method is discussed.

Further, a sensor based on a single ZnO rod demonstrated good ethanol vapor sensing properties.

Combustion CVD is a open-air, versatile, and cost-effective vapor deposition process, capable of creating various microstructures, from individual particles to porous or dense films, from nanostructures to thick coatings, using relatively inexpensive precursors (i.e. metal nitrates).[99, 137] Particularly, square-shaped $SnO_2$ nanotube arrays have been successfully synthesized using this method.[130, 242] Here, ZnO rods were grown on silicon substrate at 1050°C for 30 minutes.

ZnO rods were synthesized using a combustion CVD process, which has been recently employed to fabricate many novel nanostructures and devices. [99, 130, 137] Precursor solution was prepared by dissolving Zinc (II)-2-ethylhexanoate (Aldrich) in absolute ethanol. Deposition was carried out at 1050-1200°C for 30 minutes.

### 6.2.1 Experimental

The as-grown products were characterized using an X-ray diffractometer (XRD, Phillips PW 1800), a scanning electron microscope (SEM, LEO 1530 thermally-assisted FEG) equipped with an energy-dispersive x-ray spectroscopy (EDS) attachment, and a transmission electron microscope (TEM, JEOL 100CX II).

Platinum interdigitated electrodes were fabricated on 25.4 mm × 76.2 mm quartz slides. Titanium (20 nm in thickness) was deposited by DC sputtering on quartz slides to improve the adhesion of platinum electrodes on the substrates. The platinum electrodes were then deposited over the thin titanium layer. The patterned platinum electrode stripes are 10 μm wide and the spacing between two adjacent electrode stripes is 2 μm. There were in total 40

stripes on each pattern. Approximately 20 patterned electrodes were fabricated on each quartz slide, which was cut into individual pieces (4mm×10mm) after fabrication.

Ethanol sensing tests were conducted in a tube furnace at 400°C using ethanol vapor of 300 to 1000 ppm. Dry air and air-ethanol vapor mixture was delivered to the furnace via a three-way valve at a constant flow rate of 100 sccm. The current flowing through the $SnO_2$ sensor was measured using a Solartron 1285 potentiostat/Galvanostate interfaced with a PC at an applied constant voltage of 100 mV.

### 6.2.2 Results and Discussion

Shown in Figure 6-10 are SEM micrographs of ZnO rods synthesized using combustion CVD. The as-grown ZnO rods have relatively uniform size and are grown upwards, as seen from a top view of ZnO rods synthesized at 1050°C shown in Figure 6-10(a). The tips of the ZnO rods appear to be hexagonal and have a diameter of about 100-200 nm, as shown in Figure 6-10(b). The as-synthesized ZnO rods were nearly aligned perpendicular to the silicon substrate as shown in Figure 6-10(c). Also noticed on this micrograph is that ZnO rods did not directly grow on the underneath silicon substrate. There appears to be a layer of ZnO separating ZnO rods and the substrate. Shown in Figure 6-10(d) is ZnO rods grown at 1200°C for 30 minutes. The size of ZnO rods increased significantly with the temperature of deposition.

EDS analysis indicates that the product consists of only zinc and oxygen elements in an atomic ratio of 1:1. The X-ray diffraction (XRD) pattern shown in Figure 6-11 reveals that the as-synthesized ZnO rods has a hexagonal structure ($P6_3mc$) with lattice constants of a = 3.25 Å and c = 5.21Å (JCPDS card 36-1451).

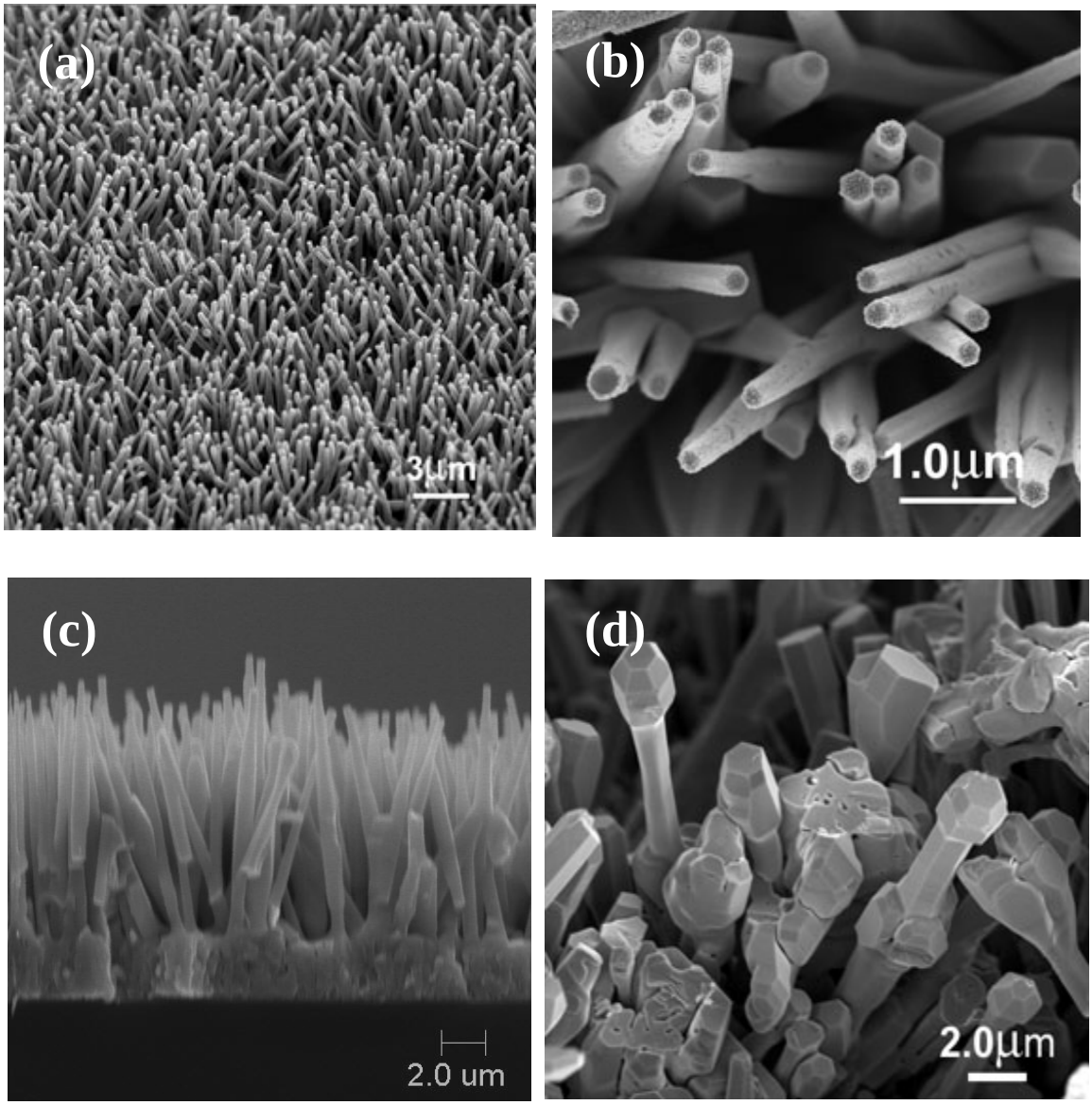


Figure 6-10 SEM images of ZnO rods synthesized using combustion CVD. (a) a top-view. (b) a higher magnification image showing the hexagonal tips. (c) a cross-sectional view of ZnO rods deposited on Si substrate at 1050°C for 30 min. (d) ZnO rods deposited at 1200°C for 30min.

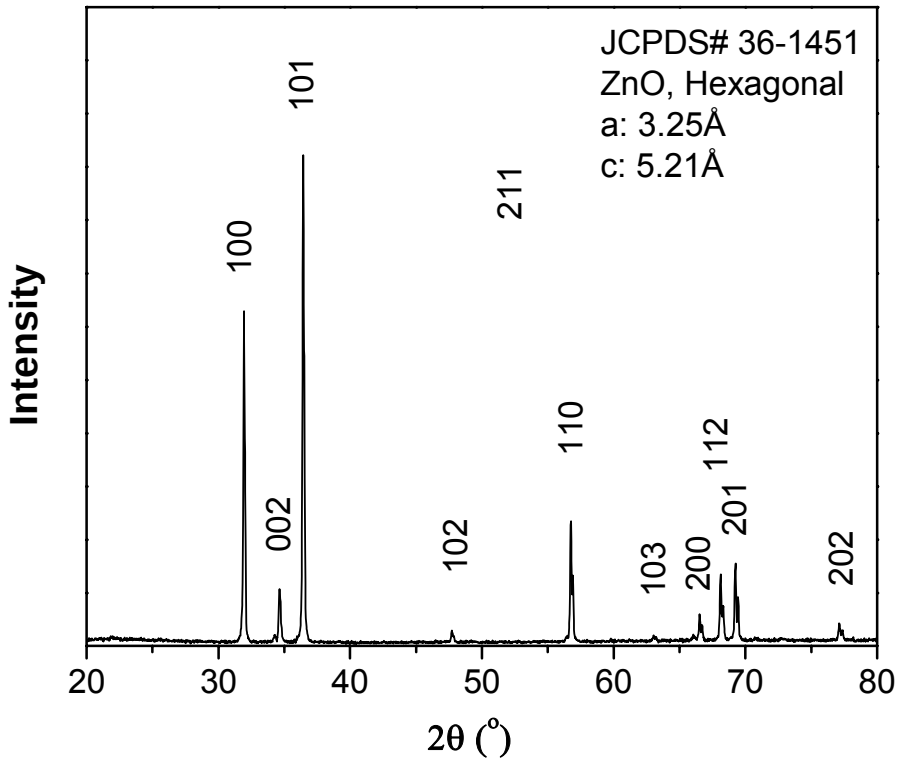


Figure 6-11 X-ray diffraction pattern of ZnO rods synthesized at 1050°C using combustion CVD, indicating the as-synthesized ZnO rods had a hexagonal structure.

The crystallographic orientation of ZnO rods was determined by TEM analysis. Shown in Figure 6-12(a) is a bright field image of a single ZnO rod. The ZnO rod is larger at the bottom and smaller at the top with the tip diameter of about 80 nm. The corresponding selected area electron diffraction (SAED) pattern as shown in Figure 6-12(b) confirmed that the as-synthesized ZnO rod is a single crystal. The growth direction is indexed as [0001], and

the six peripheral surfaces belongs to $\{11\bar{2}0\}$ planes. The orientation of the ZnO rod was also indicated by the hexagonal shape as shown in Figure 1(b).

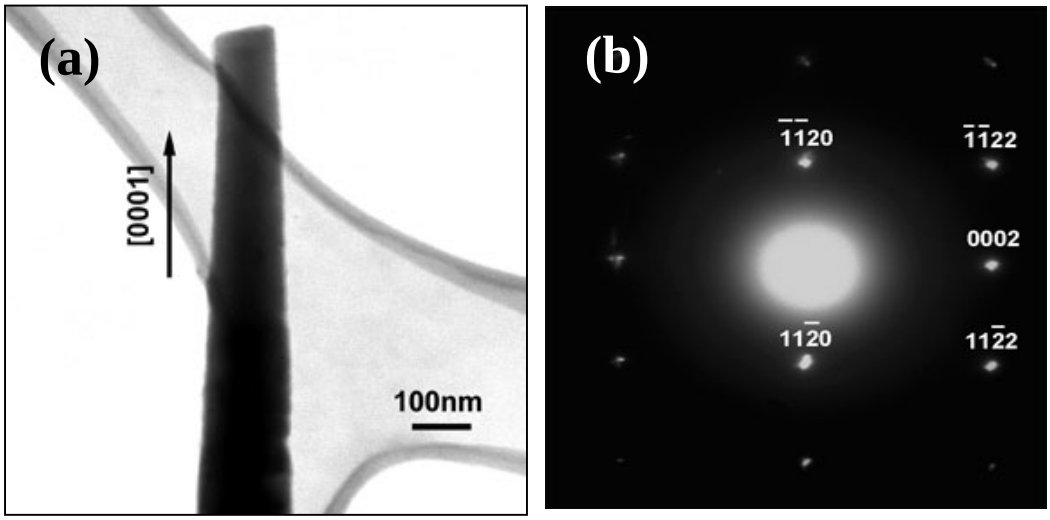


Figure 6-12 (a) TEM bright field image of a single ZnO rod. (b) The corresponging SAED pattern of the ZnO rod reveals [0001] growth direction.

With a Wurtzite structure, the hexagonal ZnO typically has three fast growth directions, $<2\bar{1}\bar{1}0>$, $<10\bar{1}0>$, and <0001>, corresponding to three low energy crystallographic planes, $\{2\bar{1}\bar{1}0\}$, $\{10\bar{1}0\}$, and $\{0001\}$, respectively. Preferential growth in a particular

direction is typically under kinetic control of synthesis conditions. For ZnO wire or rod-like structures, the growth predominantly follows <0001> orientation, regardless of pre-introduced catalysts.[234, 238, 243, 244] Lateral surface planes are usually the sets of $\{2\bar{1}\bar{1}0\}$or $\{10\bar{1}0\}$ planes, resulting in a hexagonal appearance. $<2\bar{1}\bar{1}0>$ growth direction was observed in ZnO nanobelts, where {0001} planes form the two larger peripheral surfaces, while the other two $\{10\bar{1}0\}$ peripheral surfaces grow slowly.[210]

It has been reported that substrates played an important role on the growth of ZnO nanowires. In these cases, specific surface orientations, such as (110) for α-sapphire and (111) for MgO single crystal, are preferred since lattice constants of these planes closely match some specific crystallographic planes of ZnO.[245] Other researchers found that catalysts were vital to the growth of 1-D ZnO structures.[223, 228, 235] In our case, however, it appears that a direct vapor-solid (VS) mechanism is more reasonable based on our observations. As can be seen from Fig. 1(c), a dense ZnO layer of about 2 μm thick was deposited on Si substrate before ZnO rods nucleate and grow, implying that the type of substrate had little effect on the growth of the ZnO rods. This is similar to the growth of $SnO_2$ nanotubes using combustion CVD.[130]] Thus, a self-catalyzed model seems to be appropriate for the growth of ZnO rods in the present study. In the initial stage, ZnO vapor is condensed on Si substrate, forming a uniform and dense polycrystalline film with random orientation. The number of the favorable growth sites increases as deposition continues. Simultaneous supplying ZnO vapor and extracting of heat from the backside of the substrate lead to one-dimensional growth of ZnO rods on the initially deposited bulk ZnO layer. This is in agreement with observations of other researchers.[246, 247]

Shown in Figure 6-13 is a sensor based on a single ZnO rod placed on interdigitated Pt electrodes on a quartz substrate. The gas sensing performance of this sensor was evaluated at 400°C in three ethanol vapor concentrations: 300, 500, and 1000 ppm. Shown in Figure 6-14(a) is the registered current change at a constant applied dc bias of 100 mV when the sample gas was switched from one to another. Before exposure to ethanol, the ZnO rod sensor had a resistance of about 10,000 Ω in air at 400°C. When ethanol vapor was introduced to the testing chamber, the current passing through the sensor material abruptly increased. Then the increase in current slowed down and gradually reached a plateau. The recovery process also followed a similar pattern. The speed of recovery was similar to that of response. As an example, it took about 90 seconds for the sensor to reach 90% of the full response when exposed to 300 ppm ethanol at 400°C. Shown in Figure 6-14(b) are sensitivities of the ZnO rod sensor, defined as the ratio of the electrical resistance in air to the resistance in testing gas ($S = R_{air}/R_{gas}$). Apparently, the gas concentration dependence of the ZnO rod sensor follows a power law. The sensitivities to 300, 500, and 1000 ppm ethanol vapor were 1.4, 1.6, and 2.4, respectively.

### 6.2.3 Summary

Using a combustion chemical vapor deposition (CVD) method, we synthesized single-crystal ZnO rod arrays on silicon substrate. The as-synthesized ZnO rods have diameters ranging from 50 nm to 300 nm and length up to 10 μm, depending on the temperature of deposition. TEM analysis indicates that the ZnO rods grew in the direction of <0001> with six $\{11\bar{2}0\}$ peripheral surface planes. It appears that the growth of ZnO rods followed the

self-catalyzed mechanism. A single ZnO rod solid-state gas sensor fabricated on an interdigitated electrode pattern demonstrated prompt response to ethanol vapor at 400°C.

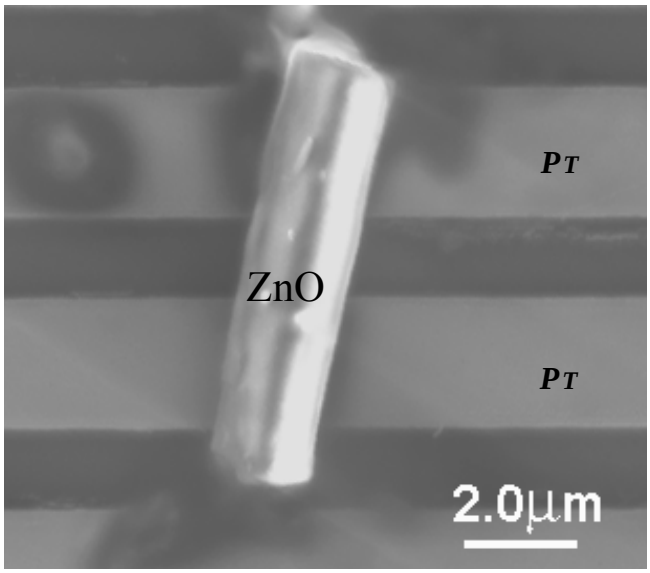


Figure 6-13 A solid-state gas sensor based on a single ZnO rod placed on interdigitated Pt electrodes on a quartz substrate.

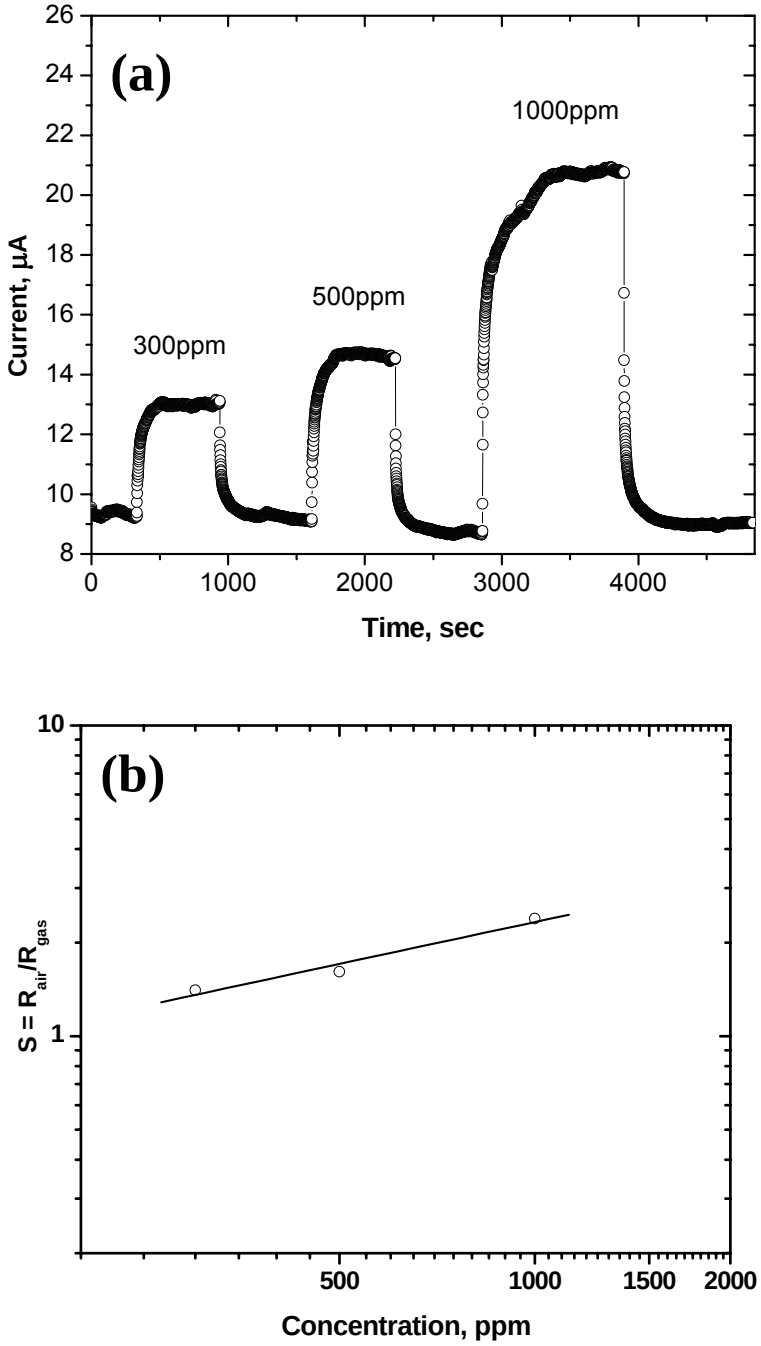


Figure 6-14 (a) Electrical response of a single ZnO rod sensor to ethanol vapor measured at 400°C. (b) sensitivity change with ethanol vapor concentrations for the ZnO rod sensor at 400°C.

## 6.3. Two Dimensional ZnO Flakes

Because of its unique properties (e.g., wide direct bandgap of $E_g$ = 3.2 eV, piezoelectric and semiconducting behavior), ZnO has found numerous applications, including UV light-emitters, solar cells, transparent high power electronics, piezoelectric transducers, and gas sensors. As one of the earliest discovered and well-established gas sensing oxides,[248] ZnO has been extensively studied for the detection of inflammable or toxic gases such as $H_2$, $C_2H_5OH$, CO and $NO_x$.[249-252] It has been recognized that gas sensors based on nanostructured fibrous ZnO exhibited greater sensitivities and faster response than those based on their bulk counterparts.[253-255] Similarly a single ZnO nanowire photodetector showed several orders of magnitude increase in conductance upon exposure to UV light. Development in integrated and smart systems requires a direct integratation of sensor elements or sensor arrays with signal processing unit within a single chip to achieve higher sensitivity and selectivity. Thus miniaturization of active sensing elements is essential.[256] To date, bulk single crystals, 1-D nanostructures, and 0-D nanoparticles of ZnO have been synthesized and tested for various applications. It is believed that the high surface to volume ratio renders these structures spectacular properties. In this section, a new 2-D ZnO structure, single crystal ZnO flakes of 50 nm to 1 μm thick, synthesized using a combustion chemical vapor deposition (CVD) process is presented. Further, a tiny gas sensor has been fabricated by placing a fraction of a ZnO flake on interdigitated electrodes on a silicon substrate. The sensor demonstrated high signal to noise ratio and fast response-recovery to ethanol vapor.

ZnO has a hexagonal (Wurtzite) crystal structure with a= 3.25 Å and c = 5.12 Å. Each Zn atom is tetrahedrally coordinated to four O atoms. Zn and O atoms alternately occupy

crystallographic planes, forming layered structure. Therefore, anisotropic growth is expected in several crystallographic directions, including $<2\bar{1}\bar{1}0>$, $<10\bar{1}0>$, and <0001>. 1-D ZnO nanostructures such as nanowires, nanobelts, and nanorings have been reported in literature.[243, 245, 246, 257] Hexagonal ZnO single crystals with {0001} exposure surfaces and $<2\bar{1}\bar{1}0>$, $<10\bar{1}0>$ growth direction, are energetically favored. Large, 2-D structures could form in this way.

### 6.3.1 Experimental

ZnO single crystal flakes were synthesized using a combustion vapor condensation process as described elsewhere.[58, 99, 129, 162] Zinc nitrate (from Aldrich) is dissolved in ethanol with a concentration of 0.005 M. The solution is then delivered to an atomizer where a fine mist of solution is generated and combusted with the assistance of a small methane flame. Si slices (1 cm×1cm) cut from a Si wafer were used as substrates. A type K thermocouple is placed in the vicinity of substrate surface to monitor deposition temperature. Depositions were performed at 1100°C for 30 min. The as-grown ZnO flakes were characterized using a scanning electron microscope (SEM, LEO 1530 Thermally-Assisted FEG) with an energy dispersive spectroscopy (EDS) attachment, a transmission electron microscope (TEM, JEOL 100C), and an X-ray diffractometer (XRD, Phillips PW-1800).

The as-synthesized ZnO flakes were scratched into an ethanol bath, and ultrasonically dispersed and broken into smaller pieces. A drop of the suspension was transported to patterned Pt electrodes and dried naturally. The dropping process was repeated until a single ZnO flake could be observed bridging two electrodes. The sensor was tested in ethanol vapor (300 and 500 ppm balanced by air) at 400°C at a gas flow rate of 100 sccm. The current

flowing through the ZnO flake was measured using a Solartron 1255 Electrochemical Interface at an applied constant voltage of 100 mV.

### 6.3.2 Results and Discussion

Shown in Figure 6-15 are some typical morphologies of the as-synthesized ZnO flakes. These ZnO flakes were randomly and fairly uniformly distributed on the substrate (Figure 6-15(a)). An angular view (Figure 6-15(b)) more clearly shows that ZnO flakes are oriented upward with respect to the underlying substrate. Higher magnification image (Figure 6-15(c)) shows that each ZnO flake has a cactus-like shape with the maximum dimension of 15 to 20 μm on the top and gradually narrowing down to the bottom. Figure 6-15(d) shows SEM micrograph of a single ZnO flake. The thickness of the ZnO flakes can be up to 1 μm as shown in Fig. 2d or as thin as 150 to 250 nm (Figure 6-15(e), (f)). The large surface appears to be very smooth while the peripheral surfaces are faceted, showing a hexagonal pattern. These features indicate each ZnO flake probably is a single crystal with {0001} flat surface.

The composition of the as-synthesized product was analyzed by SEM/EDX. As shown in Figure 6-16(a), only- Zn was detected. Typical XRD pattern shown in Figure 6-16(b) indicates that the product has Wurtzite structure with cell constants of a= 3.25 Å and c = 5.20 Å (JCPDS card # 03-0888).

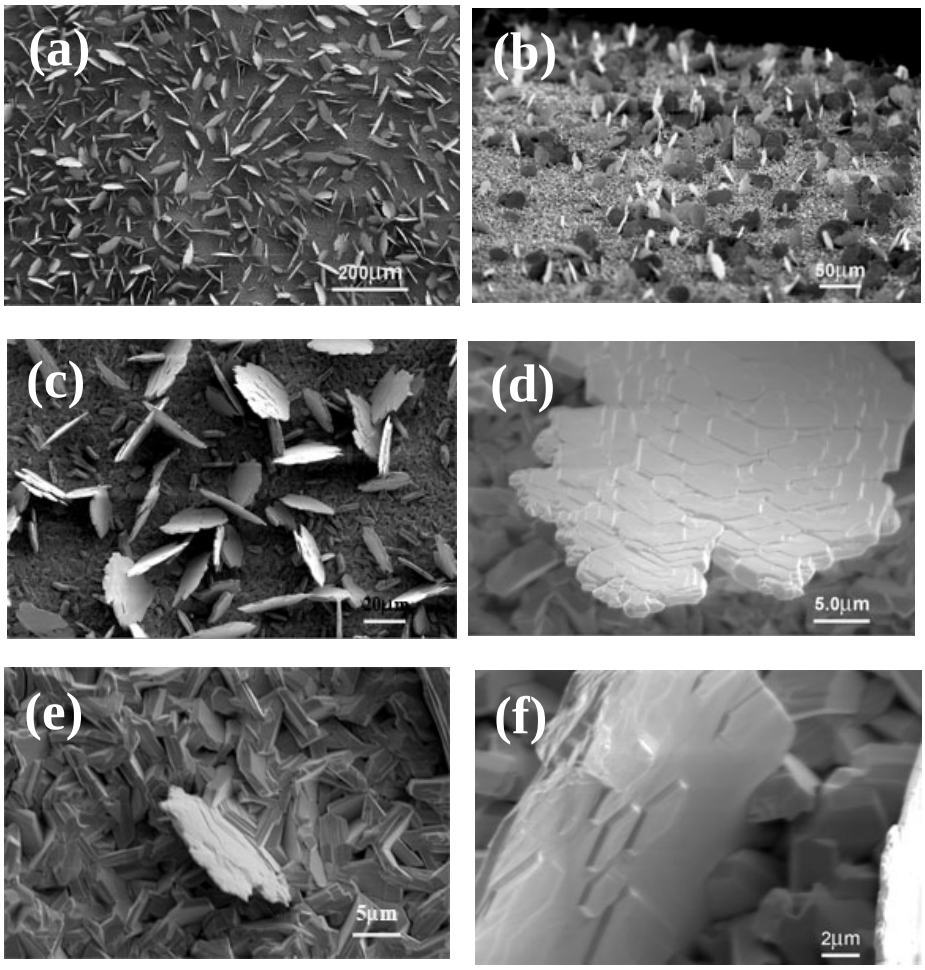


Figure 6-15 SEM images of ZnO flakes synthesized at 1100°C using a combustion CVD process.

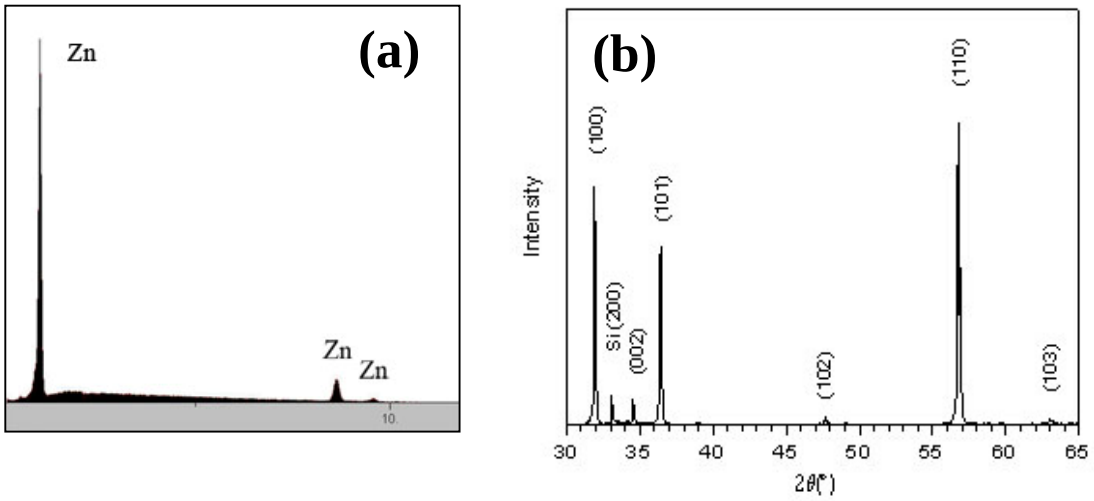


Figure 6-16 (a) EDX analysis of the ZnO flakes, and (b) XRD spectra.

These characteristics were further confirmed by TEM analysis. Shown in Figure 6-17(a) is a TEM bright field image together with an insert showing the corresponding selected area electron diffraction (SAED) pattern, indicating that each ZnO flake is a single crystal with Wurtzite structure. The peripheral facets intersecting one another at approximately 120°C were identified as $\{10\bar{1}0\}$ planes. The corresponding zone axis is determined to be [0001].

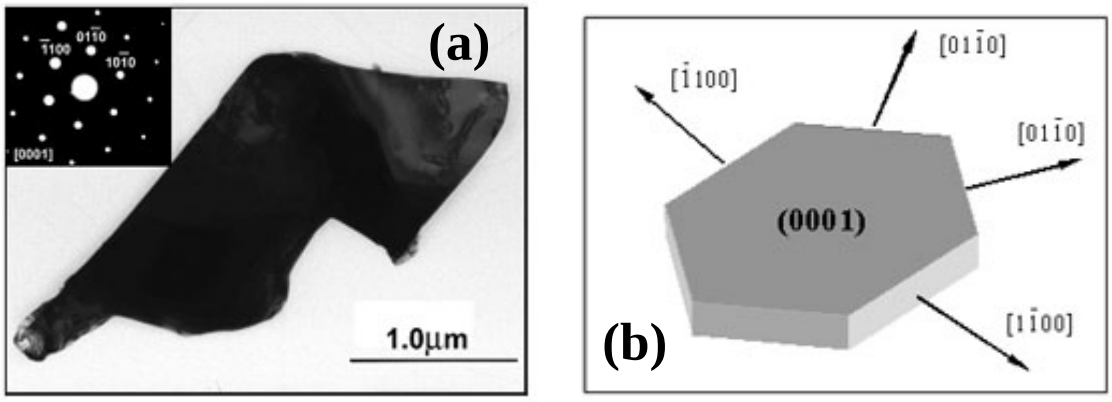


Figure 6-17 (a) TEM image and the corresponding SAED pattern of a ZnO single crystal flake, and (b) A schematic showing the preferential growth orientation.

As a Wurtzite structure, ZnO typically has three fast growth directions, <$2\bar{1}\bar{1}0$>, <$10\bar{1}0$>, and <0001>, corresponding to three low energy crystallographic planes, {$2\bar{1}\bar{1}0$}, {$10\bar{1}0$}, and {0001} respectively. Preferential growth in a particular direction is under kinetic control of synthesis conditions. For ZnO wire or rod-like structures, the growth predominantly follows <0001> orientation, independent of pre-introduced catalysts.[234, 238, 244-246] In this case, lateral surface planes are sets of {$2\bar{1}\bar{1}0$} or {$10\bar{1}0$} planes, resulting in a hexagonal appearance. The growth direction of <$2\bar{1}\bar{1}0$> was observed in ZnO nanobelts where {0001} planes form the two larger peripheral surfaces.[210] The other two {$10\bar{1}0$}

peripheral surfaces did not grow significantly. In our situation, except the dominating lateral {0001} surfaces, all the fast growth fronts were covered by $\{10\bar{1}0\}$ facets as illustrated in Figure 6-17(b).

The growth mechanism for ZnO single crystal flakes is believed to be similar to the one found for $SnO_2$ nanotube arrays synthesized using the same combustion CVD process.[130] A simple direct vapor-solid (VS) conversion model can be applied to explain the growth of ZnO single crystal flakes. Initially, Zinc (II)-2-ethylhexanoate precursor is decomposed and converted into ZnO vapor within the combustion flame. The resulting vapor species is then condensed on the relatively cold Si substrate, accumulating to a bulk layer. This stage continues for a relatively long period of time since there was no preferential growth of ZnO flakes observed under microscope even after 20 minutes of deposition. As condensation continues, the grains with energetically or kinetically favorable crystallographic planes will grow faster than the others. Once initiated, this preferential growth process will be accelerated since the top layer receives more ZnO vapor and also experience higher temperature than the layer below. SEM images shown in Figure 6-18 reveal different growth stages of ZnO flakes. Under these favorable growing conditions, ZnO single crystal flakes expend in two dimensions and gradually grow into cactus-like shape with wider top and narrower bottom. Although at a much smaller rate, ZnO vapor received at the root also contribute to increase of the height. The same mechanism has been proposed to explain the growth of ZnO nanonails, which have large caps and very slim shafts.[258] Close observation reveals that each ZnO flake consists of layered structures with each layer in the thickness of 50 to 250 nm (Figure 6-15(e), Figure 6-18(a), (b)). During deposition, some layers could grow much faster than others. The final ZnO flake can be very thin (Figure 6-15(e), (f)). It is

interesting to note in Figure 6-15(f), isolated small hexagonal ZnO layers could nucleate and grow on the surface of a larger flake. Nucleation on {0001} polar surfaces could be initiated by introducing planar defects to the polar surfaces.[259]

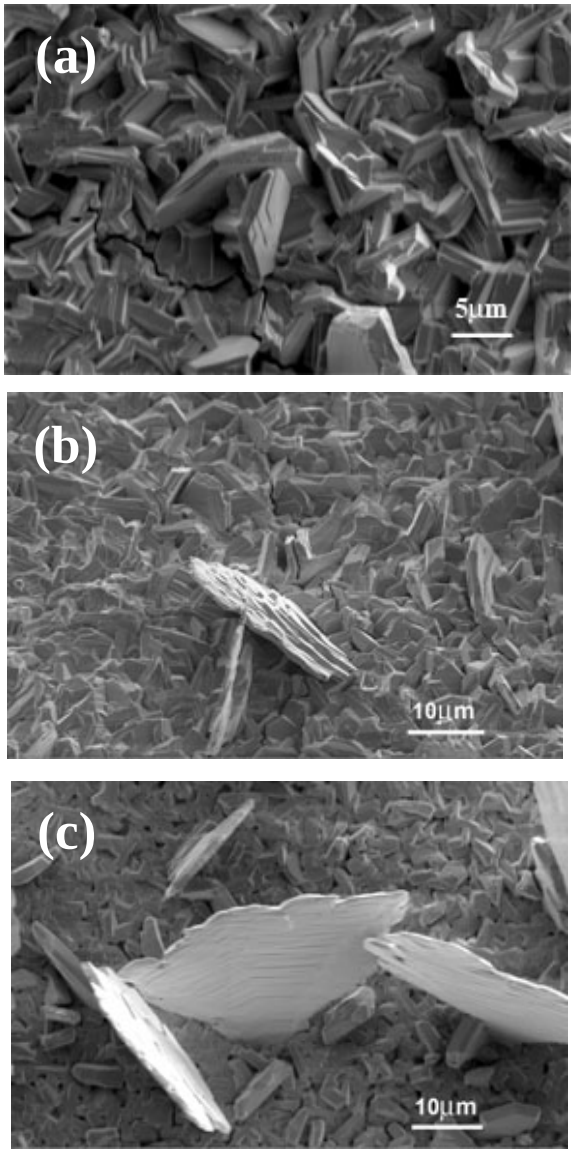


Figure 6-18 SEM images of ZnO flakes taken at different stages of growth. Synthesis temperature was 1100°C.

The width/thickness ratio of each ZnO single crystal flake ranged from 25 to 100. The large specific area of ZnO flakes would dramatically enhance the kinetics of electrochemical and catalytic processes. As a demonstration, a gas sensor was fabricated by placing a fraction of a ZnO flake onto interdigitatecd Pt electrodes, as shown in Figure 6-19(a). The thickness of the ZnO flake is about 200 nm. The sensor was tested at 400°C in ethanol vapor. The performance of the ZnO flake sensor is shown in Figure 6-19(b); the sensor responded quickly as the gas was switched from air to different concentration of ethanol vapor and recovered fully when the gas was switched back to air.

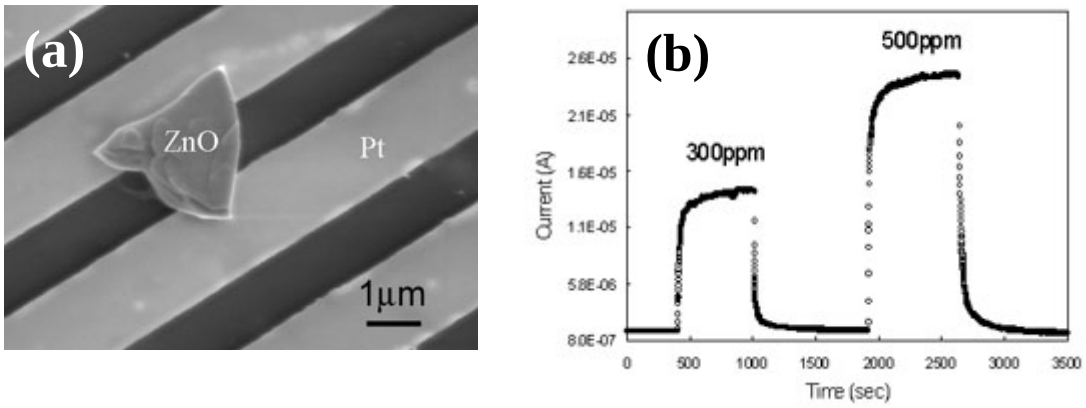


Figure 6-19 A solid-state gas sensor based a single crystal ZnO flake. (a) SEM micrograph of the sensor consisting of a ZnO flake and Pt interdigitated electrodes, and (b) Current variation with time under a constant voltage of 100 mV as sample gas was switched from air to different concentrations of ethanol vapor at 400°C. Data were collected at one-second intervals.

The response and recovery time is defined as the time needed to reach 90% of the full response ($R_f$-$R_0$), where $R_f$ is the full-scale conductance when the sensor is in equilibrium with the ethanol vapor and $R_0$ is the baseline conductance when the sensor is in equilibrium with air. As shown in insert in Fig. 6b, it took 62 seconds at 400°C for the sensor to respond to ethanol vapor (reach 90% of its full response) and approximately the same amount of time to recover. The ratio of $(R_f-R_0)/R_0$ was 7.8 and 14.3 when the atmosphere was switched from air to 300 and 500 ppm ethanol vapor, respectively.

The gas sensing behavior of a semiconducting oxide can be attributed to both surface and bulk interactions, depending on grain size or film thickness. If grain size or film thickness is much larger than the Debye length $\lambda_D$ of the material, the bulk interactions will dominate the sensor response. On the other hand, if grain size or film thickness is smaller than or in the same order of magnitude as $\lambda_D$, surface interactions will dominate the sensor behavior.[183, 184] The large surface to volume ratio and small size of the ZnO flake sample suggest that ethanol-ZnO interactions on the surface may play an important role.

The interactions between ethanol and lattice oxygen $O_O^X$ in a metal oxide such as ZnO produce more electrons and thus increase the conductivity of ZnO (n-type) upon exposure to ethanol. The dependence of conductivity on partial pressure of ethanol can be derived from these reactions using mass-action law and charge neutrality relations. It is noted, however, that these reactions are very general and schematic; ethanol molecules may dissociate to other intermediate species before oxidation at ZnO surfaces. However, identification of the intermediates requires some sensitive surface spectroscopic techniques and tremendous

effort. Investigation into the detailed sensing mechanisms is still underway and will be reported in subsequent applications.

### 6.5.3 Summary

Using a combustion CVD process, we have successfully synthesized a new two-dimensional structure, ZnO single crystal flakes. The flakes grew upward from the underneath Si substrate. The as-grown ZnO flakes were typically 200 nm thick and 10-20 μm wide. Unlike most 1-D ZnO structures with [0001] growth direction, ZnO flakes grow along $<10\bar{1}0>$ directions. Gas sensor based on a 200 μm thick ZnO flake exhibited high sensitivity and fast response to ethanol vapor.

## REFERENCES


[1] S. C. Singhal, and K. Kendall, *High Temperature Solid Oxide Fuel Cells: Fundamentals, Design, and Applications*. Elsevier: Oxford, 2003.

[2] S. C. Singhal, "Advances in Solid Oxide Fuel Cell Technology." *Solid State Ionics* **135** (2000) 305-313.

[3] U. Pal, and S. Singhal, "Electrochemical Vapor-Deposition of Yttria-Stabilized Zirconia Films." *Journal of the Electrochemical Society* **137** (1990) 2937-2941.

[4] L. J. H. Kuo, S. D. Vora, and S. C. Singhal, "Plasma Spraying of Lanthanum Chromite Films for Solid Oxide Fuel Cell Interconnection Application." *Journal of the American Ceramic Society* **80** (1997) 589-593.

[5] S. C. Singhal, "Solid Oxide Fuel Cells for Stationary, Mobile, and Military Applications." *Solid State Ionics* **152-153** (2002) 405-410.

[6] J. W. Kim, A. V. Virkar, K. Z. Fung, K. Mehta, and S. C. Singhal, "Polarization Effects in Intermediate Temperature, Anode-supported Solid Oxide Fuel Cells." *Journal of the Electrochemical Society* **146** (1999) 69-78.

[7] T. Tsai, and S. A. Barnett, "Effect of LSM-YSZ Cathode on Thin-Electrolyte Solid Oxide Fuel Cell Performance." *Solid State Ionics* **93** (1997) 207-217.

[8] E. P. Murray, and S. A. Barnett, "$(La,Sr)MnO_3$-$(Ce,Gd)O_{2-x}$ Composite Cathodes for Solid Oxide Fuel Cells." *Solid State Ionics* **143** (2001) 265-273.

[9] O. A. Marina, N. L. Canfield, and J. W. Stevenson, "Thermal, Electrical, and Electrocatalytical Properties of Lanthanum-Doped Strontium Titanate." *Solid State Ionics* **149** (2002) 21-28.

[10] H. C. Yu, and K. Z. Fung, "$La_{1-x}SrCuO_{2.5-delta}$ as New Cathode Materials for Intermediate Temperature Solid Oxide Fuel Cells." *Materials Research Bulletin* **38** (2003) 231-239.

[11] A. J. Jennings, and S. J. Skinner, "Thermal Stability and Conduction Properties of the $La_xSr_{2-x}FeO_{4+d}$ System." *Solid State Ionics* **152-153** (2002) 663-667.

[12] E. Maguire, B. Gharbage, F. M. B. Marques, and J. A. Labrincha, "Cathode Materials for Intermediate Temperature SOFCs." *Solid State Ionics* **127** (2000) 329-335.

[13] A. Hartley, M. Sahibzada, M. Weston, I. S. Metcalfe, and D. Mantzavinos, "$La_{0.6}Sr_{0.4}Co_{0.2}Fe_{0.8}O_3$ as the Anode and Cathode for Intermediate Temperature Solid Oxide Fuel Cells." *Catalysis Today* **55** (2000) 197-204.

[14] G. W. Coffey, J. Hardy, L. R. Pedersen, P. C. Rieke, E. C. Thomsen, and M. Walpole, "Electrochemical Properties of Lanthanum Strontium Aluminum Ferrites for the Oxygen Reduction Reaction." *Solid State Ionics* **158** (2003) 1-9.

[15] L. Qiu, T. Ichikawa, A. Hirano, N. Imanishi, and Y. Takeda, "$Ln_{1-x}Sr_xCo_{1-y}Fe_yO_{3-delta}$ (Ln=Pr, Nd, Gd; x=0.2, 0.3) for the Electrodes of Solid Oxide Fuel Cells." *Solid State Ionics* **158** (2003) 55-65.

[16] M. T. Colomer, B. C. H. Steele, and J. A. Kilner, "Structural and Electrochemical Properties of the $Sr_{0.8}Ce_{0.1}Fe_{0.7}Co_{0.3}O_{3-delta}$ Perovskite as Cathode Material for ITSOFCs." *Solid State Ionics* **147** (2002) 41-48.

[17] C. Xia, W. Rauch, F. Chen, and M. Liu, "$Sm_{0.5}Sr_{0.5}CoO_3$ Cathodes for Low-Temperature SOFCs." *Solid State Ionics* **149** (2002) 11-19.

[18] K. Kuroda, I. Hashimoto, K. Adachi, J. Akikusa, Y. Tamou, N. Komada, T. Ishihara, and Y. Takita, "Characterization of Solid Oxide Fuel Cell Using Doped Lanthanum Gallate." *Solid State Ionics* **132** (2000) 199-208.

[19] V. Dusastre, and J. A. Kilner, "Optimisation of Composite Cathodes for Intermediate Temperature SOFC Applications." *Solid State Ionics* **126** (1999) 163-174.

[20] E. P. Murray, M. J. Sever, and S. A. Barnett, "Electrochemical Performance of $(La,Sr)(Co,Fe)O_3$-$(Ce,Gd)O_3$ Composite Cathodes." *Solid State Ionics* **148** (2002) 27-34.

[21] S. Q. Hui, and A. Petric, "Evaluation of Yttrium-Doped $SrTiO_3$ as An Anode for Solid Oxide Fuel Cells." *Journal of the European Ceramic Society* **22** (2002) 1673-1681.

[22] S. S. Liou, and W. L. Worrell, "Electrical-Properties of Novel Mixed-Conducting Oxides." *Applied Physics A-Materials Science & Processing* **49** (1989) 25-31.

[23] S. P. S. Badwal, "Zirconia-Based Solid Electrolytes - Microstructure, Stability and Ionic-Conductivity." *Solid State Ionics* **52** (1992) 23-32.

[24] B. Riley, "Solid Oxide Fuel-Cells - The Next Stage." *Journal Of Power Sources* **29** (1990) 223-238.

[25] K. Eguchi, T. Setoguchi, T. Inoue, and H. Arai, "Electrical-Properties Of Ceria-Based Oxides And Their Application To Solid Oxide Fuel-Cells." *Solid State Ionics* **52** (1992) 165-172.

[26] C. Lu, W. L. Worrell, R. J. Gorte, and J. M. Vohs, "SOFCs for direct oxidation of hydrocarbon fuels with samaria-doped ceria electrolyte." *Journal Of The Electrochemical Society* **150** (2003) A354-A358.

[27] C. Xia, and M. Liu, "Low-Temperature SOFCs Based on $Gd_{0.1}Ce_{0.9}O_{1.95}$ Fabricated by Dry Pressing." *Solid State Ionics* **144** (2001) 249-255.

[28] T. Takahashi, H. Iwahara, and T. Arao, "High Oxide Ion Conduction in Sintered Oxides of System $Bi_2O_3$-$Y_2O_3$." *Journal of Applied Electrochemistry* **5** (1975) 187-195.

[29] T. Takahashi, T. Esaka, and H. Iwahara, "High Oxide Ion Conduction In Sintered Oxides of System $Bi_2O_3$-$Gd_2O_3$." *Journal of Applied Electrochemistry* **5** (1975) 197-202.

[30] M. J. Verkerk, and A. J. Burggraaf, "High Oxygen Ion Conduction in Sintered Oxides of The $Bi_2O_3$-$Dy_2O_3$ System." *Journal of The Electrochemical Society* **128** (1981) 75-82.

[31] Z. G. Yang, K. S. Weil, D. M. Paxton, and J. W. Stevenson, "Selection and evaluation of heat-resistant alloys for SOFC interconnect applications." *Journal Of The Electrochemical Society* **150** (2003) A1188-A1201.

[32] W. Z. Zhu, and S. C. Deevi, "Development of interconnect materials for solid oxide fuel cells." *Materials Science And Engineering A-Structural Materials Properties Microstructure And Processing* **348** (2003) 227-243.

[33] N. Q. Minh, and T. Takahashi, *Science and Technology of Ceramic fuel Cells*. Elsevier: The Netherlands, 1995.

[34] K. Q. Huang, P. Y. Hou, and J. B. Goodenough, "Characterization of iron-based alloy interconnects for reduced temperature solid oxide fuel cells." *Solid State Ionics* **129** (2000) 237-250.

[35] T. Horita, Y. P. Xiong, K. Yamaji, N. Sakai, and H. Yokokawa, "Stability of Fe-Cr alloy interconnects under CH4-H2O atmosphere for SOFCs." *Journal Of Power Sources* **118** (2003) 35-43.

[36] H. Kurokawa, Y. Oyama, K. Kawamura, and T. Maruyama, "Hydrogen permeation through Fe-16Cr alloy interconnect in atmosphere simulating SOFC at 1073 K." *Journal Of The Electrochemical Society* **151** (2004) A1264-A1268.

[37] Z. G. Yang, M. S. Walker, P. Singh, J. W. Stevenson, and T. Norby, "Oxidation behavior of ferritic stainless steels under SOFC interconnect exposure conditions." *Journal Of The Electrochemical Society* **151** (2004) B669-B678.

[38] T. Brylewski, M. Nanko, T. Maruyama, and K. Przybylski, "Application of Fe-16Cr ferritic alloy to interconnector for a solid oxide fuel cell." *Solid State Ionics* **143** (2001) 131-150.

[39] C. C. Chen, M. M. Nasrallah, and H. U. Anderson, "Synthesis And Characterization Of Ysz Thin-Film Electrolytes." *Solid State Ionics* **70** (1994) 101-108.

[40] H. Michibata, T. Namikawa, and Y. Yamazaki, "Preparation Of Stabilized Zirconia Electrolyte Films By Vacuum Evaporation." *Denki Kagaku* **58** (1990) 1070-1071.

[41] A. Negishi, K. Nozaki, and T. Ozawa, "Thin-Film Technology For Solid Electrolyte Fuel-Cells By The Rf Sputtering Technique." *Solid State Ionics* **3-4** (1981) 443-446.

[42] S. De Souza, S. J. Visco, and L. C. De Jonghe, "Reduced-Temperature Solid Oxide Fuel Cell Based on YSZ Thin-Film Electrolyte." *Journal of the Electrochemical Society* **144** (1997) L35-L37.

[43] H. Gruner, and J. Moens In *Proceedings of the Second European Solid Oxide Fuel Cell Forum*, European SOFC Forum, Oberrohrdorf, Switzerland, 1996; B. Thorstensen, Ed. Oberrohrdorf, Switzerland, 1996.

[44] C. Lunot, and Y. Denos In *Proceedings of the 1998 International Gas Research Conferences*, Chicago, IL, 1998; D. A. Dolenc, Ed. Gas Research Institute: Chicago, IL, 1998.

[45] H. Nagamoto, and H. Ikewaki In *Materials Research Society Symposium Proceedings*, Warrendale, PA, 1999; Materials Research Society: Warrendale, PA, 1999.

[46] T. Ishihara, K. Sato, and Y. Takita, "Electrophoretic deposition of Y2O3-stabilized ZrO2 electrolyte films in solid oxide fuel cells." *Journal Of The American Ceramic Society* **79** (1996) 913-919.

[47] J. Y. Dai, H. C. Ong, and R. P. H. Chang, "Structural properties of yttria-stabilized zirconia thin films grown by pulsed laser deposition." *Journal Of Materials Research* **14** (1999) 1329-1336.

[48] W. Bai, K. L. Choy, R. A. Rudkin, and B. C. H. Steele, "The process, structure and performance of pen cells for the intermediate temperature SOFCs." *Solid State Ionics* **115** (1998) 259-263.

[49] H. Uyama, N. Oka, I. Ono, and O. Matsumoto, "Formation of Yttria Stabilized Zirconia Film By Plasma MOCVD." *Denki Kagaku* **58** (1990) 564-566.

[50] S. P. Krumdieck, O. Sbaizero, A. Bullert, and R. Raj, "YSZ Layers by Pulsed-MOCVD on Solid Oxide Fuel Cell Electrodes." *Surface & Coatings Technology* **167** (2003) 226-233.

[51] A. O. Isenberg, "Energy-Conversion Via Solid Oxide Electrolyte Electrochemical-Cells At High-Temperatures." *Solid State Ionics* **3-4** (1981) 431-437.

[52] P. Holtappels, and C. Bagger, "Fabrication and Performance of Advanced Multi-Layer SOFC Cathodes." *Journal of the European Ceramic Society* **22** (2001) 41-48.

[53] T. Hatae, N. Kakuda, T. Taniyama, and Y. Yamazaki, "Low Temperature Preparation and Performance of Ni/YSZ Anode with a Multi-Layered Structure for SOFC." *Journal of Power Sources* **135** (2004) 25-28.

[54] H. W. Nie, W. H. Huang, T. L. Wen, H. Y. Tu, and Z. L. Zhan, "LSM Cathodes for SOFC Prepared by Plasma Spraying." *Journal of Materials Science Letters* **21** (2002) 1951-1953.

[55] I. Taniguchi, R. C. van Landschoot, and J. Schoonman, "Fabrication of $La_{1-x}Sr_xCo_{1-y}Fe_yO_3$ Thin Films by Electrostatic Spray Deposition." *Solid State Ionics* **156** (2003) 1-13.

[56] S. P. Yoon, J. Han, S. W. Nam, T.-H. Lim, I.-H. Oh, S.-A. Hong, Y.-S. Yoo, and H. C. Lim, "Performance of Anode-Supported Solid Oxide Fuel Cell with $La_{0.85}Sr_{0.15}MnO_3$ Cathode Modified by Sol-Gel Coating Technique." *Journal of Power Sources* **106** (2002) 160-166.

[57] R. J. Gorte, and J. M. vohs, "Novel SOFC Andoes for the direct Electrochemical Oxidation of Hydrocarbons." *Journal of Catalysis* **216** (2003) 477-486.

[58] A. T. Hunt, W. B. Carter, and J. K. Cochran, "Combustion Chemical-Vapor-Deposition - A Novel Thin-Film Deposition Technique." *Applied Physics Letters* **63** (1993) 266-268.

[59] A. Gupta, G. Koren, E. A. Giess, N. R. Moore, E. J. M. Osullivan, and E. I. Cooper, "$Y_1Ba_2Cu_3O_7$-Delta Thin-Films Grown by A Simple Spray Deposition Technique." *Applied Physics Letters* **52** (1988) 163-165.

[60] M. Koguchi, Y. Matsuda, E. Kinoshita, and K. Hirabayashi, "Preparation of $YBa_2Cu_3O_x$ Thin-Film by Flame Pyrolysis." *Japanese Journal of Applied Physics Part 2-Letters* **29** (1990) L33-L35.

[61] J. McHale, R. W. Schaeffer, A. Kebede, J. Macho, and R. E. Salomon, "Preparation of High-Tc Oxide-Films Via Flaming Solvent Spray." *Journal of Superconductivity* **5** (1992) 511-518.

[62] D. Matejka, B. Benko, J. Bielek, and M. Oresko, "Thermal-Conductivity of Plasma-Sprayed Coating of $ZrSiO_4$ Powder of Czechoslovak Production." *Kovove Materialy-Metallic Materials* **22** (1984) 121-128.

[63] L. M. Hanssen, K. A. Snail, W. A. Carrington, J. E. Butler, S. Kellogg, and D. B. Oakes, "Diamond and Non-Diamond Carbon Synthesis in An Oxygen Acetylene Flame." *Thin Solid Films* **196** (1991) 271-281.

[64] Y. Hirose, "Flame Synthesis of Diamond." *Carbon* **28** (1990) 776-776.

[65] A. J. Ghajar, and K. Y. Bang, "Parametric Effects on The Substrate-Temperature Profile In Oxy-Acetylene Flames." *Heat Transfer Engineering* **14** (1993) 48-59.

[66] W. A. Yarbrough, "Vapor-Phase-Deposited Diamond - Problems and Potential." *Journal of the American Ceramic Society* **75** (1992) 3179-3200.

[67] B. Vukasinovic, S. Sundell, and M. Oljaca, "Closed Loop Controlled Deposition of $Ba_xSr_{1-x}TiO_3$ Thin Films in Spray Flames." *Surface Engineering* **19** (2003) 179-184.

[68] M. Oljaca, H. A. Luten, T. Tomov, S. Sundell, and A. Hunt, "Deposition of $Ba_xSr_{1-x}TiO_3$ in Atmospheric Pressure Flame: Combustion Monitoring and Optimisation of Thin Film Properties." *Surface Engineering* **19** (2003) 51-57.

[69] W. B. Carter, G. W. Book, T. A. Polley, D. W. Stollberg, and J. M. Hampikian, "Combustion Chemical Vapor Deposition of $CeO_2$ Film." *Thin Solid Films* **347** (1999) 25-30.

[70] T. J. Hwang, M. R. Hendrick, H. Shao, H. G. Hornis, and A. T. Hunt, "Combustion Chemical Vapor Deposition (CCVD) of $LaPO_4$ Monazite and Beta-Alumina on Alumina Fibers for Ceramic Matrix Composites." *Materials Science and Engineering A-Structural Materials Properties Microstructure and Processing* **244** (1998) 91-96.

[71] S. S. Shoup, S. Shanmugham, D. Cousins, A. T. Hunt, M. Paranthaman, A. Goyal, P. Martin, and D. M. Kroeger, "Low-Cost Combustion Chemical Vapor Deposition of Epitaxial Buffer layers and Superconductors." *Ieee Transactions on Applied Superconductivity* **9** (1999) 2426-2429.

[72] M. J. Davis, G. Benito, D. W. Sheel, and M. E. Pemble, "Growth of Thin Films of Molybdenum and Tungsten Oxides by Combustion CVD Using Aqueous Precursor Solutions." *Chemical Vapor Deposition* **10** (2004) 29-34.

[73] T. A. Polley, and W. B. Carter, "Zone Model for Zinc Oxide Deposited by Combustion Chemical Vapor Deposition." *Thin Solid Films* **384** (2001) 177-184.

[74] T. A. Polley, W. B. Carter, and D. B. Poker, "Deposition of Zinc Oxide Thin Films by Combustion CVD." *Thin Solid Films* **357** (1999) 132-136.

[75] G. W. Book, W. B. Carter, T. A. Polley, and K. J. Kozaczek, "Preparation of $YBa_2Cu_3O_x$ Superconducting Thin Films via Combustion Chemical Vapor Deposition." *Thin Solid Films* **287** (1996) 32-35.

[76] M. R. Hendrick, J. M. Hampikian, and W. B. Carter, "Alumina Coatings Applied via Combustion Chemical Vapor Deposition and Their Effects on the Oxidation of A Ni-base Chromia Former." *Journal of The Electrochemical Society* **145** (1998) 3986-3994.

[77] B. C. Valek, and J. M. Hampikian, "Silica Thin Films Applied to Ni-20Cr Alloy via Combustion Chemical Vapor Deposition." *Surface & Coatings Technology* **94-5** (1997) 13-20.

[78] D. W. Stollberg, W. B. Carter, and J. M. Hampikian, "Combustion CVD of Magnesium Spinel and Nickel Spinel." *Surface & Coatings Technology* **94-5** (1997) 137-143.

[79] J. M. Hampikian, and W. B. Carter, "The Combustion Chemical Vapor Deposition of High Temperature Materials." *Materials Science and Engineering A-Structural Materials Properties Microstructure and Processing* **267** (1999) 7-18.

[80] M. Oljaca, Y. Xing, C. Lovelace, S. Shanmugham, and A. Hunt, "Flame Synthesis of Nanopowders via Combustion Chemical Vapor Deposition." *Journal of Materials Science Letters* **21** (2002) 621-626.

[81] M. Ohring, *The Material Science of Thin Films*. Academic Press: New York, 1992; p 195-234.

[82] H. Luth, *Surfaces and Interfaces of Solid Materials*. Springer: Germany, 1995; p 94-101.

[83] G. W. Book. Aerosol size Effects in Combustion Chemical Vapor Deposition. Georgia Institute of Technology, Atlanta, 1996.

[84] J. A. Thornton, "Influence of Apparatus Geometry and Deposition Conditions on Structure and Topography of Thick Sputtered Coatings." *Journal of Vacuum Science & Technology* **11** (1974) 666-670.

[85] B. A. Movchan, and A. V. Demchish, "Study of Structure and Properties of Thick Vacuum Condensates of Nickel, Titanium, Tungsten, Aluminium Oxide and Zirconium Dioxide." *Physics of Metals and Metallography-Ussr* **28** (1969) 653-660.

[86] C. Xia, and M. Liu, "Novel Cathodes for Low-Temperature Solid Oxide Fuel Cells." *Advanced Materials* **14** (2002) 521-523.

[87] J. P. P. Huijsmans, F. P. F. van Berkel, and G. M. Christie, "Intermediate Temperature SOFC - A Promise for the 21st Century." *Journal of Power Sources* **71** (1998) 107-110.

[88] Y. Kim, S. Yoon, and H. Kim, "Ferroelectric Properties of Lead Titanate Films Deposited by Low-Pressure Chemical Vapor-Deposition." *Journal of the Electrochemical Society* **139** (1992) 2559-2562.

[89] M. Balog, M. Schieber, M. Michman, and S. Patai, "Characteristics of Growth of Films of Zirconium and Hafnium Oxides ($ZrO_2$, $HfO_2$) by Thermal-Decomposition of Zirconium and Hafnium Beta-Diketonate Complexes in the Presence and Absence of Oxygen." *Journal of the Electrochemical Society* **126** (1979) 1203-1207.

[90] O. Unal, T. Mitchell, and A. Heuer, "Microstructures of $Y_2O_3$-Stabilized $ZrO_2$ Electron-Beam Physical Vapor-Deposition Coatings on Ni-Base Superalloys." *Journal of the American Ceramic Society* **77** (1994) 984-992.

[91] Y. Miyahara, "Characterization of Sputtered Yttria-Stabilized Zirconia Thin-Film and Its Application to A Metal-Insulator-Semiconductor Structure." *Journal of Applied Physics* **71** (1992) 2309-2314.

[92] A. Nicoll, A. Salito, and K. Honegger, "The Potential of Plasma Spraying for the Deposition of Coatings on SOFC Components." *Solid State Ionics* **52** (1992) 269-275.

[93] A. Nagata, and H. Okayama, "Characterization of Solid Oxide Fuel Cell Device Having A Three-Layer Film Structure Grown by RF Magnetron sputtering." *Vacuum* **66** (2002) 523-529.

[94] Y. S. Lin, L. G. J. Dehaart, K. J. Devries, and A. J. Burggraaf, "A Kinetic-Study of the Electrochemical Vapor-Deposition of Solid Oxide Electrolyte Films on Porous Substrates." *Journal of the Electrochemical Society* **137** (1990) 3960-3966.

[95] K.-W. Chour, J. Chen, and R. Xu, "Metal-Organic Vapor Deposition of YSZ Electrolyte Layers for Solid Oxide Fuel Cell Applications." *Thin Solid Films* **304** (1997) 106-112.

[96] K. L. Choy, S. Charojrochkul, and B. C. H. Steele, "Fabrication of Cathode for Solid Oxide Fuel Cells Using Flame Assisted Vapor Deposition Technique." *Solid State Ionics* **96** (1997) 49-54.

[97] S. Charojrochkul, K. L. Choy, and B. C. H. Steele, "Cathode/Electrolyte Systems for Solid Oxide Fuel Cells Fabricated Using Flame Assisted Vapor Deposition Technique." *Solid State Ionics* **121** (1999) 107-113.

[98] Y. Liu, W. Rauch, and M. Liu In *Nano-Particles and Nanostructured Electrodes Fabricated by Combustion CVD*, Proceedings - Electrochemical Society, 2003; 2003; pp 205-214.

[99] Y. Liu, S. Zha, and M. Liu, "Novel Nanostructured Electrodes for Solid Oxide Fuel Cells Fabricated by Combustion Chemical Vapor Deposition (CVD)." *Advanced Materials* **16** (2004) 256-260.

[100] H. O. Pierson, "Handbook of Chemical Vapor Deposition (CVD)." (1992) 32.

[101] M. Liu, and Z. Wu, "Significance of Interfaces in Solid-State Cells with Porous Electrodes of Mixed Ionic-Electronic Conductors." *Solid State Ionics* **107** (1998) 105-110.

[102] H. Y. Tu, Y. Takeda, N. Imanishi, and O. Yamamoto, "$Ln_{0.4}Sr_{0.6}Co_{0.8}Fe_{0.2}O_{3-d}$ (Ln=La, Pr, Nd, Sm, Gd) for Solid Oxide Fuel Cell Cathodes." *Solid State Ionics* **117** (1999) 277-281.

[103] L. Qiu, T. Ichikawa, A. Hirano, N. Imanishi, and Y. Takeda, "$Ln_{1-x}Sr_xCo_{1-y}Fe_yO_{3-d}$ (Ln=Pr, Nd, Gd; x=0.2, 0.3) for the Electrodes of Solid Oxide Fuel Cells." *Solid State Ionics* **158** (2003) 55-65.

[104] C. Xia, W. Rauch, W. Wellborn, and M. Liu, "Functionally Graded Cathodes for Honeycomb Solid Oxide Fuel Cells." *Electrochemical and Solid-State Letters* **5** (2002) A217-A220.

[105] N. Q. Minh, "Ceramic Fuel-Cells." *Journal of the American Ceramic Society* **76** (1993) 563-588.

[106] C. Xia, and M. Liu, "A Simple and Cost-Effective Approach to Fabrication of Dense Ceramic Membranes on Porous Substrates." *Journal of the American Ceramic Society* **84** (2001) 1903-1905.

[107] T. Suzuki, I. Kosacki, and H. U. Anderson, "Microstructure-Electrical Conductivity Relationships in Nanocrystalline Ceria Thin Films." *Solid State Ionics* **151** (2002) 111-121.

[108] B. C. H. Steele, "Appraisal of $Ce_{1-y}Gd_yO_{2-y/2}$ Electrolytes for IT-SOFC Operation at 500 DegC." *Solid State Ionics* **129** (2000) 95-110.

[109] M. Dokiya, "SOFC System and Technology." *Solid State Ionics* **152-153** (2002) 383-392.

[110] E. Ivers-Tiffee, A. Weber, and D. Herbstritt, "Materials and Technologies for SOFC-Components." *Journal of the European Ceramic Society* **21** (2001) 1805-1811.

[111] C. W. Tanner, K.-Z. Fung, and A. V. Virkar, "The Effect of Porous Composite Electrode Structure on Solid Oxide Fuel Cell Performance. I. Theoretical Analysis." *Journal of the Electrochemical Society* **144** (1997) 21-30.

[112] S. Park, J. M. Vohs, and R. J. Gorte, "Direct Oxidation of Hydrocarbons in A Solid-Oxide Fuel Cell." *Nature* **404** (2000) 265-267.

[113] E. P. Murray, T. Tsai, and S. A. Barnett, "A Direct-Methane Fuel Cell with A Ceria-Based Anode." *Nature* **400** (1999) 649-651.

[114] E. Perry Murray, and S. A. Barnett, "$(La,Sr)MnO_3$-$(Ce,Gd)O_{2-x}$ Composite Cathodes for Solid Oxide Fuel Cells." *Solid State Ionics* **143** (2001) 265-273.

[115] K. Choy, W. Bai, S. Charojrochkul, and B. C. H. Steele, "The Development of Intermediate-Temperature Solid Oxide Fuel Cells for the Next Millennium." *Journal of Power Sources* **71** (1998) 361-369.

[116] M. Liu, and H. Hu, "Effect of Interfacial Resistance on Determination of Transport Properties of Mixed Conducting Electrolytes." *Journal of the Electrochemical Society* **143** (1996) L109-L112.

[117] T. Kenjo, and M. Nishiya, "$LaMnO_3$ Air Cathodes Containing $ZrO_2$ Electrolyte for High-Temperature Solid Oxide Fuel-Cells." *Solid State Ionics* **57** (1992) 295-302.

[118] E. P. Murray, T. Tsai, and S. A. Barnett, "Oxygen Transfer Processes in $(La,Sr)MnO_3/Y_2O_3$-Stabilized $ZrO_2$ Cathodes: An Impedance Spectroscopy Study." *Solid State Ionics* **110** (1998) 235-243.

[119] S. P. Jiang, Y. J. Leng, S. H. Chan, and K. A. Khor, "Development of $(La,Sr)MnO_3$-Based Cathodes for Intermediate Temperature Solid Oxide Fuel Cells." *Electrochemical and Solid-State Letters* **6** (2003) A67-A70.

[120] S. F. Corbin, L. X. Zhao-Jie, H. Henein, and P. S. Apte, "Functionally Graded Metal/Ceramic Composites by Tape Casting, Lamination, and Infiltration." *Materials Science & Engineering, A: Structural Materials: Properties, Microstructure and Processing* **A262** (1999) 192-203.

[121] M. P. Dariel, L. Levin, and N. Frage, "Graded Ceramic Preforms: Various Processing Approaches." *Materials Chemistry and Physics* **67** (2001) 192-198.

[122] K. Maca, P. Dobsak, and A. R. Boccaccini, "Fabrication of Graded Porous Ceramics Using Alumina-Carbon Powder Mixtures." *Ceramics International* **27** (2001) 577-584.

[123] Y. Z. Yang, J. M. Tian, J. T. Tian, Z. Q. Chen, X. J. Deng, and D. H. Zhang, "Preparation of Graded Porous Titanium Coatings on Titanium Implant Materials by Plasma Spraying." *Journal of Biomedical Materials Research* **52** (2000) 333-337.

[124] A. Tampieri, G. Celotti, S. Sprio, A. Delcogliano, and S. Franzese, "Porosity-Graded Hydroxyapatite Ceramics to Replace Natural Bone." *Biomaterials* **22** (2001) 1365-1370.

[125] N. T. Hart, N. P. Brandon, M. J. Day, and J. E. Shemilt, "Functionally Graded Cathodes for Solid Oxide Fuel Cells." *Journal of Materials Science* **36** (2001) 1077-1085.

[126] N. T. Hart, N. P. Brandon, M. J. Day, and N. Lapena-Rey, "Functionally Graded Composite Cathodes for Solid Oxide Fuel Cells." *Journal of Power Sources* **106** (2002) 42-50.

[127] S. P. Simner, J. F. Bonnett, N. L. Canfield, K. D. Meinhardt, J. P. Shelton, V. L. Sprenkle, and J. W. Stevenson, "Development of Lanthanum Ferrite SOFC Cathodes." *Journal of Power Sources* **113** (2003) 1-10.

[128] C. Xia, and M. Liu, "Microstructures, Conductivities, and Electrochemical Properties of $Ce_{0.9}Gd_{0.1}O_2$ and GDC-Ni Anodes for Low-Temperature SOFCs." *Solid State Ionics* **152-153** (2002) 423-430.

[129] Y. Liu, W. Rauch, S. Zha, and M. Liu, "Fabrication of $Sm_{0.5}Sr_{0.5}CoO_{3-d}$-$Sm_{0.1}Ce0.9O_{2-d}$ Cathodes for Solid Oxide Fuel Cells Using Combustion CVD." *Solid State Ionics* **166** (2004) 261-268.

[130] Y. Liu, J. Dong, and M. Liu, "Well-Aligned "Nano-Box-Beams" of $SnO_2$." *Advanced Materials* **16** (2004) 353-356.

[131] S. Zha, W. Rauch, and M. Liu, "Ni-$Ce_{0.9}Gd_{0.1}O_{1.95}$ Anode for GDC Electrolyte-Based Low-Temperature SOFCs." *Solid State Ionics* **166** (2004) 241-250.

[132] O. Costa-Nunes, J. M. Vohs, and R. J. Gorte, "A Study of Direct-Conversion SOFC with N-Butane at Higher Fuel Utilization." *Journal of The Electrochemical Society* **150** (2003) A858-A863.

[133] G. L. Bertrand, G. Caboche, and L. C. Dufour, "Low-Pressure-MOCVD $LaMnO_{3+-d}$ Very Thin Films on YSZ (100) Optimized for Studies of the Triple Phase Boundary." *Solid State Ionics* **129** (2000) 219-235.

[134] K. Hayashi, O. Yamamoto, Y. Nishigaki, and H. Minoura, "Sputtered $La_{0.5}Sr_{0.5}MnO_3$-Yttria Stabilized Zirconia Composite Film Electrodes for SOFC." *Solid State Ionics* **98** (1997) 49-55.

[135] H. B. Wang, J. F. Gao, D. K. Peng, and G. Y. Meng, "Plasma Deposition of $La_{0.8}Sr_{0.2}MnO_3$ Thin Films on Yttria-Stabilized Zirconia from Aerosol Precursor." *Materials Chemistry and Physics* **72** (2001) 297-300.

[136] L. G. Coccia, G. C. Tyrrell, J. A. Kilner, D. Waller, R. J. Chater, and I. W. Boyd, "Pulsed Laser Deposition of Novel Materials for Thin Film Solid Oxide Fuel Cell Applications: $Ce_{0.9}Gd_{0.1}O_{1.95}$, $La_{0.7}Sr_{0.3}CoO_y$ and $La_{0.7}Sr_{0.3}Co_{0.2}Fe_{0.8}O_y$." *Applied Surface Science* **96-98** (1996) 795-801.

[137] Y. Liu, S. Zha, and M. Liu, "Nanocomposite Electrodes Fabricated by A Particle-Solution Spraying Process for Low-Temperature SOFCs." *Chemistry of Materials* **16** (2004) 3502-3506.

[138] W. J. Lackey, W. B. Carter, J. A. Hanigofsky, D. N. Hill, E. K. Barefield, G. Neumeier, D. F. Obrien, M. J. Shapiro, J. R. Thompson, A. J. Green, T. S. Moss, R. A. Jake, and K. R. Efferson, "Rapid Chemical Vapor-Deposition Of Superconducting $YBa_2Cu_3O_x$." *Applied Physics Letters* **56** (1990) 1175-1177.

[139] M. R. Zachariah, and S. Huzarewicz, "Aerosol Processing of YBaCuO Superconductors in A Flame Reactor." *Journal of Materials Research* **6** (1991) 264-269.

[140] B. D. Merkle, R. N. Kniseley, F. A. Schmidt, and I. E. Anderson, "Superconducting $YBa_2Cu_3O_x$ Particulate Produced by Total Consumption Burner Processing." *Materials Science And Engineering A-Structural Materials Properties Microstructure And Processing* **124** (1990) 31-38.

[141] C. D. Wu, A. Hu, L. Zhang, and W. B. Lin, "Homochiral Porous Metal-Organic Framework for Highly Enantioselective Heterogeneous Asymmetric Catalysis." *Journal of the American Chemical Society* **127** (2005) 8940-8941.

[142] M. Arkas, D. Tsiourvas, and C. M. Paleos, "Organosilicon Dendritic Networks in Porous Ceramics for Water Purification." *Chemistry of Materials* **17** (2005) 3439-3444.

[143] S. Uemiya, T. Matsuda, and E. Kikuchi, "Hydrogen Permeable Palladium Silver Alloy Membrane Supported On Porous Ceramics." *Journal of Membrane Science* **56** (1991) 315-325.

[144] Y. Liu, E. Koep, and M. Liu, "A Highly Sensitive and Fast-Responding $SnO_2$ Sensor Fabricated by Combustion Chemical Vapor Deposition." *Chemistry of Materials* **17** (2005) 3997-4000.

[145] B. B. Lakshmi, C. J. Patrissi, and C. R. Martin, "Sol-Gel Template Synthesis of Semiconductor Oxide Micro- and Nanostructures." *Chemistry of Materials* **9** (1997) 2544-2550.

[146] J. H. He, T. Kunitake, and T. Watanabe, "Porous and Nonporous Ag Nanostructures Fabricated Using Cellulose Fiber as A Template." *Chemical Communications* (2005) 795-796.

[147] J. S. Jie, G. Z. Wang, Q. T. Wang, Y. M. Chen, X. H. Han, X. P. Wang, and J. G. Hou, "Synthesis and Characterization of Aligned ZnO Nanorods on Porous Aluminum Oxide Template." *Journal of Physical Chemistry B* **108** (2004) 11976-11980.

[148] S. Maschio, A. Bachiorrini, E. Lucchini, and S. Bruckner, "Synthesis, Sintering and Thermal Expansion of Porous Low Expansion Ceramics." *Journal of the European Ceramic Society* **24** (2004) 3535-3540.

[149] J. J. Haslam, A. Q. Pham, B. W. Chung, J. F. DiCarlo, and R. S. Glass, "Effects of the Use of Pore Formers on Performance of An Aanode Supported Solid Oxide Fuel Cell." *Journal of the American Ceramic Society* **88** (2005) 513-518.

[150] C. S. Kong, D. Y. Kim, H. K. Lee, Y. G. Shul, and T. H. Lee, "Influence of Pore-Size Distribution of Diffusion Layer on Mass-Transport Problems of Proton Exchange Membrane Fuel Cells." *Journal of Power Sources* **108** (2002) 185-191.

[151] N. Koc, M. Timucin, and F. Korkusuz, "Fabrication and Characterization of Porous Tricalcium Phosphate Ceramics." *Ceramics International* **30** (2004) 205-211.

[152] E. S. Toberer, A. Joshi, and R. Seshadri, "Template-Free Routes to Macroporous Monoliths of Nickel and Iron Oxides: Toward Porous Metals and Conformally Coated Pore Walls." *Chemistry of Materials* **17** (2005) 2142-2147.

[153] E. S. Toberer, J. C. Weaver, K. Ramesha, and R. Seshadri, "Macroporous Monoliths of Functional Perovskite Materials Through Assisted Metathesis." *Chemistry of Materials* **16** (2004) 2194-2200.

[154] M. Panda, R. Seshadri, and J. Gopalakrishnan, "Preparation of $PbZrO_3/ASO_4$ Composites (A = Ca, Sr, Ba) and $PbZrO_3$ by Metathetic Reactions in the Solid State: Metathetic Exchange of Divalent Species." *Chemistry of Materials* **15** (2003) 1554-1559.

[155] M. Panda, M. Rajamathi, and R. Seshadri, "A Template-Free, Combustion-Chemical Route to Macroporous Nickel Monoliths Displaying a Hierarchy of Pore Sizes." *Chemistry of Materials* **14** (2002) 4762-4767.

[156] M. Rajamathi, S. Thimmaiah, P. E. D. Morgan, and R. Seshadri, "Macroporous Materials from Crystalline Single-Source Precursors through Decomposition Followed by Selective Leaching." *Journal of Materials Chemistry* **11** (2001) 2489-2492.

[157] I. Barin, *Thermochemical Data of Pure Substances*. VCH: New York, 1995.

[158] S. de Souza, S. J. Visco, and L. C. De Jonghe, "Thin-Film Solid Oxide Fuel Cell with High Performance at Low-Temperature." *Solid State Ionics* **98** (1997) 57-61.

[159] S. P. Jiang, S. Zhang, Y. D. Zhen, and W. Wang, "Fabrication and Performance of Impregnated Ni Anodes of Solid Oxide Fuel Cells." *Journal of the American Ceramic Society* **88** (2005) 1779-1785.

[160] Y. Matsuzaki, and I. Yasuda, "Electrochemical Properties of Reduced-Temperature SOFCs with Mixed Ionic-Electronic Conductors in Electrodes and/or Interlayers." *Solid State Ionics* **152-153** (2002) 463-468.

[161] S. Zha, Y. Zhang, and M. Liu, "Functionally Graded Cathodes Fabricated by Sol-Gel/Slurry Coating for Honeycomb SOFCs." *Solid State Ionics* **176** (2004) 25-31.

[162] Y. Liu, C. Compson, and M. Liu, "Nanostructured and Functionally Graded Cathodes for Intermediate Temperature Solid Oxide Fuel Cells." *Journal of Power Sources* **138** (2004) 194-198.

[163] A. Tiburcio-Silver, and A. Sanchez-Juarez, "$SnO_2$:Ga Thin Films as Oxygen Gas Sensor." *Materials Science & Engineering, B: Solid-State Materials for Advanced Technology* **B110** (2004) 268-271.

[164] J. H. Yu, and G. M. Choi, "Selective CO Gas Detection of CuO- and ZnO-Doped $SnO_2$ Gas Sensor." *Sensors and Actuators B-Chemical* **75** (2001) 56-61.

[165] A. Salehi, "Selectivity Enhancement of Indium-Doped $SnO_2$ Gas Sensors." *Thin Solid Films* **416** (2002) 260-263.

[166] C. Bittencourt, E. Llobet, P. Ivanov, X. Correig, X. Vilanova, J. Brezmes, J. Hubalek, K. Malysz, J. J. Pireaux, and J. Calderer, "Influence of the Doping Method on the Sensitivity of Pt-Doped Screen-Printed $SnO_2$ Sensors." *Sensors and Actuators B-Chemical* **97** (2004) 67-73.

[167] M. SchweizerBerberich, J. G. Zheng, U. Weimar, W. Gopel, N. Barsan, E. Pentia, and A. Tomescu, "The Effect of Pt and Pd Surface Doping on the Response of Nanocrystalline Tin Dioxide Gas Sensors to CO." *Sensors and Actuators B-Chemical* **31** (1996) 71-75.

[168] B. Y. Wei, M. C. Hsu, P. G. Su, H. M. Lin, R. J. Wu, and H. J. Lai, "A Novel $SnO_2$ Gas Sensor Doped with Carbon Nanotubes Operating at Room Temperature." *Sensors and Actuators B-Chemical* **101** (2004) 81-89.

[169] R. Banerjee, and D. Das, "Properties of Tin Oxide-Films Prepared By Reactive Electron-Beam Evaporation." *Thin Solid Films* **149** (1987) 291-301.

[170] M. H. M. Reddy, and A. N. Chandorkar, "Response Study of Electron-Beam Evaporated Thin-Film Tin Oxide Gas Sensors." *Sensors and Actuators B-Chemical* **9** (1992) 1-8.

[171] Y. S. Choe, "New Gas Sensing Mechanism for $SnO_2$ Thin-Film Gas Sensors Fabricated by Using Dual Ion Beam Sputtering." *Sensors and Actuators B-Chemical* **77** (2001) 200-208.

[172] B. K. Min, and S. D. Choi, "$SnO_2$ Thin Film Gas Sensor Fabricated by Ion Beam Deposition." *Sensors and Actuators B-Chemical* **98** (2004) 239-246.

[173] N. S. Murty, and S. R. Jawalekar, "Effect of Deposition Parameters on the Microstructure of Chemically Vapour-Deposited $SnO_2$ Films." *Thin Solid Films* **102** (1983) 283-289.

[174] C. Nayral, T. Ould-Ely, A. Maisonnat, B. Chaudret, P. Fau, L. Lescouzeres, and A. Peyre-Lavigne, "A Novel Mechanism for the Synthesis of Tin Tin Oxide Nanoparticles of Low Size Dispersion and of Nanostructured $SnO_2$ for the Sensitive Layers of Gas Sensors." *Advanced Materials* **11** (1999) 61-63.

[175] A. Rosental, A. Tarre, A. Gerst, T. Uustare, and V. Sammelselg, "Atomic-Layer Chemical Vapor Deposition of $SnO_2$ for Gas-Sensing Applications." *Sensors and Actuators B-Chemical* **77** (2001) 297-300.

[176] R. Rella, A. Serra, P. Siciliano, L. Vasanelli, G. De, A. Licciulli, and A. Quirini, "Tin Oxide-Based Gas Sensors Prepared by the Sol-Gel Process." *Sensors and Actuators B-Chemical* **44** (1997) 462-467.

[177] I. T. Weber, R. Andrade, E. R. Leite, and E. Longo, "A Study of the $SnO_2$ Center Dot $Nb_2O_5$ System for An Ethanol Vapour Sensor: A Correlation between Microstructure and Sensor Performance." *Sensors and Actuators B-Chemical* **72** (2001) 180-183.

[178] J. J. Ho, Y. K. Fang, K. H. Wu, W. T. Hsieh, C. H. Chen, G. S. Chen, M. S. Ju, J. J. Lin, and S. B. Hwang, "High Sensitivity Ethanol Gas Sensor Integrated with A Solid-State Heater and Thermal Isolation Improvement Structure for Iegal Drink-Drive Limit Detecting." *Sensors and Actuators B-Chemical* **50** (1998) 227-233.

[179] Y. W. Mo, Y. Okawa, T. Nakai, M. Tajima, and K. Natukawa, "Preparation of $SnO_2$ Films with High Sensitivity and Selectivity to $C_2H_5OH$ by Oxygen Radical Assisted Electron Beam Evaporation for Micro-Machined Gas Sensors." *Thin Solid Films* **416** (2002) 248-253.

[180] Y. Wang, X. H. Wu, Y. F. Li, and Z. L. Zhou, "Mesostructured $SnO_2$ as Sensing Material for Gas Sensors." *Solid-State Electronics* **48** (2004) 627-632.

[181] K. Ihokura, and J. Watson, *The Stannic Oxide Gas Sensor: Principles and Applications*. CRC Press, Inc.: Boca Raton, Florida, 1994.

[182] P. Ivanov, E. Llobet, X. Vilanova, J. Brezmes, J. Hubalek, and X. Correig, "Development of High Sensitivity Ethanol Gas Sensors Based on Pt-Doped $SnO_2$ Surfaces." *Sensors and Actuators B-Chemical* **99** (2004) 201-206.

[183] M. Radecka, K. Zakrzewska, and M. Rekas, "$SnO_2$-$TiO_2$ Solid Solutions for Gas Sensors." *Sensors and Actuators B-Chemical* **47** (1998) 194-204.

[184] N. Barsan, and U. Weimar, "Conduction Model of Metal Oxide Gas Sensors." *Journal of Electroceramics* **7** (2001) 143-167.

[185] D. Kohl, "Surface Processes in the Detection of Reducing Gases with $SnO_2$-Based Devices." *Sensors and Actuators* **18** (1989) 71-113.

[186] X. J. Huang, J. H. Liu, D. L. Shao, Z. X. Pi, and Z. L. Yu, "Rectangular Mode of Operation for Detecting Pesticide Residue by Using A Single $SnO_2$-Based Gas Sensor." *Sensors and Actuators B-Chemical* **96** (2003) 630-635.

[187] P. Grosse, F. J. Schmitte, G. Frank, and H. Kostlin, "Preparation and Growth of $SnO_2$ Thin-Films and Their Optical and Electrical-Properties." *Thin Solid Films* **90** (1982) 309-315.

[188] K. L. Chopra, S. Major, and D. K. Pandya, "Transparent Conductors - A Status Review." *Thin Solid Films* **102** (1983) 1-46.

[189] Y. S. He, J. C. Campbell, R. C. Murphy, M. F. Arendt, and J. S. Swinnea, "Electrical and Optical Characterization of $SbSnO_2$." *Journal of Materials Research* **8** (1993) 3131-3134.

[190] G. J. Li, X. H. Zhang, and S. Kawi, "Relationships between Sensitivity, Catalytic Activity, and Surface Areas of $SnO_2$ Gas Sensors." *Sensors and Actuators, B: Chemical* **B60** (1999) 64-70.

[191] G. Zhang, and M. Liu, "Effect of Particle Size and Dopant on Properties of $SnO_2$-Based Gas Sensors." *Sensors and Actuators, B: Chemical* **B69** (2000) 144-152.

[192] Y. Idota, T. Kubota, A. Matsufuji, Y. Maekawa, and T. Miyasaka, "Tin-Based Amorphous Oxide: A High-Capacity Lithium-Ion-Storage Material." *Science* **276** (1997) 1395-1397.

[193] F. Chen, Z. Shi, and M. Liu, "Preparation of Mesoporous $SnO_2$-$SiO_2$ Composite as Electrodes for Lithium Batteries." *Chemical Communications* (2000) 2095-2096.

[194] Z. Peng, Z. Shi, and M. Liu, "Mesoporous Sn-$TiO_2$ Composite Electrodes for Lithium Batteries." *Chemical Communications (Cambridge)* (2000) 2125-2126.

[195] S. Ferrere, A. Zaban, and B. A. Gregg, "Dye Sensitization of Nanocrystalline Tin Oxide by Perylene Derivatives." *Journal of Physical Chemistry B* **101** (1997) 4490-4493.

[196] S. Visitserngtrakul, K. Kirtikara, N. Thavarungkul, C. Koompai, P. Monthachitara, and C. M. Lampert, "Pilot Plant Production of Black Chrome in Thailand - from Science to Technology." *Solar Energy Materials* **21** (1990) 1-16.

[197] Y. N. Xia, P. D. Yang, Y. G. Sun, Y. Y. Wu, B. Mayers, B. Gates, Y. D. Yin, F. Kim, and Y. Q. Yan, "One-Dimensional Nanostructures: Synthesis, Characterization, and Applications." *Advanced Materials* **15** (2003) 353-389.

[198] X. G. Peng, L. Manna, W. D. Yang, J. Wickham, E. Scher, A. Kadavanich, and A. P. Alivisatos, "Shape Control of CdSe Nanocrystals." *Nature* **404** (2000) 59-61.

[199] J. D. Holmes, K. P. Johnston, R. C. Doty, and B. A. Korgel, "Control of Thickness and Orientation of Solution-Grown Silicon Nanowires." *Science* **287** (2000) 1471-1473.

[200] X. F. Duan, J. F. Wang, and C. M. Lieber, "Synthesis and Optical Properties of Gallium Arsenide Nanowires." *Applied Physics Letters* **76** (2000) 1116-1118.

[201] C. P. Collier, E. W. Wong, M. Belohradsky, F. M. Raymo, J. F. Stoddart, P. J. Kuekes, R. S. Williams, and J. R. Heath, "Electronically Configurable Molecular-Based Logic Gates." *Science* **285** (1999) 391-394.

[202] A. P. Alivisatos, "Semiconductor Clusters, Nanocrystals, and Quantum Dots." *Science* **271** (1996) 933-937.

[203] E. Comini, G. Faglia, G. Sberveglieri, Z. W. Pan, and Z. L. Wang, "Stable and Highly Sensitive Gas Sensors Based on Semiconducting Oxide Nanobelts." *Applied Physics Letters* **81** (2002) 1869-1871.

[204] M. Law, H. Kind, B. Messer, F. Kim, and P. D. Yang, "Photochemical Sensing of $NO_2$ with $SnO_2$ Nanoribbon Nanosensors at Room Temperature." *Angewandte Chemie-International Edition* **41** (2002) 2405-2408.

[205] D. F. Zhang, L. D. Sun, J. L. Yin, and C. H. Yan, "Low-Temperature Fabrication of Highly Crystalline $SnO_2$ Nanorods." *Advanced Materials* **15** (2003) 1022-1025.

[206] Y. Q. Chen, X. F. Cui, K. Zhang, D. Y. Pan, S. Y. Zhang, B. Wang, and J. G. Hou, "Bulk-Quantity Synthesis and Self-Catalytic VLS Growth of $SnO_2$ Nanowires by Lower-Temperature Evaporation." *Chemical Physics Letters* **369** (2003) 16-20.

[207] Z. R. Dai, J. L. Gole, J. D. Stout, and Z. L. Wang, "Tin Oxide Nanowires, Nanoribbons, and Nanotubes." *Journal of Physical Chemistry B* **106** (2002) 1274-1279.

[208] Y. K. Liu, C. L. Zheng, W. Z. Wang, C. R. Yin, and G. H. Wang, "Synthesis and Characterization of Rutile $SnO_2$ Nanorods." *Advanced Materials* **13** (2001) 1883-1887.

[209] Z. R. Dai, Z. W. Pan, and Z. L. Wang, "Ultra-Long Single Crystalline Nanoribbons of Tin Oxide." *Solid State Communications* **118** (2001) 351-354.

[210] Z. W. Pan, Z. R. Dai, and Z. L. Wang, "Nanobelts of Semiconducting Oxides." *Science* **291** (2001) 1947-1949.

[211] X. S. Peng, L. D. Zhang, G. W. Meng, Y. T. Tian, Y. Lin, B. Y. Geng, and S. H. Sun, "Micro-Raman and Infrared Properties of $SnO_2$ Nanobelts Synthesized from Sn and $SiO_2$ Powders." *Journal of Applied Physics* **93** (2003) 1760-1763.

[212] L. Abello, B. Bochu, A. Gaskov, S. Koudryavtseva, G. Lucazeau, and M. Roumyantseva, "Structural Characterization of Nanocrystalline $SnO_2$ by X-Ray and Raman Spectroscopy." *Journal of Solid State Chemistry* **135** (1998) 78-85.

[213] A. Dieguez, A. Romano-Rodriguez, A. Vila, and J. R. Morante, "The Complete Raman Spectrum of Nanometric $SnO_2$ Particles." *Journal of Applied Physics* **90** (2001) 1550-1557.

[214] P. S. Peercy, and B. Morosin, "Pressure and Temperature Dependences of Raman-Active Phonons in $SnO_2$." *Physical Review B* **7** (1973) 2779-2786.

[215] R. S. Wagner, and W. C. Ellis, "Vapor-Liquid-Solid Mechanism of Single Crystal Growth (New Method Growth Catalysis from Impurity Whisker Epitaxial + Large Crystals Si E)." *Applied Physics Letters* **4** (1964) 89-90.

[216] M. Nagano, "Growth of $SnO_2$ Whiskers by VIS Mechanism." *Journal of Crystal Growth* **66** (1984) 377-379.

[217] Z. Konya In *Carbon Filaments and Nanotubes: Common Origins, Differing Applications?* Boston, MA, 2001; L. P. Biro,C. A. Bernardo,G. G. Tibbetts, and P. H. Lambin, Eds. Kluwer: Boston, MA, 2001; p 85.

[218] P. Verardi, N. Nastase, C. Gherasim, C. Ghica, M. Dinescu, R. Dinu, and C. Flueraru, "Scanning Force Microscopy and Electron Microscopy Studies of Pulsed Laser Deposited ZnO Thin Films: Application to the Bulk Acoustic Waves (BAW) Devices." *Journal of Crystal Growth* **197** (1999) 523-528.

[219] T. L. Yang, D. H. Zhang, J. Ma, H. L. Ma, and Y. Chen, "Transparent Conducting ZnO: Al Films Deposited on Organic Substrates Deposited by R.F. Magnetron-Sputtering." *Thin Solid Films* **326** (1998) 60-62.

[220] E. A. Meulenkamp, "Synthesis and Growth of ZnO Nanoparticles." *Journal of Physical Chemistry B* **102** (1998) 5566-5572.

[221] J. F. Cordaro, Y. Shim, and J. E. May, "Bulk Electron Traps In Zinc-Oxide Varistors." *Journal of Applied Physics* **60** (1986) 4186-4190.

[222] L. F. Dong, J. Jiao, D. W. Tuggle, J. M. Petty, S. A. Elliff, and M. Coulter, "ZnO Nanowires Formed on Tungsten Substrates and Their Electron Field Emission Properties." *Applied Physics Letters* **82** (2003) 1096-1098.

[223] M. H. Huang, S. Mao, H. Feick, H. Q. Yan, Y. Y. Wu, H. Kind, E. Weber, R. Russo, and P. D. Yang, "Room-Temperature Ultraviolet Nanowire Nanolasers." *Science* **292** (2001) 1897-1899.

[224] Z. K. Tang, G. K. L. Wong, P. Yu, M. Kawasaki, A. Ohtomo, H. Koinuma, and Y. Segawa, "Room-Temperature Ultraviolet Laser Emission from Self-Assembled ZnO Microcrystallite Thin Films." *Applied Physics Letters* **72** (1998) 3270-3272.

[225] H. Zhang, X. Y. Ma, J. Xu, J. J. Niu, and D. R. Yang, "Arrays of ZnO Nanowires Fabricated by A Simple Chemical Solution Route." *Nanotechnology* **14** (2003) 423-426.

[226] B. B. Lakshmi, P. K. Dorhout, and C. R. Martin, "Sol-Gel Template Synthesis of Semiconductor Nanostructures." *Chemistry of Materials* **9** (1997) 857-862.

[227] B. Y. Geng, T. Xie, X. S. Peng, Y. Lin, X. Y. Yuan, G. W. Meng, and L. D. Zhang, "Large-Scale Synthesis of ZnO Nanowires Using A Low-Temperature Chemical Route and Their Photoluminescence Properties." *Applied Physics A-Materials Science & Processing* **77** (2003) 363-366.

[228] Q. X. Zhao, M. Willander, R. E. Morjan, Q. H. Hu, and E. E. B. Campbell, "Optical Recombination of ZnO Nanowires Grown on Sapphire and Si Substrates." *Applied Physics Letters* **83** (2003) 165-167.

[229] H. T. Ng, B. Chen, J. Li, J. E. Han, M. Meyyappan, J. Wu, S. X. Li, and E. E. Haller, "Optical Properties of Single-Crystalline ZnO Nanowires on M-Sapphire." *Applied Physics Letters* **82** (2003) 2023-2025.

[230] B. D. Yao, Y. F. Chan, and N. Wang, "Formation of ZnO Nanostructures by A Simple Way of Thermal Evaporation." *Applied Physics Letters* **81** (2002) 757-759.

[231] Y. B. Li, Y. Bando, T. Sato, and K. Kurashima, "ZnO Nanobelts Grown on Si Substrate." *Applied Physics Letters* **81** (2002) 144-146.

[232] Y. Li, G. W. Meng, L. D. Zhang, and F. Phillipp, "Ordered Semiconductor ZnO Nanowire Arrays and Their Photoluminescence Properties." *Applied Physics Letters* **76** (2000) 2011-2013.

[233] W. I. Park, D. H. Kim, S. W. Jung, and G. C. Yi, "Metalorganic Vapor-Phase Epitaxial Growth of Vertically Well-Aligned ZnO Nanorods." *Applied Physics Letters* **80** (2002) 4232-4234.

[234] J. J. Wu, and S. C. Liu, "Low-Temperature Growth of Well-Aligned ZnO Nanorods by Chemical Vapor Deposition." *Advanced Materials* **14** (2002) 215-218.

[235] Y. C. Kong, D. P. Yu, B. Zhang, W. Fang, and S. Q. Feng, "Ultraviolet-Emitting ZnO Nanowires Synthesized by A Physical Vapor Deposition Approach." *Applied Physics Letters* **78** (2001) 407-409.

[236] L. Vayssieres, "Growth of Arrayed Nanorods and Nanowires of ZnO from Aqueous Solutions." *Advanced Materials* **15** (2003) 464-466.

[237] L. E. Greene, M. Law, J. Goldberger, F. Kim, J. C. Johnson, Y. F. Zhang, R. J. Saykally, and P. D. Yang, "Low-Temperature Wafer-Scale Production of ZnO Nanowire Arrays." *Angewandte Chemie-International Edition* **42** (2003) 3031-3034.

[238] J. Q. Hu, Q. Li, N. B. Wong, C. S. Lee, and S. T. Lee, "Synthesis of Uniform Hexagonal Prismatic ZnO Whiskers." *Chemistry of Materials* **14** (2002) 1216-1219.

[239] R. Liu, A. A. Vertegel, E. W. Bohannan, T. A. Sorenson, and J. A. Switzer, "Epitaxial Electrodeposition of Zinc Oxide Nanopillars on Single-Crystal Gold." *Chemistry of Materials* **13** (2001) 508-512.

[240] R. Konenkamp, K. Boedecker, M. C. Lux-Steiner, M. Poschenrieder, F. Zenia, C. Levy-Clement, and S. Wagner, "Thin Film Semiconductor Deposition on Free-Standing ZnO Columns." *Applied Physics Letters* **77** (2000) 2575-2577.

[241] X. F. Duan, and C. M. Lieber, "General Synthesis of Compound Semiconductor Nanowires." *Advanced Materials* **12** (2000) 298-302.

[242] Y. Liu, and M. Liu, "Growth of Aligned Square-Shaped $SnO_2$ Tube Arrays." *Advanced Functional Materials* **15** (2005) 57-62.

[243] Y. K. Tseng, C. J. Huang, H. M. Cheng, I. N. Lin, K. S. Liu, and I. C. Chen, "Characterization and Field-Emission Properties of Needle-Like Zinc Oxide Nanowires Grown Vertically on Conductive Zinc Oxide Films." *Advanced Functional Materials* **13** (2003) 811-814.

[244] P. X. Gao, Y. Ding, and I. L. Wang, "Crystallographic Orientation-Aligned ZnO Nanorods Grown by A Tin Catalyst." *Nano Letters* **3** (2003) 1315-1320.

[245] P. D. Yang, H. Q. Yan, S. Mao, R. Russo, J. Johnson, R. Saykally, N. Morris, J. Pham, R. R. He, and H. J. Choi, "Controlled Growth of ZnO Nanowires and Their Optical Properties." *Advanced Functional Materials* **12** (2002) 323-331.

[246] S. C. Lyu, Y. Zhang, C. J. Lee, H. Ruh, and H. J. Lee, "Low-temperature Growth of ZnO Nanowire Array by A Simple Physical Vapor-Deposition Method." *Chemistry of Materials* **15** (2003) 3294-3299.

[247] W. Il Park, G. C. Yi, M. Y. Kim, and S. J. Pennycook, "ZnO Nanoneedles Grown Vertically on Si Substrates by Non-Catalytic Vapor-Phase Epitaxy." *Advanced Materials* **14** (2002) 1841-1843.

[248] T. Seiyama, A. Kato, K. Fujiishi, and M. Nagatani, "A New Detector for Gaseous Components Using Semiconductive Thin Films." *Analytical Chemistry* **34** (1962) 1502-&.

[249] H. W. Ryu, B. S. Park, S. A. Akbar, W. S. Lee, K. J. Hong, Y. J. Seo, D. C. Shin, J. S. Park, and G. P. Choi, "ZnO Sol-Gel Derived Porous Film for CO Gas Sensing." *Sensors and Actuators B-Chemical* **96** (2003) 717-722.

[250] D. Gruber, F. Kraus, and J. Muller, "A Novel Gas Sensor Design Based on $CH_4/H_2/H_2O$ Plasma Etched ZnO Thin Films." *Sensors and Actuators B-Chemical* **92** (2003) 81-89.

[251] W. J. Moon, J. H. Yu, and G. M. Choi, "The CO and $H_{-2}$ Gas Selectivity of CuO-Doped $SnO_2$-ZnO Composite Gas Sensor." *Sensors and Actuators B-Chemical* **87** (2002) 464-470.

[252] D. F. Paraguay, M. Miki-Yoshida, J. Morales, J. Solis, and L. W. Estrada, "Influence of Al, In, Cu, Fe and Sn Dopants on the Response of Thin Film ZnO Gas Sensor to Ethanol Vapour." *Thin Solid Films* **373** (2000) 137-140.

[253] X. L. Cheng, H. Zhao, L. H. Huo, S. Gao, and J. G. Zhao, "ZnO Nanoparticulate Thin Film: Preparation, Characterization and Gas-Sensing Property." *Sensors and Actuators B-Chemical* **102** (2004) 248-252.

[254] C. Baratto, G. Sberveglieri, A. Onischuk, B. Caruso, and S. di Stasio, "Low Temperature Selective $NO_2$ Sensors by Nanostructured Fibres of ZnO." *Sensors and Actuators B-Chemical* **100** (2004) 261-265.

[255] H. M. Lin, S. J. Tzeng, P. J. Hsiau, and W. L. Tsai, "Electrode Effects on Gas Sensing Properties of Nanocrystalline Zinc Oxide." *Nanostructured Materials* **10** (1998) 465-477.

[256] H. Kind, H. Q. Yan, B. Messer, M. Law, and P. D. Yang, "Nanowire Ultraviolet Photodetectors and Optical Switches." *Advanced Materials* **14** (2002) 158-160.

[257] Z. L. Wang, "Nanostructures of Zinc Oxide." *Materialstoday* **7** (2004) 26-33.

[258] J. Y. Lao, J. Y. Huang, D. Z. Wang, and Z. F. Ren, "ZnO Nanobridges and Nanonails." *Nano Letters* **3** (2003) 235-238.

[259] Z. L. Wang, "Zinc Oxide Nanostructures: Growth, Properties and Applications." *Journal of Physics-Condensed Matter* **16** (2004) R829-R858.